

Czech Technical University in Prague
Faculty of Electrical Engineering

Doctoral Thesis

June 2019

Martin Daněk

Czech Technical University in Prague

Faculty of Electrical Engineering
Department Control Engineering

***DESIGN OF WEAR RESISTANT
COATINGS FOR HIGH TEMPERATURE
INDUSTRIAL APPLICATIONS***

Doctoral Thesis

Martin Daněk

Prague, June 2019

Ph.D. program: Electrical Engineering and Information Technology - P2612
Branch of study: Electrotechnology and Materials - 2602V009

Supervisor: Prof. Ing. Tomáš Polcar, Ph.D.

Acknowledgment

First of all, I would like to thank all readers of this thesis, because without you there would be no meaning in spending almost five years writing it. I hope you will enjoy the adventurous journeys of atoms as they follow the treacherous paths of plasma physics and inscrutable experiments.

Special thanks are also directed to my newborn son, Ervin. Thanks to his intervention, I prolonged the enjoyable time spent working on this thesis. I would like to express my deep gratitude to my wife Pája, for willingly changing romantic evenings for tea and cakes, while I was writing more and more paragraphs.

Also, I would like to thank my supervisor, prof. Polcar, for letting me go through the doctoral study without significant limitations, his idea of establishing a spin-off company, and his clever guidance during the turbulent beginnings of this project.

I thank all of my colleagues who helped me with the research and experiments, namely Filipe, Alberto, Emilio, Antonio, Tomáš, and Paolo. Also, many thanks to Jakub, who taught me a lot about industrial coatings and strongly opposed the academic point of view on the coating process. To Ben, for reading and correcting the language so many times, that I suspect he now knows more about sputtering than me.

So for all of you and many more: May the Force be with you!

Declaration

I hereby declare that I have worked on my doctoral thesis independently and I cited the used literature consistently.

Author Share Specification:

TGA, DSC, and XRD measurements in Chapter 5.2 were conducted in Portugal by Dr. Filip Fernandes of the University of Coimbra.

Annotation

The thesis deals with the deposition and practical applications of coatings applied by the magnetron sputtering method. The thesis is divided into two main parts - theoretical and practical. The theoretical section deals mainly with a summary of our current understanding of coatings, material growth, and application of coatings for use at high temperatures. Included therein is a description of technologies for the deposition of protective coatings, with a focus on magnetron sputtering. The discussion about magnetron sputtering technology emphasizes the differences between sputtering in the laboratory and under industrial conditions. Emphasis is also placed on the industrial pre-treatment of the individual tools and materials prior to coating, so that the pre-treatment meets the desired purpose of the coating. The practical part is divided into two chapters. The first chapter deals with coatings used for modern high-speed machining without the use of a cooling liquid. This chapter details the optimization of the commonly used TiAlN coating by doping it with chromium. A sputtering model is presented, which predicts a multilayer coating structure. For the TiAlN coating and the three variants of TiAlCrN, each of which has a different chromium content - oxidation resistance, temperature resistance, wear resistance, mechanical and tribological properties are analyzed. Subsequently, these coatings are tested by machining under severe conditions. The second chapter deals with the design and testing of coatings for the protection of tools used for high-pressure aluminum casting. The mechanical and thermal stresses of these tools are analyzed. Based on this analysis, a two-layer coating architecture is designed. Within this two-layer coating the base layer has the purpose of increasing the adhesion of the coating and reducing the effect of internal stress in the steel caused by thermal cycling on the cracking of the steel substrate. The top layer protects the tool and the base layer from abrasion and adhesion of the molten aluminum. The best nitride and oxide coating candidates are selected for each of the layers. The lower layer is predominantly tested by thermal cycling, and the top layer is mechanically and chemically stressed. In the summary of the thesis, the results of the practical tests are presented, and contextualized in terms of application-specific coatings.

Key words: PVD coating, magnetron sputtering, dry machining, high pressure casting, tribology, oxidation resistance, thermal resistance, thermal cycling, TiAlN, TiAlCrN, AlCrN, $(AlCr)_2O_3$

Anotace

Dizertační práce se věnuje problematice nanášení a využití povlaků deponovaných metodou magnetronového naprašování. Práce je členěna do dvou hlavních částí – na část teoretickou a praktickou. Teoretická část se zabývá převážně shrnutím poznatků o povlacích, růstem materiálů a aplikací povlaků pro využití za vysokých teplot. Jsou zde rozebrány jednotlivé technologie pro tvorbu ochranných povlaků se zaměřením na magnetronové naprašování. U technologie magnetronového naprašování jsou zdůrazněny rozdíly v naprašování povlaků v laboratorních podmínkách a průmyslových podmínkách. Zároveň je kladen důraz na průmyslovou předúpravu jednotlivých nástrojů a materiálu před povlakováním, tak aby předúprava odpovídala požadovanému účelu povlakování. Praktická část je rozdělena na dvě kapitoly. První kapitola se zabývá problematikou povlaků pro moderní obrábění vysokými rychlostmi bez využití chlazení. V této kapitole je optimalizován průmyslově běžně využívaný povlak TiAlN dopováním chromem. Je představen naprašovací model, který předpovídá multivrstvou strukturu povlaku. Pro povlaky TiAlN a tři verze TiAlCrN povlaků s různým obsahem chromu je analyzována oxidační odolnost, odolnost proti teplotě, odolnost proti opotřebením, mechanické a tribologické vlastnosti povlaků. Následně jsou tyto povlaky testovány obráběním za náročných podmínek. Druhá kapitola praktické části se zabývá návrhem a testováním povlaku pro ochranu nástrojů využívaných pro vysokotlaké lití hliníku. Je analyzováno mechanické a tepelné namáhání těchto nástrojů. Na základě této analýzy je navržena dvouvrstvá architektura povlaku. Kde spodní vrstva má za účel zvýšení adheze povlaku a snížení vlivu vnitřního napětí v oceli, způsobeného tepelným cyklováním, na vznik trhlin v ocelovém substrátu. Vrchní vrstva chrání nástroj a spodní vrstvu před abrazí a adhezí způsobenou tekutým hliníkem. Pro každou z vrstev jsou na základě literatury a průmyslových zkušeností vybrány nejlepší povlaky na bázi nitridů nebo oxidů. Spodní vrstva je testována především tepelným cyklováním a vrchní vrstva je mechanicky a chemicky namáhána. V závěru práce jsou uvedeny výsledky testování praktické části a zároveň představeny konkrétní aplikace vyvinutých povlaků ve strojírenské praxi.

Klíčová slova: PVD povlakování, magnetronové naprašování, obrábění nasucho, vysokotlaké lití, tribologie, oxidační odolnost, tepelná odolnost, tepelné cyklování, TiAlN, TiAlCrN, AlCrN, $(AlCr)_2O_3$

Content

Czech Technical University in Prague	1
1. Introduction	11
1.1 Coating approach.....	12
1.2 Examples of coated tools	13
2. An overview of hard thin film preparation.....	16
2.1 Thin film preparation methods	16
2.1.1 Chemical Vapor Deposition	16
2.1.2 Physical Vapor Deposition.....	18
2.2 Thin film growth by magnetron sputtering process	20
2.2.1 Creation of free atoms.....	20
2.2.2 Reactive sputtering	21
2.2.3 Target poisoning and the hysteresis effect	22
2.3 Glow discharge	23
2.4 Development of magnetron sputtering.....	26
2.4.1 Magnetron sputtering	26
2.4.2 Unbalanced magnetron sputtering.....	27
2.4.3 Closed-field magnetron sputtering (CFMS)	28
2.5 Pulsed magnetron sputtering.....	30
2.5.1 Deeper insight into pulsed magnetron sputtering.....	30
2.5.2 Effect of energetic species on films	30
2.5.3 +Mechanism of the creation of high energy species	31
2.5.4 Effect of pulsing parameters on ion flux.....	34
2.5.5 Variable field magnetrons.....	35
2.6 Bias used in magnetron sputtering	36
2.7 Industrial coating preparation	36
2.7.1 The geometry of sputtering machines	36
2.7.2 Batching material, Batching process	38
2.7.3 Gas inlet, cathodes, targets, etc.	41

2.7.4	Substrate pretreatment.....	42
2.7.5	Vacuum pretreatment.....	45
2.7.6	Growth defects.....	50
2.7.7	Conditioning.....	53
3.	Thin film growth.....	54
3.1	Thermodynamics criteria of growth rate.....	54
3.2	Kinetics.....	57
3.3	Film structure.....	57
3.3.1	Structure zone models.....	58
3.4	Stress in thin film.....	60
3.4.1	The origin of thermal stress.....	60
3.4.2	The origin of intrinsic stress.....	61
3.5	Solid solution and bonding.....	63
3.5.1	Solid solution.....	63
3.5.2	Cohesive energy.....	64
3.6	Thermal behavior of thin films.....	65
3.6.1	Diffusion and its effects in the thin films.....	65
3.6.2	Atomic paths.....	66
3.6.3	Thermal stability of hard coatings.....	68
3.6.4	Recovery.....	75
3.7	Mechanical properties of coatings.....	76
3.7.1	Hardness, H.....	76
3.7.2	Young elastic modulus, E.....	78
3.7.3	H ^x /E ^y ratios.....	79
4.	State of the art industrial coatings.....	80
4.1	Industrial used PVD nitride coatings.....	80
4.1.1	Binary nitrides.....	81
4.1.2	Ternary nitrides.....	82
4.1.3	Quaternary nitrides.....	86

4.1.4	Coatings morphology	89
4.2	Coatings of cutting tools	92
4.2.1	Motivation.....	92
4.2.2	Types of cutting tools and processes	94
4.2.3	Failure mechanism of cutting tools	97
4.2.4	Cutting tool materials.....	100
4.3	Coatings for forming tools.....	101
4.3.1	Types of forming processes	101
4.3.2	Coating of aluminum high-pressure die casting (HPDC) tools	103
5.	Experimental approach.....	106
5.1	Evaluating techniques	106
5.1.1	Mechanical properties	107
5.1.2	Tribological testing	110
5.1.3	Structural and chemical composition	111
5.1.4	Thermal properties	114
5.1.5	Cutting properties.....	114
5.1.6	Sputtering chamber.....	115
5.2	Development of temperature-resistive coatings for cutting tools.....	116
5.2.1	Rotation model.....	117
5.2.2	Testing samples for tool coating.....	122
5.2.3	Sputtering process	123
5.2.4	Coating evaluation	125
5.2.5	Results and discussion – cutting tools.....	125
5.2.6	Conclusion – Cutting tools.....	149
5.3	Development of coating for aluminum high pressure die casting	150
5.3.1	Motivation.....	150
5.3.2	Base layer development.....	151
5.3.3	Shield layer development	153
5.3.4	Results and discussion – High pressure die casting.....	155

5.3.5	Conclusion – Aluminum high pressure die casting	171
5.4	Chosen industrial applications solved in AdvaMat s.r.o.	174
5.4.1	High pressure aluminum die casting.....	174
5.4.2	Cutting.....	176
5.4.3	Glass molds	178
6.	Summary.....	180
6.1	Summary of the research	180
6.2	Summary of industrial part.....	182
	References.....	183
	List of publications.....	191
	* Percentage is based on V3S database	192
	Annexes:	193

Preface

The primary motivation of my Ph.D. study was to undertake some kind of industrial Ph.D., which is not common in Czech universities. Recognising that my supervisor, Prof. Polcar, has a vast knowledge of R&D in the area of thin films, and I had some previous experience in entrepreneurship, we decided to establish a new company, ideally university spin-off, dealing with PVD coatings specializing in research and development. In the town of Jihlava, 130 km from Prague, there is the VTP Vysočina scientific and technical park, with whom we agreed a mutually advantageous cooperation. Based on this cooperation, we gained access to a industrial PVD sputtering unit CemeCon 880/9 MLT and some basic measuring and peripheral technologies.

The agreed setup for the company, named AdvaMat s.r.o. (AdvaMat = Advanced Materials), was that Prof. Polcar would be the only owner with 100% equity, and that I should serve as CEO with all decision rights and sole access to bank accounts. Prof. Polcar invested 100 000 CZK (ca 4000€) as a starting capital and I dealt with all legislative issues still existing in the Czech Republic that concern starting a new company. AdvaMat s.r.o. was successfully established on the 2nd of June 2014. Due to our ongoing work at the Czech Technical University in Prague (CTU), we were trying hard to obtain clearly defined legal status. In many countries, the universities are usually keen to establish their spin-off or spin-out companies, where the university owns a share in the company. This is not the case at CTU, and mostly we were the pioneers in this effort, in which we have not succeeded entirely. As a partial success, we developed a special coating in close cooperation between AdvaMat and CTU, and licensed this coating for AdvaMat. Based on this cooperation, AdvaMat obtains the status “CTU Start-up.” According to the deal closed between AdvaMat and CTU, AdvaMat s.r.o. pays fees for the use of the licensed coating, while it can use the name, logo and other PR channels of CTU. Over the last four years, we had to move all sputtering equipment twice. The first time was due to the scientific park in Jihlava going bankrupt, which happened because of some internal management issues. We moved our equipment to another coating company. Throughout the next 18 months, we were fighting legal battles with a bankruptcy administrator to maintain control over the sputtering apparatus, resulting in our purchase of the equipment from a new owner. Yet, despite all the problems, we established a new company solidly at the market, we generate profit and are in discussion of a massive company development with several investors.

From the very beginning, AdvaMat was active in Europe and Czech research funding grants. In 2014 we worked on FP7 project “AGRISENSACT”, creating soil sensors for smart

agriculture. The result of that project was later monetized and sold to a company in accordance with project rules. In 2016, we were granted funding for project "ICARUS" from the H2020 FET Open project call. We became only the second company in the Czech Republic to win this very competitive project. Although Czech funding opportunities almost eliminate young companies from funding calls, our close cooperation with other Czech companies brought in some interesting projects; the value of these totaled almost 4 000 000 € for the Czech Technical University, and greatly helped with the development of our research group.

1. Introduction

The increasing demand for more efficient manufacturing in industry leads to many applications of manufacturing technologies. Standard technologies such as a die casting, machining, forging, *etc.* have been well studied for decades, and so it is difficult to make any serious progress in these areas - at least in terms of the engineering of bulk material. This gives greater scope for emerging technologies based on nanotechnology and materials science, namely thin films and coatings. These coatings can easily grant superior performance to standard tools, thus increasing their lifetime significantly. The coatings described in this study are generally created by the physical vapor deposition (PVD) technique. The apparatus used for this purpose is a magnetron sputtering device, guaranteeing high uniformity and low roughness to the coating. One of the main advantages of magnetron sputtering is that the coating composition can be varied easily, which hastens the development process for new films.

The typical problems solved by wear-resistant high-temperature coatings take place in machining and forming industry. The machining industry is the biggest customer for PVD deposited super hard coatings. Applications of these coatings include cutting tools such as drills, mills, cutting inserts, *etc.* Performance metrics that each coating must satisfy are thermal stability, high hardness, toughness, low friction and adhesion resistance. Nowadays, titanium aluminum nitride (TiAlN) is the most widespread coating because of its sufficient thermal stability (up to 900°C), high hardness, oxidation resistance and adhesion resistance. The ability of TiAlN to retain its hardness even at high temperatures is based on the spinodal decomposition of the structure. A metastable cubic solid solution of TiAlN decomposes into c-AlN and c-TiN. Upon a further increase in temperature, domains of c-TiN and c-AlN grow, and c-AlN is transformed into a stable - but softer - h-AlN, and the hardness of the coating decreases. Adding chromium to TiAlN is supposed to hinder the spinodal decomposition by slowing the diffusion and formation of c-TiN and c-AlN domains. Unlike titanium, chromium nitride has much better oxidation resistance and its segregation to grain boundaries in the surface regions significantly improves oxidation resistance.

Other prospective industries for the application of PVD coatings is the aluminum die casting industry and forging industry. In both cases, there appear extreme temperatures and very high pressures. The main properties that a coating for these industries needs to have are thermal stability up to 1000°C, low-temperature conductivity to suppress heat propagation, high thermal cycling fatigue resistance due to the constant cooling and heating of the material, and sufficient toughness to withstand the abrasion from steel and/or hard silicon clusters in aluminum compounds. Surprisingly, the most important property of coatings for high pressure die casting (HPDC) of aluminum is the inertness of the coating with respect to the aluminum.

This feature suppresses the sintering of aluminum to the coated specimens (molds, pins, etc.). Sintered aluminum on the rods needs to be cleaned off manually, thus prolonging the downtime of the molding process drastically. The inertness of the coating, reduced aluminum wettability, can be engineered by inducing strong covalent bonds in the coating, so no binding energy is directed outwards. Until now, the most widely used coating for aluminum molding is AlCrN, which improves the performance to some degree. However, there are other options for the coating such as titanium diboride (TiB₂) or alumina (Al₂O₃). Both of these coatings have very high hardness and a lower aluminum wettability than AlCrN coatings due to the strong covalent bonds between the atoms. Another way of improving the properties of the coatings for molding and forging applications is decreasing the thermal diffusivity. The coefficient of thermal diffusivity represents the ability of the coating to conduct heat. Heat is conducted through the material by phonons. The inner structure of the coating can be engineered in such a way that it restricts and/or scatters more phonons, thereby slowing the propagation of heat. It has been shown that this can be achieved by introducing a fine structure with induced boundaries such as multilayers. Multilayers also increase the toughness of the coating by decreasing the brittleness.

In all cases, the structure and composition of the coating are responsible for its properties. Therefore, in the first chapters, I focus on the growth of the film as well the parameters of the sputtering apparatus influencing the growth of the film. Up to now, the parameters are more connected with the sputtering machine than to physical fundamentals. The transfer from one apparatus to another regularly causes a problem as the conditions for coating growth are unique and varies widely with the techniques used.

1.1 Coating approach

All coatings developed in cooperation with AdvaMat s.r.o., and later studied and presented in this work, were based on specific customer needs or some problem faced in the industry. In many cases, the final evaluation was performed by the customer. It should be noted that the testing performed by the customer is also a crucial parameter, which depends strongly on the operator. Many tool failures happen when workers are not handling the tool properly, e.g. crushing into the mold at full speed, where a careful approach is actually needed. Also, the operational staff are not usually directly involved in the development, or, worse still, are not willing to change processes or suppliers. Thus, proper evaluation of some long running processes (high-pressure die casting) took years.

In order to find areas of industry where I should begin with thin coatings improvement or development, I visited various manufacturing companies in the Czech Republic (mainly metal machining, metal forming, and plastic forming). In all instances I was not introducing our product, but rather I was trying to understand their problems and requirements. Based on this I selected three main areas of industry on which to focus – (i) high-speed, non-cooled steel machining (ii) high-pressure aluminum die casting (HPDC) and (iii) plastic processing. The latter one is not part of this thesis, due to the fact that the need for high-temperature resistivity is not the main issue. It should be noted that AdvaMat s.r.o. almost withdraw from PVD coatings for cutting tools, even though we have a very competitive solution, because the competition in this area is exceptionally strong in the Czech Republic, and prices are subsequently driven down. Real application testing of HPDC was carried out in Aisan industries CZ, where, during the first year, up-to-date coatings (AlTiN + Al₂O₃) were tested and compared with almost all available coatings provided by competitors. Based on the results and observed failure mechanisms, new coatings have been developed, as shown in the experimental part of this work.

1.2 Examples of coated tools

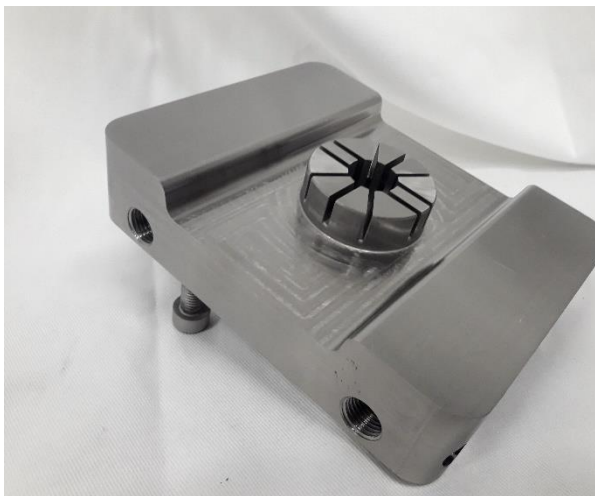


Figure 1-1 Steel mold coated with CrN



Figure 1-2 Steel mold for HPDC coated with AlTiN

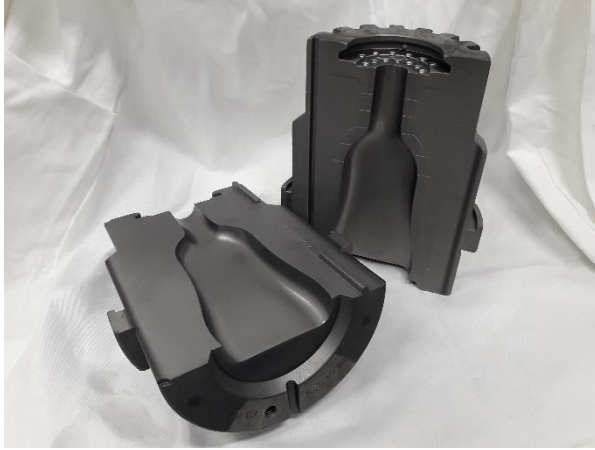


Figure 1-3 Glass molds with TiAlCrN coating



Figure 1-4 Forming pins with TiAlCrN coating



Figure 1-5 Plastic forming pins with CrN coating



Figure 1-6 Steel molds with TiAlCrN coating



Figure 1-7 Metal forming mold with TiAlCrN coating



Figure 1-8 Drills with $(\text{CrAl})_2\text{O}_3$ coating



Figure 1-9 Cutting tools with TiN coating

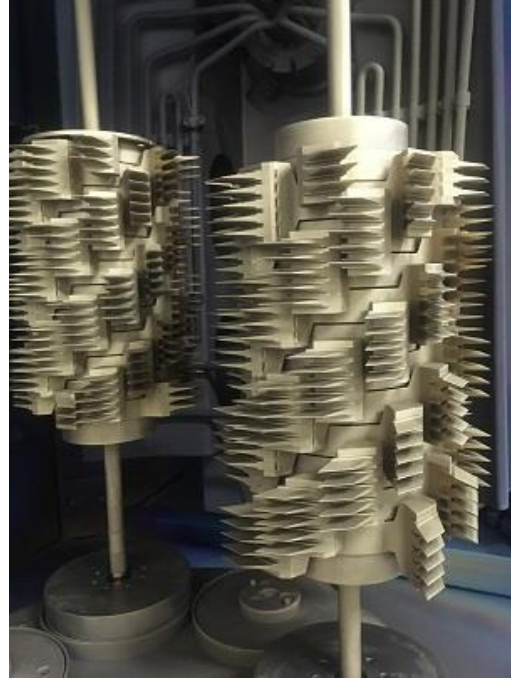


Figure 1-10 Mills with TiN coating

2. An overview of hard thin film preparation

The formation of a film and its microstructure is strongly dependent on the technique of its preparation and the conditions used. In this section, we describe the technique of magnetron sputtering and present a review of the film properties investigated. In the next chapter, the atomistic approach to thin film growth is presented, and the significance of many sputtering parameters is assigned to the mechanical and structural properties of the final material.

All techniques of physical vapor deposition share the common trait that, due to the relatively low deposition temperature, the assembly kinetics of the growing film is limited. This phenomenon allows us to control the material in such a way that defects, supersaturated and metastable phases are easily induced into the film. This phenomenon is used to create a broad range of unusual properties in the material, which can't be created by any other processing method.

2.1 Thin film preparation methods

The two main techniques used to prepare thin films for tools are physical vapor deposition (PVD) and chemical vapor deposition (CVD). Both of them have found their field of use in the coating of tools, and both of them are applied in a vacuum environment. They are quite flexible, and also very well studied, so they can produce coatings with different chemical composition and different architectures (single layer, multilayer, composite and nanostructured). Also, crystal structure, surface morphology, and orientation can be controlled by both methods.

2.1.1 Chemical Vapor Deposition

CVD coatings are formed by chemical reactions taking place in the vicinity of the substrate. To facilitate the reactions, high temperatures in the range of 700 – 1050°C are necessary. The atoms are taken from precursor gasses and introduced to the reactor chamber. A schematic representation is shown in Figure 2-1. The advantage of requiring high temperature is that the coating does not form on the walls, nor other non-heated surfaces of the reactor, and the growth of the film can be controlled on the tool or another surface. That said, these high temperatures restrict the choice of substrate to high-quality tungsten carbide and eliminates tool steels and other temperature sensitive materials. Another difference between CVD and PVD processes - and the main advantage of CVD coatings - is the fact that CVD is not a line-of-sight process, so very complex geometries can be coated as well.

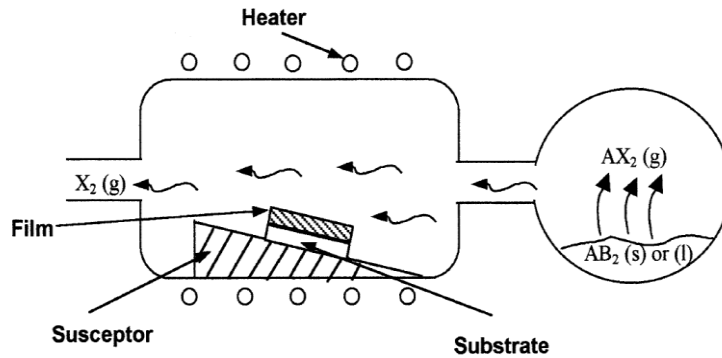
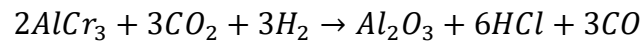


Figure 2-1 A schematic diagram of the CVD coating [1]

An example of Al_2O_3 reaction [1]:



Equation 2-1

The most widely used CVD coatings nowadays are α - Al_2O_3 , TiN and TiCN. All of these coatings can achieve very high hardness and great wear resistance. While TiN and TiCN coatings can also be prepared by PVD, high quality α - Al_2O_3 is only achievable by CVD. The α - Al_2O_3 coating is chemically inert with low thermal conductivity, and can be coated at thicknesses of tens of microns. Moreover, the CVD process has a faster deposition rate than most PVD processes. This advantage is used when coating cutting inserts for turning and other cutting operations. Recently, good quality CVD diamond coatings have been introduced to the market. These coatings perform very well in the cutting of modern carbon composite and hard to cut materials such as nickel and titanium alloys.

The main drawbacks of CVD coatings are the usage of toxic, corrosive and environmentally non-friendly precursor gases. Also, for more complicated solutions, it is difficult to maintain the correct stoichiometric, because more precursors gasses are needed. Each precursors gas has different vaporization rates, leading to a complex problem.

There are many modifications of the basic CVD process such as plasma-assisted CVD, plasma-enhanced CVD, photo-assisted CVD, aerosol-assisted CVD, *etc.* Every one of these modifications deals with the drawbacks, and more information can be found in Choy's summary [1].

2.1.2 Physical Vapor Deposition

PVD coatings are formed from vapors of elements obtained by physical means such as heat, kinetic energy or ablation. The vapors are then transported and condensed on the substrate, forming a coating. The physical vapors can be obtained either from solid materials (metal targets) or from injected gasses that are decomposed by a plasma. The most regularly used PVD processes are evaporation and sputtering.

2.1.2.1 Cathodic arc evaporation (CAE)

Cathodic arc evaporation is the most commonly used technique of preparation of thin films for tool applications. The coating chamber is filled with non-reactive (predominantly argon) gas. There is a high-power low-voltage electric arc discharged on the target at a single cathode spot. The localized temperature reaches around 15 000°C. The target is equipped with metal material which absorbs heat dissipated from the discharge. A small area of the target is then evaporated, and the atoms are accelerated - in the form of 'jets' - towards the substrates.

Moreover, the energy densities of the CAE process are very high, and the atoms accelerating from the targets are ionized. The level of ionization is 30 – 100%. Later, the ionized atoms can be directed or filtered with use of electromagnetic fields. Usually, a negative bias is applied to the substrates, so the atoms coming from the cathodes are accelerated even faster and impact perpendicular to the substrate surface. This performance leads to more dense coatings produced by cathodic arc evaporation than by magnetron sputtering [2].

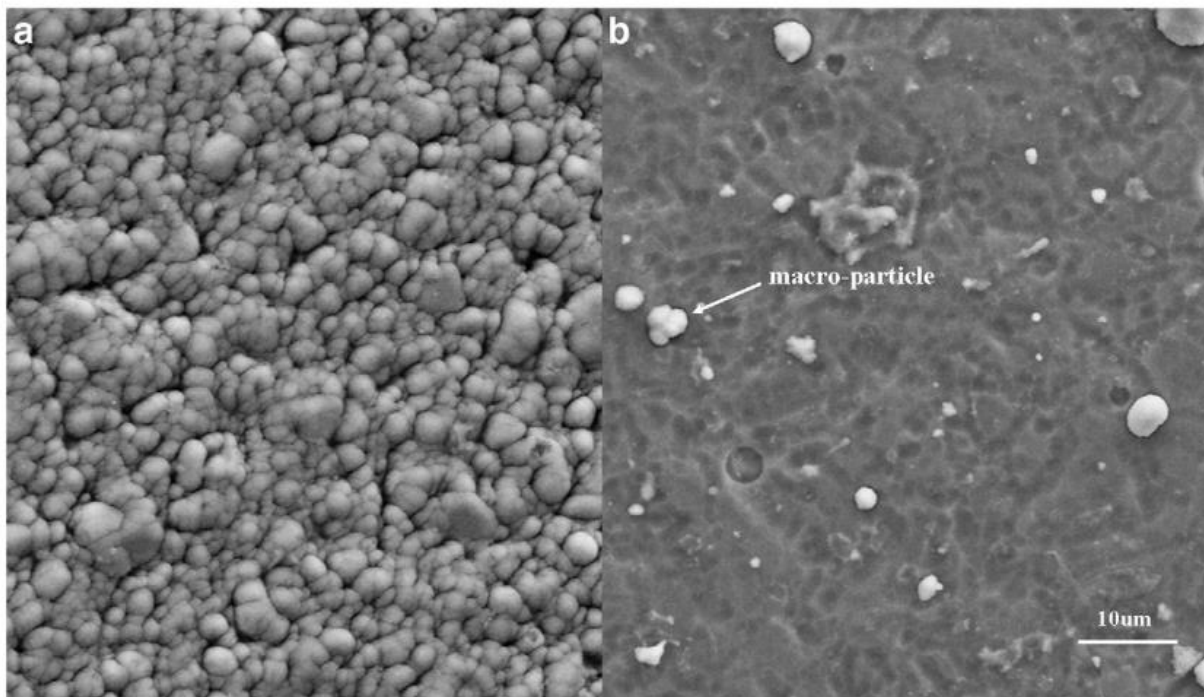


Figure 2-2 SEM surface morphology of TiAlN coatings by magnetron sputtering (a) and arc evaporation (b) [3]

The drawback of CAE is the fact that during the evaporation process not only single atoms are ejected, but clusters and macro-particles. These macro-particles then form droplets, causing soft spots in the hard coatings. At the beginning of film formation, the droplet propagates to the surface, potentially causing failure of the coating.

2.1.2.2 Magnetron sputtering

The fundamental operational principle of 'sputtering' is the ejection of atoms from the target surface by ion bombardment. If the atoms of a target material are bombarded by positive ions, the process is referred to as 'cathodic sputtering'. The sputtering chamber is evacuated to a low pressure of approximately 1 mPa. Then, the working gas is injected into the chamber. The working gas is usually argon, although in some cases it can be substituted with krypton, which due to its greater atomic mass has a higher sputtering rate for some materials. The working gas pressure is held between 300 and 700 mPa, and it is one of the crucial parameters influencing the growth and properties of the film. A sufficiently large voltage of around 600 V is then applied between the substrate and the target to form a glow discharge plasma; more details are described below. As the argon is ionized, it decomposes to Ar⁺ ions and free electrons ionizing more argon gas. The Ar⁺ ions are attracted to the negative electric potential at the target. Under the target, there are magnets that cause the free electrons to follow a spiral path in the plasma, thus increasing their energy. [4] Atoms from the target are scattered from the target towards the substrate. Usually, the degree of ionization of the target atoms is low, so it is not possible to direct their path or accelerate them to higher energies. On the approach to the target, the working atoms are also scattered by the ions from the working gas. Thus, a higher working pressure reduces the energy with which the atoms impact the substrate.

2.1.2.3 Other

Other PVD deposition techniques used for the preparation of hard coatings include electron beam deposition and pulsed laser deposition. The principles are the same as for the other PVD techniques. Electron beam deposition uses material vapors obtained by evaporation of the surface by the targeted electron beam. On the other hand, pulsed laser deposition uses laser ablation to vaporize the material.

There are combinations of PVD techniques such as laser-triggered cathodic arc evaporation, where a laser is used to trigger the cathodic arc on a precise spot and a line on the rotating cathode.

2.2 Thin film growth by magnetron sputtering process

2.2.1 Creation of free atoms

To eject atoms from the target, ions must have sufficient energy. According to Vossen [4], the energy of the ions is given by:

$$\bar{E} = \frac{2\lambda_{fp}}{L} \cdot eV_c$$

Equation 2-2

Where L is the distance between the cathode and the anode, λ_{fp} is the mean free path of the sputtering ion, V_c is the voltage used for the discharge and e is the electron charge. The mean free path is the average distance the particle travels without colliding with another particle. As the pressure is increased, the number of particles in a given volume is increased and so the probability of collision rises. Thus, the mean free path is proportional to $1/p$ in accordance with the Paschen relation.

The sputtering yield is the characterization of the effectiveness of an atomic species in causing ion ejection. It states the ratio between particles impacting and particles scattered. In other words, the number of atoms that are reflected from the target after ionic impact. The relation for sputtering yield is given by the formula :

$$S = \frac{3\alpha}{4\pi^2} \cdot \frac{m_1 * m_2}{(m_1 + m_2)^2} \cdot \frac{E}{U_0}$$

Equation 2-3

Where U_0 is the surface binding energy of the target material, α is the monotonic increasing function of m_2/m_1 , where m_1 and m_2 are the mass for impacting ion and target atom respectively. The values of α are in the range of 0.17 to 1.4 for an m_2/m_1 ratio between 0.1 and 10. Equation 2-3 is valid for ion energies up to 1keV [2]. The sputtering rate is then

$$\varphi_0 = S \cdot I_+$$

Equation 2-4

Where I_+ is the ion current flow to the target and S is the surface area of the target.

The bombardment of highly energetic ions on the target surface can initiate many other processes on the surface (other than atom ejection):

- 1) Creation of secondary electrons
- 2) Ion is reflected from the surface
- 3) Ion is implanted to the surface
- 4) Ion can cause radiation damage
- 5) Ion creates emission of X-rays

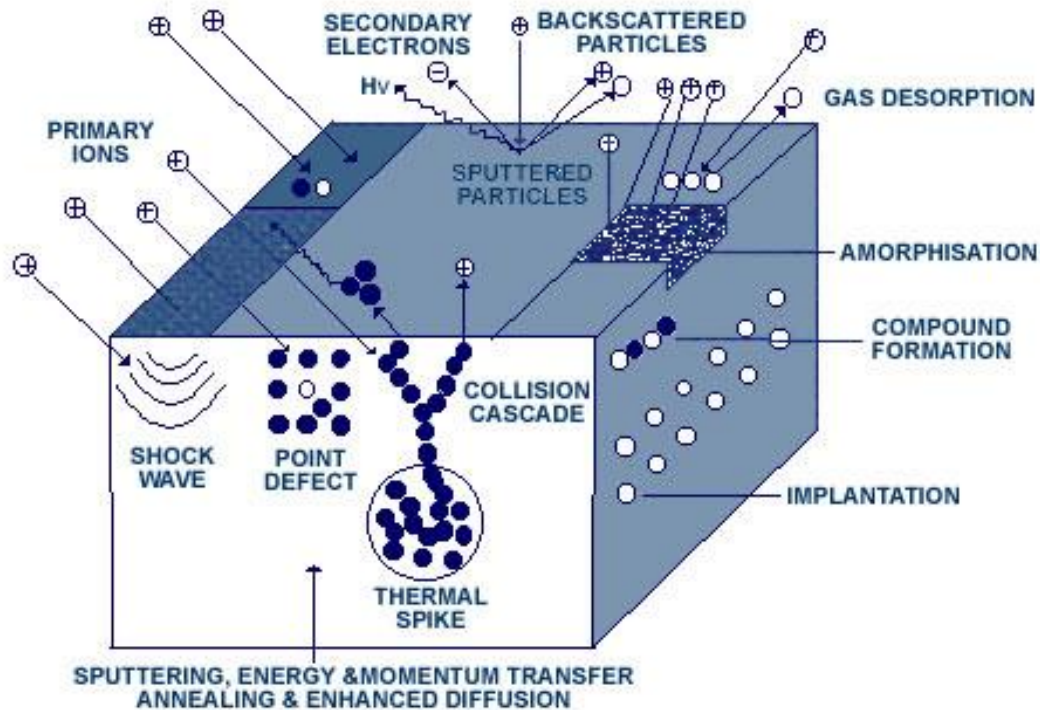


Figure 2-3 Schematic view of processes occurring after the impact of the energetic ion on the target surface [5]

Figure 2-3 also demonstrates the other effects of the impacting ions and their effect on the target material.

2.2.2 Reactive sputtering

The principles described above are related to non-reactive sputtering, where the coating is created purely from condensed atoms from the target. When nitrogen, oxygen or any other gases should be implanted in the material, the technique is called reactive sputtering. The gas is injected into the chamber *via* jets. The ratio of the pressure of this reactive gas and the working pressure is usually kept at 1:5. The partial pressure of the reactive gas controls the percentage of its atoms in the compound produced. It can be stoichiometric or under-stoichiometric.

2.2.3 Target poisoning and the hysteresis effect

When the gas is injected into the chamber, it does not only react with the sputtered material on the substrate, but actually the whole chamber as well as the targets. As the gas reacts with the targets, it is making compounds with a higher binding energy; thus, the sputtering rate is decreased, as is apparent from equation 2-2. Keeping the partial pressure at a level whereby the target is not poisoned, and the gas reacts mainly with the substrate, is the main technological issue. With the less gas injected into the chamber, the coating can be under-stoichiometric, causing serious structural problems. Target poisoning leads to the hysteresis effect, which is schematically shown in Figure 2-4.

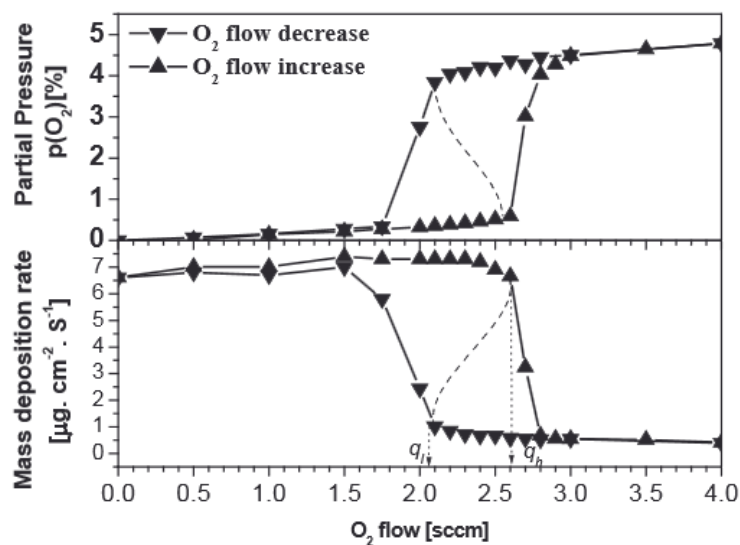


Figure 2-4 Hysteresis effect of target poisoning. Influence of oxygen flow on the process [6]

Figure 2-4 shows the partial pressure of the reactive gas, oxygen in this case, and the mass deposition rate on the reactive gas inlet flow. As the inlet volume flow is increased up to the value q_i , the partial pressure increases linearly with the mass deposition rate. All of the reactive gas is consumed for the coating formation. This is called a metallic phase. As the reactive gas flow exceeds the threshold, the sputtered metal is unable to absorb all injected gas, and the compound also begins forming on the targets. This leads to a rapid decrease of the mass deposition rate, as the binding energy of the solution is usually much higher than the binding energy of the target material. With less material sputtered, less reactive gas is consumed, and the partial pressure steeply rises by one order of magnitude. This is referred to as the transition phase. Decreasing the reactive gas flow exhibits only a small effect until reaching another threshold value of q_i , when the target is fully healed, and the sputtering is again working in the metallic phase.

The threshold for starting the poisoning of the target, q_h , is usually the best working point for the system, as the deposition rate is high and the compound is absorbing all reactive gas and has good stoichiometry. The q_1 point can be influenced by the power applied to the target, the working pressure, and the temperature. When higher power is applied to the cathodes more material is released from the target and can react with the gas. A higher working pressure means more gas particles are available in the plasma, thus target poisoning is more likely. This can be controlled by a feedback system which controls the pressure in the chamber and varies the inlet flow. The temperature increases the pressure in the plasma without increasing the number of atoms of the reactive gas. This can lead to the wrong selection of the working point. The working pressure must be selected according to the temperature used.

Another drawback of the reactive sputtering is arcing. This is a serious problem for non-conductive coatings such as oxides. Arcing is caused by a breakdown due to the high electric field strength in the thin insulating layer of the coating. Arcing can cause parts of the targets to melt and create droplets on the coating. Also, in the past it was detrimental for the power sources as it led to the negative resistivity of the plasma and a rapid increase in power. Arc events, in summary, are a grave problem. They affect the composition and mechanical properties of the growing film, and can cause damage to the magnetron power supply.

Arcing can be suppressed by using a pulse power source in RF or MF frequencies. When the duty cycle is in idle mode, the charged particles in the insulating layer are discharged before more electric charge is added. The drawback of RF sputtering is a decrease in the sputtering rate on half values.

2.3 Glow discharge

The crucial stage of magnetron sputtering is the formation of the glow discharge. From the glow discharge, the energetic particles that are emitted bombard the target to create the sputtering effect. Figure 2-5 displays the voltage-current relationship for current conduction in gasses at low pressures. As can be seen, the graph is divided into three main areas according to the amount of current: dark discharge, glow discharge, and arc discharge.

Discharge in the gasses is created when two electrodes with sufficient voltage are present. As shown in the dark region, upon increasing the voltage there is an increase the conductivity of the gas, as there are almost no charge carriers present in the gas.

After passing the breakdown voltage, there is a sudden drop in the voltage needed to conduct the current. This is because the glow discharge undergoes chain reactions and the current carriers (electrons) are generating more carriers. It can be seen that it is possible to

increase the current flow by almost four orders of magnitude without increasing the voltage. This gives us control over the process.

After passing point G, a greater voltage is needed to increase the current flow because there is another effect of current carrier creation present. After passing point H, there is an arc formed, and even more ionized particles are created. The formation of the arc leads to the virtually negative resistivity of the plasma and the current increases rapidly without control. This could damage the power source. Also, sometimes local defects in the target can lead to a rapid switch from the abnormal glow to the arc, so a power source with fast protection is needed. The protective electronics kill the current before the source is damaged.

The working point for magnetron sputtering is in the area of abnormal glow. As is explained below, this ensures uniform bombardment of the cathode/target.

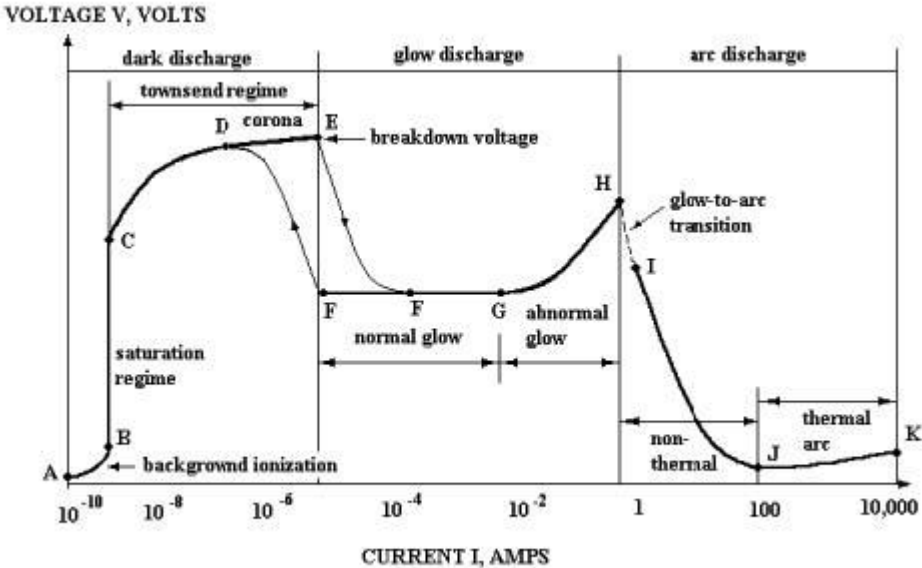


Figure 2-5 Voltage-Current characteristics for low-pressure discharge [7]

The breakdown voltage for glow discharge, point F, is defined by Paschen’s law [4] as:

$$U_b = A \frac{pd}{\ln(pd) + B}$$

Equation 2-5

Where U_b is the breakdown voltage, A and B are the material related constants, p is the pressure, and d is the distance between the electrodes. When the breakdown voltage is

reached, the discharge is self-sustainable. Figure 2-6 Regions in a glow discharge, electrical field and electrical shows the regions in the glow discharge.

Regions in the glow discharge:

Aston dark space (A): The electrons from the cathode are accelerated, but don't yet have enough energy to excite atoms

Cathode glow (B): Electrons have sufficient energy to excite gaseous atoms. The return of the excited atoms to the ground state causes the glow.

Cathode dark space (C): Electrons are accelerated to higher energies. In this region, most of the ionization of atoms occurs. Electrons induce the emission of other electrons. In this area, there is the steepest voltage drop.

Negative glow (D): The electrons have lost most of their energy due to collisions with the gas. They are moving much slower and are recombining with ions as well as exciting them. Recombination causes a glow which is visible in sputtering machines.

Faraday space (E): The energy of electrons is very small as is the electric field.

Positive column (F): Elastic collisions driven by coulomb forces are typical for this region.

Anode glow (G): Boundary of anode sheath.

Anode dark space (H): Higher potential fall due to electrons being accelerated towards the anode.

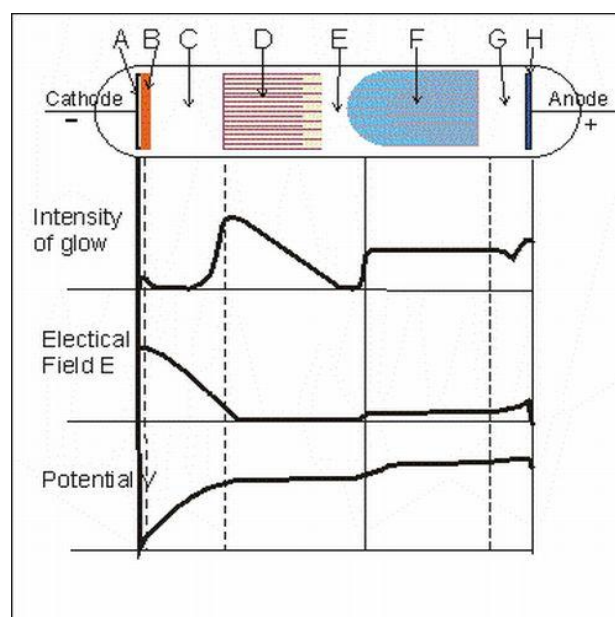


Figure 2-6 Regions in a glow discharge, electrical field and electrical [8]

To achieve the highest ratio of electron creation, the cathode dark space is most important, and so the distance of cathode (target) and anode (substrate) is held on the end of the Faraday dark space. Therefore, the positive column and farther regions (*i.e.*, anode glow and anode dark space) are not visible in the glow discharge used for sputtering. The minimum separation length between cathode and anode is twice the dark space thickness. If it is less than the dark space length, the discharge is distorted and extinguished. The secondary electrons created by impacts of ions on the target are necessarily important to sustain the glow. The breakdown voltage is the limit when impacting ions are generating enough secondary electrons to sustain the glow.

2.4 Development of magnetron sputtering

The first magnetron sputtering apparatus, a balanced one, was introduced in 1970. The unbalanced magnetron was developed in 1980, and since 1990 the magnetrons used in industry have a multi-source setup. Recent developments in non-conductive coatings and other materials led to the use of pulsed magnetron sputtering (PMS). PMS helped to prevent arcing and has a significant effect on the stabilization of the processes. Another setup is magnetrons with varying magnetic field, allowing one to control ion current delivery by changing the magnetic field. Nowadays, the development of new methods of industrial magnetron sputtering include duplex processes such as plasma nitriding in combination with magnetron sputtering.

2.4.1 Magnetron sputtering

Conventional sputtering (diode sputtering without magnets) led to high substrate heating effects. In magnetron sputtering, magnets of different strength are placed under the targets in such a way that the magnetic field is perpendicular to the electrical field [9]. One pole of the magnets is situated in the central axis of the target, and the pole is on the outer ring of the target, as is shown in Figure 2-8. This setup works as an electron trap, causing the electrons emitted from the cathode to move in the spiral trajectory instead of a direct one towards the anode. As such, the motion of the electrons is constrained in the vicinity of the target. The trapping of the electrons increases the chance of ionization of the gas atoms. Hence, the electron-atom collision occurrence is more probable.

The spiral movement of the electrons allows for more time for an electron to gain higher energy. The velocity can be described as [6]:

$$v_e = \frac{q_e \cdot E}{m_e} t$$

Equation 2-6

Where q_e is the electrical charge of the electron, E is the strength of the electrical field, m_e is the mass of electron, and t is the time. As the energy is proportional to velocity squared this setup creates a more energetic plasma than without the magnets. This leads to much higher sputtering rates than conventional sputtering techniques.

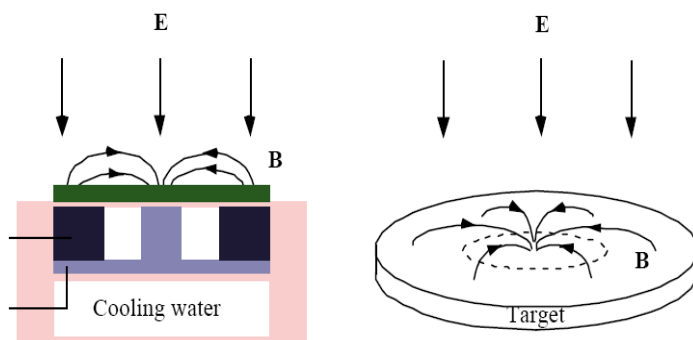


Figure 2-8 Design of magnetron target. Electrical and magnetical field [9]

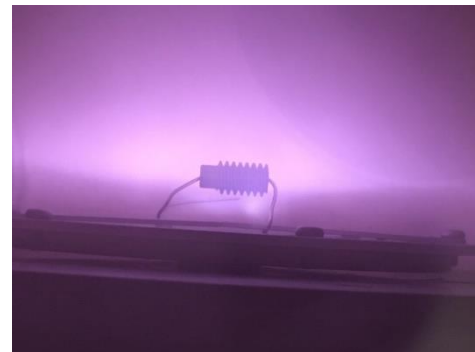


Figure 2-7 Gear under a target while depositing a coating

Easier ionization of magnetron sputtering allows for decreasing the working pressure by about one order of magnitude, and the required voltage can be reduced to 500 V from 3 000 V compared to conventional (non-magnetron) sputtering [9].

2.4.2 Unbalanced magnetron sputtering

A small difference in construction led to big changes in the performance of magnetron sputtering. Whereas the balanced magnetron sputtering (BMS) has an ion current lower than 1 mA/cm², the unbalanced magnetron sputtering (UMS) achieves fluxes much higher than 2 mA/cm². The substrate in UMS was located at a distance of 60 mm from the target, but for BMS there is already a low plasma density region because the plasma is focused on the target, so the substrate is placed 2 mm from the target. To obtain more energetic particles, higher ion bombardment was used so as to maintain the higher density of the film. Higher bombardment causes higher stresses in the film, causing negative effects on the performance.

In UMS, the outer ring of magnets is stronger than the inner ring. Not all field lines are closed. Some of the magnetic field lines are directed towards the substrate. Some secondary

electrons follow these lines, making the plasma denser in the regions near the substrate. This means that the plasma is not so strongly confined to the target and high current densities can be extracted from the plasma. The ion flux is higher by one order of magnitude than that achieved by BMS. Also, weaker ion bombardment is needed to create dense films, so the stresses in the coatings are, in general, lower. In a different setup, where the inner pole of the magnets is stronger, it is possible to produce very porous coatings. The porosity is 1000 times higher than in the conventional setup.

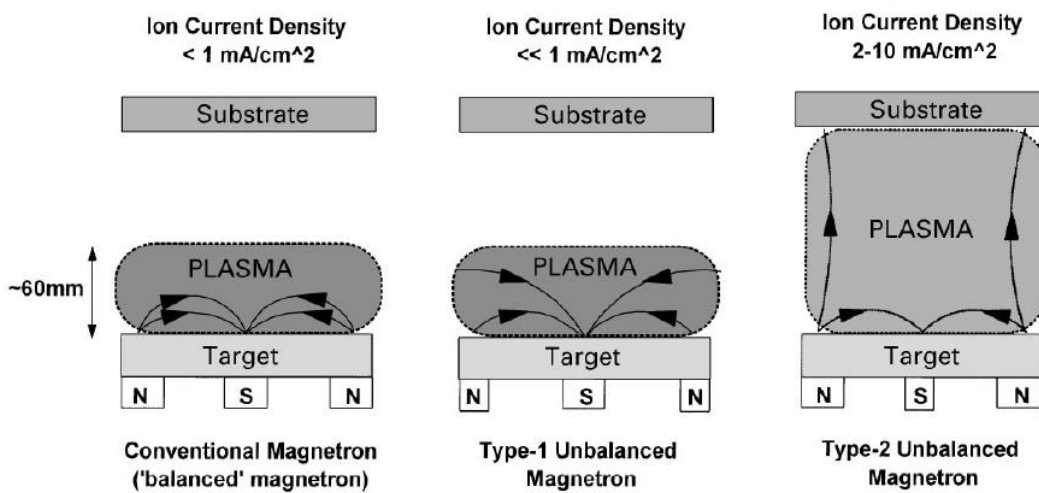


Figure 2-9 Schematic representation of the plasma confinement observed in conventional and unbalanced magnetrons [9]

2.4.3 Closed-field magnetron sputtering (CFMS)

As shown in Figure 2-9, closed-field magnetron sputtering is a setup where multiple targets are used. Magnetic arrays of opposing targets are configured identically, or mirrored with respect to each other.

Mirrored configuration: Secondary electrons are directed towards the chamber door, resulting in high loss of electrons and low plasma density.

Closed field configuration: Field lines are connected. Substrates are located in the high-density region, and the loss of electrons is much lower

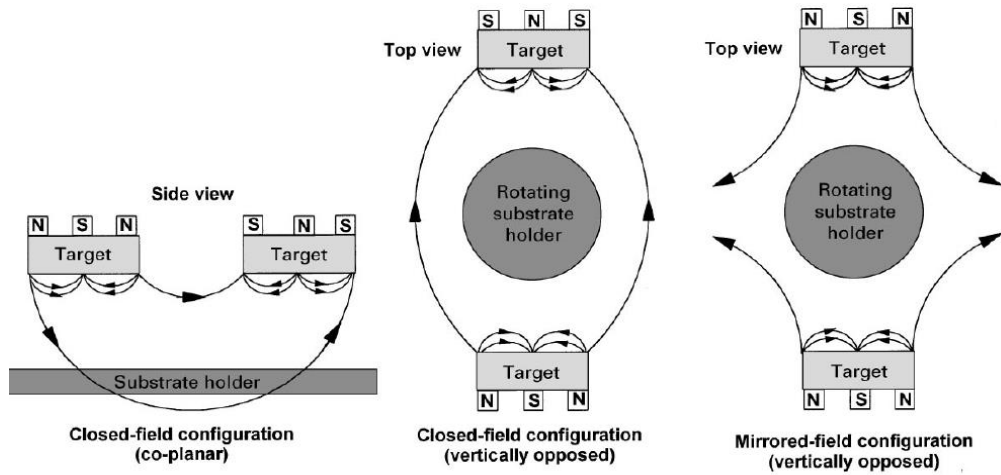


Figure 2-10 Closed field setup [9]

The development of the closed field configuration shifted the magnetron sputtering technique from a purely scientific technology to an industrial one. The CFMS is two to three times more efficient than mirrored or single target configuration. The Teer Company was the first commercial company to use these magnetrons. In the industrial chamber design, there is an even number of magnetrons opposed to one another, and there is usually a rotating substrate holder in the center for uniform distribution of the coating. The use of high strength rare earth magnets increases the ion current significantly, and an increased field strength leads to greater ionization; all of these effects induce high ion currents in plasma.

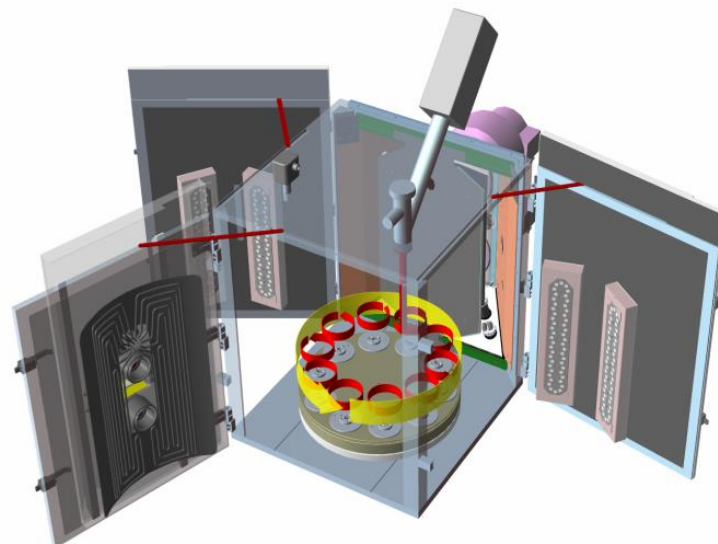


Figure 2-11 Conventional setup in industrial magnetron sputtering chamber [12]

2.5 Pulsed magnetron sputtering

Pulsed magnetron sputtering (PMS) enables stable, arc-free deposition and limits plasma heating on the substrate. While the pulsed plasma generally has higher energy, PMS enables the creation of coatings with the same quality but at lower deposition temperatures. PMS is widely used in industry for the production of insulating films.

Seeing as the power on the target is pulsed (this is elaborated on below) the deposition speed is lower than standard direct current magnetron sputtering. Usual frequencies for PMS are in the range 10-200 kHz. This frequency reduces arcs effectively. The high deposition rate of ceramics films, on the order of tens of μm per hour, can be achieved.

The pulsed voltage is typically in the range 400 – 500 V. It can be pulsed in two modes:

- 1) Unipolar (0 - -400V)
- 2) Bipolar (+40 - -400V)

For bipolar mode the overshoot is controlled, usually at 10%-20% of the voltage, due to the much higher electron mobility leading to faster dissipation. The reverse time is at least 10%. Increasing the reverse voltage leads to an increased sputtering rate because the target is effectively cleaned and the target poisoning is reduced.

2.5.1 Deeper insight into pulsed magnetron sputtering

According to [10], plasmas generated by oscillation currents have greater densities and are more energetic. One of the lesser known advantages of an MF plasma is that there are very energetic species (ca. hundreds of eV) found in the plasma. The creation of such energetic species is influenced by pulsing parameters of the plasma, mainly the frequency and reverse time. Also, in a system with more magnetrons, it depends on whether the magnetrons are pulsed in the same phase or not. These more energetic species prove to be very useful for film formation. They can help to create denser films with smaller grains. On the other hand, if the species are too energetic (ca 200 eV) this leads to increased strain in the coatings and a higher number of defects. In comparison, the threshold energy for conventional DC magnetron sputtering is 10 eV.

2.5.2 Effect of energetic species on films

By controlling plasma parameters, one can control ion energy and ion flux. The more energetic species can add kinetic energy to the whole system by “pushing” other ions and atoms. This increase of kinetic energy leads to enhanced adatom mobility on of the growing film. Thus, the atoms have a higher possibility of finding an energetically more favorable place. Another effect

of greater kinetic energy is a higher back-sputtering rate, which, on the one hand reduces the growth rate, but on the other resputters the atoms which do not reside at an energetically favorable site and are thus more likely to be back-sputtered. Then, other atoms can fill the voids that would be covered by the shadowing effect explained below.

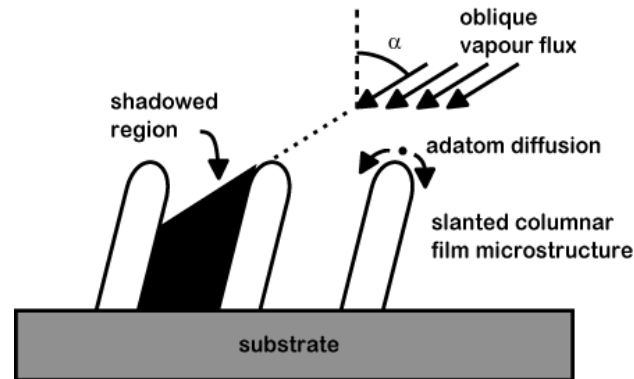


Figure 2-12 Shadowing effect [75]

Another advantage of high-energy atom bombardment is the restriction of grain growth and an increased number of nucleation sites, which leads to a finer-structured nanocrystalline film. The ion bombardment introduces the atoms in the interstitial position, which causes more compressive stresses in the coating. These compressive stresses are favorable because they increase the film hardness (resistance against penetration of another object) but, with increased film thickness, cause delamination of the film and therefore lower adhesion. This phenomenon is described more precisely in section 3.4. Stress in thin film

During sputter cleaning and plasma etching, the very energetic ions have enough energy to knock off some metal atoms and increase roughness on the order of angstroms. The energy of incident species can also influence the crystallographic orientation of the growing film. The influence on the crystallographic orientation is due to the increase in surface free energy.

2.5.3 Mechanism of the creation of high energy species

The plasma bulk is always more positive than the surface. This is because of the positive ions creating the plasma and the sheathing phenomena [11]. During the pulsing of the targets, when the target is switched from negative to positive, there is a steep voltage overshoot in the plasma. This overshoot plays an important role because of the high voltage. This voltage adds an extra accelerating potential for all the species in the plasma. According to [10], there are three energy regions identified in the plasma during sputtering. The energy measured in the previously mentioned work is the energy of N_2^+ ions during the deposition of an AlCrN film. These regions are shown in Figure 2-13.

Region A: Low energy region which corresponds to the negative pulse period of the cycle. In this period, the material is sputtered. Energies are in the range 0-10 eV, and these are the energies obtainable by conventional DC magnetron sputtering.

Region B: Energy is in the range of 20-50 eV. This energy comes from the oscillation between the positive and the negative period of the cycle. The voltage on the target is reversed from ca -500 V to ca 50 V.

Region C: The high energy in this region is gained from the fast and steep voltage overshoot at the beginning of a positive period. The energies are as high as 200 eV.

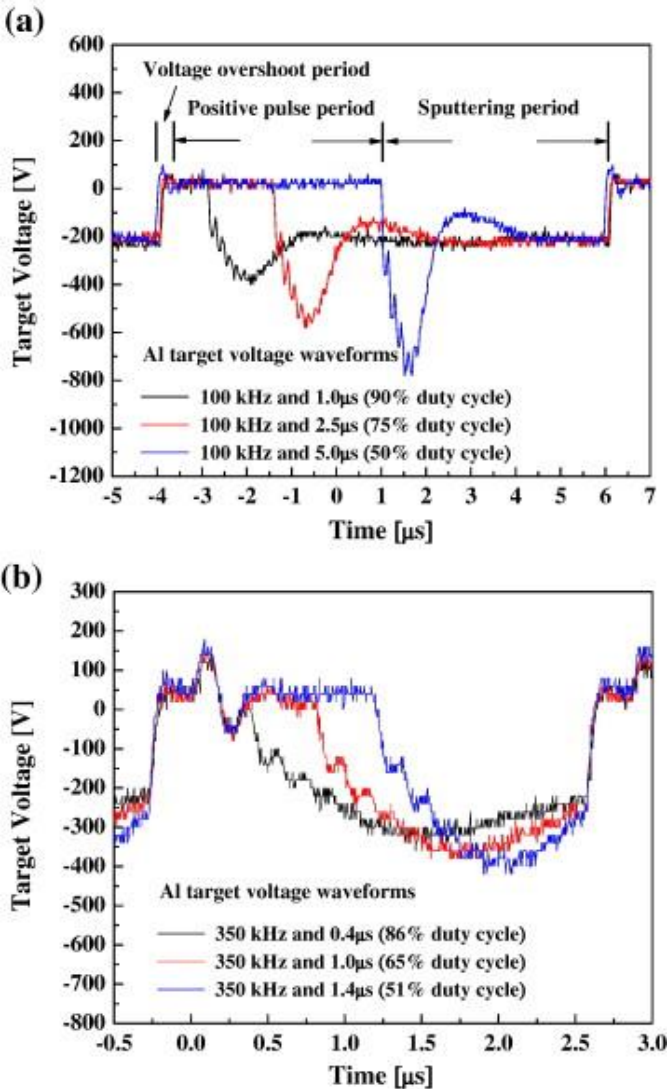


Figure 2-13 Different shapes of voltage overshoot [10]

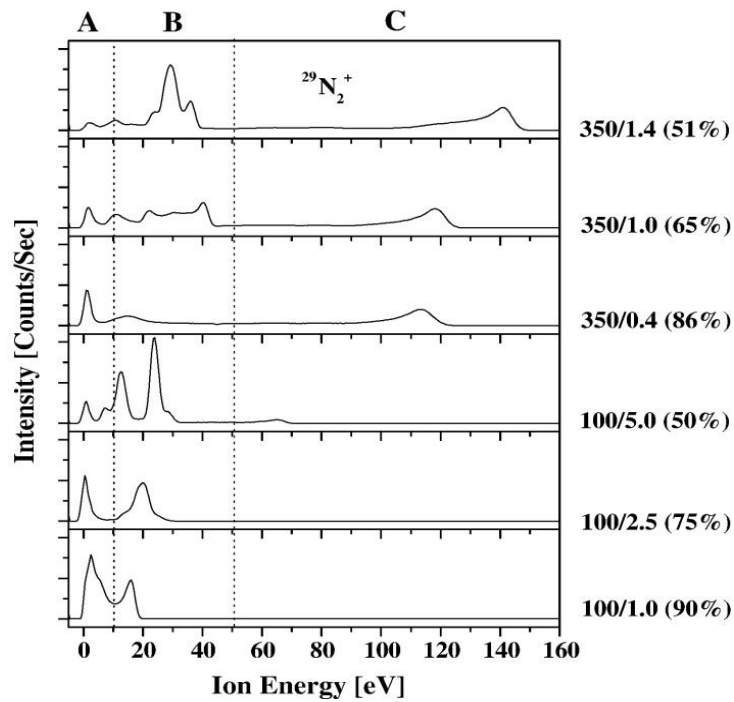


Figure 2-14 Energy regions for ions in P-CFUMS while using a different frequency and duty cycle [10]

The energies mentioned above are relevant for one given case of sputtering conditions used in [10]. The actual energy level depends on all sputtering conditions such as target power, pressure in the chamber, reactive gas composition, frequency, and duty cycle. Also, all targets have to be in the pulsing mode, and the target positive periods need to overlap.

Figure 2-14 shows the relation of ion energy on the sputtering conditions (right). The first value denotes frequency (100 or 350 kHz) and the second number is the reverse time represented by the duty cycle (time of the positive voltage/time of the whole period). As can be seen, higher energy (for this experiment) was obtained with a higher frequency and a longer reverse time.

2.5.4 Effect of pulsing parameters on ion flux

From Figure 2-15, it can be seen that the plasma exhibits a higher integrated ion flux when using a higher frequency as well as a higher reverse time. Region A is influenced by an increased reverse time, in such a way that the ion flux is decreased.. The ion flux in regions B and C is increased when using a higher reverse time. This behavior can be correlated with the target voltage during the cycle, as the ion energy is dependent on the voltage difference between the target and plasma.

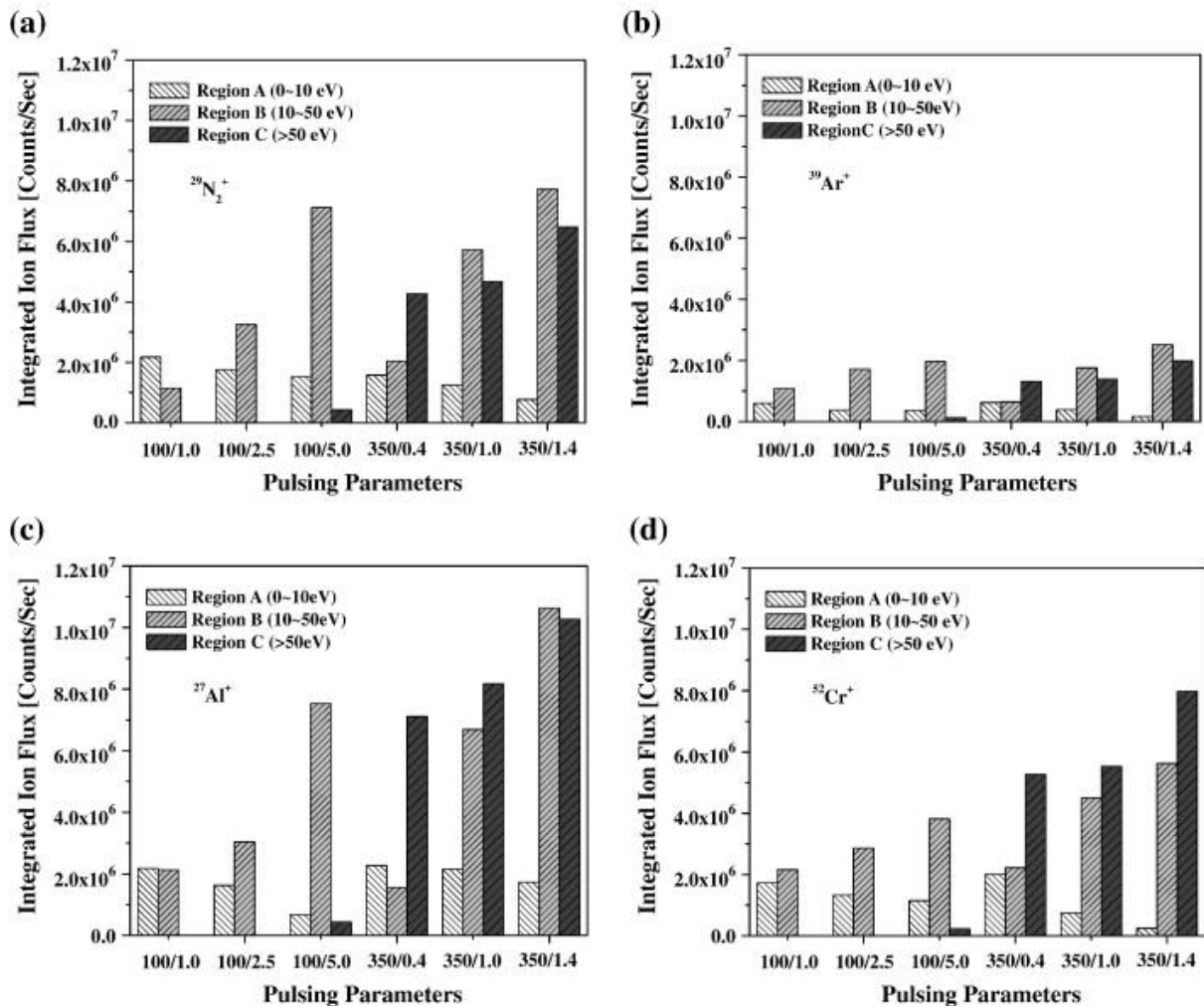


Figure 2-15 Integrated ion flux for N2+ a), Ar+ b), Al+ c), Cr+ d) in varying pulsing parameters [10]

The ions in the A region (low energy region) are generated mainly in the negative sputtering period of the cycle, *i.e.*, the longer reverse time, the more ions will be generated in region A. This negative sputtering period is the regime in which conventional DC magnetrons are working, so all the ions in DC sputtering have an energy of 0 – 10 eV. The creation of ions in the B region is dominated by the positive reverse voltage in the cycle. Most C region ions are generated with higher frequencies. As is visible in Figure 2-13, the waveform at 100 kHz and 350 kHz jumps significantly in the voltage overshoot period, when the voltage is switched

from negative to positive. So, the C region ions are generated due to this voltage overshoot. In other words, the higher the voltage difference that is created, the more energetic the ions.

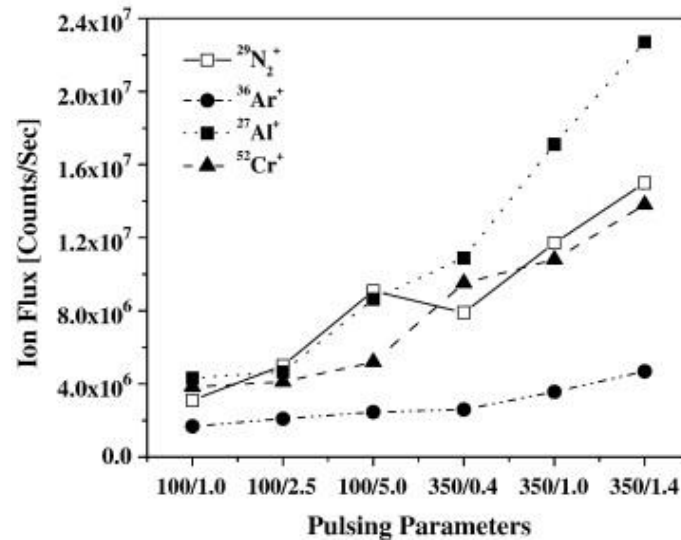


Figure 2-16 Amount of ions generated under different pulsing parameters [10]

The different number of ions from the three energy regions heavily influences the properties of the film. For example, higher ion energies induce the preferential growth of (111) structures over (200) structures due to the greater influence of strain energy, rather than surface energy, on the growth of the film. A higher frequency increases the ratio of lighter elements in the compound to the detriment of the heavier ones (Al and Cr for example) because the lighter species undergo a more rapid velocity increase in the same potential field compared to the heavier species. Residual stress is higher for a more energetic plasma, especially in the presence of ions from the energy region C, as it bombards the growing film with higher energy. This also leads to a higher number of defects, as well as gas implantation to the film. A more energetic ion flux also increases the hardness and Young's modulus, and causes brittleness of the film as it hinders dislocation movement as more atoms are in interstitial positions. The coefficient of friction and the wear rate also increase for higher ion energies. Both can be associated with higher hardness and so less resistance to plastic deformation, thus a more difficult pass for the counterpart ball. Lower wear resistance is associated with the brittleness of the harder material. More detailed information is available in the work of Lin *et al* [10].

2.5.5 Variable field magnetrons

Recent changes in the design of magnetrons include varying the degree of unbalancing. The inner and outer set of magnets can be moved relative to each other (from balanced to

unbalanced) and the ion-to-atom ratio can be varied at any stage of deposition. Tuning the parameters during the process was shown to have a positive effect on the properties of the coating. The fluxes of atoms and ions incident to the substrate can be varied during the process. A higher level of ion bombardment is beneficial at the initial stage, but detrimental at the final stage.

During the process, as the targets are eroded, it is necessary to change the process parameters in order to maintain the same quality; this can be achieved with VFM.

2.6 Bias used in magnetron sputtering

To increase the density of the coatings, the substrate is biased. As mentioned before, atoms of the sputtered material have no electrical charge, thus, their energy can't be directly increased. The negative bias on the substrate attracts the positive ions in the plasma, forcing them to bombard the growing film on the substrate. The bias can be direct current or pulsed. Pulsed DC bias on the substrate achieves the highest saturation current. This increases the current drawn to the substrate as the bias voltage is increased (with DC bias, there is a saturation current). The saturation current also increases with frequency. According to [9], the exact mechanism is not yet clear.

2.7 Industrial coating preparation

2.7.1 The geometry of sputtering machines

There are two main types of machine used for industrial magnetron sputtering. The first is with a plane geometry, where the substrates are opposed by the source on one side and the samples have to be coated only in one dimension (e.g. glasses, mirrors, car lightning); the second type is a cylindrical machine with complex substrate rotations. The latter have samples located in the inner cylinder. Targets and heaters are usually situated evenly around the vertical axis.

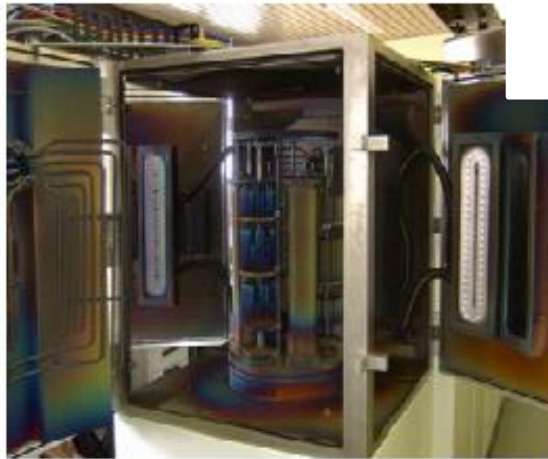


Figure 2-17 CemeCon 880/9 MLT sputtering machine

The holder for the samples is called a rotation table. On the table, there are towers whose rotation depends on the rotation of the table, itself driven by a planetary gear placed on the bottom of the table. On the towers, there are other circular discs with pins and hollow cylinders, which can also rotate if necessary. Due to this set-up, it is possible to coat complex geometries with a uniform distribution of the coating. This type of set-up is mostly used for rotating tools, especially those used in the cutting industry.

Figure 2-17 shows the CemeCon magnetron sputtering machine, which was used in later parts of this work. Figure 2-18 explains the 2D geometry of the targets, heaters, cathodes and table dimension and angles. It is important to mention that the geometry has a tremendous effect on the final performance of the coating.

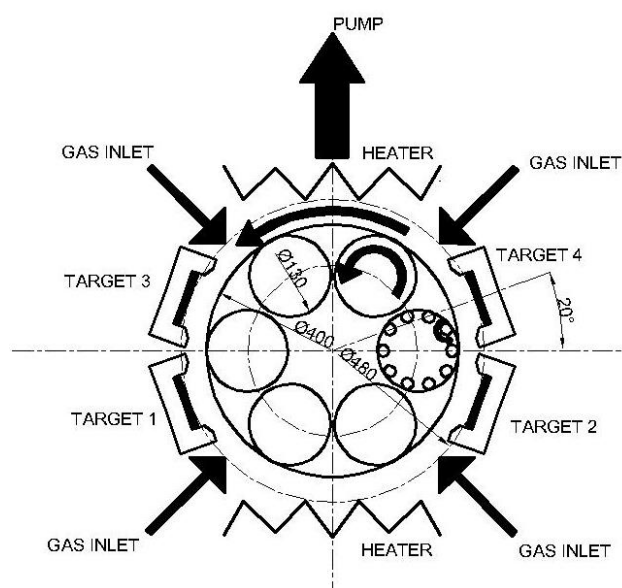


Figure 2-18 Geometry of 2D cut of CemeCon 880/9 MLT sputtering machine

2.7.2 Batching material, Batching process

The quality of the coating in the batch is also dependent on the distribution of the material in the chamber. Several factors influence the thickness and quality of the coating:

- a) The axial position of the material in the chamber
- b) Volume density of the material, shadowing
- c) Concave or convex geometry
- d) Number of rotations

Ad a) The sputtering rate along the axial position is not uniform. This is due to the different sputtering yield from the targets. Later in this work, the issue of radiation from the targets is addressed in more detail. The uniformity of radiation can be set by the magnetic field strength and shape. Most sources have the highest density in the center, with sputtering yield declining at the ends. For a working sputtering distance where the difference between the center and the end is less than 10%, this corresponds, in our geometry, to 80% of the length of the cathode. The cathode is 500 mm long, but the working height is 400 mm.

Ad b) Generally, the more uniform the distribution of material in the chamber, the more stable and uniform the coverage of the material. The amount of atoms sputtered from the cathodes is given by the set power; thus, with an increased surface of the sample material, the film layer will be thinner. To avoid this behavior, it is advantageous to fill empty spaces in the batch with dummy material to ensure uniformity of the thickness. Another advantage of using dummy material is in the growth of more dense coatings, which arises because the material is sputtered at (almost) all times perpendicular to the substrate surface. See Figure 2-19.

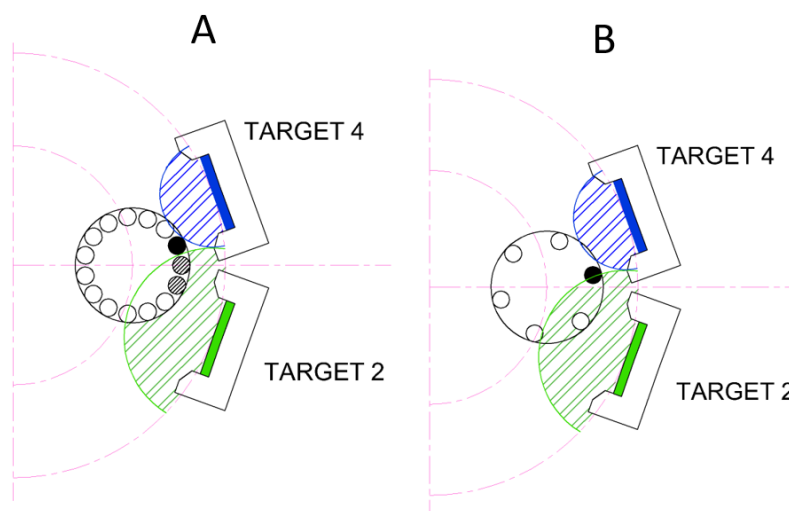


Figure 2-19 Shadowing effect on the rotating tower

The atoms impacting the material surface in the first case are impacting from different angles, thus increasing the shadowing effect (explained in 2.5.2). The result is a porous coating with worse mechanical properties.

Another aspect of the nonuniform distribution of material in the chamber is the electrical conditions. There is always a current flow from the cathode to the substrate (anode). Sputtering conditions fix the current flow in the process. If the total surface area of the material is too low, the current density on the surface is increased, in turn changing the sputtering conditions and also leading to arcing in the process.



Figure 2-20 Batching with dummy tower

Ad c) As most of the coatings are deposited at an elevated temperature of around 400°C, thermal dilatation plays an important role. The substrate material gains volume during the coating process and the surface area is increased. For a 10 mm steel rod with a diameter of 10 mm, the increase is about 50 µm in thickness.

The coating is sputtered over a larger area for convex shapes. When the substrate is cooled to room temperature, the surface area decreases. For convex shapes, this decrease in volume creates compressive stresses. As explained in section 3.4, the residual compressive stresses

that arise from the sputtering process harden the coating. Convex geometries increase the compressive stress even more, as the coating has less freedom to change shape.

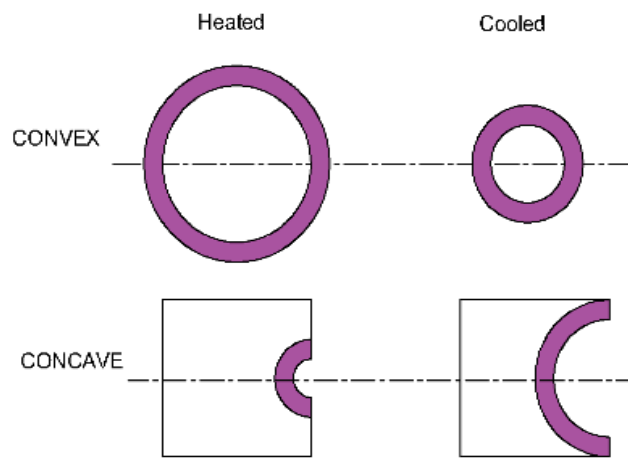


Figure 2-21 Cooling effect on the volume change of sputtered coating

The surface area of the concave section increases with cooling, leading to tensile stresses in the coating, causing it to crack. This decrease in surface area leads to a significant drop in adhesion. Generally, when sputtering concave geometries, the thickness of the coating should be lower than that for convex geometries. Another method to overcome this is the use of a thinner coating and a lower sputtering temperature, as the main compressive stresses are thermally induced.

Ad d) The thickness of the coating is driven by the time the material spends facing sputtering sources. Thus, as it rotates more, its thickness decreases. Generally, the ratio of the film thickness in one-, two- and three-fold rotation is approximately 4:2:1, though for less conductive coatings this can change, as the conductivity and electrical conditions are varying with increasing film thickness.

To overcome all challenges described, a specialized batching material has to be used. The emphasis is on the speed of batching, *i.e.*, reducing idle time and, primarily, on the uniformity of the coating. Figure 2-22 shows our batching material from CemeCon AG catalog.

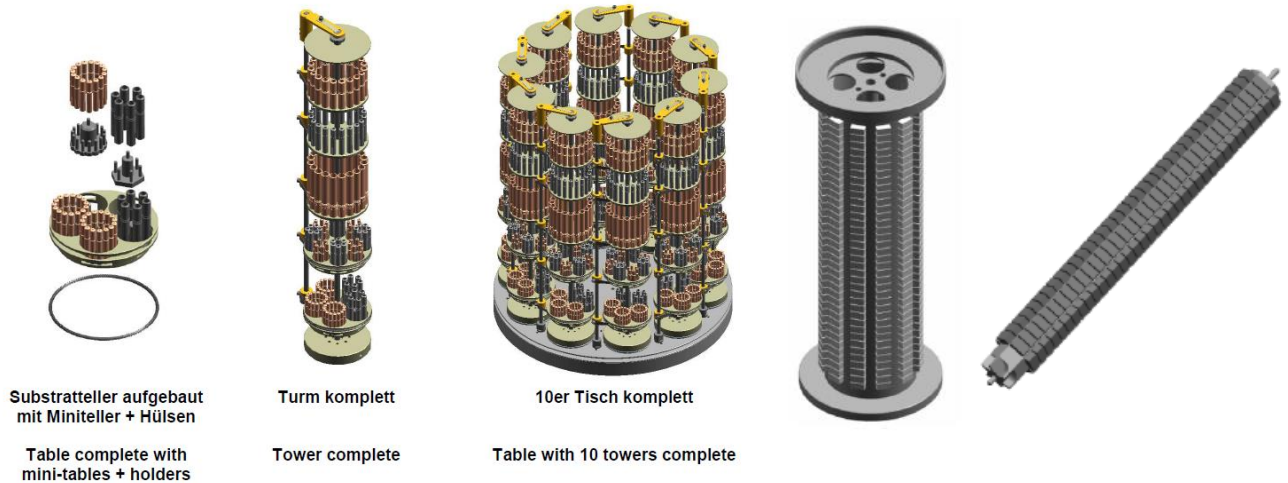


Figure 2-22 Different batching material used in CemeCon AG machine systems

2.7.3 Gas inlet, cathodes, targets, etc.

The type and position of gas inlets and cathodes directly influence the coating quality. Gas inlets can be positioned regularly around the chamber to ensure equal distribution throughout the whole chamber, or can be directed from one particular spot to create a gradient of gas density in the chamber.

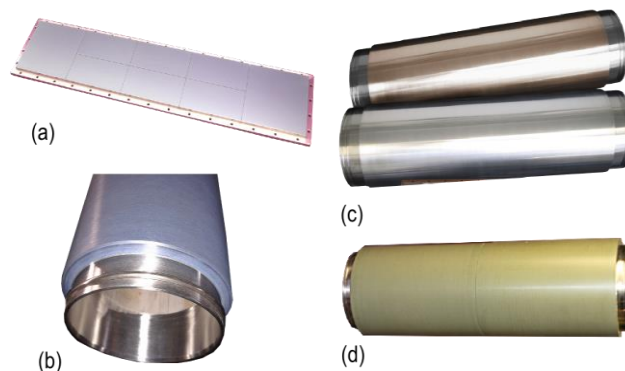


Figure 2-23 Planar and cylindrical targets

The alternative configuration is used, for example, when the gas is ionized before entering the chamber (shown later) or when the reactive gas is directed towards the cathode. The mixture of reactive and working gas (for example, nitrogen and argon) occurs before entering the chamber. As the process of forming the coating decreases the ratio of working and reactive gas, it is advantageous to use a uniform distribution in larger industrial machines.

There are two types of cathode geometry (and accordingly targets) used in industry: planar and cylindrical (see Figure 2-23 Planar and cylindrical targets). The planar cathodes have a much simpler design and are cheaper to manufacture. The same can be said for the targets,

which are basically “plates” of pure metal. The disadvantage of a planar geometry is the very high ratio between sputtered material and waste material. The material is sputtered from the racetracks, where the magnetic field forms the electron trap, while the rest of the target (ca. 80%) is unused. The cylindrical targets are more expensive to manufacture, while they are usually thermally sprayed material on some bonding material. During the process, they are rotating along the vertical axis and are uniformly sputtered over their entire surface, leading to almost complete consumption on the coatings.

2.7.4 Substrate pretreatment

Substrate pretreatment is a key issue for any coating. It strongly influences the adhesion of the coating to the substrate. Therefore, it is necessary to master the process. Most coating failures in the industry are caused by incorrect pretreatment, rather than a problem with the sputtering process.

Schematics of a real surface prior to coating is shown in Figure 2-24. The coating has to be sputtered on the metal surface. Thus, all other impurities have to be removed.

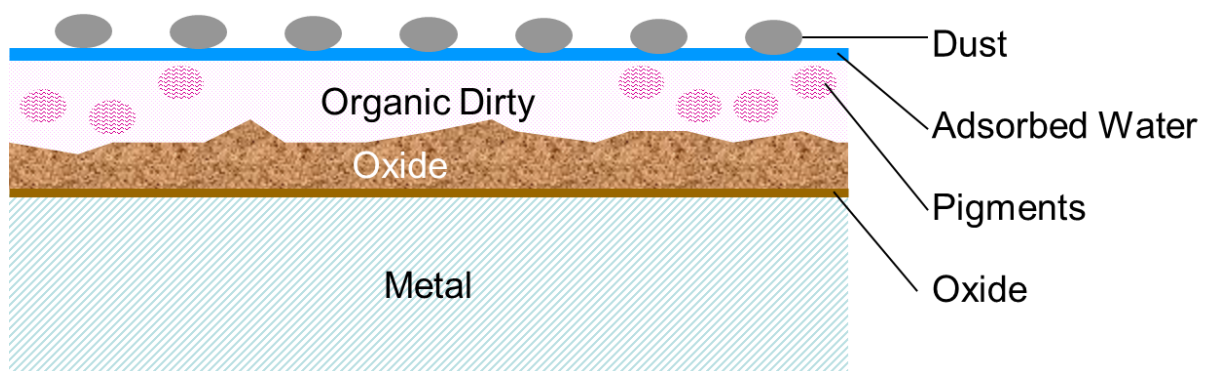


Figure 2-24 Schematic of a real dirty surface before cleaning [12]

Figure 2-25 presents pretreatment methods that are commonly used in industry, with a focus on blasting and cleaning, *i.e.*, chemical removal of dirt.

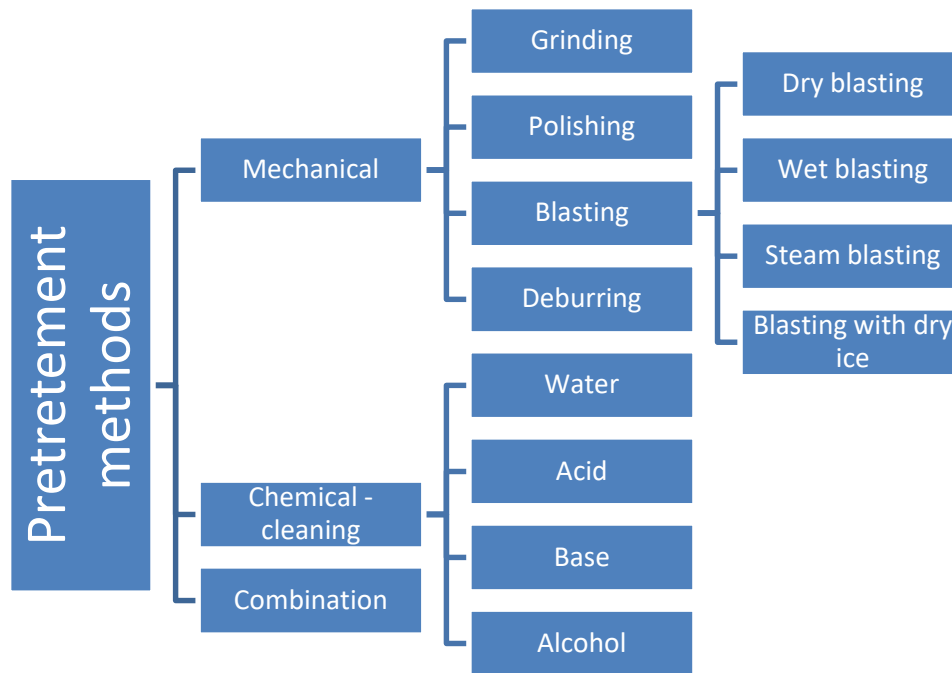


Figure 2-25 Commonly used pretreatment methods

2.7.4.1 Blasting

Blasting can remove dirt, impurities and change surface morphology. Blasting is in principle based on the impact of more or less abrasive energetic media on the substrate surface. Blasting is performed before the coating is used for activation of the surface (mechanical removal of material) or changing shape (roughening and rounding ability).

The advantages of using blasting with less abrasive media as the activation process are the removal of loose particles, removal of fats and oils, and not damaging the surface. On the other hand, weakly abrasive media does not remove oxides. For the removal of oxides, a more aggressive medium has to be used.

Blasting with solid particles is divided into 'dry blasting', where the blasting media is sucked from the dispenser (usually with low pressure) and 'wet blasting', where the abrasive particles are mixed with water, forming a slurry. The slurry is driven to the material with the aid of a pump. Glass, sand, and corundum is usually used as the blasting medium. The effect of blasting is dependent on the number of abrasives, pressure, time, and the shape of the edges of the blasting agents.

Blasting is commonly used as a pretreatment process for tools where a change of surface morphology is desired. These processes are:

- a) Rounding of the edges of cutting tools – a very sharp edge, with an edge radius of less than 2 μm , is sometimes undesirable because of possible breakage of the coating due to insufficient support of the substrate. The radius of the edge strongly influences the cutting process
- b) Removal of nitride compounds on forming tools - Removing a white layer of carbides formed after the nitriding process. This outer layer is composed of Fe_2N , and other nitrides diffuse on the surface that do not strongly adhere to material. Coatings deposited on this white layer would spall immediately
- c) Roughening of flat surfaces – when coating large flat surfaces, there is usually huge stress accumulation, especially when polished. Increasing the roughness of the surfaces creates convex and concave geometries, which can relax the stresses, leading to better adhesion.

2.7.4.2 Cleaning

Chemical cleaning is a mild process for removing contaminants from the surface. It does not damage the surface mechanically, but when misused it can damage the surface chemically (oxidizing, dissolving, *etc.*). Different detergents are used to dissolve the contaminants:

- a) Water (demineralized)– for dissolving salts
- b) Base solutions - for dissolving fats, oils, and salts
- c) Alcohol-based (Isopropanol, Acetone, n-Heptane) - for dissolving fats and oils
- d) Acid-based - for dissolving waxes, oxides, and salts

The whole cleaning process consists of many subprocesses. To increase the lifetime of a chemical bath, precleaning to remove rough dirt is recommended. After cleaning, the cleaning agent has to be removed from the tools submerged in water, usually with additional rinsing steps. After rinsing, the material has to be dried to suppress the corrosion, and the tools should be placed immediately in the sputtering chamber, or a noncorrosive environment, as it is a temperate area (with a temperature higher than 50°C) which is effectively dry air. A diagram of the industrial drying process is shown in Figure 2-26.

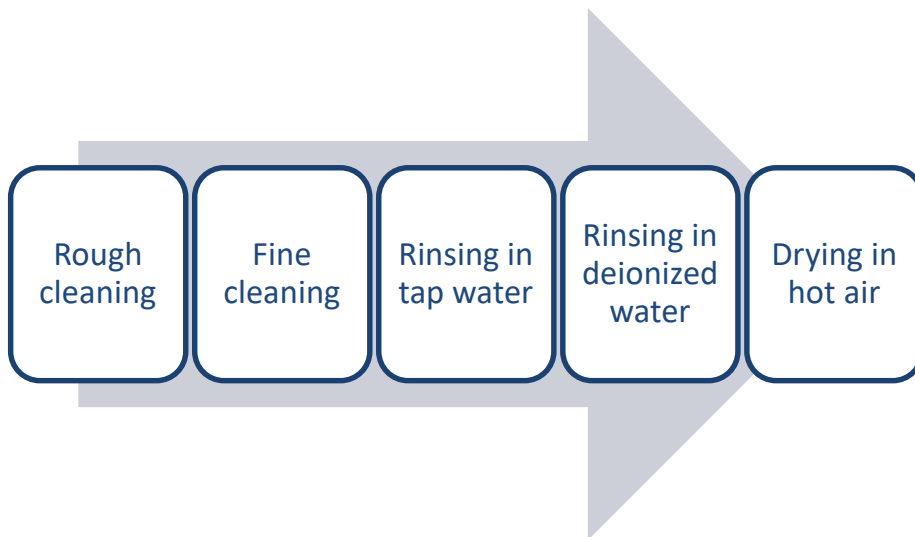


Figure 2-26 Industrial cleaning process setup

For the cleaning process, an ultrasonic bath is used. An ultrasound generator creates waves with frequencies that create implosions of air bubbles in the water. These imploding bubbles hold huge energy and are very effective in cleaning the surface. While cleaning, mechanical movement of the tools creates flows in the liquid, removing the solid dirt from the surface, and so helping the chemical agent to interact better with the surface. It is necessary to fix the cleaned tools or components so that they do not touch each other, as they could damage the edges or polished surfaces of neighbouring tools.

2.7.5 Vacuum pretreatment

2.7.5.1 Base pressure

The vacuum chamber has to be evacuated to a base pressure before the next coating stages can start. The purpose is to pump out most of the oxide and water vapor, which could form oxides on the surface of the substrate material in the heating process. For substrates that are difficult to oxide, e.g. tungsten carbide, it is possible to have a higher base pressure (~ 9 mPa), whereas for substrates that are easy to oxide, e.g. steel, lower base pressures (~ 2 mPa) are used. Pumping to base pressure is purely idle time in the coating process. It can be sped up with a higher pumping power of the turbomolecular vacuum pumps.

2.7.5.2 Heating

Before beginning the coating process, the heating phase is necessary to improve the adhesion further. As shown in Figure 2-24, water and other gas molecules are adsorbed on the surface. While heating, the molecules diffuse (desorb) faster to the surface due to the

higher temperature, and are evacuated with the rest of the gas from the chamber. If the heating stage is not included, the water molecules desorb anyway during the coating phase, due to the power produced by the sputtering power of the magnetrons. The desorbed water is then dissociates in the plasma into oxygen and hydrogen atoms, forming an oxygen layer on the surface by reacting with sputtered atoms. This oxygen layer does not adhere to the substrate very well, thus, the final coating is also weakly adhered.

Heaters used in industry are usually resistance heaters, situated around the substrates, as shown in Figure 2-27. For smaller machines, lamp heaters or other radiating heaters can be used. The transfer of heat from the heater to substrate in a vacuum is the only radiative process, which is not very effective. To increase the heating efficiency, heating in the non-reactive process gas is also possible.

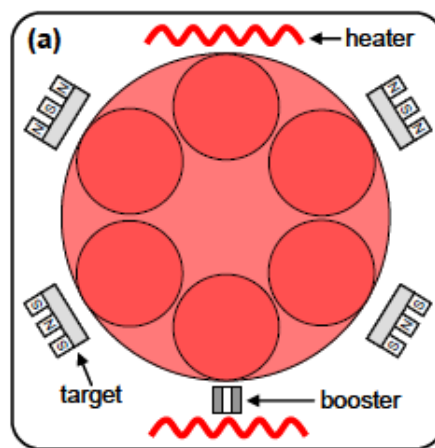


Figure 2-27 Heating process schematics

At this stage, it is crucial to not heat the material above its annealing temperature, as this will cause softening of the substrate material. Generally, tungsten carbide can be heated to temperatures above 500°C, hot working tool steels to 450°, thermally treated cold working steels to 250°C, and aluminum alloys to 150°C. Moreover, there are special annealing thresholds for each material that also depend on the time for which they are subjected to a given temperature.

The evolution of pressure, temperature, and heater power during the heating stage is shown in Figure 2-28. At the beginning of the process, the chamber has to be evacuated to base pressure (below 10 mPa) at room temperature. After that, the heater is activated, increasing temperature on the heater and substrate, which always has some delay because of the thermal capacity. Also, the substrate temperature never reaches the heater temperature due to back-radiation of the heat.

The pressure in the chamber is increased in the first stage, as the gas is desorbed. The gas pressure in the chamber can reach pressures as high as 1 Pa, depending on pretreatment, cleaning process, and exposure of the substrates to humid air before the coating process. The highest production of gas is caused by the chamber walls and heaters, as their surface area is higher than the surface area of the substrates. The evolution of gas due to diffusion exhibits exponential behavior, following the equation:

$$\dot{m}(t) = m_0 \cdot e^{-kt}$$

Equation 2-7

Where $\dot{m}(t)$ is the mass flow from the material, m_0 is the mass of gases accumulated in the material, and k is a constant. The total pressure in the chamber follows the equation:

$$p(t) = m_0(T) + \dot{m}_{subs}(A, T) + \dot{m}_{wall}(A, T) + \dot{m}_{leak}(\Delta p_1) - \dot{m}_{pump}(W, \Delta p_2)$$

Equation 2-8

Where $p(t)$ is the actual pressure, m_0 is the pressure from particles in the chamber at the beginning of pumping, \dot{m}_{subs} corresponds to pressure generated by mass flow from substrates, \dot{m}_{wall} corresponds to pressure generated from mass flow from the walls and heaters, \dot{m}_{leak} corresponds to pressure generated by particles sucked into chamber through any leaks, \dot{m}_{pump} corresponds to mass flow from the chamber through the turbomolecular pump, T is the temperature, A is surface area, W is the power applied to the turbomolecular pump, and p_1 and p_2 are the pressure differences between the chamber and atmosphere, and the chamber and the rough pump pressure, respectively.

After a peak in pressure is reached, the pressure is decreasing to a set pressure limit. This procedure usually takes a few hours and is an inefficient step of the coating process. Decreasing the heating time is advantageous, as we can increase the efficiency of the coating process. As seen in equation 2-7, decreasing the heating time can be achieved by:

- 1) Decreasing the number of absorbed gas molecules in substrates. Vacuum drying after the cleaning stage is an efficient method.
- 2) Decreasing the number of absorbed gas molecules in the chamber walls. To achieve this, short opening times of the chamber are beneficial. Some coating chambers can

heat the chamber walls during their opening times. Also, it is advantageous to leave the chamber evacuated when it is in standby mode.

- 3) Decreasing gas leaking in from the atmosphere. In practice, every chamber has some minor leaks. Constantly checking for them and controlling strategic parts can decrease leak pressure. Leaks can be water leaks, when water gets sucked pro cooling system, or gas leaks, when gas is sucked from the atmosphere.
- 4) Increasing pumping volume. The pumping volume can be increased with the addition of a parallel turbomolecular pump, exchanging the turbomolecular pump for one with a higher power, or decreasing the pressure difference in the first stage pumping using a rotary pump and lower chamber pressure. It is also possible to connect the vacuum capacitor to the chamber in order to speed up the initial phase of evacuating of the chamber.

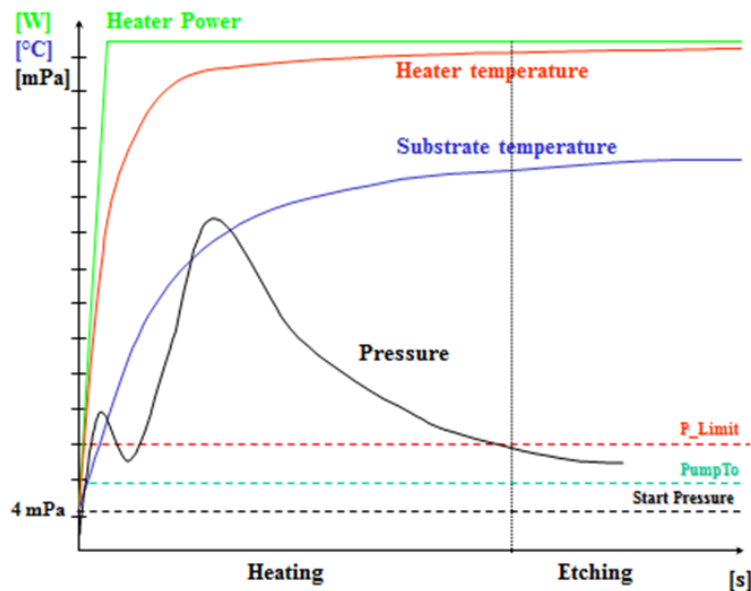


Figure 2-28 Heating process. Typical development of temperature and pressure in the chamber [12]

2.7.5.3 Etching

Ion etching is the last pretreatment process before the coating stage. Its purpose is to remove a few atomic layers of the surface, usually consisting of oxides and other inorganic dirt that has not been removed during the cleaning process, or that has formed after the cleaning process when the substrates are exposed to ambient air. There are many forms of etching used in industry including MF etching (Figure 2-29 MF etching process schematics), hollow cathode (booster) etching (Figure 2-31), Cr⁺ ion etching, etc. The basic principle is the same as a sputtering process.

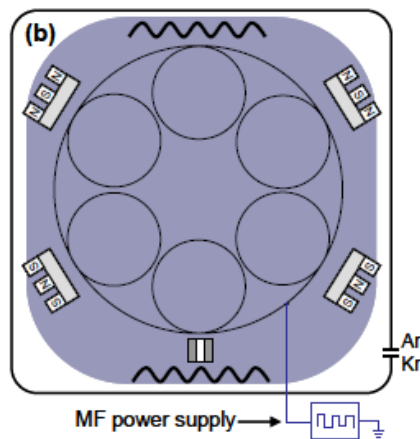


Figure 2-29 MF etching process schematics [12]

2.7.5.4 MF etching

In plasma, positively charged ions of any of the heavier elements are formed (Ar, Kr). A negative potential is applied to the substrate holder, accelerating the charged ions to the table where they impact the surface. Sputtering efficiency is dependent on the frequency and shape of the exciting waveform. For more information see [13]. MF etching is used for substrates with complex geometries, *i.e.*, various components, molds, and dies. The energy of the impacting ions is lower in comparison to other etching techniques, but the whole surface is etched equally, and softer substrates are not damaged.

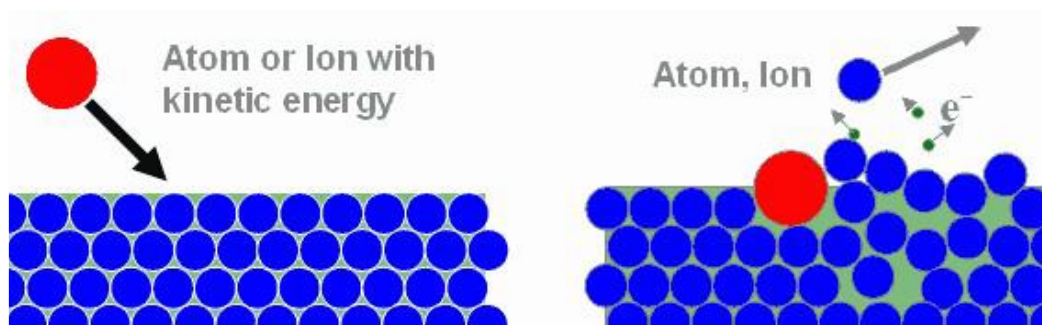


Figure 2-30 Principle of ion etching [12]

2.7.5.5 Hollow cathode (booster) etching

Booster etching is more effective for substrates where etching of outer diameters and edges is primarily needed, *i.e.*, round cutting tools. Booster etching has a more concentrated energy with flux from one source on the front chamber wall, *i.e.*, the booster, to the outer wall cathodes (see Figure 2-31). The booster functions as a hollow cathode. It is charged with a negative potential of 50 V and a current of around 20 A. The working gas is injected through it and aimed at the opposing cathodes within the chamber. The ion flux flows through the substrate table, impacting any substrate it meets on its way. The energy is more concentrated, leading to a higher removal rate on the outer surfaces of the tools, a slight rounding of edges, and the removal of surface layers of harder materials such as tungsten carbide. The drawback is the shadowing of parts of substrate surfaces by complex geometries. For example, a basic drill will be well etched on the cutting edges, but only mildly so in the grooves under the edges. This is sufficient for round cutting tools, where only the cutting edge is necessary for good efficiency, but insufficient for forming tools, where the whole surface is the working surface necessary for good performance.

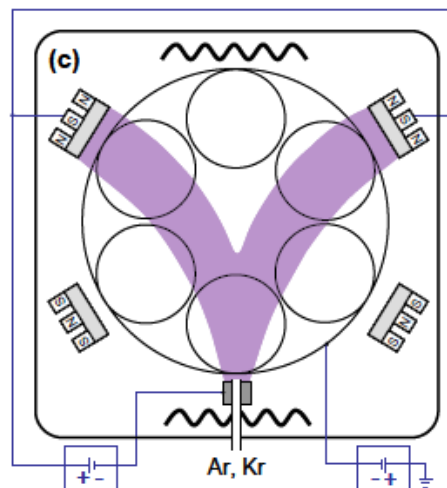


Figure 2-31 Hollow cathode etching process schematics [12]

2.7.6 Growth defects

Due to the real sputtering conditions and the nonideal morphology of the substrates, the growing films are never perfect [14]. The density of defects depends on deposition time, deposition technique, deposition parameters, substrate position in the vacuum chamber, its orientation and rotation mode. The final performance of the coating is dependent on the defect density; the defects reduce adhesion, increase roughness, cause higher sticking of the working material, and lower corrosion resistance.

All substrate irregularities such as pits, asperities, ridges, and grooves, are magnified during the coating process. Uneven materials (carbides, composites, some steels, etc.) suffer more from substrate defects because of their nonuniform hardness on the substrate and the greater possibility of loosening harder particles. Polishing or ion etching has a different effect on various parts of the surface, increasing roughness.

Growth defects originate in particles generated both before and during the coating process. According to Panjan et al. [14] most defects appear during the deposition. They concluded that the main cause of defects is the delamination of coatings from fixturing and other batching material, as the flakes delaminate more with higher deposition time. Vetter et al. [15] reported 10 times lower defect density when using additional shielding during the process. These shields were able to eliminate the movement of dust in the chamber during the coating process. A further decrease in defect density was achieved by lowering the deposition temperature. A lower deposition temperature decreases the internal stresses in the coating, while decreasing amount of dust generated.

The defects can be divided into a few categories:

Flakes form defects – these are defects formed from asperities and foreign particles on the surface. The typical size is 5 – 40 μm . These surface imperfections are the preferential size to induce nucleation with a faster growth speed. Panjan et al. [14] showed that most of these particles are iron-based, thus suggesting that they originate from the substrate, i.e., polishing residue, metal dust, and pieces of particles formed during etching period.

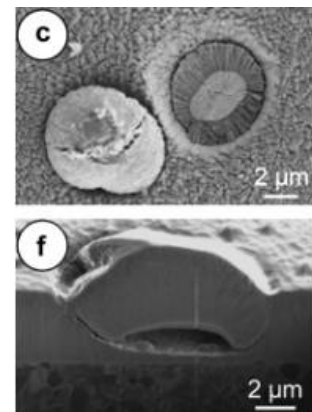


Figure 2-32 Flakes form defects [14]

This hypothesis is also supported by our findings, which show that after the deposition process there is magnetic dust around the cathodes. The only magnetic material in the chamber is the substrate tool steel, or cobalt from the tungsten carbide tools. So, decreasing the etching time could lead to lower defect density, but also lower adhesion. In specific processes, where corrosion resistance is more important than adhesion, this can be advantageous.

Open void defects – Defects in the form of open voids originate from delamination of flakes. Delamination can occur during the sputtering process, meaning that the void is covered with a thinner coating layer, or it can occur at the end of the coating process, leaving

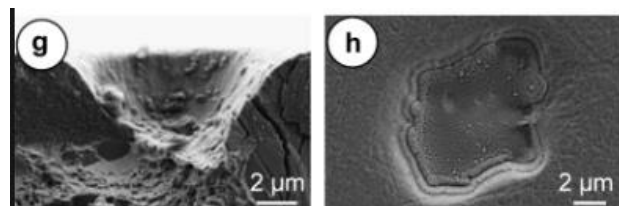


Figure 2-33 Open voids defects [14]

the substrate uncovered. The cause of delamination is usually thermal stress during the cooling stage.

Cone-like defects – As discussed in [14], these defects have a size of around 1 μm and originate from fine particles formed during deposition. During deposition, the coating is growing on chamber components, shields, *etc.*, and the compressive stresses also increase. When a critical level of internal stresses is reached, small particles (size 100 – 400 nm) begin flaking out. Such small particles can be ionized and are driven towards substrates, where they stick due to electrostatic forces. The density of these defects increases with deposition time, as more particles are formed. The chemical composition measured in [14] shows that it is the same as the growing coating.

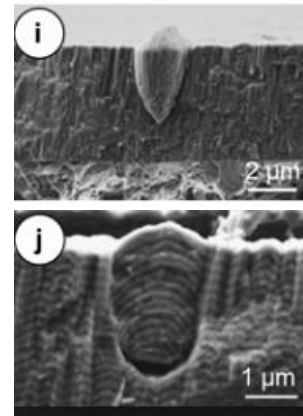


Figure 2-34 Cone like defects [14]

Pin-holes – Pin-holes originate from defects on the surface. Pin-holes usually propagate through the whole coating. These defects can originate during polishing or blasting processes, or indeed other surface treatments. The narrow surface defect is not coated in the whole volume due to shadowing. The coating is preferentially deposited on the flat front side. Smaller pin-holes are closed during the coating process, whereas the larger are not. Due to the shadowing effect, the coating in the pinholes is porous and becomes a weak spot on the final coating.

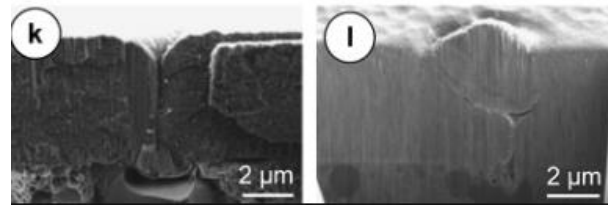


Figure 2-35 Pin holes defects [12]

Arcing defects – Microdroplets usually stem from arc processes. The arc evaporating target material has high energy, and the atoms are sometimes vaporized with material around, which is melted and not vaporized. These droplets are then impacting the substrate, forming metal impurities in the coating. Arcing can also occur during magnetron sputtering. It can be caused by lower conductivity of the target, or when the substrate is too close to the cathode. Nowadays, the sputtering sources can monitor, control, and suppress the arc during the processes. In magnetron sputtering, the arcs are formed between the cathode and the substrates, damaging the target as well as the substrate.



Figure 2-36 Arcing defects on tool steel

2.7.7 Conditioning

Conditioning is a special process used for coating chambers; it is used to prepare the inner space of the chamber and batching material for the next sputtering process, yielding coatings with excellent quality. The conditioning process should have a strong heating stage for evaporating all water and oil in the batching material, an etching stage to prepare the interior of the chamber for good adhesion of the coating, and a coating stage to create a strongly adhering coating on the batching material, so that it does not delaminate during the process.

Conditioning batch is used after every process when non- or low-conductive coatings (DLC or oxides) are used. The non-conductive coating can cause massive arcing during the etching and coating stage, damaging the coated batch. Also, conditioning is necessary after depositing coatings containing carbon or sulfur. These elements create a lot of dust and are loosened from the batching material under vacuum, later becoming incorporated into the growing film. Again, this causes lower adhesion and changes the chemistry of the coating. When using new or chemically treated batching material, shields, or rods, conditioning batch should be applied in order to prevent the outgassing interacting with the well-cleaned tools, and other coated components in the process.

3. Thin film growth

The growth of the film is a multi-parameter problem that is dependent on bound parameters, characteristics of the material, and deposition apparatus, alongside unbound variable parameters. The process occurs *via* nucleation and growth stages. The formation of the film is dependent on the growth conditions, *e.g.* temperature will influence atom mobility on the surface, or ion bombardment will cause densification or even destruction of the film. These conditions are controllable during the process. The material parameters, film substrate combination, binding energy *etc* are later shown in section 3.7.

3.1 Thermodynamics criteria of growth rate

As mentioned above, the film is not formed under equilibrium conditions. That said, the thermodynamic criterion developed by Bauer [16] allows for a basic understanding of the process, even though it is valid only for equilibrium growth:

$$\Delta\sigma = \sigma_f + \sigma_i - \sigma_s$$

Equation 3-1

Where σ_f is the surface energy of the film, σ_s is the surface energy of the substrate and σ_i is the surface energy of interface. If $\Delta\sigma < 0$, the surface energy of the substrate is higher than the surface energy of the film and interface, and the adatoms are bound strongly to the substrate. This is the case for 'wetting', and is referred to as Frank-van der Marwe growth. Conversely, when adatoms are bound together (rather than to the substrate) and island growth is observed, we observe Volmer-Weber growth.

The surface energy is not constant, as it can change with other parameters such as stress, temperature, ion bombardment, *etc*. As such, it is possible that the dominating factor for growth is changed during the deposition. The Stranski-Krastanov mechanism is the combination of the previous two, where the layer is growing according to the wetting mechanism until some thickness is reached, and then continuous with island growth.

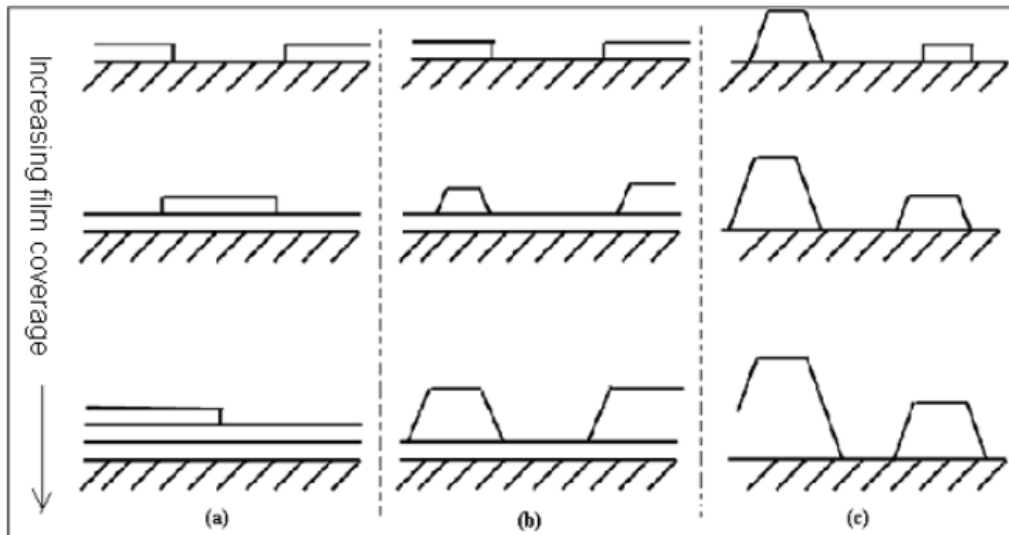


Figure 3-1 Schematic growth modes of thin films: Morphology of a growing film for (a) layer-by-layer, (b) island plus layer and (c) island growth upon increased coverage with monolayers (adapted from: [17])

Figure 3-2 and Figure 3-3 show result of simulated deposition of Zr/Nb coating using molecular dynamics simulation technique. The first coating was deposited with high energy atoms and the coating is smoother and denser. The coating deposited with low energy atoms (higher sputtering pressure, no bias, low cathode power) is a nice representation of Frank-van der Marwe growth shown previously. As it is exhibited in Figure 3-4, sputtering with low energy atoms leads to shadowing effect and less dense coating as will be explained later.

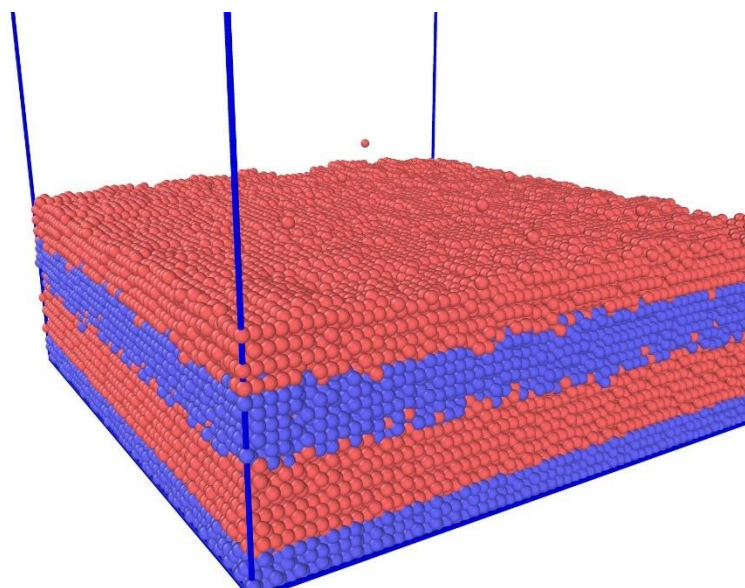


Figure 3-2 Molecular dynamics simulation of Zr/Nb coating deposited with high energy atoms

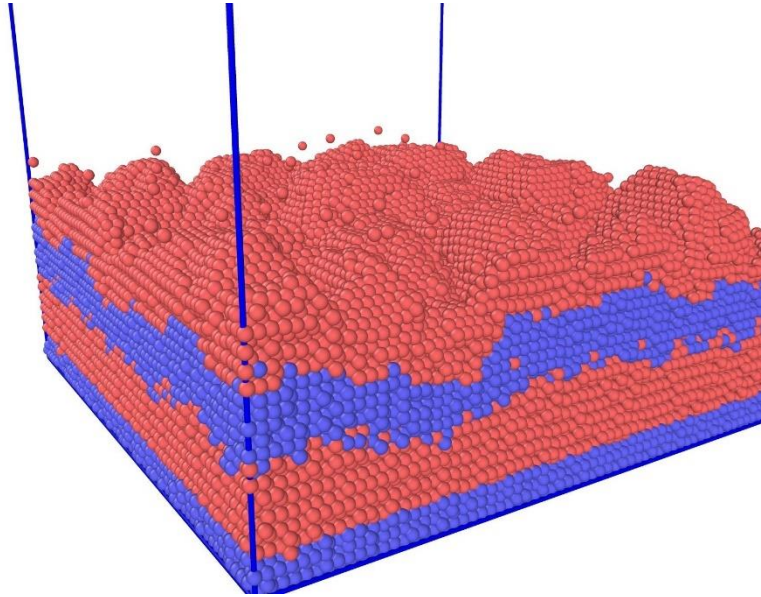


Figure 3-3 Molecular dynamics simulation of Zr/Nb coating deposited with low energy atoms

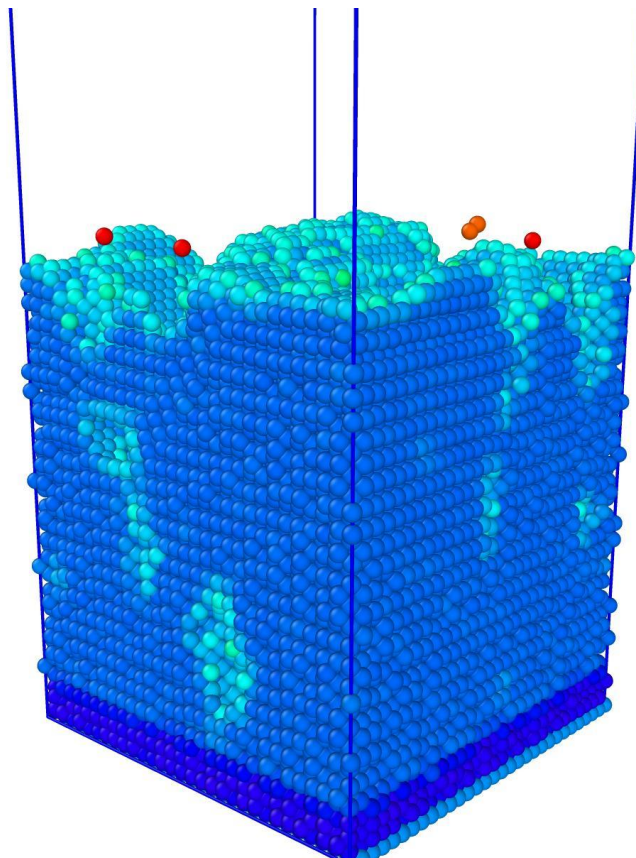


Figure 3-4 Simulated coating with highlighted imperfections

3.2 Kinetics

The impacting atoms are not immediately bound to the surface, and many processes can effect the incident atom. An atom will usually travel on the surface until it is bounded to another atom, or is re-evaporated. As mentioned above, the resulting film is not thermodynamically stable, as the process of growth is guided strongly by the assembly kinetics. To move the atom across the surface, the atom needs to overcome an energetic barrier given by bonding already establish with the substrate. The mechanism by which an atom travels is diffusion. The diffusion coefficient is given by:

$$D = \frac{a^2}{4} \nu_0 e^{\frac{-E_d}{kBT}}$$

Equation 3-2

Where a is the lattice constant, ν_0 is in the order of vibrational frequency of the atom, and E_d is the activation energy of diffusion. The migrating atom is more likely attached to a step interface when one is encountered, as there are more atoms to bind with. When migrating atoms reach a terrace edge and descend to a lower level, this is energetically unfavorable, as the binding force has only a short range due to there being no atoms to bind with. This mechanism prevents layer-by-layer growth, even if it would be thermodynamically preferable. According to equation 3-2, growth requires the thermal energy to overcome the energy barrier.

Migrating atoms can also hit other atoms on the same level and form clusters. As the critical size of the cluster is reached, it is stable and does not decay. The total free energy change of the cluster is given by equation 3-3:

$$\Delta f = 4\pi r^2 \gamma + 4/3\pi r^3 \Delta F_v$$

Equation 3-3

Where Δf is the total free energy change, r is the radius of the cluster, ΔF_v is the Gibbs free energy change per unit volume, and γ is the surface energy per unit area. As the Gibbs free energy is negative, it can be easily concluded that there exists a critical radius of the cluster, r^* , an increase in which reduces the free energy of the cluster, thus stabilizing it.

3.3 Film structure

Section 3.1 presented the equilibrium case of thin film formation for which the atoms have unlimited mobility to change their position. In section 3.2 it was proved that the film structure depends on the kinetics of the adatoms. The mobility of adatoms is influenced by temperature,

as well as any other energy sources interacting with the film. The transport of atoms can also be controlled by the geometry of the apparatus, working pressure, and the substrate bias applied, as discussed in section 2.6. The diffusion steps are controlled by ion bombardment and temperature. Based on these parameters, the model predicting the structure of the coating was created.

3.3.1 Structure zone models

The main parameter in the structure zone models is the homologous temperature. It is the ratio between the actual absolute temperature, T , and the melting temperature, T_m [9]. The melting temperature is another way of representing the strength of the bonds inside the material.

$$T_h = \frac{T}{T_m}$$

Equation 3-4

The homologous temperature is the diffusion parameter. In the first zone, where the temperature is low, diffusion is slow. The growth of the film, and the resulting structure, is influenced by the shadowing effect. The impacting adatoms don't have enough energy to overcome the energetic barriers. The film adopts a strong columnar structure with large voids between them. The low mobility of particles leads to the creation of structural units such as macro columns, microcolumns, and nanocolumns, as well as the corresponding macro-, micro- and nanovoids. Tensile stress is present in this zone, originating from the interaction between the grain boundaries. Extra bombardment results in gas entrapment and atomic peening. This can lead to compressive stress. Energetic particles are the main source of compressive stress.

Zone 2 is characterized by surface diffusion. The temperature is higher, and so is particle mobility. The adatoms migrate and are fill the voids effectively. The film still exhibits a columnar structure, and the columns have a small diameter, thus is denser. Zone 2 usually starts at a value of $T_h=0,5$.

Bulk diffusion, as the dominant process in zone three, means that the atoms diffuse through the whole film, making the film very dense. However, this also leads to grain coarsening, as the small clusters recrystallize. The film loses its unique properties that stem from the non-equilibrium growth conditions.

The working pressure influences the microstructure in such a way that higher pressure favors a less dense film, even at higher temperatures. This due to the fact that the impacting atoms lose energy when they are sputtered because of collisions with atoms of the working gas.

The zone T was added to the structure zone model (SZM) for magnetron sputtering. It is the inner configuration of zone 1, and is achievable only by magnetron sputtering.

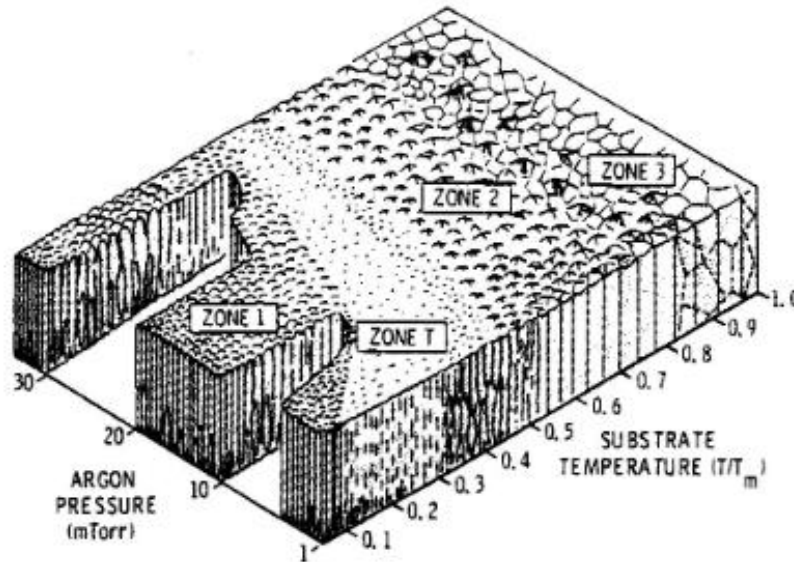


Figure 3-5 Microstructure zone diagram for metal films deposited by magnetron sputtering. T is the substrate temperature, and T_m is the coating material melting point [18]

Messier [19] later showed the same behavior for substrate bias, concluding that pressure and bias have the same effect, by increasing the energy of impacting ions.

Recently, Kelly et al. [9] revised the previous SZM with use of the modern closed field unbalanced magnetron sputtering. They concluded that CFUMS effectively suppresses the formation of porous zone 1, which was not present even at a low homologous temperature of 0.13. They also introduced a new parameter to the SZM model – an ‘ion-to-atom ratio’ that represents ionization of the sputtered particles.

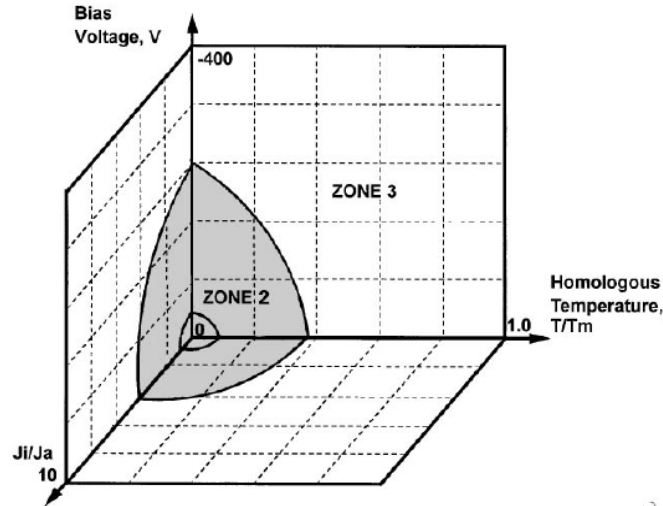


Figure 3-6 Structure zone model relating CFUBMS system in which structures are described regarding homologous temperature, ion-to-atom ratio and bias voltage [9]

3.4 Stress in thin film

Stress in thin films has a very important role, as it influences the main mechanical properties, *i.e.*, the hardness and young elastic modulus. These are the most important properties in coatings. The stress depends on both the sputtering method and sputtering conditions. For example, CVD coatings generally exhibit tensile stresses, but PVD coatings exhibit compressive stresses. The stresses are predominantly caused by ion bombardment during the deposition process, as well as temperature changes after cooling. Because the sputtering process has a low ionization ratio of impacting atoms ejected from the targets, the residual stresses are mainly controlled by ion bombardment when a bias voltage applied to the substrates. Ion energies are on the order of hundreds of eV [20].

The stress in the coatings is given by:

$$\sigma = \sigma_{ext} + \sigma_{therm} + \sigma_{intrext}$$

Equation 3-5

Where σ_{ext} is the stress from external forces, σ_{therm} is the stress caused by differences in thermal expansion coefficients, and σ_{int} is the intrinsic stress caused by the sputtering conditions; the intrinsic stress is the most important.

3.4.1 The origin of thermal stress

The main cause for thermal stress is the difference in the coefficient of thermal expansion of the substrate and coating:

$$\sigma_{therm} = \Delta\alpha \cdot \Delta T \cdot \frac{E}{1 - \nu}$$

Equation 3-6

Where $\Delta\alpha$ is the difference in thermal expansion coefficient, T is the temperature, ν is the Poisson ratio, and E is the elastic modulus of the material. The thermal stresses are dependent on the substrate material and deposition temperature. Figure 3-7 highlights the dependence of stress on the sputtering temperature and substrate material. As can be seen, the steel substrate produces compressive stresses, and a change of sputtering temperature of roughly 200°C leads to an increase in compressive stresses of about 0.5 GPa. The maximum sputtering temperature used in PVD processes is usually 500°C, so the thermal stress is usually less than 1 GPa.

3.4.2 The origin of intrinsic stress

Intrinsic stress in the film is caused by the mode of film growth, structure, and microstructure-sensitive properties; it can be influenced by contaminants and many other factors. There are three leading theories on intrinsic stresses: Atomic peening model [21], momentum transfer model [22] and the mathematical approach presented by Davis [23].

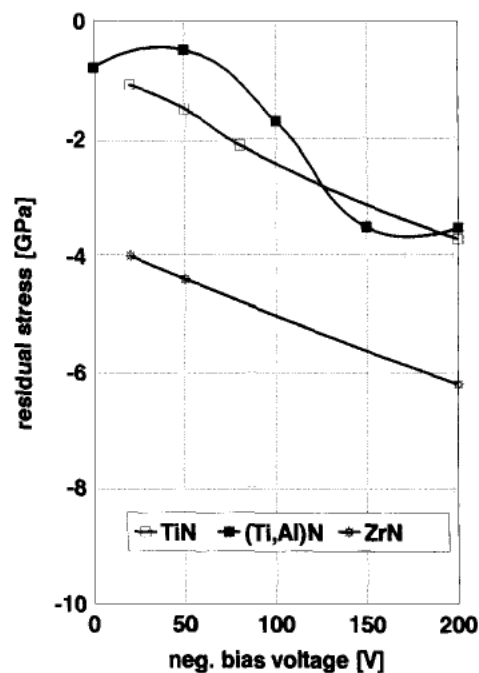


Figure 3-7 Influence of negative bias on residual stresses [20]

From these theories, one can infer that the stress depends on the atom energy, atomic flux, and the angle of incident particles. While high pressure is used for sputtering, there is a

loss of energy by atom-atom collisions and, therefore, an increase in the angle of sputtering. Films are tensile due to atomic shadowing. By using a lower pressure, particle scattering is reduced, and the particles impact with higher energy. This leads to densification of the coating. As explained by the momentum transfer model, the mass of incident ions is also important. Heavier elements (*W, St, Y, etc.*) are scattered at a lower rate than lighter elements (*Al, S, C, etc.*). The mass of the elements can affect the stoichiometry of the coating as well.

The bombarding atoms cause defects in the crystal lattice such as atomic substitution, the displacement of atoms to interstitial sites, or various other defects caused by the displacement spikes. The origin of the stress is in the volume change, $\Delta V/V$. For example, if a TiN coating is bombarded with Ar ions during sputtering, and Ar atom substitutes a larger Ti atom ($\text{radius}_{\text{Ar}} = 0,1 \text{ nm}$, $\text{radius}_{\text{Ti}} = 0,14 \text{ nm}$), compressive stress arises. The total intrinsic stress is dependent on the nature of the bombarding atoms and the number of lattice defects, which are both caused by substrate bias.

There exists a maximum level of intrinsic stress [20], which is derived from the shear strength of the material. After a certain level of stress, the strength of the film is overcome, and the film deforms plastically. This explains why residual stresses are lower when a deposition is made at a higher temperature. For example, a TiN coating loses 50% of its hardness between 300°- 400°C, so the maximum stress accommodable in the coating is lower. Figure 3-8 shows how stress in the TiN coating is dependent on the distance from the substrate: the highest stress is located near the substrate. Thus, the effect is caused by grain size increase during film growth, and the consequent reduction of critical flow value.

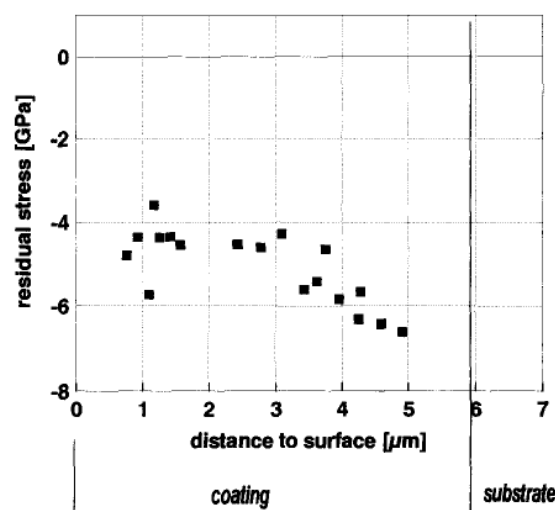


Figure 3-8 Coating stress dependent on the distance from substrate [20]

3.5 Solid solution and bonding

3.5.1 Solid solution

A solid solution is a homogeneous mixture in which the atoms or molecules of one substance are dispersed randomly in the matrix of another substance. The properties of the mixture are uniform. There are two kinds of solid solution: substitutional and interstitial. The solute atoms substitute a place in the lattice of the original atom, without significantly changing or distorting the lattice. For absolute solubility, the difference in radii should not exceed 8%, and both solvents should have the same lattice structure:

The Hume-Rothery rules [24] are used for determining if one metal will be soluble in another, thus forming a substitutional solid solution:

Crystal structure criteria: For the elements to be fully soluble they should have the same crystal structure; it follows that they have the same number of neighboring elements.

Atomic radii criteria: The metallic elements should have a difference in radii of less than 15%. If the difference is bigger, the strain energy in the lattice is increased, which is unfavorable.

Valence criteria: A metal with higher valency will dissolve a metal more likely than with a lower valency. The more electron deficient atom can dissolve more of another.

Electronegativity criteria: Metals with a high difference in electronegativity will form compounds rather than solutions. This will lead to the formation of intermetallics in the solution.

The interstitial solid solution occurs when the solute atoms are small enough to fit in the interstition positions between elements. The elements forming this type of solid solution are hydrogen, carbon, nitrogen, and boron. Solids may form a solution in the very same way liquids do. The formation of the solution depends on the interatomic interactions of the pure components, as well as on the interactions between two different components. The solubility in different materials varies greatly.

There are two types of interaction forming the solution: entropic and enthalpic. The enthalpic interaction is based on the cohesive energy of the bonds formed, and the entropic interaction is based on the fact that the solution is more probable than the pure substance (because there are many more ways to arrange constituents within the solution than in the pure phase, where there is only one possibility).

By way of thin film synthesis, it is possible to create a solution that does not occur naturally. This is due to the rapid incorporation of the immiscible elements into the lattice during the rapid loss of energy during the sputtering process.

3.5.2 Cohesive energy

The cohesive energy is the energy gained when atoms are arranged in a lattice with respect to the gas phase. The number of bonds depends on the type of lattice, and the bond energy depends on the nature of the elements. So, the cohesive energy can be calculated as [25]:

$$H_a = \frac{1}{2} Z n_A W_{aa}$$

Equation 3-7

where Z is the number of neighboring atoms, n_A the number of moles of A in the lattice, W_{aa} the bond energy between elements A. The formula for the difference in cohesive energy when taking into account a solid solution is given by:

$$dH_{sol} = \frac{Z}{2} dW x_A x_B$$

Equation 3-8

where x_A and x_B are mole fractions of substance A and B, respectively; dW is the energy change for a mole of the solution and is define as:

$$dw = 2W_{AB} - W_{AA} - W_{BB}$$

Equation 3-9

From this equation, one can state that if $dW > 0$, the formation of the solution is endothermic and the bonds in the solution are stronger than in the pure substance. On the other hand, when $dw < 0$, the reaction is exothermic, and bonds in the pure solution are stronger.

The energy W_{xx} can be estimated from the energy needed to vaporize the condensed state of the substance. In case all the substances have the same type of lattice, the melting temperature can determine the energy of the bond, as the vaporization energy is technically the energy needed to break each bond between an atom and all its neighbours. From the point of view of the cohesive energy interaction, the formation of a solution with stronger bonds is unfavorable.

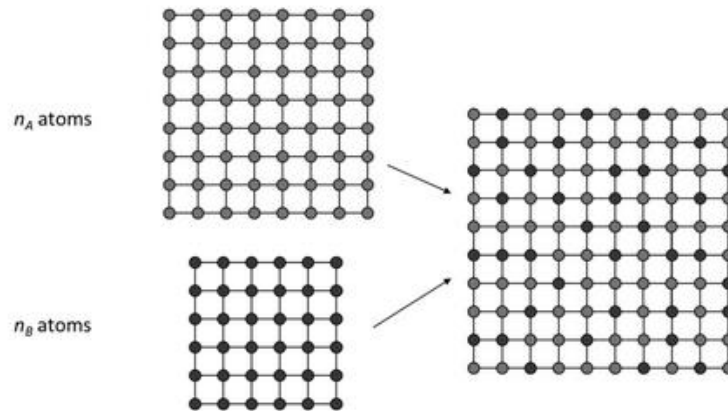


Figure 3-9 The mixing of n_A moles of A and n_B moles of B [25]

3.6 Thermal behavior of thin films

3.6.1 Diffusion and its effects in the thin films

Diffusion, as a transport phenomenon, is the driving mechanism for atoms to change places in a solid solution. It is the predominant mechanism of atomic movement in thin films. As diffusion is based on the thermal motion of atoms, it is not dependent only on the concentration gradient in solution, but also occurs without the gradient and leads to the random displacement of atoms. The coefficient of diffusion is exponentially dependent on temperature, so diffusion - and from that, the outgoing speed of elemental mixing - is heavily dependent on the deposition temperature, as was shown in section 3.3.1.

3.6.1.1 Mechanism of diffusion

The most reasonable mechanism of diffusion is that suggested by Frenkel and Schottky. This mechanism is based on defects (vacancies) in a crystal lattice, which work as channels for an atom to move (diffuse) through the crystal. The concentration of these vacancies can be derived from statistical calculations. The solids are polycrystals consisting of grains. The rate of diffusion is higher on the grain boundaries (surfaces of the grains). The highest diffusion rate is then on the surface, so [26]:

$$D_{\text{volume}} < D_{\text{boundary}} < D_{\text{surface}}$$

$$E_{a \text{ surface}} < E_{a \text{ grain boundary}} < E_{a \text{ volume}}$$

In more complex solutions (oxides, glasses, ceramics) consisting of many elements, the rate is different for every element, depending on its size and bonding strength.

The reason diffusion occurs is the accompanying decrease in Gibbs free energy [27]. Sometimes, when an alloy contains a miscibility gap (the area on the phase diagram where the 'solution' exists only as the separate phases), as shown later in section 3.6.1.1, on spinodal decomposition of TiAlN coating. The curvature for the Gibbs free energy is negative at low temperatures, and the diffusion is actually towards higher concentration. Thus, it means that the driving force for diffusion is the chemical gradient, not the concentration.

We observe two mechanisms for diffusion: a substantial number of atoms diffuse through vacancies, whereas interstitial atoms diffuse by forcing their way between the larger atoms. Normally, all atoms are vibrating; as vibrational energy is proportional to $3.k.T$, it increases with increasing temperature. Since vibrational frequency is almost constant ($\nu=10^{13}$ Hz) for the atoms, the amplitude, and thus displacement, is increased with absolute temperature. Normally, the atom is stationary, but when there is a neighboring vacancy, it may shift towards the open space.

Interstitial vacancies are important in materials such as steels, where there is a low concentration of interstitial atoms, *i.e.*, carbon. However, for thin films, substitutional diffusion is much more favorable because the atoms in nitrides are close-packed, and there is not so much space left in the structure.

The diffusivity for substitutional diffusion depends on the lattice type. For example, fcc has 12 neighboring atoms (12 bonds to break) whereas bcc only has 8, along the distance between adjacent atoms. Moreover, according to David [27], it can be stated that materials with a similar lattice structure and bond type will have a similar fraction of their melting temperature:

$$D \left(\frac{T}{T_m} \right) = const.$$

Equation 3-10

where T/T_m is the homologous temperature.

3.6.2 Atomic paths

The ideal view of diffusion considers a perfect crystal. Of course, in reality, materials are polycrystalline and contain crystal defects such as grain boundaries, phase boundaries, and dislocations. From first Fick's law, it can be shown that diffusion stops when concentration equilibrium is reached. However, this is not true in the real material, because many atoms lower their energy as they segregate to these lattice defects, and so become more concentrated at defect sites. This usually happens for large atoms within a lattice of smaller atoms. The larger atoms induce strain around their positions in the matrix, so their segregation

to grain boundaries is favored due to the lower free energy of the whole system. This is the case where the potential chemical gradient is more valid than the concentration gradient.

It has been shown experimentally [27] that diffusivity along the open surface (surface, grain boundary) is higher than in the lattice. Diffusivity of the grain boundary may be written as:

$$D_B = D_{B0} \cdot e^{-Q_b/RT}$$

Equation 3-11

where D_b is the grain boundary diffusivity, D_{b0} is the frequency factor, and Q_b is the experimentally determined value for the activation energy for diffusion. At any temperature, D_b is higher than D_l (D_l lattice).

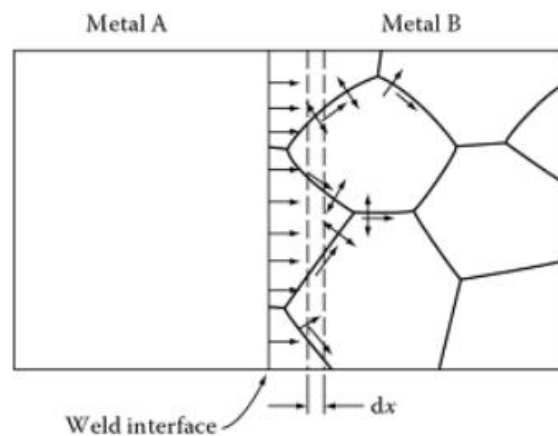


Figure 3-10 The effect of grain boundary diffusion combined with volume diffusion [28]

In this case, the grain boundaries work as a composite material. The effective width of the grain boundary is around 5 nm, and the grain size in “normal bulk” material (steel) varies from ca 1 – 1000 μm , and the effectiveness of the grain boundary varies accordingly. As we are dealing with nanostructured materials (thin films) the usual size of the grain is tens of nm (and as low as 5 nm) and the grain boundary size is about 2 nm. As explained earlier, the diffusivity is strongly dependent on the temperature.

Therefore, for most fcc metals we can state that the diffusivity along grain boundaries is the leading mechanism of atom transport in thin coatings. This effect is even more pronounced at lower temperatures, where, because of a lower activation energy for grain boundary diffusion, the diffusion is driven only by grain boundary diffusion.

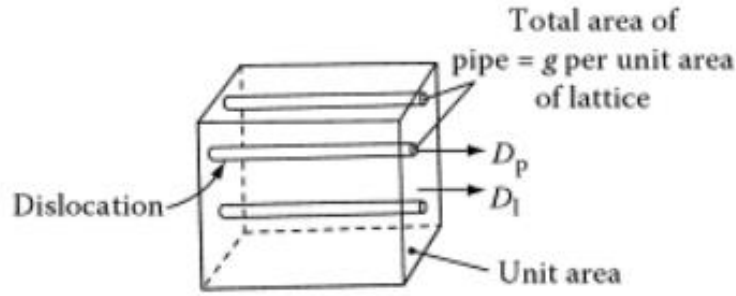


Figure 3-11 Dislocation act as high conductivity path through the lattice [28]

3.6.3 Thermal stability of hard coatings

Thermal stability means resistance against thermal recovery and recrystallization, which usually occurs if the working temperature of the material exceeds the deposition temperature. A typical method for improving thermal stability is introducing more phase boundaries. Because PVD coatings are in a thermodynamically metastable, non-equilibrium, state, thermal stability is crucial for their use in applications where high temperature is needed. This state is characterized by compressive stresses, small grain sizes, and metastable phases. To further increase thermal stability, nanolayered coatings can be synthesized. As every single layer creates another phase boundary, diffusion is effectively slowed down.

3.6.3.1 Age hardening:

Age hardening is a process whereby supersaturated phases are formed, and later decomposed, with post-deposition annealing. As previously mentioned, due to the relatively low deposition temperature, it is the assembly kinetics of the growing film limited that help to control the material in such a way that defects, supersaturated and metastable phases are easily induced in the film. The film is usually far from its equilibrium state. Other energetic particles or effects, *i.e.*, ion bombardment and plasma pulsing, can increase the energy of the assembly kinetics if desired. Therefore, the structural properties are highly influenced by different deposition techniques and the growth conditions.

The driving force for changes in any material is the Gibbs free energy, which tells us if the mixture is stable, metastable or unstable. It is defined as:

$$\Delta G_{mix} = \Delta H_{mix} - T\Delta S_{mix}$$

Equation 3-12

Where ΔH_{mix} is the enthalpy of mixing, T is the absolute temperature, and ΔS_{mix} is the entropy of mixing. As explained in [26], entropy by mixing always increases, therefore has a positive sign. ΔH_{mix} can be positive or negative.

If the ΔH_{mix} is negative, *i.e.*, an exothermic solution, the mixture is stable for any composition. The case for when ΔH_{mix} is positive (*i.e.*, endothermic) is illustrated in Figure 3-12, for the most widely used industrial coating, TiAlN.

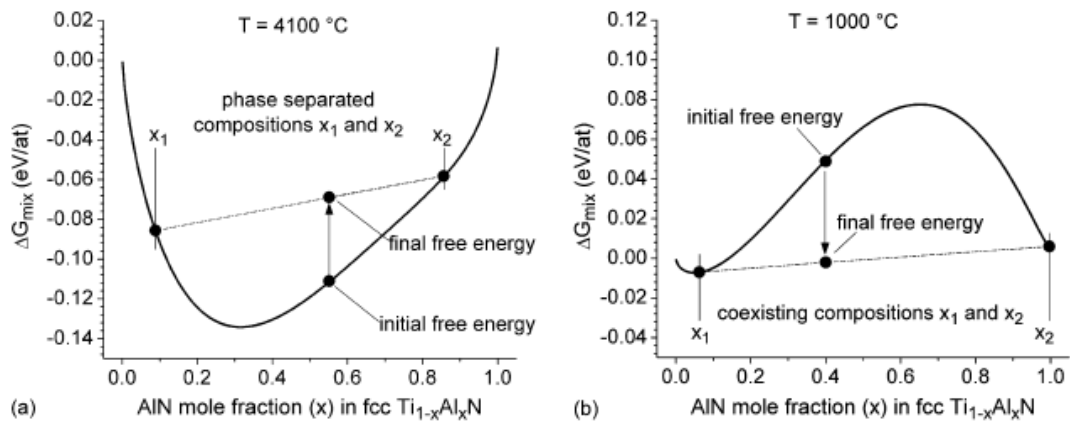


Figure 3-12 Free energy of mixing as a function of composition for fcc TiAlN with (a) $TdS > dH$ and (b) $TdS < dH$ [26]

At higher temperatures, the free energy of mixing has positive curvature, and the mixture is stable. Hence, for lower temperatures, the mixture develops negative curvature in the middle, *i.e.*, it is not stable for all compositions. For any composition between x_1 and x_2 the total energy is reduced if the mixture splits into two compositions, *i.e.*, the solution is supersaturated. By increasing temperature, the separation between x_1 and x_2 reduces, thus forming a miscibility gap. A material under supersaturated conditions seeks the equilibrium composition by separating the two phases. Diffusion and time are the driving power for this decomposition.

3.6.3.2 Decomposition of supersaturated phases

The reason for decomposition is always to reduce the free Gibbs energy. The system is not directly transforming into its equilibrium, stable structure. The decomposition is time-dependent and during this process undergoes further transitions into other phases with different kinetics. Understanding these transitions helps to engineer the process of age hardening.

As shown in Figure 3-12, even if the free energy for the given mixture is lowest when the phases are separated, there are certain instances when separating into two phases actually increases the free energy. This occurs when separation of the phases would lead to a general

increase in the energy. This separation takes place by nucleation growth. In this metastable composition, the system has a potential energy barrier corresponding to grain size.

In the point b, any phase change - even with a small fluctuation - will lead to a total energy decrease, so the composition is intrinsically unstable and will rapidly decompose into two separated phases. The point where the mixture rapidly decomposes is defined with [26]:

$$\frac{\delta^2 G_{mix}}{\delta x^2} = 0$$

Equation 3-13

The mechanism for decomposition is called spinodal decomposition, and is in opposition with nucleation and growth, as is in the case for X_a .

3.6.3.3 The spinodal decomposition of TiAlN

Historically, Al has been added to TiN films in order to increase the oxidation resistance of the coating by forming an Al_2O_3 oxide layer on top of the coating. The Al atoms substitute Ti atoms in the NaCl like lattice. The incorporation of Al into the TiN lattice increases the hardness of the material due to the increase of compressive stress; this is achieved by increasing lattice distortion and the annihilation of points defects. The lattice parameter decreases with the addition of Al into the coating. PVD deposited TiAlN coatings show a supersaturated solid solution. The solubility of Al in TiN depends on the deposition technique, but is generally around 0,66:0,34 Al:Ti in the NaCl fcc structure.

Figure 3-13 shows the behavior of the $Ti_{0.34}Al_{0.66}N$ coating while annealing in an Ar atmosphere. There are exothermic reactions evident in the differential scanning calorimetry (DSC) measurement. Reactions A, B and C can be associated with recovery, lattice defect annihilation, stress relaxation and decomposition of TiAlN to TiN- and AlN-rich domains. Reaction D corresponds to hcp AlN formation, grain growth, and recrystallization.

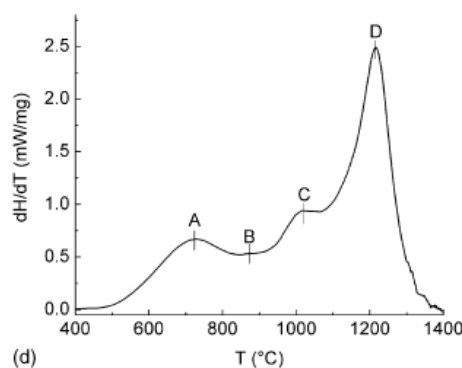


Figure 3-13 DSC traces of annealing TiAlN coating up to 1400°C [26]

During annealing at a temperature slightly above point B, the average size of TiAlN domains is around 1.2 nm. The exothermic reaction around 720°C (point A) is associated with recovery and onset of the decomposition process. The phases measured by XRD around this temperature remain the same, and the peaks are still broad.

Around point B, there is the start of the formation of an AlN domain, as indicated by an asymmetric peak in the XRD spectra. When the temperature reaches point C, 1030°C, the coating consists of three different phases of: fcc TiAlN, fcc AlN, and fcc TiN. The AlN domains that formed at a temperature of 890°C by spinodal decomposition are now coarsening, and are losing their hardness. However, this hardness decrease is retarded by the formation of TiN domains. At a temperature of 1400°C the solutions are fully decomposed to fcc TiN and hcp (wurtzite) phases.

Figure 3-14 represents the age hardening effect and the inner development of phases in the solution. There is a visible hardness increase in the range between 650 and 900°C. The hardness decrease of the TiN coating is caused by stress recovery of defects induced in the coating by deposition process and recrystallization, which does not occur in the TiAlN coating. Also, there is a visible retardation of hardness decrease while the AlN domains coarsen and new TiN domains are formed.

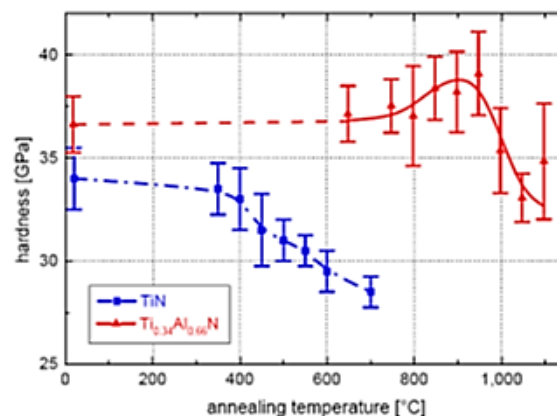


Figure 3-14 Development of hardness of TiN coating and TiAlN coating while annealing in different temperatures [12]

The starting temperature for spinodal decomposition varies. It is dependent on chemical composition as well as the deposition method. The difference is in the activation energy of surface and bulk diffusion. For example, Ti_{0.5}Al_{0.5}N deposited by magnetron sputtering can have an activation temperature of T_a , >540°C, and Ti_{0.34}Al_{0.66}N deposited by reactive arc evaporations has an activation energy at 790°C.

The activation energy is also dependent on the heating rate, and the reaction is accelerated when the heating rate is higher. The higher heating rate also shifts the activation temperature to higher values. The activation energy for reactions A and C was determined to be 3.4 eV. The value is similar for both reactions, because both of them are diffusion-driven in a one phase solution. The activation energy for reaction D is 3.6 eV. This is the energy necessary for the transformation to a wurtzite structure, where, in addition to diffusion, more energy for nucleation is needed.

According to [26], the fact that the activation energies for these reactions is associated with spinodal decomposition and the energy needed for Ti diffusion on the TiN surface (3.5 eV), one can say that the spinodal decomposition for this structure is facilitated by defect-assisted diffusion processes.

3.6.3.4 The hardening effect

Hardening during the decomposition is facilitated by a few processes. The mismatch in the lattice constant for fcc AlN ($a=0.406$ nm) and TiN ($a=0.424$ nm) induces new stresses into the coating, and hardening via Hall Petch mechanism can occur. Another effect is the difference in shear modulus, which hinders the dislocation movement in the film for larger domains.

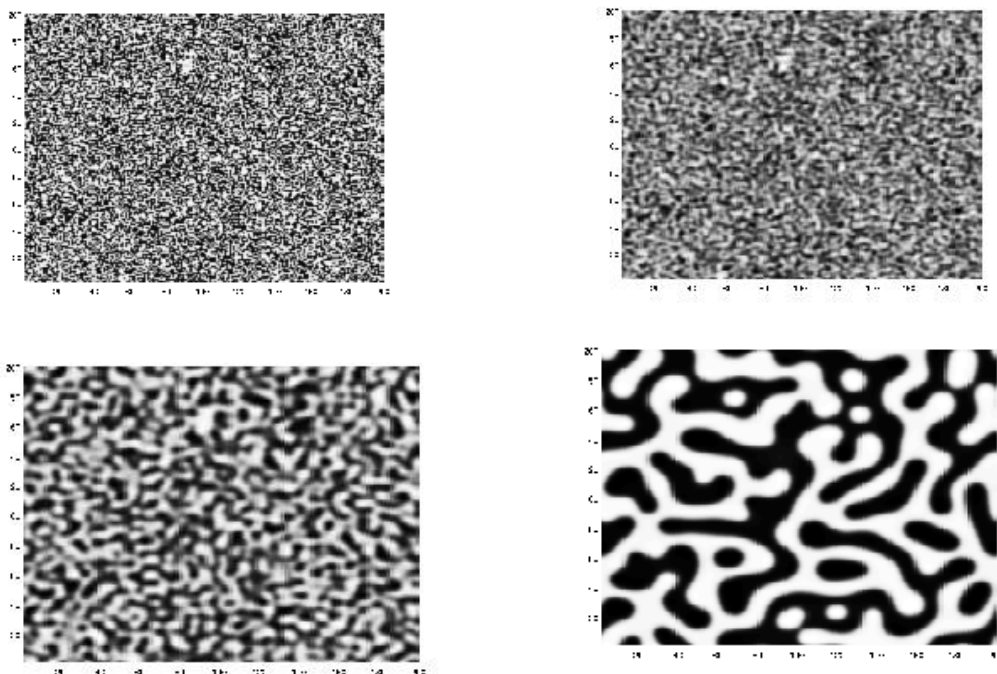


Figure 3-15 Images are showing the development in time of the spinodal decomposition. Black represents the TiN domain and white the AlN domain. The timeline begins in the top-left image, finishing in the bottom-right. [29]

3.6.3.5 Spinodal decomposition for TiAlCrN

TiAlCrN exhibits higher hardness and lower wear rate due to the altered bond state caused by the high (ca 20%) amount of added chromium.

The curvature of the Gibbs free energy can be altered by adding different amounts of Cr into the TiAlN solution. The driving force for the spinodal decomposition can thus be changed - both in magnitude and direction - by directly engineering the content of Cr [30].

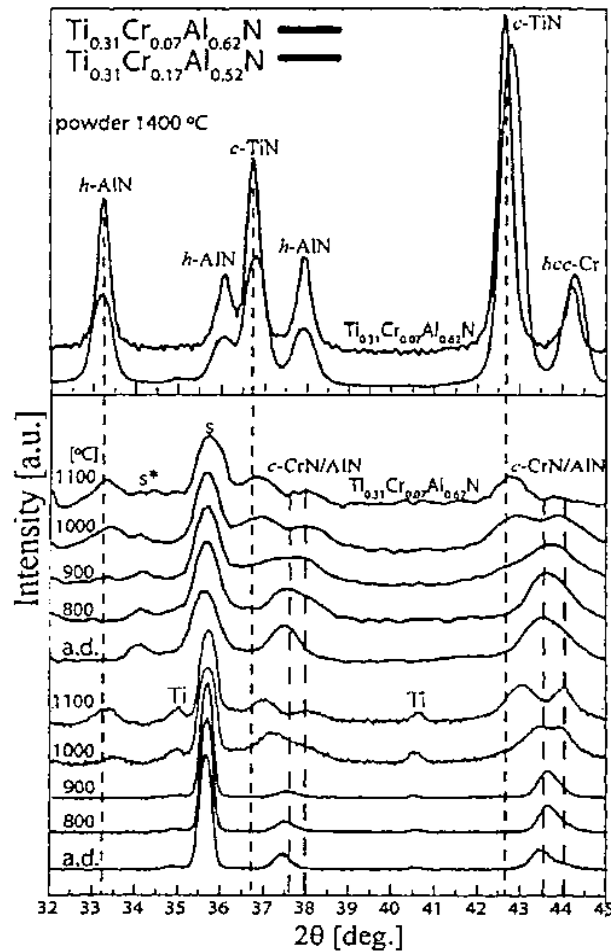


Figure 3-16 XRD diffractograms of TiCrAlN coatings of powder samples heated to 1400°C [30]

Figure 3-18 shows the XRD diffractogram of two coatings, $\text{Ti}_{0.31}\text{Cr}_{0.07}\text{Al}_{0.62}\text{N}$ and $\text{Ti}_{0.31}\text{Cr}_{0.17}\text{Al}_{0.52}\text{N}$, for the as-deposited state (a.d.) and samples annealed for 2 hours. The upper image shows samples heated to 1400°C. The peaks corresponding to the fcc-TiCrAlN coating are at 37.5° and 43.2° for (111) and (200), respectively, in the as-deposited state. By annealing at a higher temperature, the splitting to Al-rich and TiAlN-rich TiCrAlN domains for the $\text{TiCr}_{0.07}\text{AlN}$ sample occurs at a temperature of 800 – 900°C, while for the sample with a higher Cr content, the splitting starts at a temperature of 1000°C. For the

sample with a lower Cr content, the third peak, corresponding to hcp-AlN, is formed at a temperature of 1000°C and is more pronounced at 1100°C, where the fcc-AlN is barely detectable. For the TiCr_{0.17}AlN coating, the fcc-AlN peak remains up to 1100°C.

After heating to 1400°C there are three phases in the solution: hcp AlN, bcc CrN and fcc-TiN. For the coating with a higher Cr content, the peak of TiN is shifted slightly towards higher angles, suggesting that there is a small amount of Cr in the TiN phase.

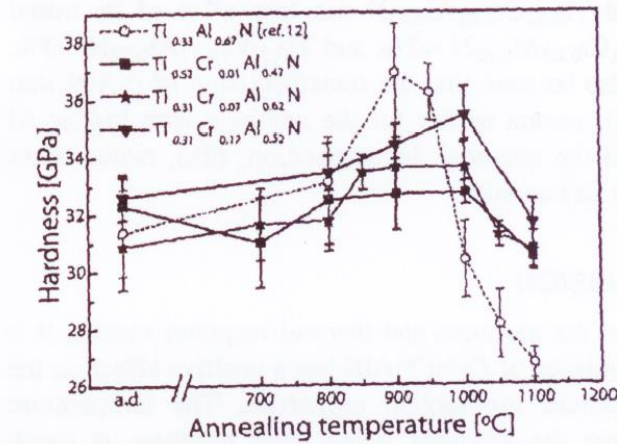


Figure 3-17 Age hardening effect for different compositions of TiAlCrN coating [30]

As with the TiAlN coating, the age hardening effect is also visible for the TiAlCrN coating, but the increase in hardness is not as pronounced as for TiAlN. However, there is still a visible increase in the hardness of coatings containing Cr. The decrease in hardness after reaching a temperature of 950°C is also gradual, and the hardness for TiAlCrN after annealing at a temperature of 1100°C is almost the same as for the as-deposited coating.

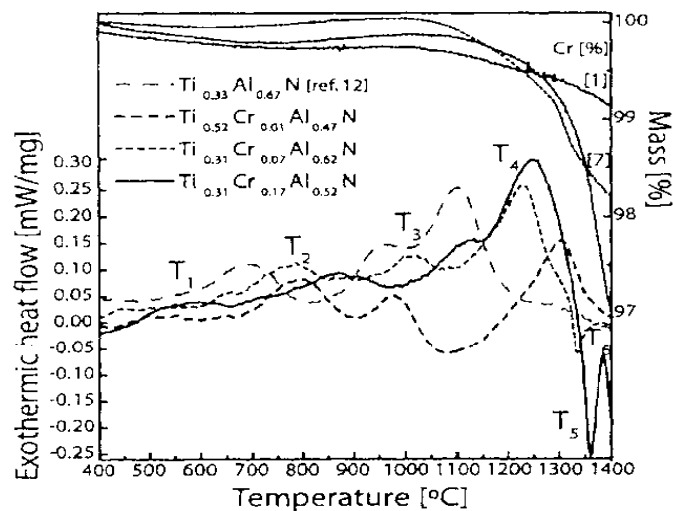


Figure 3-18 Thermal responses by DSC of different TiAlCrN coatings [30]

Figure 3-18 shows thermal responses to annealing for four coatings with different amounts of chromium. As was seen in the spinodal decomposition for TiAlN, the first two peaks, T1 and T2 at 500°C and 800°C respectively, correspond to defect annihilation. Peaks T3 and T4 are assigned to spinodal decomposition and transformation of fcc-AlN to hcp-AlN. The peak T5 is endothermic and is assigned to nitrogen release. Peak T5 is not seen on TiAlN and TiCr_{0.01}AlN samples. At an even greater temperature of 1350°C, Cr₂N decomposes to bcc-Cr, and this is the exothermic peak T6.

The transformation of c-AlN to hcp-AlN (T4) appears at a lower temperature for coatings with a lower aluminum content. Also, a higher Cr content shifts the spinodal transformation (T3) to higher temperatures.

3.6.4 Recovery

Recovery is the appearance of new stress-free grains. This is caused by atom migration, the annihilation of point defects, and dislocation. Recovery is associated with relaxation (lowering of stress) in the coating. While a material is recovering, the Schottky point defects are being annihilated, thus the volume of the coating decreases. This mechanism provides tensile stress. To start the recovery process, a 'driving force' is required to overcome the activation energy. This energy is practically induced during heating of the coating. Once the temperature exceeds the deposition temperature, the recovery begins. While high hardness is usually induced in super hard coatings by high compressive stresses, this mechanism also means that very hard coatings have poorer thermal stability

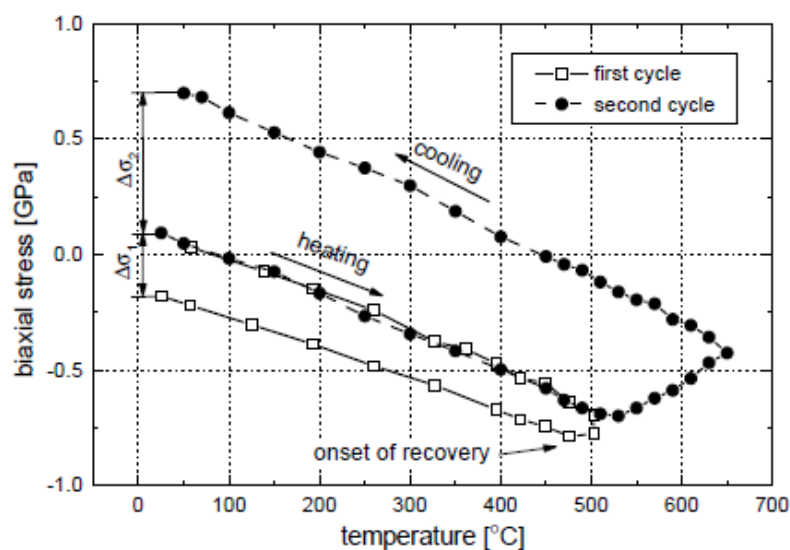


Figure 3-19 Repeated recovery cycles [31]

Superhard nanocomposite coatings can overcome this problem, as they can reach higher hardness with smaller grain sizes, which are almost defect-less, thus the driving force for recovery is much lower. The activation energy for grain growth in the as-deposited state increases with grain size.

3.7 Mechanical properties of coatings

Properties of the coating depend fundamentally on the nature of bonding between the neighboring atoms and on nature of their microstructure. During plastic deformation, the atoms move with respect to each other. There are two ways for atoms to move – gliding or creep processes (climbing over dislocations). Climbing of dislocations requires crystal imperfections such as vacancies. This process is highly dependent on thermal activation and is related to diffusion. Creep rates in polycrystals depend strongly on the grain size, d . The ratio of creep processes can be d^2 up to d^3 , according to the mechanism of creep process. The effect of increased stress development - and thus strengthening due decreasing of grain size - can be described with Hall Petch relations [32] and [26] .

$$\sigma_Y = \sigma_0 + K_{HP} \frac{1}{\sqrt{d}}$$

Equation 3-14

Where σ_Y is the yield stress, σ_0 is the stress induced by other means, K_{HP} is the material constant, and d is the average grain diameter.

3.7.1 Hardness, H

In conventional metals, hardness is increased with plastic deformation due to an increase in dislocation density. This can be obtained by increasing the grain boundary fraction, i.e., decreasing grain size. The strengthening mechanisms, which occur in thin films, are based on the hindering of dislocation movement. There is a high density of point defects and line defects (generated during growth), internal boundaries such as grain, phase and columns, second phase particles, solutes, age hardening. Reducing the grain size has a negative effect on creep strength. Nanostructural pure metals are much stronger and less ductile than conventional ones.

Mechanical properties such as hardness can be understood in terms of the propagation of a radius of dislocation density at a given stress with grain size, describing the microstructure.

The effect of grain size on yield stress can be described with Hall Petch relation, as detailed above in 3.7.

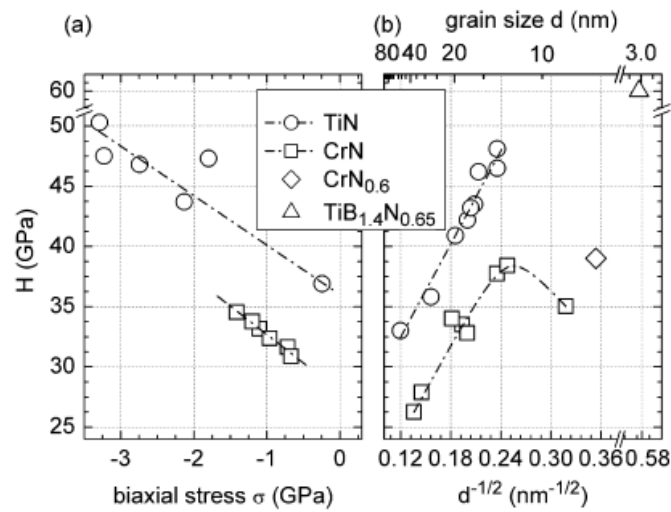


Figure 3-20 Figure Hall Petch relation for different materials. [26]

The limit of validity of the Hall Petch relation is that at least one dislocation loop must fit the grain size. According to [31], for CrN this limiting grain size is 12 nm. At this grain size, the hardness reaches its highest value of 38 GPa. At lower grain sizes, the sliding is dominated by grain boundary sliding instead of dislocation-driven plastic deformation. This transition size determines the highest hardness achievable for a single-phase low stress sputtered coating. For other materials - TiN, TiAlN, etc. - the same hardness can be achieved even at higher grain sizes by alloying with another material or by increasing stress during the deposition.

A completely different method for producing a superhard material is making a nanocomposite structure where neighboring grains consist of another material with a different lattice crystal structure, and therefore a different slip system. For example, fcc CrN and hcp Cr₂N, or a TiN and TiB mixture, where grain boundary sliding can be prevented down to a grain size as low as 3 nm. This helps to create a coating with low stresses and still retain a very high hardness (60 GPa for TiN/TiB).

A similar behavior occurs for multilayered coatings. The hardness is a function of the thickness of single layers. Callisti et al. [33] showed, that for Zr/Nb system with nanomultilayers ranging from 6 nm to 16, there exists a threshold with the highest hardness at 27 nm, proving that the Hall Petch relationship is also valid for multilayers. High hardness has been reported to be caused by the blocking of dislocation motion at the layer interfaces, due to differences in the

shear moduli of the individual layer materials, and by analogy, strain is causing periodical strain-stress fields in the case of lattice mismatched multilayered films [34].

A further increase of the period thickness led to a progressive decrease of the coating hardness, up to a point that remains fairly constant, due to the total loss of the superlattice effect. At this point, multilayers start to behave as individual layers, and the hardness of the films can be represented by the weighted average of the hardness of the individual layers.

3.7.2 Young elastic modulus, E

As well as the hardness, Young's elastic modulus depends on the number and nature (strength) of bonding between adjoined atoms. In comparison to bulk materials, the elastic modulus of nanostructured coatings has a few different behaviors. In a real coating, the elastic modulus also depends on the dislocation density and the density of the coating [35]. The dislocation density is very closely connected to the grain size of the material.

Due to the very small grains in nanostructured coatings, many atoms appear in the grain boundaries. The smaller the grains are, the greater the fraction of atoms sitting on the boundary. Some authors claim that the elastic modulus is reduced with grain size, although some results are contraindicatory.

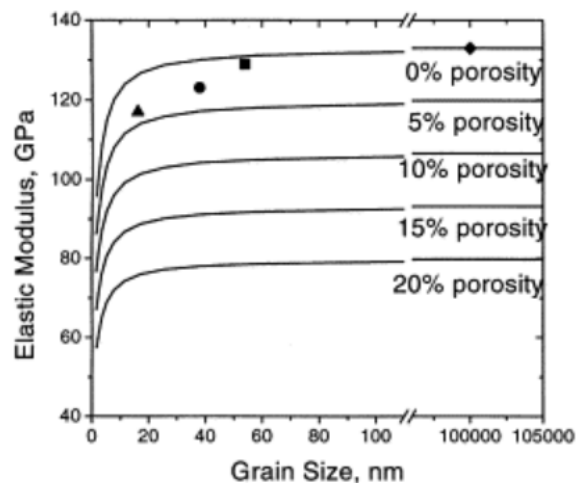


Figure 3-21 Effect of porosity and grain size on simulated Pd crystal [35]

Kim et al [35] inspected the influence of grain size and porosity of the material on the evolution of E. They simulated two different influences on the modulus, intrinsic effects (grain size, interfacial volume, atomic distance) and extrinsic influences (porosity). As can be seen from the simulation results, Figure 3-21, porosity has a greater effect on the elastic modulus

than grain size. This is a crucial issue because grain size is quite easily measurable by XRD methods, but measuring the porosity of the coating is not so simple.

As for the development of the elastic modulus in multilayers systems, again Callisti et al. [33] showed that the elastic modulus correlates well with hardness, thus increases with a decrease in single layer thickness to some extent, and then decreases.

3.7.3 H^x/E^y ratios

The two most common used ratios concerning hardness and elastic modulus are H/E and H^3/E^2 . The former is usually defined as the resistance of the material to elastic deformation [36]; the higher the value is, the material is more flexible. It is very important to maintain a high value for this ratio ($>0,1$ [37]) when the coating is applied on a bendable surface (thin glass or metal sheet tool). By increasing this ratio, the material develops a higher resistance to cracking. The latter, H^3/E^2 , correlates with the ability of a material to dissipate energy at plastic deformation under load [38]. This can be associated with the ductility of the material. A higher H^3/E^2 ratio corresponds to a greater toughness of the material.

It should be noted that increasing both ratios can be achieved by increasing the hardness of the material and decreasing the elastic modulus. The importance of these ratios is demonstrated by thermal cycling tests in experimental section 5.3.4.1.3. Also, due to the stresses applied to the coating during deposition, higher H^x/E^y ratios lead to better adhesion of the coating to the substrate [38].

4. State of the art industrial coatings

Improving material performance and value for money is as old as humanity. Even in brief steps, the transition from the stone age to the bronze age, iron age and to the present 'composite age', drove humanity to introduce and develop new materials to suit their needs. As there is always space to improve the bulk material, nowadays there are often more efficient methods to achieve the goal. For many applications, and mainly for those where the size of objects is decreasing, the added value of better, more durable, shinier or a more active surface is more important than the properties of the bulk material. The added value of an object - later in this work generalized as a 'tool' - depends on the surface properties, because the surface is the first interface at which any external body reacts with the tool.

In this thesis, the main focus is given to industrial applications of tools for high-temperature applications. Although there are many possible applications such as welding, machining, die casting, stamping, *etc.*, the main objectives of this work are high-speed dry machining of hard steel and high pressure die casting of aluminum. The first topic is important because of the widespread usage of PVD and other coatings on cutting tools in modern industry, and the economic gain is enormous; the latter one because of increasing demand of aluminum products, and because the coating of tools for high-pressure aluminum die casting is not yet common practice in the industry.

For both processes, surface interactions play the most important role. As Wolfgang Pauli once said: "*God made the bulk; surfaces were invented by the devil*", so it is necessary to analyze and explain all processes which occur on the surface during the high-temperature use of the coatings discussed herein.

4.1 Industrial used PVD nitride coatings

The history of commercial PVD coating starts in 1980, when the first titanium nitride coating was applied. This followed the success of CVD hard coatings in the industry. PVD and CVD coatings differ in many properties, as explained in section 2.1.1, but the initial motivation was the need of the application of hard coatings at lower deposition temperatures, especially for tool steels. This need is fulfilled by PVD coatings, where the deposition temperature is ordinarily around 450°C, while for CVD the deposition temperature is at least 800°C, demanding a substrate which can withstand these temperatures. The success of TiN coatings was followed by the PVD $Ti_{0.5}Al_{0.5}N$ coating, which was introduced by CemeCon AG and is still the most applied PVD coating today.

4.1.1 Binary nitrides

Binary nitrides consist of nitrogen plus another metal. In the manufacturing industry, a few binary nitrides are used: Titanium nitride (TiN), Chromium nitride (CrN) and Zirconium nitride (ZrN). The two most common are CrN and TiN.

4.1.1.1 Titanium nitride – TiN

Titanium nitride (TiN) was the first physical vapor deposited hard, wear-resistant coating used widely in the manufacturing industry from the 1980s. It successfully protects cutting and forming tools against wear, and is suitable for a wide range of applications such as the machining of carbon stainless steels, cast irons and aluminum alloys, and also protecting molds, dies and stamping and forming tools. Although it is the oldest example, it is still widely used in industry thanks to its toughness.

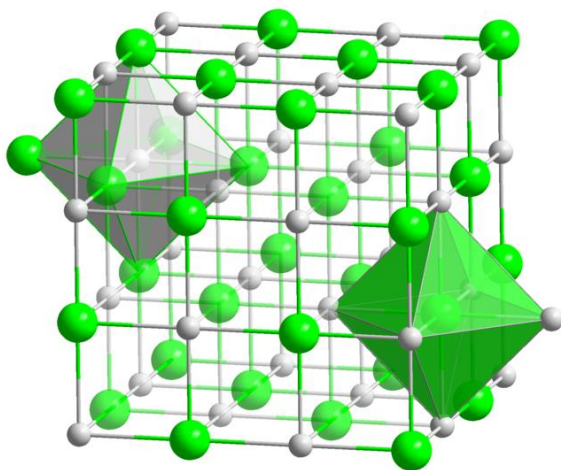


Figure 4-2 TiN inner hallite structure [87]



Figure 4-1 Taps coated with TiN coating

The drawback of the TiN coating is its relatively low (compared to other modern sputtered materials) thermal stability. The use of TiN coatings is limited to 550°C, whereupon rapid oxidation starts. Moreover, titanium dioxide (TiO₂) does not passivate the surface, but is channeling even more oxygen underneath the surface, leading to the fast destruction of the coating. TiN has a typical industrial hardness of around 25 GPa, and it is used for forming tools (punching, broaching) and cutting tools - mostly taps.

4.1.1.2 Chromium nitride - Cr_xN

Alongside titanium nitride and other hard nitrides, chromium nitride has an fcc lattice structure. A key advantage of chromium oxide is that it is very resistant to corrosion. Therefore, it is often

used to replace the chromium plating process, although in comparison to chrome plating it yields poorer corrosion protection. Another difference to TiN is its higher temperature stability (up to 700°C) and ductility, but usually lower hardness. The hardness of industrially coated CrN is around 20 GPa, but can reach up to 38 GPa (see section 3.7.1) when the grain size is on the nanometer scale.

Nowadays, with the boom of the plastic industry, CrN is a very important surface treatment of molding dies and cores. The elements in CrN are bonded with relatively weak covalent bonds, thus do not react strongly with polymers, making CrN a universal coating for plastic processing. Chromium nitride can be deposited either as stoichiometric CrN or as Cr₂N. In the latter, additional Cr atoms are trapped in an interstitial position, and the compound is quite stable and hard. Moreover, it is a byproduct of the thermal decomposition of CrN. CrN and (to an even greater extent) Cr₂N have the highest sputtering rate from hard coatings due to the high sputtering yield of Cr (4x higher than titanium), so coatings more than 10 μm thick can be formed rapidly.

Hard CrN coatings are used for cold metal forming processes such as shearing, punching, rolling, extrusion of Al, *etc.* For cutting purposes, CrN is used for the machining of non-steel metals such as brass, copper, aluminum, *etc.*

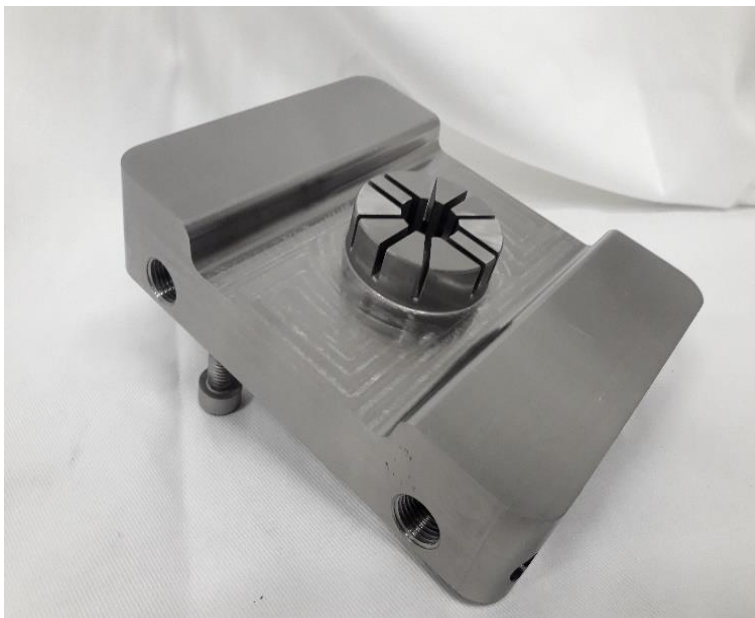


Figure 4-3 Plastic mold coated with CrN for processing glass reinforced polyamide



Figure 4-4 Aluminum extrusion cylinder coated with CrN

4.1.2 Ternary nitrides

Ternary nitrides are compounds consisting of nitrogen and two other metal elements. Ternary nitrides used in industry possess an fcc crystal structure, 50% of which is filled with nitrogen, with the rest occupied by other elements. For the properties of the coating, not only is the

nature of the other elements important, but so is their concentration. The most commonly used ternary nitrides are AlTiN, TiAlN, AlCrN, TiSiN (usually as nanocomposite (TiN + Si₃N₄)).

4.1.2.1 *Titanium aluminum nitride - TiAlN*

TiAlN is a coating based on supersaturated phases of TiN and AlN. Aluminum atoms substitute some of the Ti atoms in the TiN crystal structure. Aluminum is added to this solid solution to increase oxidation resistance by forming an Al-rich oxide layer on the surface. Another effect of adding aluminum is the increase of compressive stresses due to hindering of point defect annihilation, which leads to increased lattice distortion.

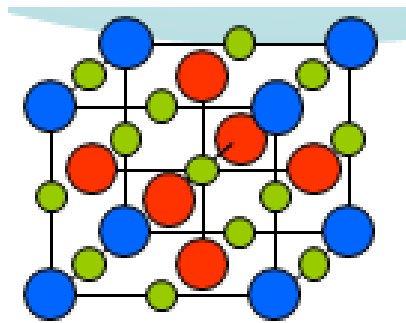


Figure 4-5 TiAlN crystal structure [12]

The properties of TiAlN coatings are related to the concentration of Ti and Al, as well as deposition conditions. Maximum solubility is also dependent on deposition conditions. The maximum molar concentration of Al is around 0,7 [26]. At higher concentrations, a wurtzite AlN structure is formed, as shown in Figure 4-7. Another effect of increasing the aluminum content is decreasing the lattice parameter from 0.425 nm (no aluminum) to 0.406 (100% Al in solution), as shown in Figure 4-6.

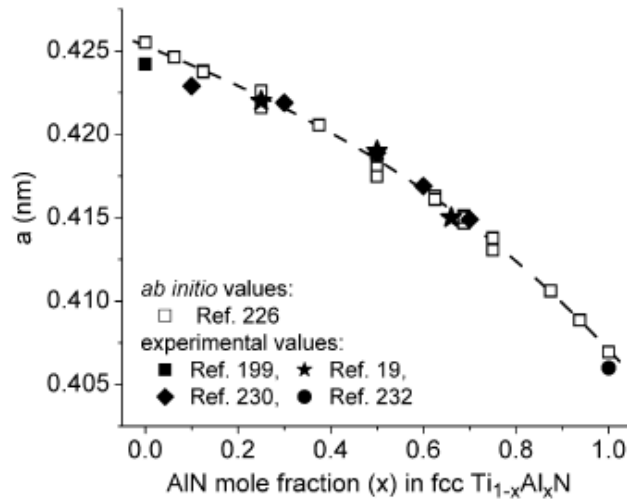


Figure 4-6 Lattice parameter an fcc TiAlN films as a function of the AlN mole fraction [26]

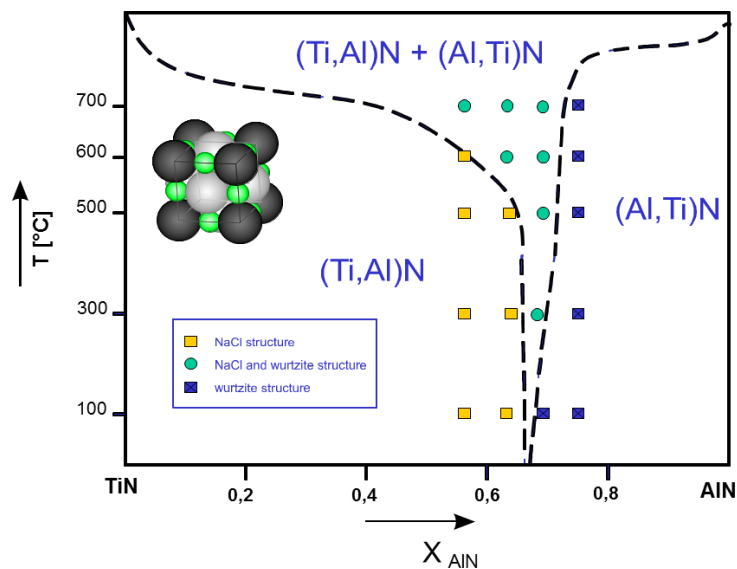


Figure 4-7 Phase diagram for TiAlN coating deposited at different temperatures [12]

TiAlN coatings are thermally stable up to a temperature of around 750°C. Above this temperature starts the process of age hardening by spinodal decomposition, as explained in section 3.6.3.3. A solid solution of TiAlN decomposes to fcc-TiN, fcc-AlN. Due to this decomposition, the hardness of the coating increases due to the many small grains. The onset temperature of rapid oxidation is around 800°C, as will be shown in section 5.1.4.

As TiAlN coatings have been intensively studied, many modifications also exist. Multilayer growth is a method to increase the lifetime of TiAlN. They have a lower wear rate than conventional TiAlN, and can suppress the formation of hcp AlN. The effect of multilayers was

shown in section 3.7.1, and will be intensively discussed in section 5.1.3. TiAlN can also be alloyed with different elements to improve performance.

Vanadium has a low melting temperature and oxides easily. Due to these properties, multilayer TiAlN/VN materials have been created. Vanadium forms oxides: Magnelli phases with a low coefficient of friction, [39].

Adding yttrium to an alloy effectively hinders diffusion. The yttrium atom has much bigger radius than titanium, so it segregates at grain boundaries, thereby closing boundary channels for diffusion (see section 3.6.1.1). [40] It also slows the decomposition of the TiAlN compound.

The effect of Cr on the spinodal decomposition of TiAlN coating was discussed in section 3.6.3.5, and all its effects will be discussed later. Other alloying elements include W and Mo, which form high resistance oxides when exposed to oxygen at high temperatures.

4.1.2.2 Aluminum chromium nitride

The disadvantage of TiAlN coatings is that in many applications their performance is dependent on the Al_2O_3 outer layer formed in an oxidizing atmosphere. After the destruction of this layer, the coating can deteriorate very fast. For this reason, titanium was replaced by chromium in some applications. Although this behavior has been known for some time, until recently, there was no need in the industry to switch to Cr-rich coatings. Its ability to withstand higher temperatures is advantageous only if high speeds are applied in the cutting process, *i.e.*, better cutting machines are needed, and the tool substrate also has to withstand higher temperatures. The influence of working temperature on hardness is shown in Figure 4-8. Note that in this figure the hardening of TiAlN is not visible. The reason is another deposition process. Thus, it is always necessary to compare material properties of coatings produced using the same manufacturing method.

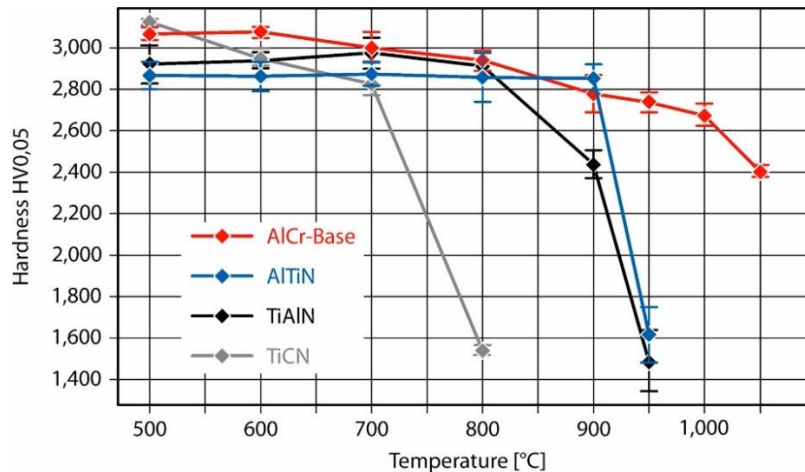


Figure 4-8 Hardness evolution of hard nitrides coating depending on temperature [41]

4.1.3 Quaternary nitrides

Again, adding another element to ternary nitrides leads to many changes in the performance of the coating. In the following sections, we study in particular the behavior of the Ti-Al-Cr-N coating (TiAlN alloyed with Cr), but there are also other quaternary nitrides used in industry such as AlTiSiN, CrAlSiN and other alloys of TiAlN, as mentioned in 4.1.2.1.

4.1.3.1 Titanium aluminum chromium nitride

The usual amount of Al in TiAlN coatings is about 67%, which is the highest concentration possible to form a supersaturated solid solution. By adding Cr into the alloy, the structure could be stabilized up to an Al content of 73%. Adding Cr into the compound creates strong metal Al-Cr bonding, where Cr is a donor and Al an acceptor. This chromium aluminide forms three-dimensional nano-islands during growth. The composition of these Cr-Al domains is CrAl₇ according to the study of Rabinovich et al. [42]. As a result of this, the amount of the AlN phase in TiAlCrN is lower than in TiAlN coating.

Electron configuration determines the mechanical properties of the material. More plastic metal bonds are formed by weakly bound electrons, while electrons with higher binding energies form stronger covalent bonds, as determined by XPS analysis. The strength of bonding, and therefore mechanical properties, can be determined from the density of states (DOS) and its distance to the Fermi level. High DOS at the Fermi level for Ti_{0.33}Al_{0.67}N compound corresponds to Ti 3d and Al 3p, leading to metallic bonds in TiAlN; this results in lower hardness and higher plasticity. The Ti_{0.1}Al_{0.7}Cr_{0.2}N compound exhibits lower DOS at the Fermi level and has higher DOS at higher binding energy. This leads to higher room temperature (and hot) hardness and lower plasticity. It is obvious that the concentration of Cr

controls the hardness and plasticity properties for this compound by regulating the amount of Al-Cr metallic bonds.

According to [42] TiAlCrN creates a face-centered cubic structure of supersaturated solid solution. There is a TiN halite structure with a full lattice of N atoms, and Ti atoms are substituted for Al and Cr. They also report the columnar growth of grains with a size of 20 nm and higher.

Alloying TiAlN with Cr improves its high-temperature stability and significantly increases the possibility to machine hardened steels. Because of stronger bonds between atoms, TiAlCrN is not able to dissipate energy produced by plastic deformation, and therefore impact fatigue resistance is lower than for TiAlN coatings. On the curves of flank wear rate there is a visible, slow wear increase region after the drill is used for some time. Moreover, the hardness of the workpiece extends into the slow region. Another improvement is that the coating reduces the cutting force needed to cut the workpiece with the same feed rate and speed. Reduction of the force required leads to a decrease in heat generation when cutting, therefore, the drill is working in lower temperatures. Naturally, the force used on the drill is transferred as heat.

Although the TiN coating exhibits the same hardness as TiAlCrN, and has a lower coefficient of friction, the cutting performance of the TiAlCrN coating is in fact superior. This can be explained by the low oxidation resistance of the TiN coating. As mentioned before, the oxidation resistance of TiN ends at a temperature of around 550°C, where TiO₂ oxide is formed, and the TiN coating loses its hardness rapidly. Because the CrN coating exhibits greater oxidation resistance at higher temperatures, this plays the most important role in the improvement of cutting performance.

According to [42], the microhardness does not show a visible decrease up to 600°C. Then it drops slightly and once again increases as the temperature exceeds 900°C; this hardness is maintained by brittle oxides (Al₂O₃, Fe₂O₃, Cr₂O₃, etc.) and in real life it is not possible to use this hardness for superior cutting performance.

4.1.3.2 Already tested compositions

Composition	Deposition Technique	H [GPa]	E [GPa]	H/E	H ² /E ³	T _{max}	Source
Ti1Cr39Al60N	Arc	32,5				700	[30]
Ti2Cr38Al60N	Arc	33				800	[30]
Ti11Cr28Al61N	Arc	30				1100	[30]
Ti31Cr7Al62N	Arc	31				1050	[30]
Ti33Al67N	Arc	31				970	[30]

Cr32Al68N	Arc	31				700	[30]
Cr66Al34N	HiPIMS	28	340	0.078	0.17		[43]
Ti5Cr65Al30N	HiPIMS	34	360	0.086	0.26		[43]
Ti10Cr61Al29N	HiPIMS	40	425	0.088	0.32		[43]
Ti13Cr58Al29N	HiPIMS	36	380	0.085 5	0.26		[43]
Ti20Cr54Al26N	HiPIMS	34	370	0.085 5	0.25		[43]
Ti28Cr48Al24N	HiPIMS	32	360	0.084	0.23		[43]
Ti40Cr43Al17N	HiPIMS	30.5	350	0.08	0.19		[43]
Ti53Cr33Al14N	HiPIMS	30.5	350	0.079	0.19		[43]
Ti64Cr26Al10N	HiPIMS	29	350	0.078	0.18		[43]
Ti33Al67N	Arc	31				950	[44]
Ti52Cr1Al47N	Arc	31				1000	[44]
Ti31Cr7Al62N	Arc	32				1000	[44]
Ti31Cr17Al52N	Arc	33				1100	[44]
Cr50Ti30Al20N	Arc	38	319	0.119			[45]
Ti10Cr20Al70N	Arc	28					[42]
Ti33Al67	arc	22					[42]
Coatings developed in this thesis and discussed in section 5.2.5							
Ti50Al50N	Pulsed MS	24	446	0.053	0.067 8		
Ti30Cr25Al45N	Pulsed MS	17	343	0.05	0.041 8		
Ti27Cr41Al32N	Pulsed MS	17	335	0.05	0.042 0		
Ti26Cr50Al28N	Pulsed MS	20	348	0.057	0.064 1		

Table 4-1 Different composition of TiAlCrN coatings already studied in mentioned works and their mechanical properties. T_{max} refers to maximum temperature until the coating loses its hardness.

4.1.3.3 Other published results concerning TiAlCrN

Rabinovich *et al.* [42] tested the behavior of $Al_{0.66}Ti_{0.33}N$ and $Ti_{0.10}Al_{0.70}Cr_{0.20}N$ coatings in the machining of soft steel, hard steel and Inconel in dry conditions. They concluded that the advantage of using the TiAlCrN coating is most pronounced when machining extremely hard

steel, rather than machining very tough Inconel. This is because of the greater Cr-Al bond strength in the TiAlCrN film, which leads to greater oxidation protection, but renders the material more brittle. Meanwhile, the AlTiN coating without chromium exhibits better toughness, *i.e.* H/E ratio, therefore is more capable of withstanding the toughness of Inconel.

The team of Bai et al. [46] tested TiN and TiAlCrN coatings in drilling conditions and have suggested the use of the TiAlCrN coating for use in harder steel. However, the TiN coating exhibited higher hardness and a lower coefficient of friction than the TiAlCrN coating. They concluded that when machining harder steel, the higher oxidation protection and thermal stability is more important than the coefficient of friction and hardness of the coating.

Another method of increasing the performance of TiAlCrN is the multilayered structure. The multilayered structure usually exhibits lower wear rate, as shown by Polcar et al. [47] and Alberdi et al. [48]. There are many ways of designing multilayers with different compositions and thickness. The most pronounced multilayer effect is shown when a single layer thickens from 5 to 15 nm, as was discussed in section 3.7.1.

Luo et al. [40] studied the design of multilayered structure with yttrium doping. A TiAlYN layer was added to the TiAlCrN coating every 1,7 nm. The doped coating exhibited better performance in cutting as well as other structural tests. The yttrium functions as both an oxidation and diffusion barrier. The yttrium doping also leads to the denser microstructure of the coating and lower thermal conductivity. The same group also explored TiAlCrN doped with vanadium. Vanadium is a metal element with a low melting temperature of 650°C. Once this temperature is reached, vanadium diffuses rapidly towards the surface, forming a thin liquid layer on the surface of the coating. This layer reduces friction and works very well as anti-sticking protection while machining sticky materials such as titanium alloys and aluminum alloys.

4.1.4 Coatings morphology

One of the advantages of the PVD coating process is the ability to grow hard coatings with different morphologies.

The basic type of coating is a solid solution. The coating has one phase consisting of fully mixed elements. For nitride coatings, a columnar morphology is typical, as shown in Figure 4-9.

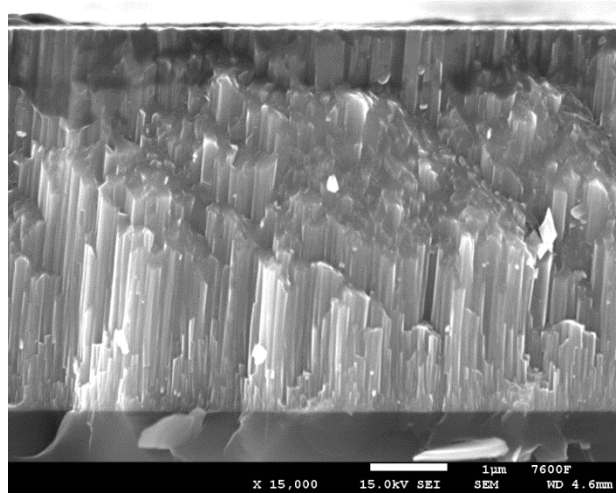


Figure 4-9 Columnar morphology of a TiAlN coating

Another possibility is to grow multilayered coatings. Each multilayer usually has a different chemical composition and different mechanical properties. By carefully tuning these properties, it is possible to obtain a final coating with different bulk mechanical properties than those exhibited by the separate layers. The properties of the final coating depend on the thickness of the single layers. Figure 4-10, 4-10, 4-11 and 4-12 show two CrN/AlCrN coatings with bilayer thicknesses of 64 and 25 nm, respectively. Both coatings started with a 1 µm thick bonding layer of pure CrN, and CrN/Cr multilayers were deposited on top of it. Although all sputtering conditions were the same for the multilayered system, the 64 nm thick multilayers continued with columnar growth and columnar morphology, which is visible through the whole coating. However, a bilayer thickness of 25 nm leads to a change of coating morphology to ‘fully dense’, which is typical for nanocomposite nitride coatings.

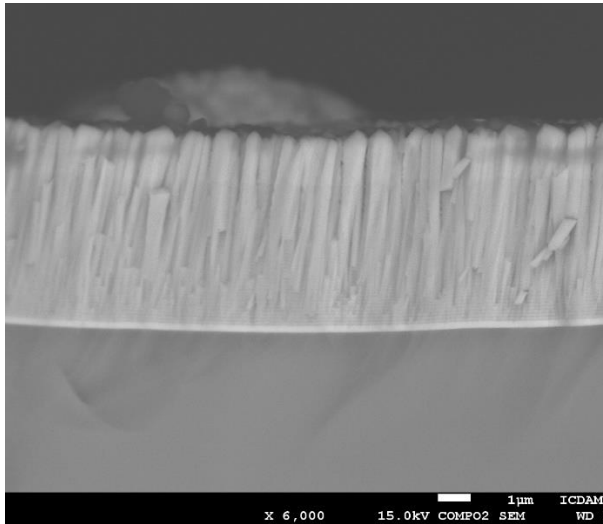


Figure 4-10 CrN/AlCrN coating with bilayer thickness 65 nm

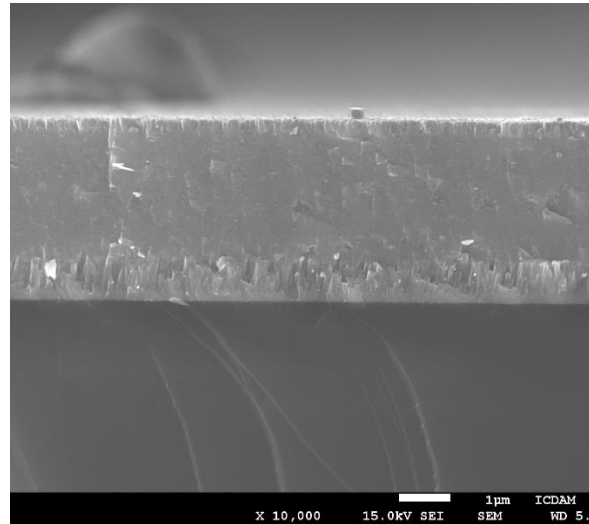


Figure 4-11 CrN/AlCrN coating with bilayer thickness 25 nm

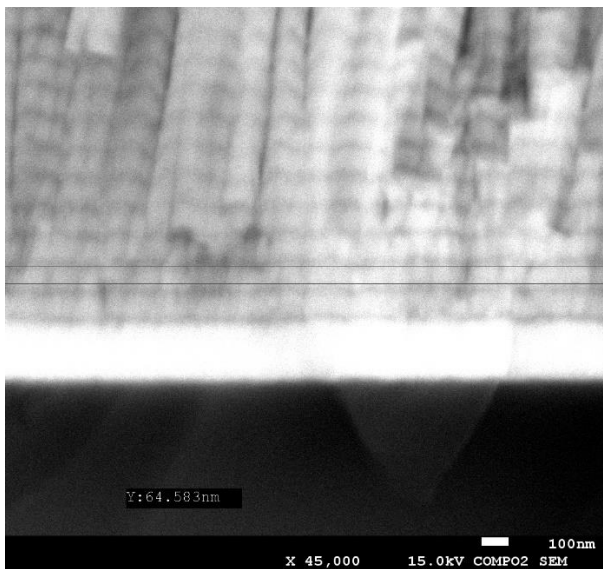


Figure 4-12 CrN/AlCrN coating with bilayer thickness 65 nm

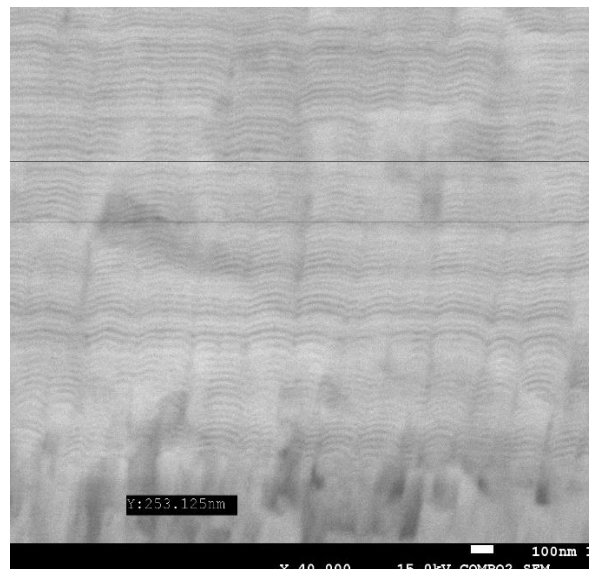


Figure 4-13 CrN/AlCrN coating with bilayer thickness 25 nm

Nanocomposite coatings are formed from two phases, where one is amorphous and the second is nanocrystalline. Typical coatings with this structure are tungsten, chromium or silicon doped DLC coatings, where WC, CrC or SiC nanograins are formed in an amorphous carbon matrix, or TiSiN coatings where TiN nanograins are embedded into an amorphous Si_xN_x matrix. These coatings usually have interesting properties such as high hardness, but usually suffer from low ductility.

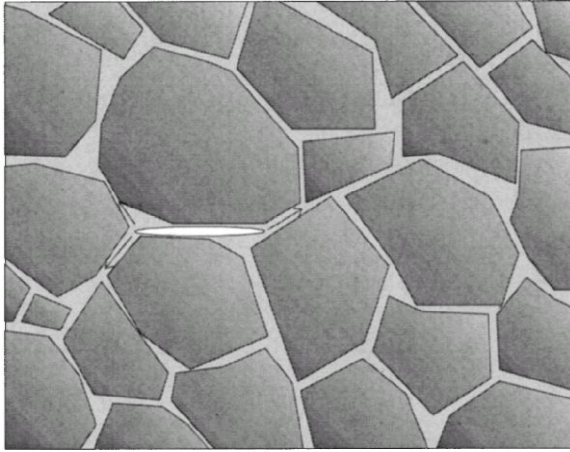


Figure 4-14 Schematic structure of nanocomposite coatings [12]

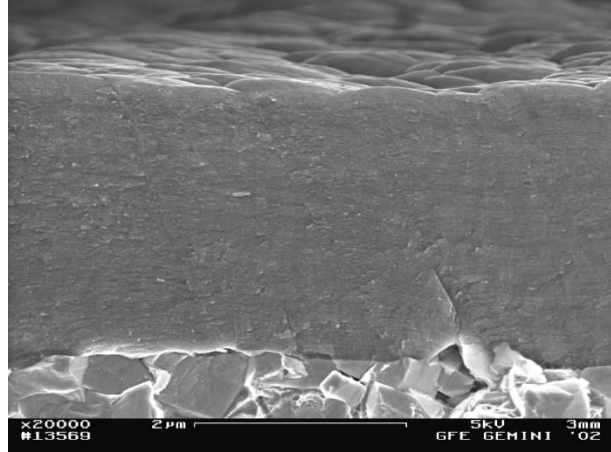


Figure 4-15 SEM cross-section of nanocomposite TiN/SiN coating [12]

4.2 Coatings of cutting tools

4.2.1 Motivation

As many coatings are already used in industry, the demand for properties such as high hardness, low thermal conductivity, reasonable toughness, controlled adhesion, minimum diffusion, and low friction at working temperatures continues to increase. The most widespread use of thermally stable, hard coatings is in the cutting tools industry.

The machining of metals is still the most efficient way of producing metal products. The world market of cutting tools, according to the study “Cutting Tools 2014” from Dedalus Consulting, [49] in the year 2013 was worth a total of 16,33 billion USD.

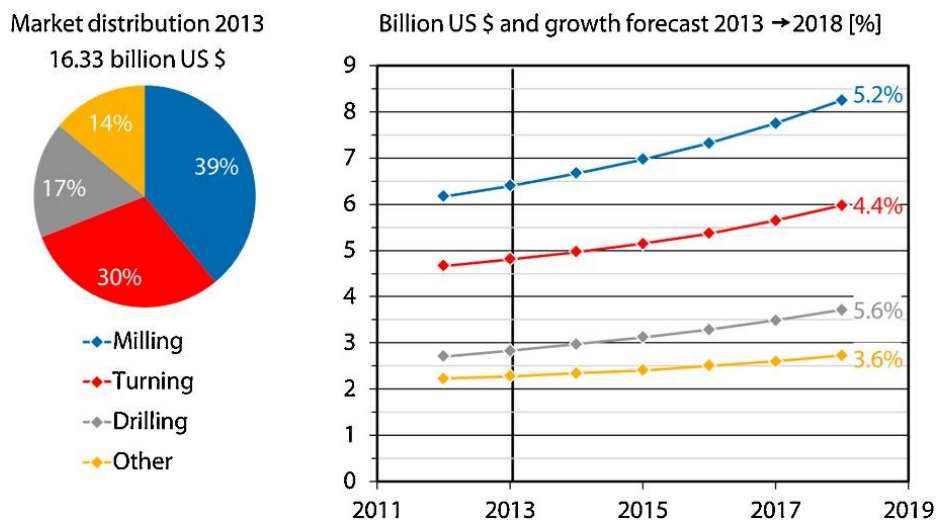


Figure 4-16 Cutting tools market distribution [49]

Milling and turning applications occupy more than three-quarters of the market, leaving 17% for drilling and 14% for other applications. According to the study, the general trend of the increasing market size in metal machining applications is a slight increase of a few percent per year.

Figure 4-17 shows the cutting materials used as the bulk material for cutting tools. The most commonly used material is cemented carbide at 53%, followed by high-speed steel at 20%. From the study, the fastest growing use of the material is predicted to be PCD (polycrystalline diamond). This corresponds very well with the drive for lightweight constructions and components, which will be discussed later. PCD cutting materials have the strongest benefit for cutting of aluminum alloys.

This predicted increase in market share of different cutting tools materials is driven not only by the development of new fabrication methods of bulk materials, but also the use of new product materials such as aero superalloys (Inconel, titanium solution), Al compounds, and very tough austenitic steels.

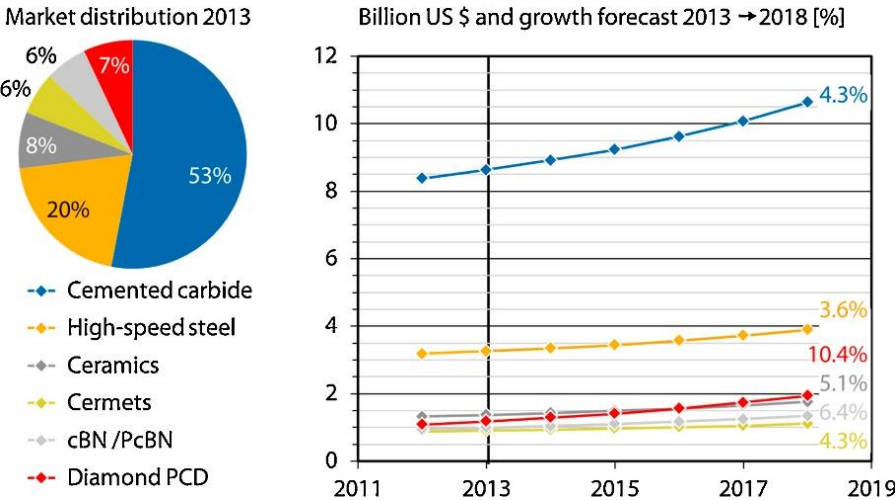


Figure 4-17 Cutting materials serving as a substrate for the coatings [49]

To increase productivity sufficiently, the cutting process should meet the following parameters:

- 1) Low or no lubrication
- 2) High cutting speeds
- 3) High cutting performance

All of the above mentioned properties lead to an increase in cutting temperature., *i.e.*, decreased cooling on the tool surface, or increasing thermal load from the heat generated by friction when using higher cutting speeds.

Machining cost distribution per workpiece is shown in Figure 4-18. As can be seen, the standard cutting tool is only 3% of the total cost of the workpiece, thus, an increase in tool life of about 50% decreases the cost for the component by only ~1,5 %. However, the increase in cutting speed used by the cutting tool also reduces labor costs and machine expenses per component. According to [49], very well adjusted cutting parameters, with an increased cutting speed of about 20%, can lead to a cost reduction of 15% per machined component.

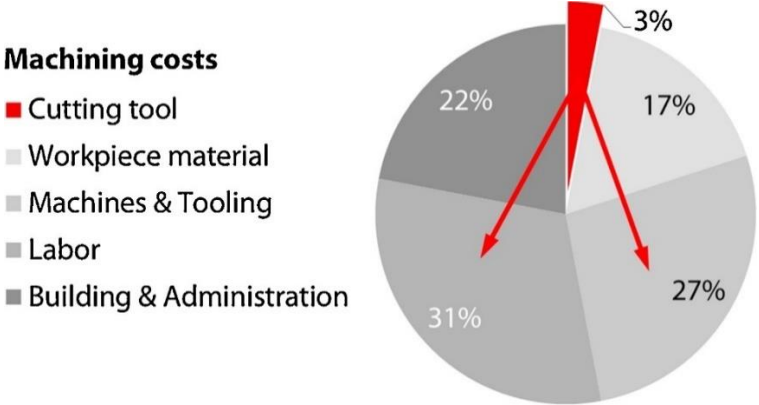


Figure 4-18 Distribution of machining cost per workpiece [49]

4.2.2 Types of cutting tools and processes

4.2.2.1 Turning

Turning is the simplest of all metal cutting processes, so it can easily demonstrate very basic principles. In turning, the main motion is performed by the workpiece. It is turning along its axis, and the cutting tool is moving parallel to this rotation axis. The cutting speeds of the basic tool against steel workpiece are around 200 m/min. Nowadays, the cutting tool is a cutting insert



Figure 4-19 Turning [86]

fixed in the tool holder. There are hundreds of geometries and sizes available for cutting inserts. During turning, the cooling liquid must have very good access to the tool so that it can dissipate the heat very effectively. advantage is that the tool is working at constant load, so here is no thermal cycling. However, this means that the tool does not have any time to cool down.

4.2.2.2 Drilling

Drilling is the fundamental operation for making holes. Contrary to turning, the rotation movement is performed by the tool, *i.e.*, the drill. Drilling either ‘through holes’ or ‘blind holes’ is possible, but different machining conditions have to be used, primarily due to the more problematic cooling of blind holes. Another important distinction is the length of the hole, which is usually defined as a multiplier of the drill diameter (3D, 5D, 15D, etc.). The longer the hole, the more problematic it is, because the drilling forces increase and breakage of the drill can occur. The biggest challenge when drilling is to cool down the drill, because all of the edges are under constant load and the cooling liquid has very poor access to the cut spot. Therefore, drills with inner canals are manufactured to help with cooling. The canals can be either straight or spiraled. Drilling operations have the most pronounced need for thermal stability of the coating because of the insufficient cooling. That said, the drilling operation is usually a shorter one when manufacturing a workpiece (in comparison to milling), so the need for speeding up the drilling process is not so important.



Figure 4-20 Tungsten carbide drill with complex cooling system [79]

4.2.2.3 Milling

Milling is performed with a multi-edged cutting tool. The main movement is rotary, and it is combined with sliding; this movement is performed by the tool. The feed movement is performed by the workpiece. Original setups had the movement occurring in 3 axes, but modern cutting centers offer up to 6-axis movement to complete very complicated tasks. The mills can be produced from a single monolith cylindrical substrate with 2 – 10 edges, usually tungsten carbide, and can consist of a holder with many cutting inserts, such as for the turning tools (Figure 4-22) or can be “hobs” consisting of tens to hundreds of single cutting edges (Figure 4-21). The hobs are preferably made from powder metallurgical steel to increase the toughness of the material rather than hardness. Hobs are used for gear cutting.

During the milling operation, only a fraction of the cutting edges is in use at any given moment, so the load is interrupted. During milling, there are peaks in thermal load as the edge heats up during cutting, and is then cooled down either by air or liquid cooling. Using a cooling liquid can lead to cracking of the tool edge for fragile materials. For example, when ceramic (Si₃N₄) cutting inserts are used, they are not coated to increase the hardness of surface, but rather to protect the fragile substrate before thermal spikes.



Figure 4-22 Mills with replaceable cutting inserts [80]



Figure 4-21 TiN coated hob used to produce gears

As machining centers are supplied with modern control units that allow for performing more operations with a single tool, more complex tools have to be designed to be fit for purpose. For example, Figure 4-23 shows typical multipurpose tools suitable for more operations such as drilling with milling, drilling with reaming, etc.



Figure 4-23 TiB₂ coated multipurpose machining tools for aluminum cutting

4.2.3 Failure mechanism of cutting tools

Figure 4-24 presents the main tool failure mechanism based on the cutting temperature. As is evident, adhesion is the main failure mechanism at low and medium temperatures. This effect was observed and discussed very well with our industrial partner, Hofmeister s.r.o., who specialize in producing cutting tools. According to their findings, adhesion is more important than mechanical properties after a certain level of hardness.

The effect of abrasion on the failure of the cutting tool is the same for all cutting speeds. At a temperature of around 500°C, oxidation and (to a greater extent) diffusion start to be the main failure mechanisms. The oxidation of the coating destroys the dense coating structure and tailored properties. The more porous the coating, the faster the oxidation propagates. Diffusion in the cutting process again changes the tailored morphology of the coating. Also, as most of the working coatings are nitrides and oxides, the oxygen and nitrogen atoms have greater movement in the bulk coating, and they diffuse out of the coating to the workpiece or elsewhere, leaving the bulk coating material oxygen- or nitrogen-poor. The lack of nitrogen in the solid solution coating causes degradation of the mechanical properties and makes the coating less dense, leading to the destruction of the coating. With an increase of temperature, the failure effect caused by diffusion is more and more pronounced, because of the quadratic increase of diffusion speed with the temperature (as shown in section 3.6.1), while the effect of oxidation on the failure mechanism remains almost constant after reaching a threshold temperature – as shown in the TGA results in section 5.1.4.1.

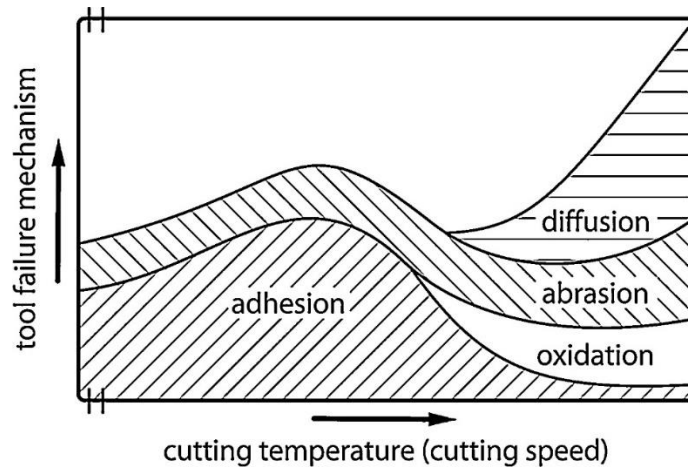


Figure 4-24 Main failure mechanism depending on cutting speed [41]

As can be seen from figures Figure 4-25 and Figure 4-, the high demand for thermal stability and high thermal hardness is rather logical. According to [50], 97-99% of work is transferred into heat by drilling and other machining techniques. High temperatures can start the recrystallization process in a material, leading to the loss of hardness and the whole integrity of the bulk coating. The loss of hardness is caused by grain growth and the loss of energy stored in the grain boundaries.

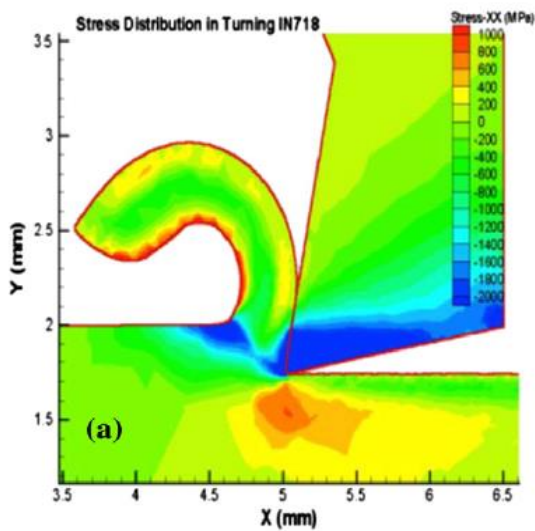


Figure 4-25 Finite element analysis simulation of stress distribution at the cutting edge [67]

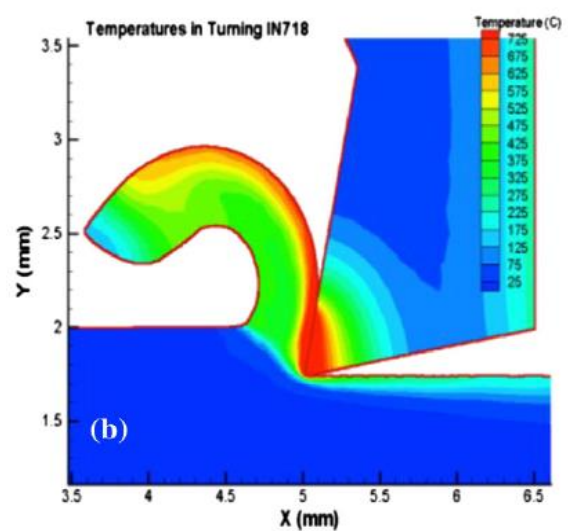


Figure 4-25 Finite element analysis simulation of temperature distribution at the cutting edge [67]

4.2.3.1 Failure types

Figure 4-26 shows images of the four most common failure types of cutting edges. The schematic shown is a cutting insert, but the type of wear corresponds very well with different types of cutting edges on any type of cutting tool:

Flank wear: Flank wear is the preferable type of wear. Usually, it develops steadily and offers a predictable and stable tool life. It is caused by too high a cutting speed, a tough workpiece material, insufficient wear resistance of the coating, or the lack of a coolant. It can be decreased by using a harder cutting tool material or coating, as abrasion is the main issue.

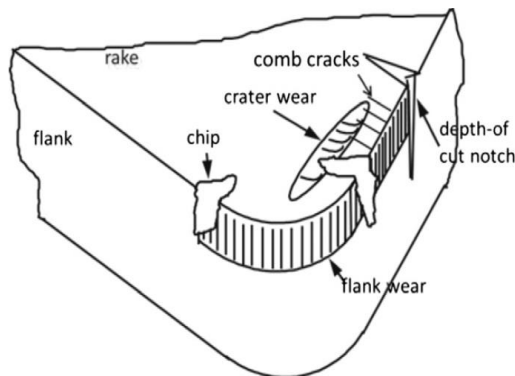


Figure 4-26 Schematic representation of main failure types on cutting edge [67]

Adhesion, Build-up edge: This type of wear is caused by adhesion of workpiece material on the tool. As the cutting process is continuous, the adhered material grows larger, increasing the cutting force until it detaches, sometimes taking part of the cutting tool with it. The causes are low cutting speed and an incorrectly selected coating. The adhesion failure can be decreased by optimizing the coating chemistry and lowering surface roughness. Adhesion failure is a major problem because of the possible rapid destruction of the cutting tool and decreased surface quality of the workpiece.

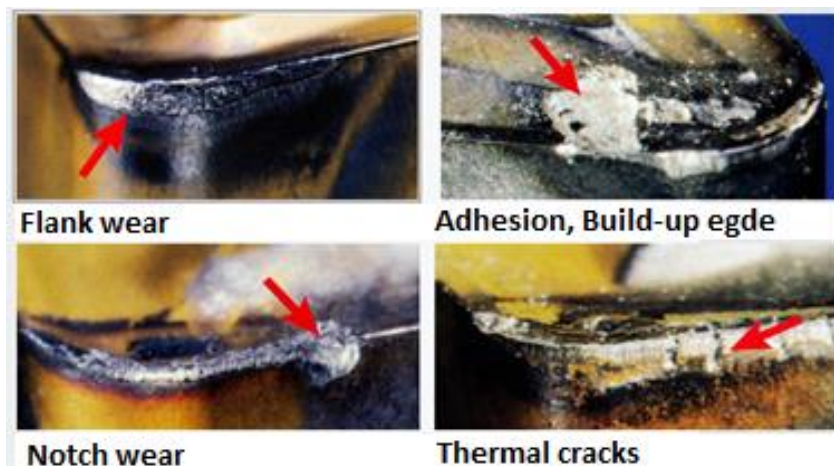


Figure 4-27 Images of four main failure types of cutting edge [77]

Notch wear: Notch wear occurs when using a very hard workpiece material or when the material has the ability of work-hardening. Also, it can appear when harsh cutting conditions are used, *i.e.*, high cut depth or when too negative a tool geometry is used. If the pressure of the workpiece material is too high, the brittle tool material can crack easily. It can be overcome by changing cutting conditions *e.g.* using a sharper cutting edge tool, decreasing the cut depth, or choosing an appropriate PVD coating with a lower coefficient of friction.

Thermal cracks, comb wear: Thermal cracks arise from a change in temperature during the cutting process. Usually, it happens when processing a material with low thermal conductivity (Inconel, titanium, stainless steel) at high cutting speed with a coolant. There is a high-temperature difference in the place of cut and outside of it, where the coolant is applied. Lowering cutting speed helps to overcome this type of wear. Another possibility is to apply a PVD coating, which serves as a temperature barrier. Usually, comb wear appears when a PVD coating delaminates from the cutting tool because the cutting conditions are too severe for the uncoated tool to survive.

4.2.4 Cutting tool materials

The materials used in cutting tools are exposed to large strains. That is because of the never-ending development of harder (and therefore more difficult to machine) materials such as hardened tool steels (H13) or high-temperature, strong aerospace materials such as Ni-based superalloys (Inconel) and Ti-based alloys. As there is strong competition between machining companies, machining speeds are pressed to their limits, which leads to higher temperatures and forces being applied to cutting tools.

The main degradation processes are mechanical (abrasion, spalling, adhesion, *etc.*), thermal (recrystallization, annealing) or chemical (oxidation) in nature, as shown above.

Cutting tools should have high hardness and at the same time high toughness, which is usually not possible. Figure 4-28 shows a selection of modern cutting materials.

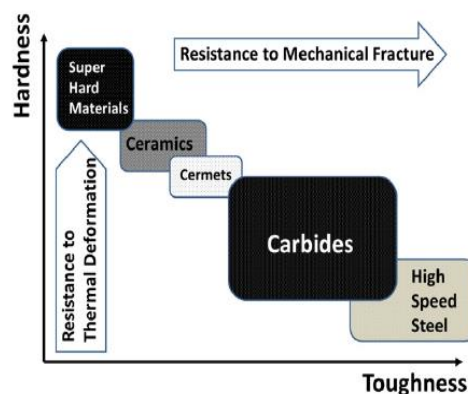


Figure 4-28 Cutting tool materials and the relevant hardness/toughness properties [67]

The most commonly coated materials are carbides for cutting tools, followed by high-speed steels. Other materials are also coated, but not as frequently as these. Also, there are different reasons and problems connected with particular materials. Tool steels have great ductility and are resistant against stress shocks, but they are not very hard and cannot withstand very high temperatures. Carbides are quite hard, but there is a composite material composed of tungsten carbide grains (of micron or submicron size) connected with the cobalt (or other) matrix. Exposure of the binding metal to high temperatures or corrosive environments leads to fast destruction of the tool. Ceramic materials (Si_3N_4 , Al_2O_3) are exceptionally hard (in fact, sometimes exceeding the hardness of the coating) but are fragile and sensitive to rapid temperature changes. Many of these problems are solved by using PVD coatings, but it is necessary to understand the cause of tool performance failure.

4.3 Coatings for forming tools

4.3.1 Types of forming processes

There are many types of forming processes, which can be divided into many categories. Although plastic forming is nowadays a significant customer base for PVD coatings, it is outside the scope of this work. Metal forming can be divided according to the forming temperatures:

Cold forming takes place at temperatures less than 30% of the melting temperature of the formed material. The material is hardened; the grains are deformed in the direction of forming. The properties of the workpiece exhibit anisotropic behavior.

Hot forming processes are performed at a temperature that is more than 70% of the melting temperature of the formed material. The forming speed is so fast that the hardening of the workpiece by the forming process disappears. There is no anisotropic behavior, but hot forming is usually accompanied by grain coarsening, which changes the mechanical properties. Another division is according to the pressure applied. The forming processes are the following: die casting, forging, rolling, drawing, shearing, bending, *etc.*

Coating the forming tools has a huge impact on performance of these processes. Usually, it protects before abrasion by cold forming processes, diffusion of workpiece material in the hot forming processes, adhesion of the material to the tool and heat checking damage by forging, and high pressure die casting, as shown later in section 5.3.

4.3.1.1 Forging

The main issue in forging is the tool life. Tools have complex shapes and are subjected to temperatures around 1000°C (for steels) and high pressures repeatedly. The low cycling

fatigue is accelerated with high temperature, and temperature cycling takes place. Additionally, the tool is made from fairly expensive tool steel (H11, H12, H13, etc.).

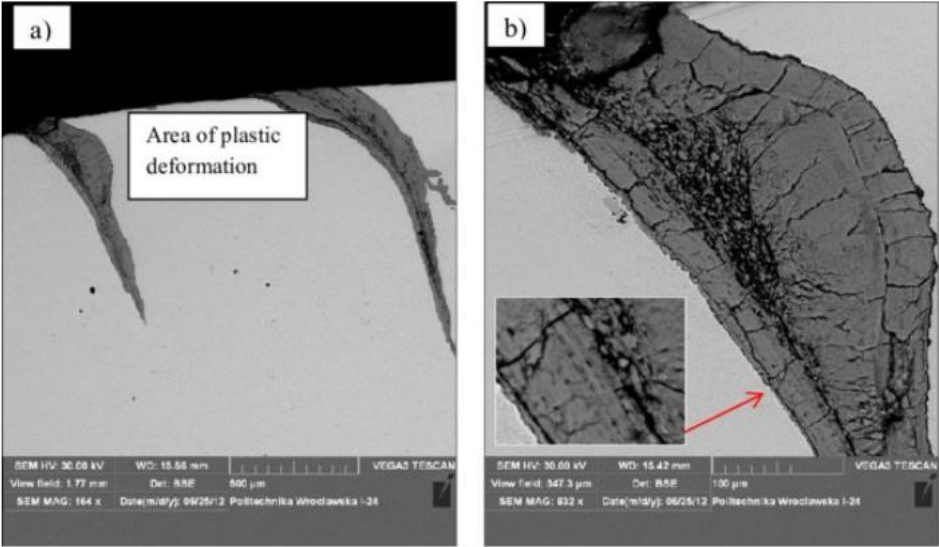


Figure 4-29 Cracks in steel tool in forging [51]

The cracking of the steel surface appears when the tool is damaged, as shown in Figure 4-29. In industry, the replacement of tools is not easy, because the forging takes place in complicated manufacturing lines. The heating of these lines takes a couple of hours, as does the cooling. The lines work in cycles, and breakage of the tool before the cycle is finished leads to the loss of tens of production hours.

4.3.1.2 Rolling, shearing, drawing bending

These processes can be performed in both hot and cold environments. The main issues are usually adhesion and sticking of the material on the tools, mainly because of the high pressures used to form the material. Also, abrasion resistance is a critical property of the coating. The general hardness of the steel, or any other material, is relatively low in comparison to the tool hardness, because steel contains grains of carbides, aluminum grains of alumina, etc. These hard contaminants are abrasive and so damage the tool. A low coefficient of friction also



Figure 4-30 Wire forming dies

increases tool productivity, as the forming forces are decreased. In almost all cases, a lubricant is applied to help lower the coefficient of friction. As environmental regulations force manufacturers to lower the number of lubricants used, many operations are forced to be water-lubricated. To help this, hard DLC coatings are used.

4.3.2 Coating of aluminum high-pressure die casting (HPDC) tools

4.3.2.1 Motivation

The continuous growth in mobility has placed an increasing demand on the transport industry to manufacture vehicles at reduced cost, while ensuring that they operate efficiently, are friendly to the environment, and meet the safety requirements. This is particularly important in the aerospace and automotive industries, where the use of lightweight airframes, as well as the global improvement of the materials' mechanical properties, encourage the integration of composite materials in a large number of structural components [52]. The rapid boom of electric cars, where the main limitation is still the effective range, presses the industry to produce car components in aluminum alloys due to their very high weight-to-strength ratio. Aluminum components (e.g., engine blocks, carburetor bodies, transmission cases, and valve bodies, etc.) are being produced mainly by high pressure die casting (HPDC).

4.3.2.2 HPDC process

The process of HPDC consists of a big forming die, which is filled by molten aluminum under high pressure, then cooled, and used for many cycles. In fact, the process is usually continuous, and each mold allows for the production of tens or hundreds of thousands of components. Nevertheless, the solidification conditions led to the premature failure of the molds due to washout problems (i.e., corrosion, erosion, and soldering) and thermal fatigue (heat checking), therefore, industry is pressing for an improvement in their performance and

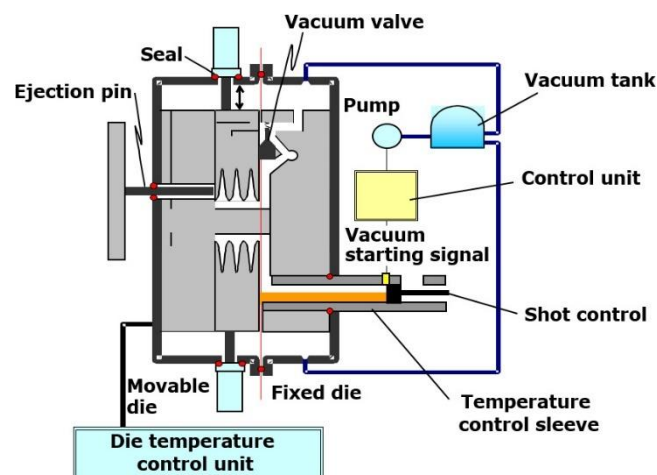


Figure 4-31 The high pressure die casting proces [78]

lifetime. The aluminum is injected under pressure of hundreds of tons with an inlet speed of 50-70 m/s.

The whole die is filled with Al for 3 seconds, and then it is cooled down for 30s. So, the tool is subjected to heat checking and must withstand some elastic deformations. The molten Al injected in the die contains a small amount of alumina crystals, which causes abrasion of the die cavities. Melted Al causes mold corrosion, erosion, soldering damaging to the die, and finally difficulty with injecting the piece. Often, the material used for HPDC die production is H13 tool steel in Europe, and cheaper H11 tool steel in the US. The main problem for die casting is the development of cracks in the die surface. With every new injection, the cracks are filled with molten Al, which sticks, increasing the difficulty of the removal of the part and often leads to surface aspect failures, removal of material from the injecting part, the appearance of sheaths, and roughness problems, which can lead to rejection of the Al product. A typical core pin (Dievar steel, D10mm, working length 50 mm) lasts 1000 cycles without any coating before needing to be replaced or cleaned, whereas when it is coated it can work for more than 10 000 cycles, while the desired lifetime is 50 000 cycles. To further increase the service life of the components, new coatings solutions should be applied and developed.

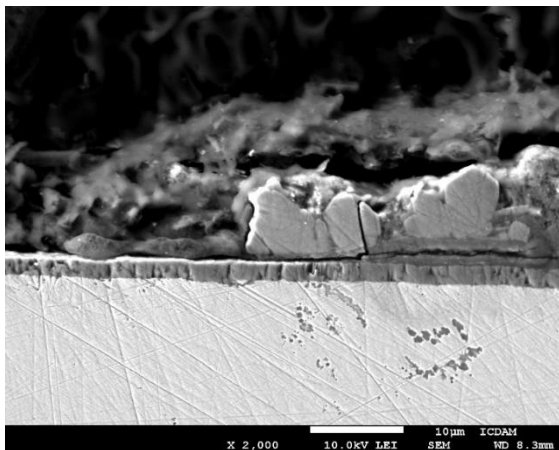


Figure 4-33 Damaged coating on core pin

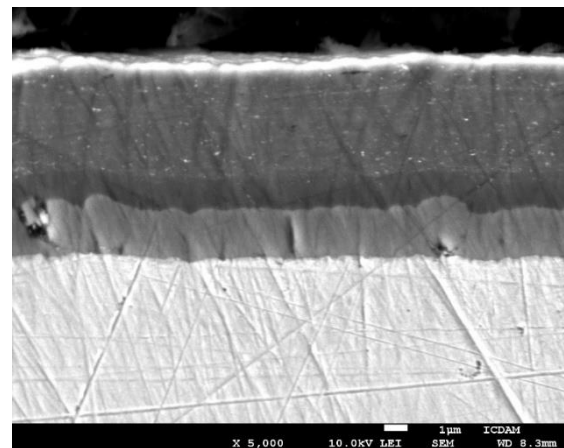


Figure 4-32 Undamaged coating on core pin

Such coatings should be: wear resistant to protect the die surface against hard alumina particles, oxidation resistant up to 750°C to avoid oxidation, soldering, erosion, corrosion, thermal (fatigue) and adhesion (anti-stick) problems.

4.3.2.3 State of the art

Coatings currently used throughout industry to protect the die surfaces are TiAlN and AlCrN. These coatings have successfully improve the life cycles of the tools, however, there is plenty of room for improvement by testing/developing new coating systems and designing new

coating architectures such as multilayer coatings, which, in one way increase the coatings' mechanical properties (due to the well-known super lattice effect) [33] and, on the other, allows for cracking deflection [47]. Researchers and companies have extensively studied and applied new coating systems to improve the lifetime and performance of these tools. For example, S. C. Chu [52] tested and compared different coating systems supplied by different industrial producers (i.e., TiAlCrSiCN, CrTiAlN-CrON, and TiAlCrN-CrON) and observed that the TiAlCrSiCN coating performed the best because of its stable hardness at high temperature, anti-adhesion properties, and low coefficient of friction at high temperature.

Salas et al. [53] compared the mechanical and tribological behavior of 15 coatings with the standardized condition to find the best coatings with adhesion and wear resistance. Among the tested coatings, TiAlN, TiN/TiCN, and two CrN coatings showed the best performance. Cooke et al. [54], who applied CrTiAlN and CrTiAlON coatings on the surface of extrusion aluminum dies, observed the excellent behavior of these coatings during service. Srivastava et al. [55] explored the application of coatings and surface treatments to prevent crack initiation during the thermal cycling of die casting operations. They investigated the behavior of an uncoated H13 steel and compared the same material coated with an oxide coating (Titan coat™) with thick TiAlN supporting layer, applied on H13 steel. They observed that a thin oxide layer provides adequate thermal protection barrier, and it is advantageous to use a thick TiAlN coating as a support layer to act as diffusion barrier, leading to a reduction of average crack depth and density.

Lin, San Diego [56] suggested a multilayered structure as an optimum solution for HPDC tools. In their work they designed a coating architecture composed of i) modified substrate (nitriding, carbonitriding), ii) adhesion layer, either Cr or Ti, iii) intermediate layer of TiAlN or AlCrN, and iv) a working layer of CrN, TiAlN, TiBC, TiBCN and (Al, Cr)₂O₃. They tested the previously mentioned working layers and concluded that the better performing were those that displayed the best non-wetting ability.

5. Experimental approach

As described earlier, all possible applications and motivation of our research are focused on increasing the thermal stability of hard coatings and, especially for high pressure die casting, to increase resistance to heat checking behavior of coatings, and the coatings ability to withstand a severe load under high temperatures in harsh environments..

To increase the lifetime of high-performance cutting tools, alloying TiAlN with chromium was chosen as the best approach because of promising results summarized earlier in section 4.1.3.1. The coatings were tested and characterized under laboratory conditions, and later tested on real applications: they were applied on tungsten carbide drills under standard industrial conditions. For coatings intended for high pressure die casting, a matrix of commonly used coatings with different material properties was chosen to perform the analysis and to extract key features. As shown in section 4.3.2.3, previous studies compare coatings produced by different PVD techniques. In this work, I compare the tribological performance of five commercial, highly oxidation-resistant coatings AlTiN, CrAlTiN, AlTiSiN, AlCrTiSiCN and $(\text{CrAl})_2\text{O}_3$ deposited by magnetron sputtering in similar sputtering conditions. These coatings have the potential to be used for the protection of the surface of HPDC molds against aluminum at room, and more importantly at high temperature (650°C), aiming to reproduce as closely as possible the interaction between aluminum to the HPDC die surface and in order to rank their applicability as a coating material.

5.1 Evaluating techniques

To ensure precise comprehension of measuring techniques, procedures and from them the outgoing results, the following summary of techniques is presented.

5.1.1 Mechanical properties

5.1.1.1 Rockwell C indentation test

The Rockwell C indentation test is a technique used to evaluate the adhesion of a coating to a substrate. The coated test sample is put under the tip of a standard cone Rockwell diamond tip, as used for measuring the hardness of bulk material. The applied load is 150 N. The applied load causes plastic deformation of the coating substrate. The test proves the coating's ability to endure stresses trying to rip the coating from the substrate. After performing the indentation,

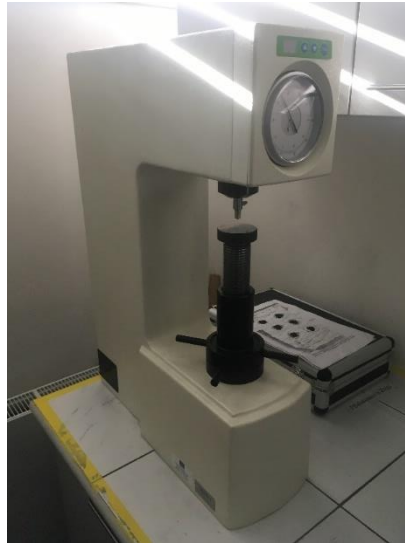


Figure 5-1 Rockwell hardness tester

the indent is examined under light microscopy to distinguish between 6 standardized failures (HF1 - 6) as shown on Figure 5-2. This test is a fast and (partially) reliable method for testing adhesion of the coating to substrates commonly used in industrial quality control.

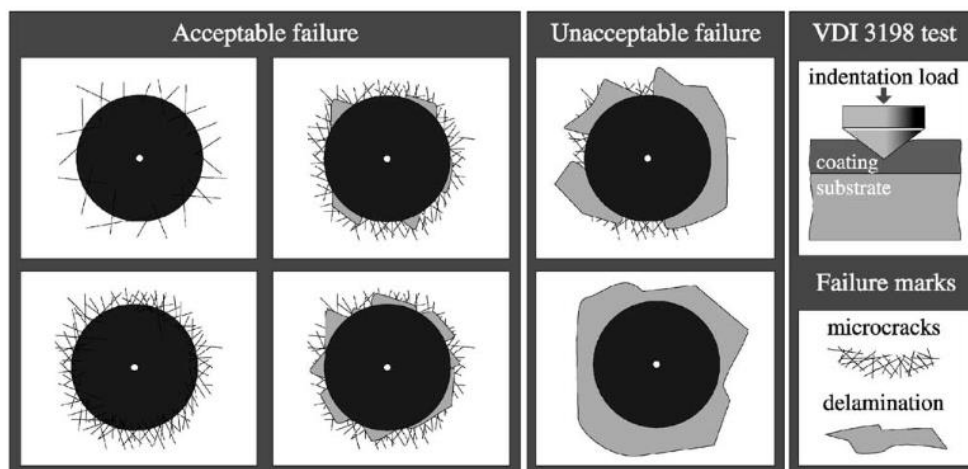


Figure 5-2 Standardized table for the Rockwell adhesion test

5.1.1.2 Scratch test

Scratch testing is another technique used to evaluate the adhesion of the coating to the substrate. The sample must be flat and ideally polished. The sample is put under a diamond cone indenter. The cone has the same dimension as the Rockwell C tip. A defined loading force is applied for a defined scratch length. The scratch tester has different modes, but in this work, linear loading starting at 1 N and finishing at 100 N was applied. The loading rate was 1 mm/s and the scratch length 10 mm. After the scratch is performed, different failure mechanisms give the origin of different failures. The loading force under which a failure occurs

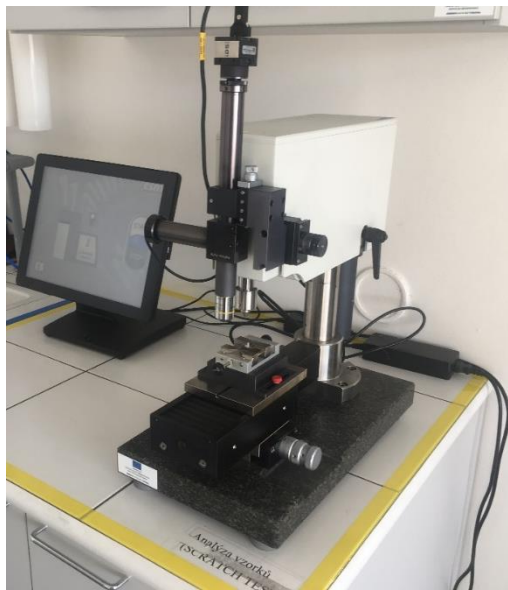
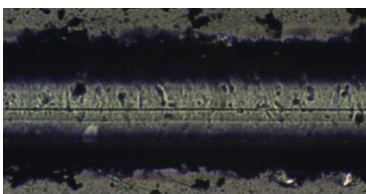


Figure 5-3 CSM Revetest scratchtester

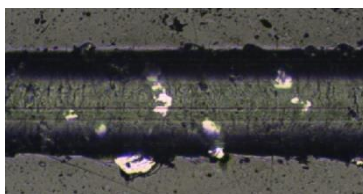
is called the critical load (LC). LC1 is usually assigned to cohesion failure due to plastic deformation, LC2 is first adhesion failure, and LC3 is critical adhesion failure where the coating is continually stripped from the substrate.

LC1



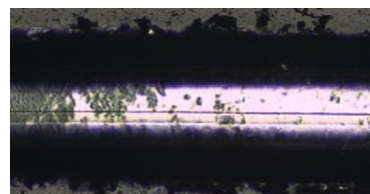
Cohesion failure

LC2



Adhesion failure

LC3



Critical adhesion failure

Figure 5-4 Critical failures Lc1, Lc2 and Lc3

5.1.1.3 Nanoindentation

Nanoindentation is a standardized technique to evaluate the mechanical properties of the coating. During this research, a nanoindenter from Nano-Test Platform 4, Micro-Materials Ltd. and a CSM nanoindenter were used to evaluate coating nano-hardness and young elastic modulus. The coating hardness and elastic modulus are evaluated based on the shape of the loading curve applied by a Berkovich pyramidal diamond tip. Because the forces applied are very small (few mN), the measurement is very sensitive to the environment (vibrations, temperature changes) and the roughness (smoothness) of the test sample.



Figure 5-5 CSM nanoindenter

The nanoindentation was performed in fixed depth mode for coatings used in section 5.3, and in maximum force mode for coatings in section 5.2. The depth was set to 200 nm, thereby not exceeding 10% of the coating thickness in any case. The experiments were carried out using a loading/unloading rate of 0.1 mN/s and a holding time at maximum load of 20 s in order to saturate creep effects before unloading. Mechanical properties were evaluated, based on the average of more than ten measurements obtained from selected and corrected load-displacement curves.

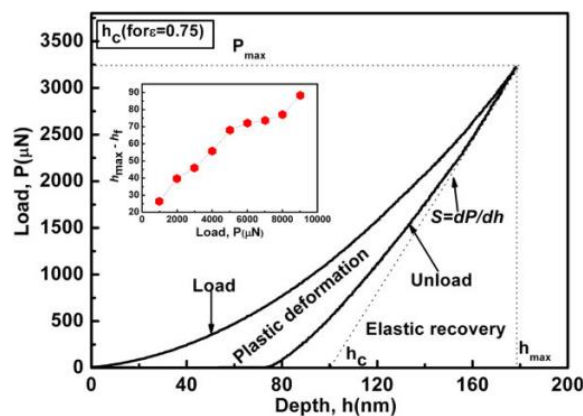


Figure 5-6 Theoretical loading displacement curve

5.1.2 Tribological testing

5.1.2.1 CSM Tribometer – pin on disc

A high-temperature pin-on-disc CSM tribometer was used to examine the wear rate and friction of sputtered coatings. As a counterpart, a 6 mm Al_2O_3 ball was used to test resistance against abrasion, and aluminum balls to test the adhesion of aluminum to the coatings. The measurements can be performed in the temperature range from RT to 700°C. The applied load was in general 5N, sliding speed 10 $\text{cm}\cdot\text{s}^{-1}$, and the number of laps was set to 5000. The wear rate was computed as a volume of material worn out per applied normal load per sliding distance.

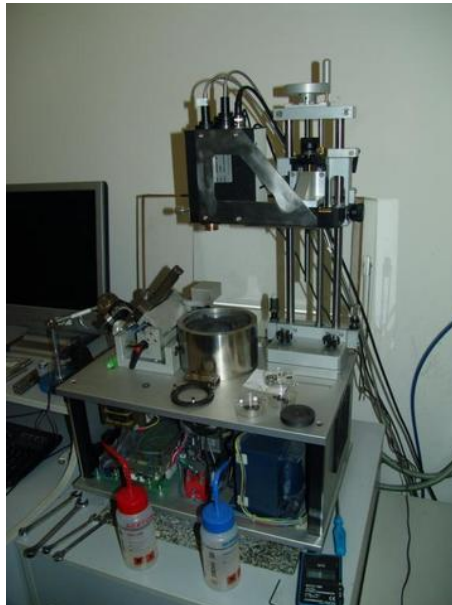


Figure 5-7 CSM high temperature tribometer

5.1.2.2 Zygo NewView

To examine the surface of the coatings, surface roughness, and the wear tracks after tribometer tests, the 3D white light profilometer Zygo NewView 7200 was used. It allows for noncontact three-dimensional scanning of the surface with white light interferometry. The vertical resolution is better than 0.01 nm, and the lateral resolution is up to 0.36 μm , depending on the optical lens.



Figure 5-8 Optical 3D profilometer Zygo NewView

5.1.3 Structural and chemical composition

5.1.3.1 *Calo test*

Calo test, or ball cratering test, is the simplest destructive technique to determine the thickness of a coating. A rotating ball with a defined diameter (usually 30 mm) is pressed by gravitational force into the specimen. A polishing diamond solution is added to the contact, and the ball is ground into the specimen. Afterwards, the substrate is inspected by optical microscopy. There are circles visible, as shown in Figure 5-10, and from the diameter of the circle and the ball, one can simply calculate the thickness of the coating. This technique also works very well for multilayered coatings.



Figure 5-9 CSM calo tester

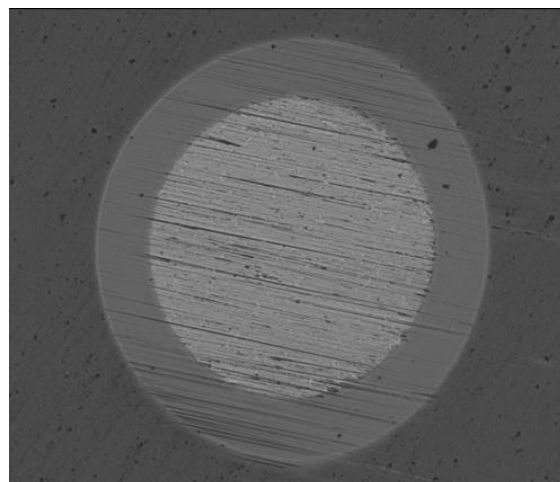


Figure 5-10 Calo test optical image of a single-layered TiAlN coating

5.1.3.2 SEM/EDS

Scanning electron microscopes (SEM) from different manufacturers were used during this study. The SEMs were used in different regimes to show cross-section morphology of the coatings, to analyze the chemical composition and the nature of the compounds formed on the wear tracks after tribological testing. Special emphasis was placed on energy dispersive spectroscopy (EDS) as the chemical composition of the coatings after oxidation was performed.

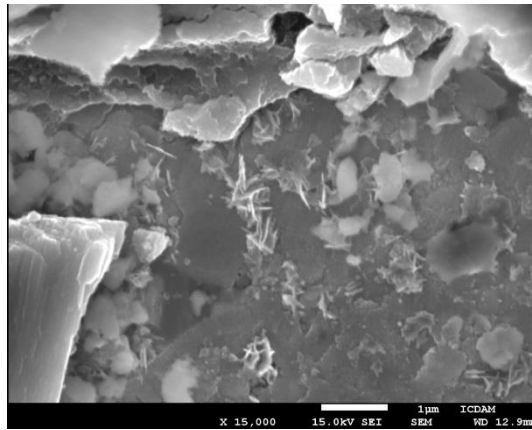


Figure 5-11 SEM image of oxidized wear track

The SEM was also used for determination of the multilayered nature of the coatings. On the SEM images, lighter atoms are displayed in brighter colors while heavier ones with darker colors. Though EDS can measure chemical composition, the values for lighter atoms (C, N, O) can be taken more as approximate values, as the measurement is not very precise and more powerful techniques are necessary. Electron microprobe analysis was used to calibrate the nitrogen content in the TiAlCrN coatings presented later.

5.1.3.3 XRD

X-ray diffraction is a technique used for the determination of crystallographic structure and stresses in materials. It uses incident X-rays with a wavelength similar to the interatomic

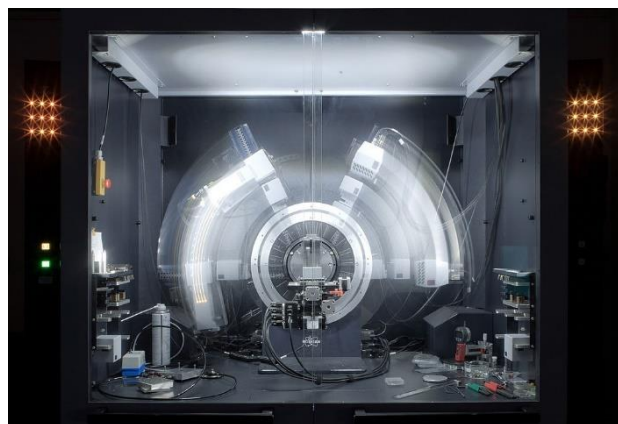


Figure 5-12 XRD spectroscopy [88]

distance in the substances examined. The instrument used to measure XRD diffraction was the X' Pert Pro MPD diffractometer, with a Cu irradiating source. The X-ray is diffracted at specific angles. These angles correspond to the atom-atom distance, crystal lattice, and the type of compound. XRD was used to get the pattern of different compositions of the TiAlCrN and AlTiN coatings. For the TiAlCrN coatings in section 5.2, the partial representation of (111) and (200) as well as qualitative identification of grain size is performed. The XRD was used in standard mode.

For the AlTiN coatings in section 5.3, the change of internal stresses was determined by the shift of specific peaks. The XRD was working in grazing incidence mode, to exclude the influence of deeper layers.

From XRD peak position, the lattice constant can be computed using Bragg's law, combined with equation for cubic lattice spacing. The resulting equation is:

$$\left(\frac{\lambda}{2a}\right)^2 = \left(\frac{\lambda}{2d}\right)^2 \frac{1}{h^2 + k^2 + l^2}$$

Equation 5-1

where λ is the X-ray wavelength, a is the lattice spacing of cubic crystal, and h,k,l are the Miller indices.

5.1.3.4 Mechanical cyclers - MTS 880

An MTS 880 servo-hydraulic testing machine was used for thermal cycling, for the determination of thermo-mechanical fatigue. The thermal cycling conditions were chosen to copy the thermal conditions used in the aluminum die casting process. The temperatures ranged from 45 to 650°C. The increase of temperature was 5°C/s, and cooling 3°C/s. The cycling was performed 100 times



Figure 5-13 Thermo mechanical cycling machine MTS 880

5.1.4 Thermal properties

5.1.4.1 TGA

Thermogravimetric analysis was used for testing oxidation resistance of the TiAlCrN coatings. The onset point of oxidation was evaluated by thermogravimetric analysis (TGA) using industrial air (99.99% purity). The coatings were heated up to 1200 °C at a rate of 20 °C/min, and the mass gain was acquired at regular 2 s intervals using a microbalance with an accuracy of 0.01 mg. Another set of specimens was then isothermally exposed at different temperatures (800 and 900 °C for TiAlN film, and 900 and 1000 °C for Cr-rich coatings) for 2 hours.



Figure 5-14 TGA analyzer

5.1.5 Cutting properties

5.1.5.1 CNC Mill - FV 25 CNC

A small industrial CNC machining center FV 25 CNC was used to test the performance of cutting tools coated with TiAlCrN coatings. The cutting speeds were 50, 100 and 200 m/min. The tools were drilling blind holes. After five holes, the measurement of drill wear was stopped



Figure 5-15 CNC machining center FV 25 CNC

to evaluate the performance of the drill and its wear. No cooling was used to evaluate the performance in harsh conditions.

5.1.6 Sputtering chamber

A CemeCon 880/9 MLT coating chamber was used to deposit all further mentioned coatings. The geometry of the chamber is shown in Figure 2-18 Geometry of 2D cut of CemeCon 880/9 MLT sputtering machine. It consists of a rotary table with three-axis rotation. The chamber is equipped with four cathodes working using an unbalanced close field configuration. The cathodes are cooled with a water cooling system, which is separated from the targets by a copper plate. The dimensions of the targets are 88x500 mm, with a thickness of 10 mm.

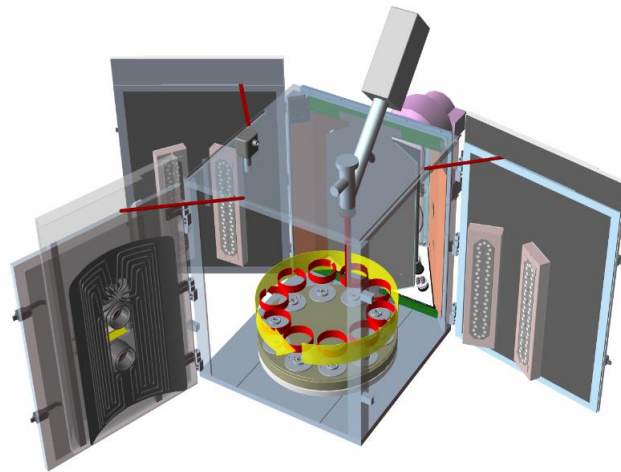


Figure 5-16 CemeCon sputtering chamber [12]

There are two sputtering sources (source: Pinnacle+ and Advance Energy – Astral waveform generator) connected to the cathodes, generating MF pulsed DC plasma. Each of the sources is connected to two cathodes on one side of the chamber (1+3 and 2+4). Running 1 to 4 cathodes at a time is possible. Moreover, power source 1 may be connected to a “booster”. The booster is a hollow cathode in the front door; it is used during the etching process to generate a plasma jet to facilitate etching. The rotation table is connected to MF pulsed bias supplied by the Pinnacle+ source. It usually works at 250 kHz with a 1600 ns duty cycle.

There are six gas inlets to the chamber. Argon and krypton are used as the working gas; nitrogen, acetylene and oxygen are used as the reactive gasses. Helium is used for cooling after the process. The gas inlet is around the chamber walls, but can be reconnected to the booster. The chamber is controlled by the “Dataview” system, itself programmed by the

chamber manufacturer. In comparison to other manufacturers, this system is very open, with the possibility of controlling almost every element of the program both offline and online. The control system includes a closed-loop control mechanism, allowing the user to automatically vary the gas inlet depending on the total pressure *etc.* Figure 5-17 presents the Dataview control screen. The yellow variables are adjustable during running process.



Figure 5-17 Dataview control screen

5.2 Development of temperature-resistive coatings for cutting tools

The purpose of this part of the work was to evaluate the effect of chromium content of the TiAlCrN coating on thermal stability, oxidation resistance, tribological properties, and cutting properties, with the main aim of improving the cutting properties of the TiAlN coating.

As described in 4.1.4, the multilayered coating system shows some significant advantages over single layered coatings. From all of the different multilayer transitions achievable in industrial applications, the blurred transition was chosen. The main advantage is that it can be tailored by careful distribution of targets in the chamber during three axis rotation, which takes place in almost every industrial-size machine. In order to control the thickness of individual bilayers, a rotation model simulating the growth of the coating had to be created.

5.2.1 Rotation model

The coating stage and the growth of the coating is well described in Section 2.7 of this work. The difference between theoretical laboratory conditions and industrial processes is the commonplace three-fold rotation in industrial chambers. The growth of the coating is not continuous, but is interrupted as the surface is rotated in the chamber (see Figure 2-18) and

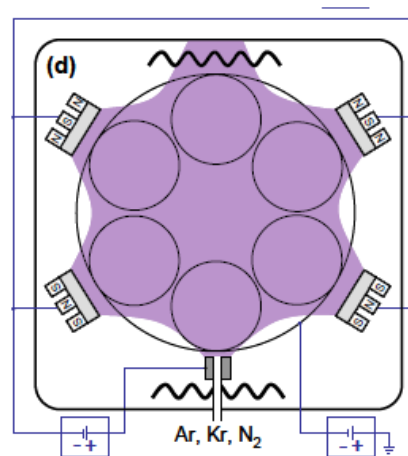


Figure 5-18 Coating process schematics [12]

the surface is exposed to different cathodes, different incident angles of impacting atoms, and shadowed by other substrates coated in the same batch. Each of the cathodes may or may not have the same elemental composition; moreover, they may or may not be turned on during the process. This leads to the formation of complex, multilayered coating morphologies, which are usually unwanted, as it is not easy to understand their effect on the performance of the final coating. The multilayered growth is more pronounced when using targets at high sputtering yield, such chromium or aluminum, at the same time as targets with a lower sputtering rate, *i.e.* titanium, or when changing the power applied to the targets. The formation of multilayers can be suppressed with a higher rotation speed of the table.

For a better understanding of multilayer formation, a numerical model for the chamber was programmed. This model follows a universal reference spot on the chamber table and summarizes contributions of all targets during the deposition.

5.2.1.1 The sputtering angle of a single target

5.2.1.1.1 The sputtering angle from a single point

As was explained in section 2.2.1, the atoms are emitted from the target with the impact kinetic energy of working gas ions. The emitted atoms are not ionized in the magnetron sputtered technique. Therefore, their flight direction is driven by the impact mechanics. The direction is dependent on the incident angle of working gas ions and the strength of bonds in the target

material. Martynenko et al. [57] studied the radiation of atoms from the target for different materials, and created two formulae for two different behaviors of the sputtered material. The angle-dependent intensity of sputtering follows Equation 5-2 for materials with weaker bonds (Al, Cu, ...):

$$I = (A \cdot \cos \varphi)^n$$

Equation 5-2

And the angle-dependent intensity of sputtering follows the Equation 5-3 for materials with stronger bonds (Ti, Cr, ...):

$$I = (A \cdot \cos \varphi)^n - (B \cdot \cos \varphi)^m$$

Equation 5-3

Where A, B, n, and m are material dependent constants and φ is the angle of the sputtered atoms. Results for both equations for constants A= 1 and n = 0,62 for aluminum, and A=1,77, B=0,9, n = 0,95 and m=3,28 [57] for chromium, are plotted in a polar plot in Figure 5-19.

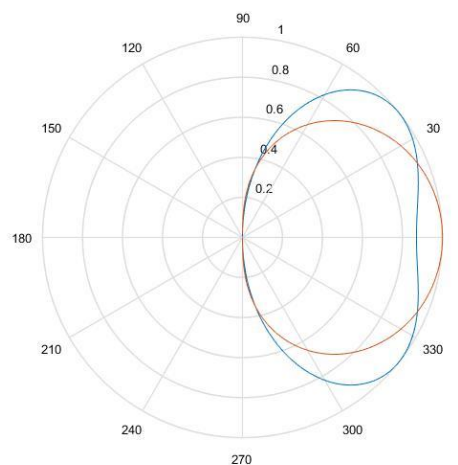


Figure 5-19 Polar distribution of sputtering intensity for aluminum (red) and chromium (blue) single point of sputtering target

From the plot, it is clear that weaker materials have their maximum intensity of sputtering perpendicular to the spot of an impacting ion, while materials with stronger bonds have their maximum approximately 40° to the direction of the impacting ion; even at an angle of 60°, their sputtering intensity is 80% of the maximum.

5.2.1.1.2 Sputtering angle and intensity from a real target

Later in the work, three different targets (Cr, Al, TiAl) were used. Thus, the real atom radiation from these targets is taken into account in this paragraph. The magnetic field of the cathode is driving the incident ions of working gas into a specific region of the target called a 'race track'. The exact mechanism is described earlier in section 2.1.2.2. So, the point emitting target atoms is, in reality, some area (represented as a 2D horizontal cut for simplification of the model) between the two spots in the center of the racetrack, positioned 47 mm from each other are the atoms emitters. The intensity of each of these spots (yellow and orange line) and their summation (blue line) is plotted in Figure 5-20. The final sputtering intensity of the planar target

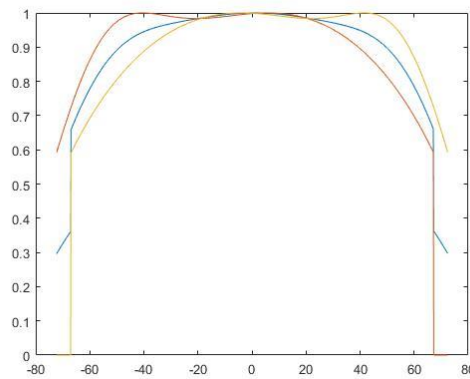


Figure 5-20 Distribution of angular sputtering intensity of planar target

is almost the same as for the angles between -40° to 40° , and reaches 70% at an angle of 60° from the vertical axis of the target.

Because different target materials have different abilities to be sputtered, laboratory tests were performed in order to determine the sputtering rate of TiAl, Al, and Cr, with respect to each other. Deposition from TiAl, Al and Cr targets, at an applied power of 5000 W, showed the



Figure 5-21 Titanium target with aluminum plugs (left) and aluminum target (right) with visible racetracks

following intensity ratios: Al:Cr:TiAl = 1,12: 1,68: 0,40, where the values correspond to the sputtering speed $\frac{m}{s.W} \cdot 10^{-12}$.

5.2.1.1.3 Rotating position and shadowing

For the sputtering model, it is necessary to determine when the testing reference spot will be positioned within range of the target. To determine this, two- and three-axis rotation was simulated. First two axis, table, and towers are rotating smoothly and dependently. They are connected with a planetary gear. The tower makes 3.083 turns per 1 rotation of the table. However, the third rotation (cylindrical holder) is driven by a plane spring, and the rotation happens once per turn in negligible time, and the holder rotates 195°.

After the angle of reference spot, P, in respect to the vertical axis of the chamber is determined, it is possible to adjust conditions for the individual target, in order to add a contribution of the specific target material to the final coating matrix.

The exact form of the conditions is exhibited in the program code in the appendix. The logic of the conditions is that the table, tower, and angular holder position, must face the sputtering angle of the target in some angular interval. For every rotation, there are three possibilities:

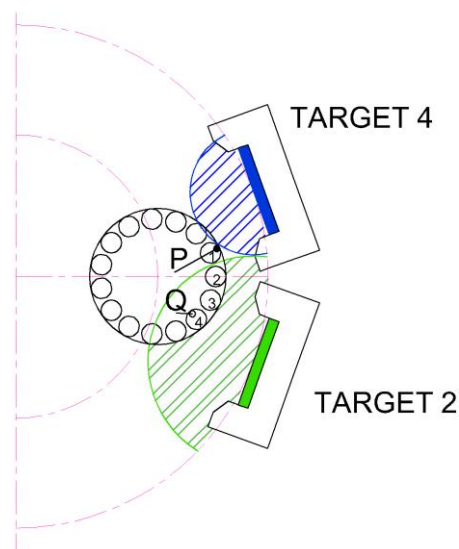


Figure 5-22 Radiating of the targets in the sputtering chamber

1. The reference spot is near the heater, so the contribution of target 1 is lower,
2. or the reference spot faces target 1 and, thanks to mutual target geometries, also gets a smaller contribution from target 2,
3. or the reference spot is in the middle of targets 1 and 2, getting equal contributions from both targets

5.2.1.1.4 Evaluation of the model and comparison to the real process

Figure 5-23 shows the resulting figure from the model for the TiAlCrN coating with two TiAl targets, with an applied power of 7000 W, at positions 2 and 4 (right side in figure Figure 2-18), one Al target, with an applied power of 4000 W, and one Cr target, with an applied power of 3700 W, at positions 1 and 3 (left side in Figure 2-18). The SEM cross-section from the same coating is presented in Figure 5-24.

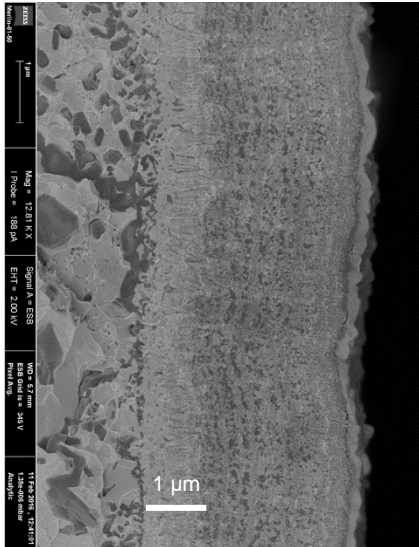


Figure 5-24 Real morphology of TiAlCrN coating observed by SEM

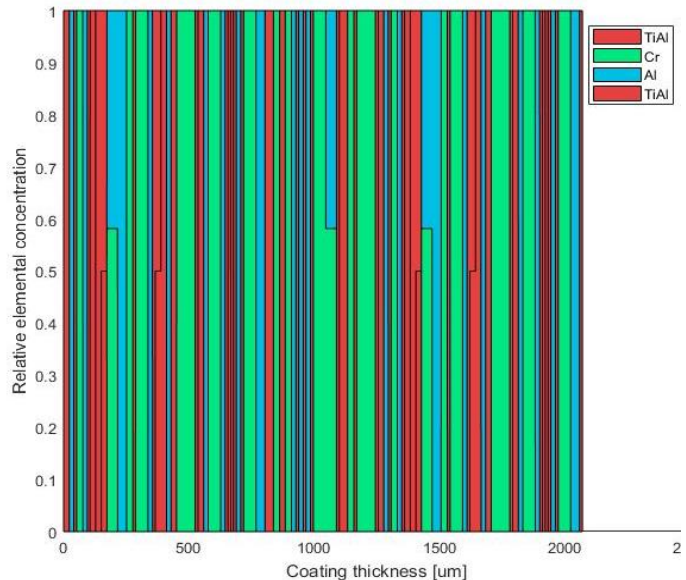


Figure 5-23 Simulated morphology of TiAlCrN coating

The simulated coating cross-section shows a strong multilayered structure of TiAlN layers (red), CrAlN layers (blue and green) and CrN (green) layers. As the sputtering rate for chromium is significantly higher than for TiAl and Al, clear, thick layers consisting of pure chromium are formed. These layers are also visible on the cross-section of the real coating. To determine the chemical composition of the layers, the EDS measurement was used. The lighter layers correspond to the Cr-rich coating, and darker layers correspond to the TiAl-rich coating. By comparing these two figures, one can see that the number of Cr-rich layers corresponds very well to the real coating. So, the rotation effect can predict very well the multilayer formation in industrial coatings originating from rotation of the substrate table.

Figure 5-25 and Figure 5-26 show the same sputtering system (same targets with the same power) but with only 2-axis rotation applied. The rotation speed was 2 rpm and 1 rpm, respectively. One can see that there is some frequency visible in the coatings, especially for the lower rotation speed. There are regions in the coatings when almost no TiAlN coating is present. The three-axis rotation model (Figure 5-23) was computed with a rotation speed of 2

rpm. Compared to Figure 5-25, the three-axis model has a more regular distribution of the elements, thus improving the isotropy of material properties through the coating.

According to the results presented herein, one can also see the effect of rotation speed on the morphology of the sputtered coating. It is not possible to obtain an anisotropic coating by only varying rotation speed. The rotation of the towers is fixed on the table, thus, there will always be TiAlN-rich and CrAlN-rich sections in the coating. The rotation speed can, however, change the thickness of these layers, and it is possible to use it to vary the multilayer thickness. For an even distribution of elements in the coating, another configuration of the target in combination with the use of three axes of rotation is necessary.

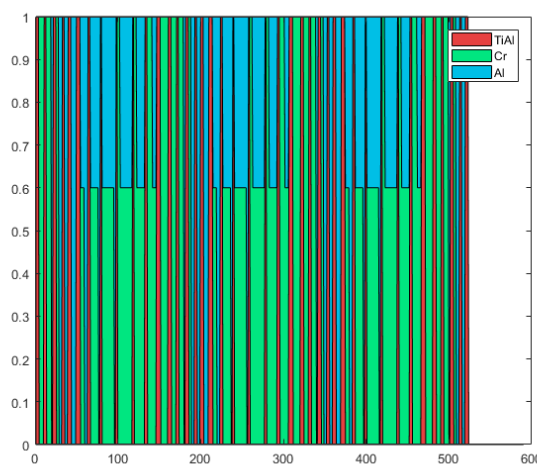


Figure 5-25 Simulated morphology of TiAlCrN with two axes of rotation with rotation speed two rotation per minute

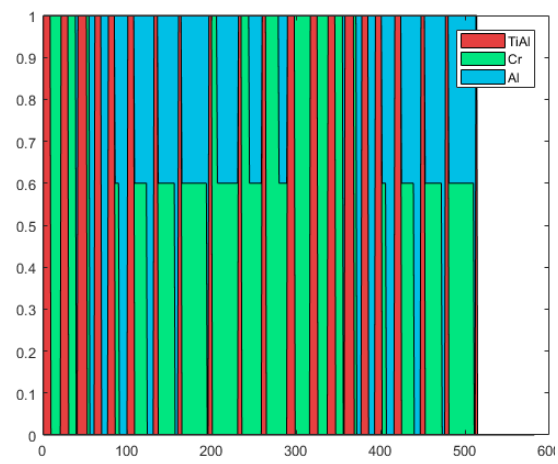


Figure 5-26 Simulated morphology of TiAlCrN with two axes of rotation with a rotation speed of one rotation per minute

5.2.2 Testing samples for tool coating

To test the coating properties, different testing samples were used. For cross-section morphology analysis, thickness measurements, hardness measurements, and chemical composition evaluation, polished tungsten carbide substrates with a diameter of 16 mm and a thickness of 1 mm were used. FeCrAl alloy substrates (72,8% Fe, 22% Cr, 5% Al, 0,1% Y, 0,1% Zr) with dimensions 20x20x1 mm were used for oxidation tests and XRD diffraction analysis. The FeCrAl alloy substrates had a small hole drilled in the middle to help completely cover the whole surface. To test cutting performance, 6 mm diameter drills made from tungsten carbide were deposited using three axis rotation.

Prior to the depositions, all the substrates were ultrasonically cleaned in acetone for 10 min, and isopropanol for 15 min. The substrates were mounted in a substrate holder which underwent three axis rotation, and the mean target to substrate distance was 60 mm, as shown in Figure 5-27.



Figure 5-27 Image of testing samples placed in the chamber

5.2.3 Sputtering process

Multilayered TiAlCrN coatings were deposited in an industrial sputtering chamber described in section 5.1.6. Two Ti targets, containing 48 Al pellets evenly distributed along the race track, were placed on cathodes 2 and 4, together with Al and Cr targets (cathodes 1 and 3). The substrate holder was rotated in front of the targets in the following order: TiAl, TiAl, Cr and Al. This corresponds to the rotation model presented in the previous section. The power applied to the TiAl targets was constant. For understanding the effect of chromium content and thickness of the CrAlN layer, the power of Al and Cr targets progressively decreased and increased, respectively. In this way, coatings with similar Ti (to remove the influence of Ti on the coatings properties), increasing Cr, and decreasing Al contents were produced.

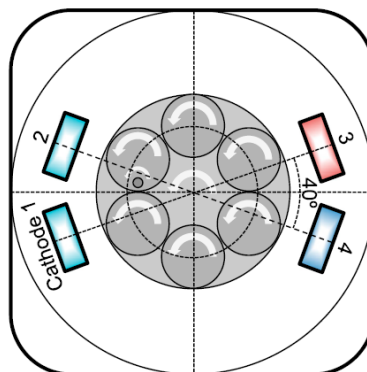


Figure 5-28 Schematic representation of the chamber geometry

A reference average industrial quality TiAlN coating was deposited from four TiAl targets with 48 Al pellets each.

Before the start of the coating stage, heating and etching processes were performed as a common praxis described in section 2.7.5.1. The substrates were heated to 450 °C and then etched with Ar MF plasma, with 650V and a frequency of 350 kHz, for 60 min. In all the depositions, the total working gas pressure was kept constant at 580 mPa, using an argon flow of 240 sccm and increasing N₂ flow from 110 to 130 sccm, with increasing power applied to the Cr target. The TiAlN film was produced using an N₂ flow of 110 sccm. All the depositions were performed using a pulsed bias of 40V (250 kHz). The deposition time for the TiAlN coating was 135 min, and for Cr-doped films 200 min. A summary of the deposition conditions is shown in Table 5-1. It should be noted that the N₂ flow was the dependent variable, and it is a result of the sputtering rates of different metal elements. This is because the control system tries to achieve a total pressure of 580 mPa, and it is controlled by nitrogen flow.

Sample designation	TiAlN	TiAlCrN 1	TiAlCrN 2	TiAlCrN 3
Plasma etching	Ar plasma for 60 min under substrate bias -650 V and 350 kHz (MF power supply)			
Designed period thickness (nm)	-	21	30	39
Power applied to target TiAl ₄₈ (W)	4 × 7000	2 × 7000	2 × 7000	2 × 7000
Power applied to target Al (W)	-	2200	1000	500
Power applied to target Cr (W)	-	1750	3000	3700
Working pressure (mPa)	580	580	580	580
Substrate temperature (°C)	350	350	350	350
Ar flow (sccm)	240	240	240	240
N ₂ flow (sccm)	110	125	127	130
RF substrate bias (V)	40	40	40	40
Coating thickness	2.2	3.6	4	4.3

Table 5-1 Sputtering conditions of developed coatings

5.2.4 Coating evaluation

After deposition of the coating, a series of tests were run on the samples. The measurement techniques applied to the coatings depended on the coating properties, and are summarized in Figure 5-29

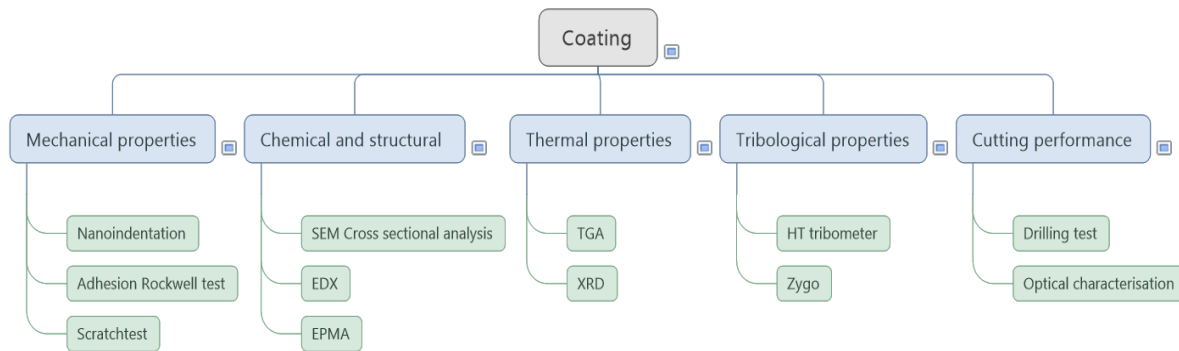


Figure 5-29 Tests applied on the coating

Mechanical property tests on tungsten carbide substrates were performed at room temperature. Chemical and structural analysis was performed on the as-deposited samples, and oxidized ones, to inspect structural changes. Oxidation tests were carried out on the FeCR alloy samples. After oxidation tests, X-ray diffraction was performed on the oxidized surface of the specimens. The cross section morphology of the coatings was characterized by scanning electron microscopy (SEM) equipped with EDS. EDS elemental lines along the cross sections of the annealed samples were acquired to characterize the distribution of the main elements in the films, and consequently to distinguish the different oxide scales. Tribological properties were tested at two temperatures: room temperature (RT) and 650°C, and the wear track was inspected by using the Zygo profilometer. Drilling tests consisted of drilling blind holes to a depth of 10 mm, until the destruction of drill occurred, or a flank wear of 3 mm was reached. During drilling tests, the flank wear and chisel wear were inspected after 5 holes. The color and shape of the metal chip was also inspected.

5.2.5 Results and discussion – cutting tools

5.2.5.1 Chemical composition

The elemental chemical composition of the coatings measured by EDS is shown in Table 5-2. As expected, by increasing and decreasing the power applied to the Cr and Al targets, respectively, while maintaining a constant power applied to the TiAl targets, gives rise

to coatings with an approximately constant Ti content, lower Al contents and higher Cr content. The reference TiAlN coating shows a stoichiometric composition and higher Ti content than Cr- rich coatings.

On the other hand, the Cr containing coatings are nitrogen-depleted, with nitrogen decreasing from 50 at% down to 48 at%, with increasing power applied to the Cr target. Although the nitrogen flow was adjusted (increased) with the power applied to the Cr target - to ensure the same deposition pressure as for the reference TiAlN coating - the chemical composition suggests that the nitrogen flow was not sufficient to produce fully stoichiometric films.

It is well known that Ti reacts much more readily with nitrogen than aluminum or chromium; this is due to its higher value of enthalpy energy (80.8 kcal/mol) in comparison to AlN (76.2 kcal/mol) and CrN (29.8 kcal/mol) [58]. Thus, the incorporation of N is less effective with an increase in Cr content. The increase of the total power applied to the Al and Cr targets (3950, 4000 and 4200 W) used on the depositions also strengthens this effect, since more metallic atoms are available for the same content of N₂ in the deposition chamber. This corresponds very well with the increased N₂ flow in Table 5-1 Sputtering conditions of developed coatings. For easy coating identification, from now on, the coatings will be designated as Ti_xAl_yN and Ti_xAl_yCr_zN, where x, y, and z denotes the Ti, Al and Cr content in the films.

Sample	Ti	Al	Cr	N
TiAlN	24	24	-	52
TiAlCrN 1	14	23	13	50
TiAlCrN 2	14	16	21	49
TiAlCrN 3	13	15	24	48

Table 5-2 Chemical composition of coatings measured by EDS (at.%)

5.2.5.2 Cross section morphology and structure

A typical cross-section morphology of the coatings is shown in Figure 5-30. All coatings displayed a columnar morphology, with columns extending from the substrate to the surface. No significant variations in column size are observed upon addition of Cr. The Ti_{0.24}Al_{0.24}N film is 2.2 μm thick. Although the total power applied to the targets to produce Cr-rich coatings was lower than for the reference film, the thickness of the Cr-containing coatings was much higher, which is in good agreement with their higher deposition time. The progressive increase of the power applied to the Cr target led to the increase of the thickness of the coating (3.6, 4.0 and 4.3 μm for Ti_{0.14}Al_{0.23}Cr_{0.13}N, Ti_{0.14}Al_{0.16}Cr_{0.21}N and Ti_{0.13}Al_{0.15}Cr_{0.24}N films). They are taking into

account the low enthalpy of formation of CrN, as compared to AlN and TiN, and the non-stoichiometric composition of Cr-rich films in relation to N content (slightly lower than 50 at%); it is likely that the increase of the thickness of the coatings with Cr content is due to the reduction of the poisoning of the Cr target.

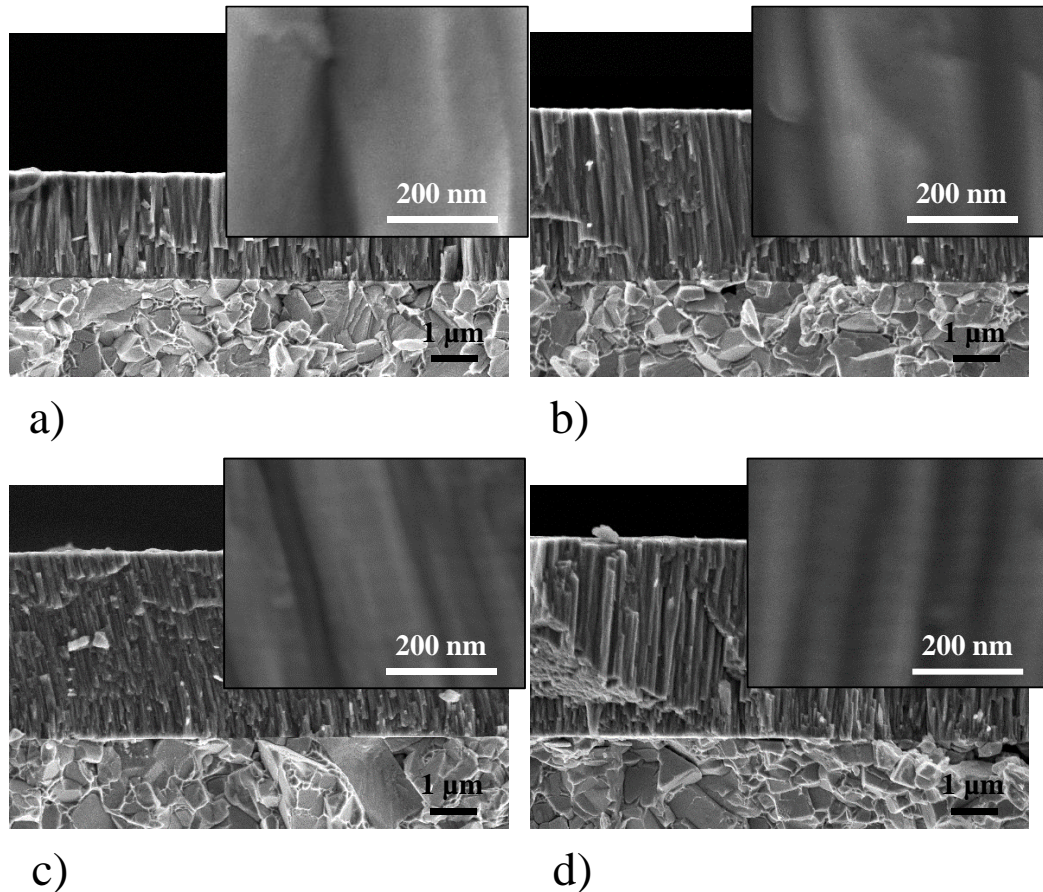


Figure 5-30 Cross section morphology of films. a) $\text{Ti}_{0.47}\text{Al}_{0.46}\text{N}$, b) $\text{Ti}_{0.30}\text{Al}_{0.46}\text{Cr}_{0.26}\text{N}$, c) $\text{Ti}_{0.28}\text{Al}_{0.34}\text{Cr}_{0.42}\text{N}$, d) $\text{Ti}_{0.28}\text{Al}_{0.31}\text{Cr}_{0.51}\text{N}$.

A closer look at the coatings reveals that the reference $\text{Ti}_{0.24}\text{Al}_{0.24}\text{N}$ film displays a monolayer structure, while an expected multilayer structure with a period of 30 and 39 nm has been formed for $\text{Ti}_{0.28}\text{Al}_{0.34}\text{Cr}_{0.42}\text{N}$ and $\text{Ti}_{0.28}\text{Al}_{0.31}\text{Cr}_{0.51}\text{N}$ films, respectively. EDS analysis performed on the multilayer structure shows that the bright phase is much richer in Cr than the dark phase, suggesting that the first is CrAlN with Cr and Al in solid solution, and the latter is TiAlN with Ti and Al in solid solution. It should be pointed out that the multilayered structure is in good agreement with the rotation model, as shown in section 5.2.1.1.4. It is expected that there is the formation of intermixed layers with a gradient interface. A SEM picture of the coating with low Cr content does not show a multilayer structure. Taking into account the target arrangement inside the deposition chamber, and the preview thickness of each individual layer, based on the total power applied to the Al and Cr target as compared to the other Cr-rich coatings, there is no reason for this not to be observed. The reason for this can be a low

contrast in the observation between TiAlN and CrAlN layers, in addition to extensive intermixing. Together it makes it very difficult to distinguish the multilayer arrangement. More powerful techniques, such as high-resolution transmission electron microscopy, would be required to distinguish the blurred multilayers.

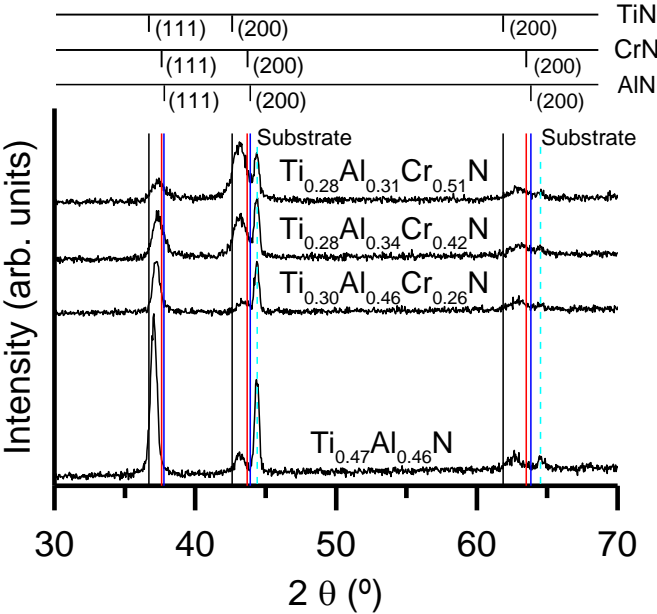


Figure 5-31 XRD spectra of the as-deposited coatings

Figure 5-31 shows the XRD patterns of the as-deposited coatings on FeCrAlY alloy substrates obtained in conventional mode. Excluding the substrate contribution, all the coatings show diffraction peaks assigned to an fcc NaCl-type structure. The Ti_{0.24}Al_{0.24}N film shows a preferential [111] orientation. The XRD diffraction peaks of this film are slightly shifted to higher and lower angles when compared to the reference TiN (87-0633) and AlN (25-1495) ICDD cards, respectively, suggesting that a solid solution is being formed. Therefore, it can be assumed that both elements (Ti and Al) occupy the lattice positions in the single fcc Na-Cl type structure randomly. Indeed, as Al has a lower atomic radius (0.143 nm) than Ti (0.147 nm), it constrains the lattice, with the XRD peaks placed between the TiN and AlN standards. This result agrees well with those in the literature, where Ti_{1-x}Al_xN coatings with an fcc substitutional solid solution structure have always been produced for Al concentrations lower than 35 at.% (i.e., x < 0.7) [59]. However, the diffraction peak positions can also be influenced by the intrinsic and thermal residual stresses.

The addition of Cr leads to a significant broadening of the diffraction peaks. This can be interpreted, based on the above-suggested microstructure of the Cr-containing coatings, as follows:

- a) the presence of a multilayer consisting of two similar structural phases, but with different chemical composition (TiAlN and CrAlN) and, thus, different lattice parameters, which should give rise to XRD diffraction signals placed at different angles;
- b) the existence of large chemical composition gradient interfaces between the two layers should lead to a sequence of shifts of the diffraction peaks in the XRD pattern when compared to the positions of the individual layer phases.

Both of these factors contribute to a widening of the diffraction peaks, determined by the existence of a sequence of lattice parameters, from that of the TiAlN to the CrAlN phase. The deconvolution of the XRD peaks is not easily performed due to the contribution of the interface mixing. However, the progressive change of the peak intensity ratio of the coatings with the increased Cr content supports this interpretation. In fact, for a higher Cr content, a decrease of the (111) and an increase of the (200) diffraction peak intensities is observed, which is in accordance to the ICDD card (76-2494) of the CrN phase, which has the highest intensity for the (200) peak; therefore, the Cr-rich phase (CrAlN layer) should give rise to a higher (200) intensity.

5.2.5.3 Mechanical properties of the coatings

5.2.5.3.1 Hardness and Young's Modulus of coatings

The evolution of the hardness and Young's modulus of the coatings upon Cr addition is presented in Table 3.

Sample	Hardness [GPa]	E [GPa]	H/E []	H ³ /E ² [GPa]
Ti _{0.24} Al _{0.24} N	23.8	446	0,053	0.068
Ti _{0.14} Al _{0.23} Cr _{0.13} N	17.0	343	0.05	0.042
Ti _{0.14} Al _{0.16} Cr _{0.21} N	16.8	335	0.05	0.042
Ti _{0.13} Al _{0.15} Cr _{0.24} N	19.8	348	0.057	0.064

Table 5-3 Mechanical properties of the developed coatings

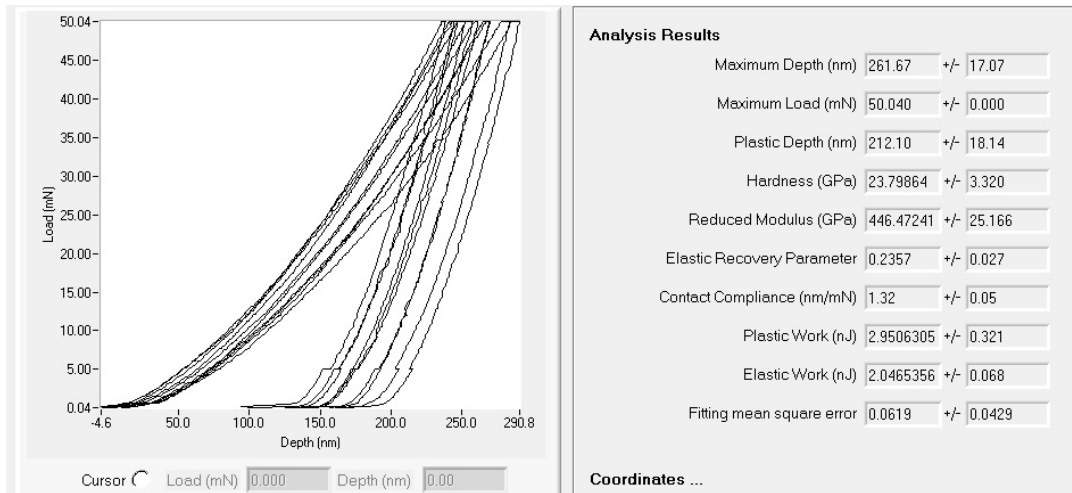


Figure 5-32 The loading displacement curve for nanoindentation of the TiAlN coating

The higher hardness of the reference $Ti_{0.24}Al_{0.24}N$ can be explained by the solid solution hardening effect, as suggested by the XRD diffraction results. Moreover, it is clear from the results presented in Table 5-3 that the coatings with added Cr are softer and have a lower Young's modulus than $Ti_{0.24}Al_{0.24}N$. As is well known from the literature, the superlattice effect (significant hardness enhancement) produced by a multilayered film arrangement is dependent on the thickness of the multilayers. In many material combinations, the evolution of the hardness as a function of the bilayer modulation period shows a characteristic behavior, with maximum hardness values typically obtained for λ between 2 and 15 nm, as was discussed in section 3.7.1.

Thus, the lower hardness and Young's modulus of Cr-containing coatings cf. $Ti_{0.24}Al_{0.24}N$ can be interpreted by the high period thickness of the multilayer structure, which avoids the establishment of the superlattice effect, and the presence of the CrAlN layer, which is softer than TiAlN. Unexpectedly, an increase of the hardness and Young's modulus was also observed with an increase in the Cr content, which counters the previous statement, since a larger CrAlN phase is present. Nevertheless, XRD showed a progressive increase of the (200) and decrease of the (111) peak intensities upon Cr addition, which has been reported to give higher TiN and CrN hardness values [28, 29], thus, justifying the hardness increase.

5.2.5.3.2 Adhesion of the coatings

The film-substrate adhesion is critical for achieving longer wear life and durability, particularly for highly-loaded components such as cutting tools. According to the adhesion critical load values, all coatings adhered well on tungsten carbide substrates, Table 5-4. The first coating cracking value of $LC_1 > 100$ N was reached for all coatings, except for $Ti_{0.30}Al_{0.46}Cr_{0.26}N$, where LC_1 was 75 N. The Mercedes test (Rockwell C indentation) confirmed excellent adhesion with

HF1 failure mode for all films. However, identical adhesion tests on the samples after tribological testing at 650 °C showed a significant decrease in adhesion.

Adhesion critical loads				
	As-deposited		Annealed at 650 0C (after tribology)	
	Scratch tester - LC1 failiure	Mercedes	Scractch tester - LC1 failure	Mercedes
$Ti_{0.24}Al_{0.24}N$	>100 N	HF1	20	HF6
$Ti_{0.14}Al_{0.23}Cr_{0.13}N$	75 N	HF1	65	HF6
$Ti_{0.14}Al_{0.16}Cr_{0.21}N$	>100 N	HF1	20	HF6
$Ti_{0.13}Al_{0.15}Cr_{0.24}N$	>100 N	HF1	20	HF6

Table 5-4 Adhesion of the films

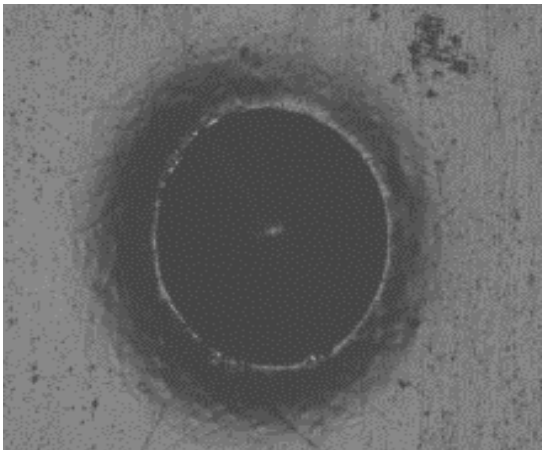


Figure 5-33 HF1 Mercedes test adhesion before tribological testing

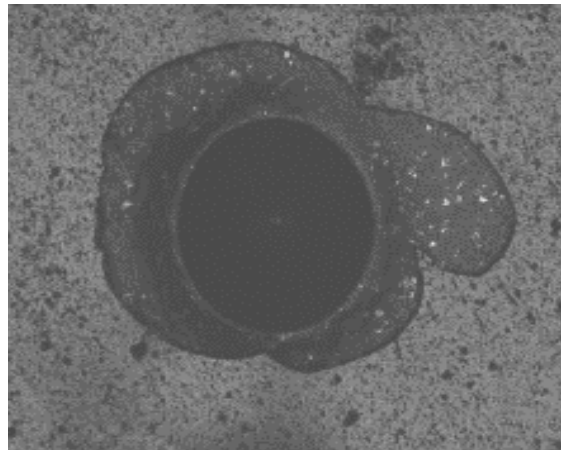


Figure 5-34 HF1 Mercedes test adhesion after tribological testing

5.2.5.4 Continuous and isothermal oxidation in air

Figure 5-35 shows the oxidation weight gain curves of the coatings acquired at a continuous increase of temperature (RT to 1200 °C, at 20 °C/min). The onset point of oxidation of the $Ti_{0.47}Al_{0.46}N$ film is 850 °C. The mass gain of the $Ti_{0.47}Al_{0.46}N$ film increases rapidly in the temperature range of 1000 – 1100 °C, suggesting a fully oxidized coating. Alloying the TiAlN coating with Cr leads to a higher onset point of oxidation (increment of about 200 °C) and a clear progressive decrease of the oxidation weight gain as a function of Cr content. Donohue et al. [60] reported an onset point of oxidation of 920 °C for a $Ti_{0.44}Al_{0.53}Cr_{0.03}N$ film with low Cr

content. Yamamoto et al. [61] have also shown that, when deposited with a monolayer structure, alloying TiAlN films with Cr leads to a higher onset point of oxidation by $\sim 200^\circ\text{C}$.

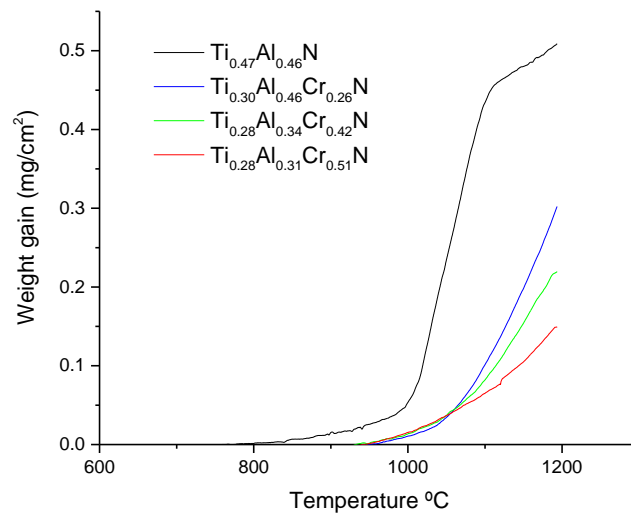


Figure 5-35 Thermal gravimetric oxidation rate of coatings deposited on Al_2O_3 substrates: experiments performed at a linear-temperature ramp (RT to 1200°C at $20^\circ\text{C}/\text{min}$).

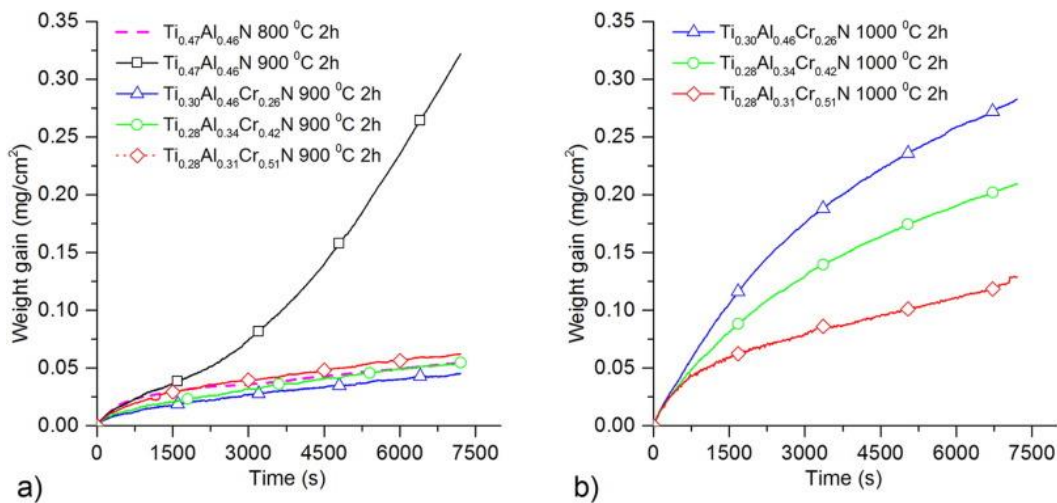


Figure 5-36 Isothermal oxidation weight gain of coatings tested at dissimilar temperatures during two hours. Reference $\text{Ti}_{0.47}\text{Al}_{0.46}\text{N}$ film tested at 800 and 900°C . Cr-rich coatings tested at 900 and 1000°C .

The results of the thermogravimetric analysis performed on the films at different isothermal temperatures are shown in Figure 5-36. The reference $\text{Ti}_{0.47}\text{Al}_{0.46}\text{N}$ film was exposed to temperatures of 800 and 900°C , while Cr-containing coatings were tested at 900 and 1000°C . The oxidation weight gains of the $\text{Ti}_{0.47}\text{Al}_{0.46}\text{N}$ film tested at 800°C , and Cr-rich coatings tested at 900°C , follow a parabolic evolution as a function of time, suggesting the formation of

a protective oxide layer. Increasing the test temperature to 900 °C suddenly decreases the oxidation resistance of the $Ti_{0.47}Al_{0.46}N$ film, which follows an exponential evolution.

This behavior was observed in the literature and has been attributed to the fast growth of an outer TiO_2 oxide layer [62]. Chen et al. [59] showed an improvement in the onset point of oxidation of TiAlN films and, consequently, an increase of the oxidation resistance of the films with increasing Al content. All Cr-doped coatings annealed at 900 °C displayed comparable oxidation weight gains, which was at least six times lower when compared to the $Ti_{0.47}Al_{0.46}N$ film. This reveals the clear beneficial influence of Cr addition on the oxidation resistance of TiAlN films. The increase of the isothermal test temperature to 1000 °C results in the increase of the oxidation weight gain of Cr-rich coatings, due to the enhanced diffusion controlling the oxidation process. All of the curves still display a parabolic evolution as a function of time, as a consequence of the presence of a protective oxide layer.

5.2.5.4.1 Oxidation behavior of TiAlN

To understand the oxidation behavior, XRD, SEM and EDS analyses were performed after oxidation tests, with the main emphasis focused on the formation and composition of the surface oxide layers. Figure 5-37 shows the XRD diffraction patterns of the annealed coatings.

The $Ti_{0.47}Al_{0.46}N$ film oxidized at 800°C exhibits a small shift of the fcc diffraction peaks toward higher angles, and a slight decrease of their intensity, with a simultaneous broadening when compared to the as-deposited film (spectrum ii) in Figure 5-36 a)). This suggests that only minor structural changes occurred at this temperature. The shift of the fcc diffraction peaks to higher 2θ angles during annealing might be attributed to the release of residual stresses. Additionally, a small left shoulder of the (111) peak appeared. The cross-section morphology of the oxidized film (see Figure 5-39 a) shows the presence of a thin two-layer oxide structure (total thickness ~130 nm), with a porous inner layer and an outer compact and continuous layer.

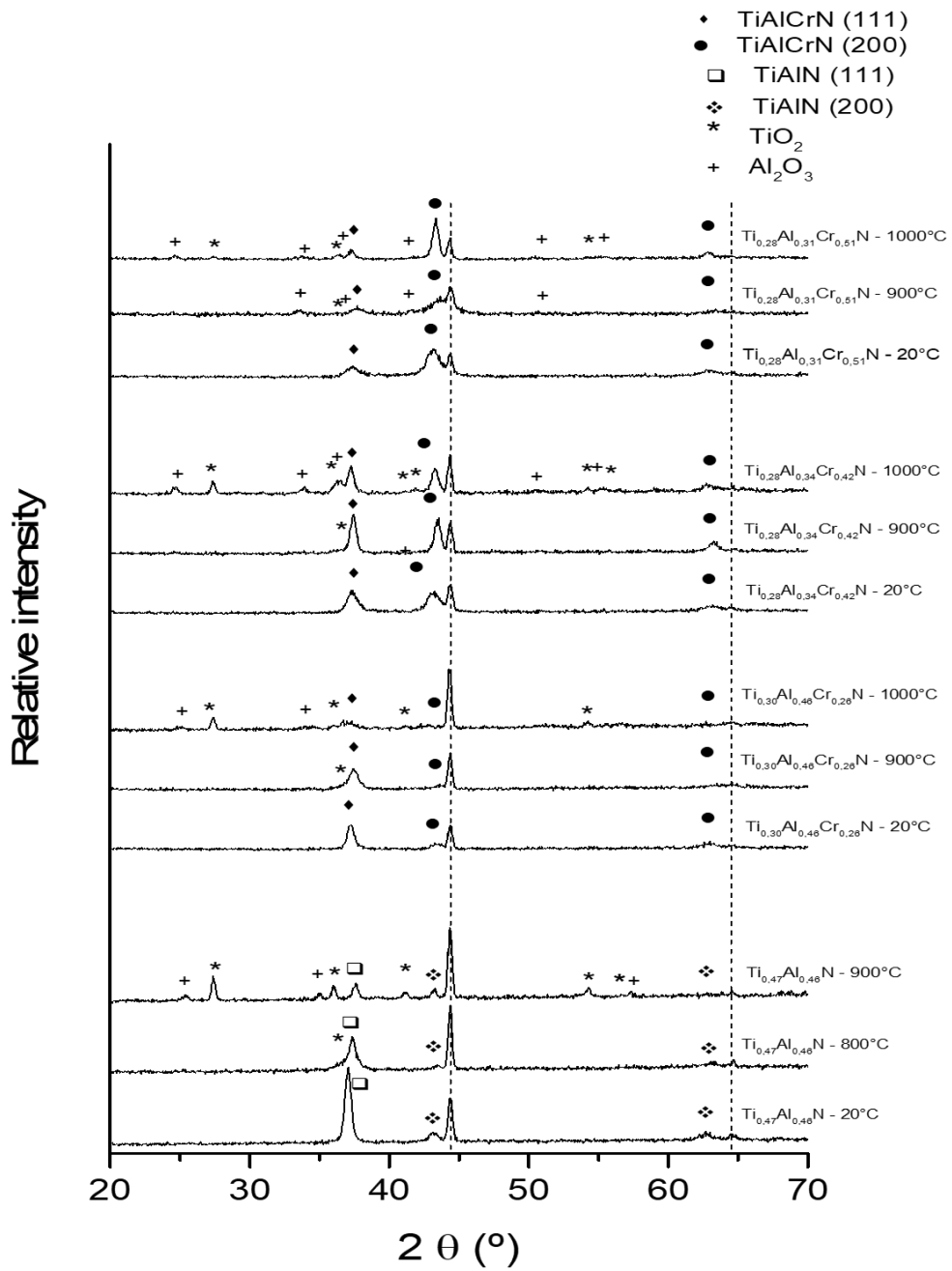


Figure 5-37 XRD diffraction patterns of dissimilar coatings after annealing in air at different temperatures

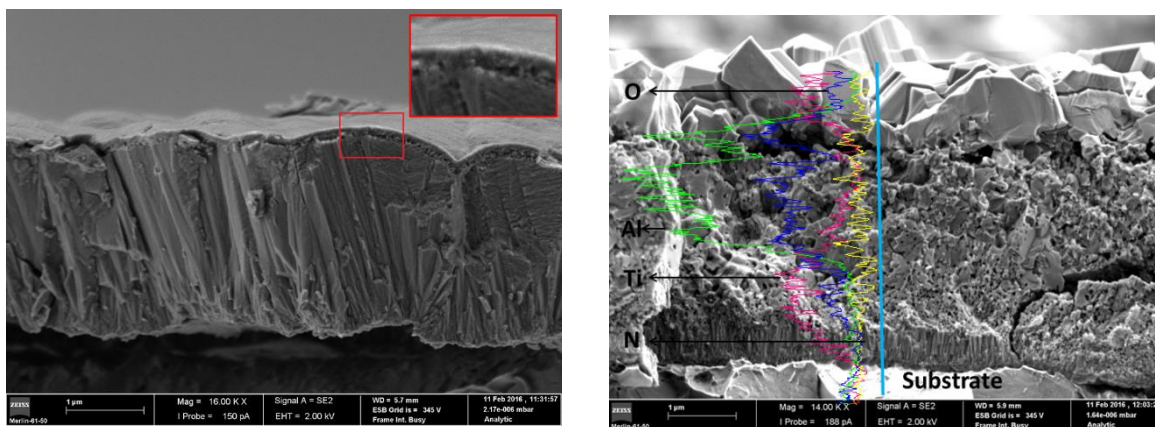


Figure 5-38 Fracture cross-section morphology and EDX line scan of annealed $\text{Ti}_{0.47}\text{Al}_{0.46}\text{N}$ film: a) at 800 °C 2h, b) at 900 °C 2h.

EDS analysis revealed that the porous layer was Ti-rich, whereas the denser top layer was Al-rich. This agrees well with the results from previous works, where the scale of the layered oxide $\text{Ti}_{1-x}\text{Al}_x\text{N}$ coatings was attributed to the simultaneous outward diffusion of Al through the oxide/air interface, to form Al_2O_3 , and inward diffusion of O toward the oxide/nitride interface, to grow a porous TiO_2 layer [59]. Although the analysis indicated the presence of a double, thin oxide layer, XRD diffraction peaks related to the oxide phases are missing. Close to this temperature, $\text{Ti}_{1-x}\text{Al}_x\text{N}$ films also undergo spinodal decomposition, as explained in section 3.6.1. Thus, the broadening of the fcc peak, as well as the appearance of the left shoulder peak, can be attributed to either the $\text{Ti}_{1-x}\text{Al}_x\text{N}$ spinodal decomposition, or the first weak traces of oxidation of the film. Both c-TiN, w-AlN (ICDD card 03-1144) and TiO_2 (ICDD card 76-0649) phases can fit the shoulder in the diffraction peak (see insert in Figure 5-37).

During the oxidation of the $\text{Ti}_{0.47}\text{Al}_{0.46}\text{N}$ film at 800 °C, Al first reacts with oxygen due to their selective oxidation (see Ellingham diagram [63]). At the same time, Ti diffuses to the interface of the unoxidized coating/oxide surface layer, where, due to the inward diffusion of O, porous TiO_2 is grown. The formation of porous Ti-O is reported to be caused by the generation of compressive residual stresses, which can cause crack formation and thereby fast oxidation with its growth [64]. Then, Al diffuses through the Ti-O porous layer to the coating surface to form Al-O. Once the thickness and compactness of the Al-O layer at the surface are sufficient, it acts as a very effective diffusion barrier, limiting ion diffusion and protecting the coating from further oxidation. The establishment of a continuous, compact and protective Al-O layer on the surface explains the parabolic weight gain evolution of the coating with time, as displayed in Figure 5-36.

At 900 °C, all the XRD diffraction peaks relating to the cubic fcc phase disappeared (see spectrum iii) in Figure 5-37 a) and, instead, reflections of TiO_2 and corundum-type Al_2O_3

(ICDD card 02-1373) are detected. This corroborates the cross section EDS profiles and the morphology presented in Figure 5-38, which showed the complete oxidation of the coating. A dual oxide layer structure, composed by an outer layer of large crystals, corresponding to TiO_2 , and an inner layer formed by two phases, corresponding to islands of TiO_2 embedded in a matrix of a porous Al_2O_3 phase, was formed. According to Xu et al. [64], the fast Ti ion diffusion through the oxide scale to the surface, to form TiO_2 , inhibits the formation of a protective and compact Al–O layer, thus degrading the oxidation resistance of the coatings.

5.2.5.4.2 Oxidation behavior of TiAlCrN films

5.2.5.4.2.1 Annealing at 900 °C

Regarding the Cr-doped coatings, the XRD patterns of the coatings annealed at 900 °C displayed only small changes, in good agreement with their small weight gain values and the very thin oxide scale formed. Similarly to the reference $\text{Ti}_{0.47}\text{Al}_{0.46}\text{N}$ film, we observe a shift of the fcc diffraction peaks to higher 2θ angles, their broadening, and a small shoulder on the (111) peak of the XRD diffraction patterns of the $\text{Ti}_{0.30}\text{Al}_{0.46}\text{Cr}_{0.26}\text{N}$ and $\text{Ti}_{0.28}\text{Al}_{0.34}\text{Cr}_{0.42}\text{N}$ films. Elemental line profiles of the $\text{Ti}_{0.30}\text{Al}_{0.46}\text{Cr}_{0.26}\text{N}$ and $\text{Ti}_{0.28}\text{Al}_{0.34}\text{Cr}_{0.42}\text{N}$ films revealed that a Ti-O-rich zone was formed on the top, followed by an Al-Cr-O rich zone, whose signal increased as the probe moved to the interior of the coating (see Figure 5-37 for $\text{Ti}_{0.30}\text{Al}_{0.46}\text{Cr}_{0.26}\text{N}$ film). The Ti-O-rich zone was thicker for the film with lower Cr content, showing the beneficial influence of chromium alloying on the decrease of Ti diffusion to the surface. None of the previous oxide phases were detected by XRD; however, the TiO_2 is indicated by the left shoulder of the (111) peaks.

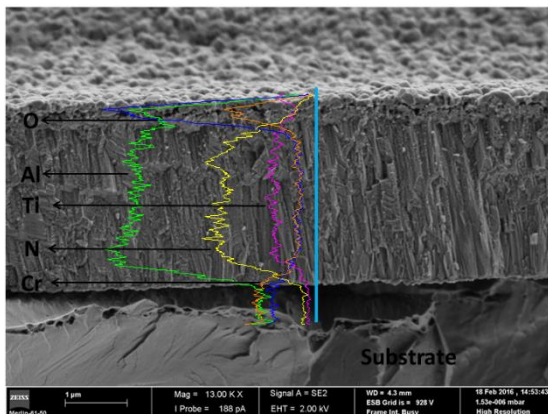


Figure 5-39 Fracture cross-section morphology and EDX line scan of $\text{Ti}_{0.30}\text{Al}_{0.46}\text{Cr}_{0.26}\text{N}$ after oxidation at 900 °C for 2h.

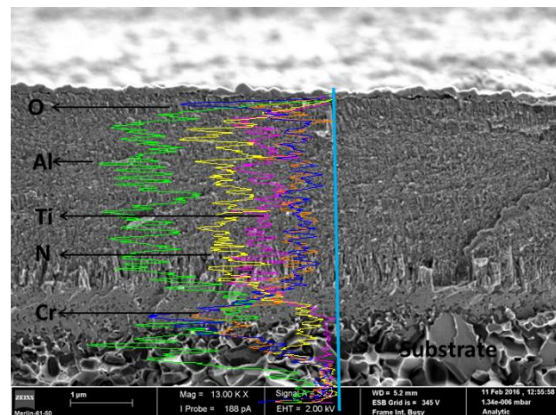


Figure 5-40 Fracture cross-section morphology and EDX line scan of $\text{Ti}_{0.28}\text{Al}_{0.31}\text{Cr}_{0.51}\text{N}$ after oxidation at 900 °C for 2h.

Nevertheless, taking into account the spinodal decomposition, which often occurs for this coating system for annealing temperatures above 800 °C (see section 3.6.1), the

broadening of the fcc diffraction peak and the appearance of the shoulder peak can be interpreted as either the phase transformation or a weak signal from the oxidation of the film. The continuous Al-Cr-O rich phase, formed at the film/oxide interface, grows amorphously, as no crystalline peaks were detected by XRD. However, such a phase should protect the coating from oxidation, as revealed by the very low mass gain registered by TGA.

The broadening and shift to higher angles of the fcc diffraction peaks, as well as the appearance of a left shoulder to the (111) peak, was also observed for the coating with the highest Cr content ($\text{Ti}_{0.28}\text{Al}_{0.31}\text{Cr}_{0.51}\text{N}$). Again, it can be correlated to the spinodal decomposition and/or the oxidation of the film. However, crystalline peak reflections from Cr_2O_3 (ICDD 38-1479) were also indexed. EDS analyses, carried out at the oxidized surface, showed discontinuous and evenly distributed islands rich in the Ti-O phase on the top of a Cr-O rich layer. The cross-section morphology and elemental line profile analyses confirmed the formation of a continuous and compact oxide layer of Cr-O (Figure 5-40), in good agreement with the XRD signal of the Cr_2O_3 .

Although the position of the XRD peaks of the Cr_2O_3 phase is very close to the ICDD reference position, and the EDS analysis distribution in the top layers clearly shows that Cr intensity is increasing towards the surface inversely to the Al signal, one cannot disregard the Al presence in solid solution in the Cr-O phase.

In summary, for the isothermal tests performed at 900 °C, alloying the TiAlN coating with Cr delays the fast diffusion of Ti to the surface due to the formation of an inner protective amorphous layer of Al-Cr-O or, for the coating with the highest Cr content, a crystalline $\text{Cr}(\text{Al})_2\text{O}_3$ layer. Such layers inhibit either Ti ion diffusion to the surface, or the inwards O diffusion to the TiAlCrN film and, thus, improve the oxidation resistance. It is evident that the addition of a minimal amount of Cr addition is sufficient enough to improve the oxidation resistance. A higher Cr content, although reducing the thickness of the oxide scale slightly and promoting the formation of a $\text{Cr}(\text{Al})_2\text{O}_3$ inner protective layer, does not further improve the oxidation resistance, as demonstrated in Figure 5-36.

5.2.5.4.2.2 *Annealing at 1000°C*

Cr-rich coatings annealed at 1000 °C exhibited structural changes at lower temperatures. According to XRD patterns, the main oxide phases detected on oxidized $\text{Ti}_{0.30}\text{Al}_{0.46}\text{Cr}_{0.26}\text{N}$ and $\text{Ti}_{0.28}\text{Al}_{0.34}\text{Cr}_{0.42}\text{N}$ films were: TiO_2 and a phase with XRD peaks positioned in-between the standard positions of Cr_2O_3 , and corundum-type Al_2O_3 oxides, which can be identified as a $(\text{Cr}, \text{Al})_2\text{O}_3$ compound. On the other hand, Cr_2O_3 and TiO_2 (sole peak at 27.4 °) phases were indexed in the case of the highest Cr content film ($\text{Ti}_{0.28}\text{Al}_{0.31}\text{Cr}_{0.51}\text{N}$). Again, in spite of the close position of the peaks to the ICDD Cr_2O_3 standard, the presence of Al in this phase cannot be ignored. All the fcc diffraction peaks of TiAlCrN films are shifted to angles closer to the

reference TiN card as compared to the corresponding diffraction patterns of the coatings annealed at 900 °C, in accordance with the occurrence of spinodal decomposition.

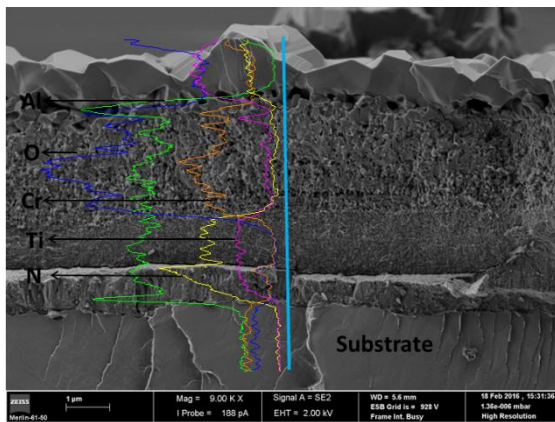


Figure 5-41 Fracture cross section morphology and EDX line scan of $\text{Ti}_{0.30}\text{Al}_{0.46}\text{Cr}_{0.26}\text{N}$ after oxidation at 1000 °C 2h.

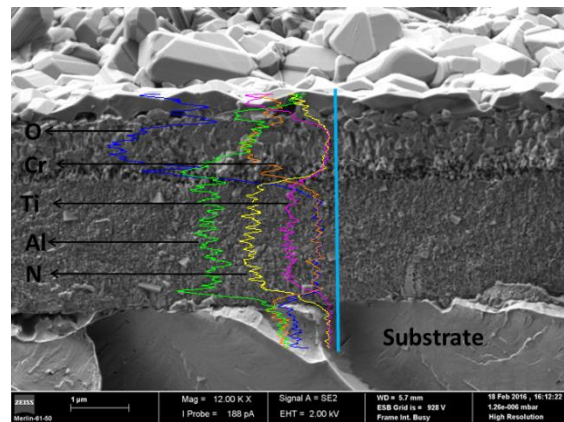


Figure 5-42 Fracture cross section morphology and EDX line scan of $\text{Ti}_{0.28}\text{Al}_{0.34}\text{Cr}_{0.42}\text{N}$ after oxidation at 1000 °C 2h.

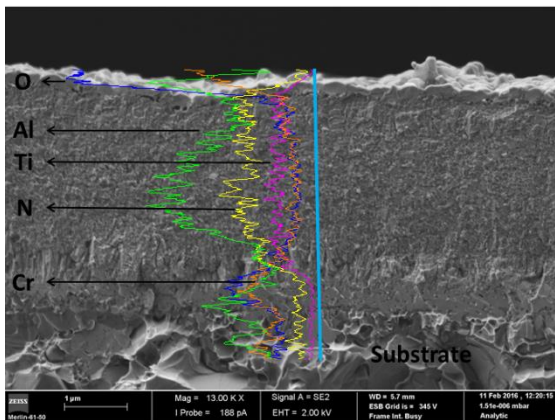


Figure 5-43 Fracture cross section morphology and EDX line scan of $\text{Ti}_{0.28}\text{Al}_{0.31}\text{Cr}_{0.51}\text{N}$ after oxidation at 1000 °C 2h.

The cross-section morphology of the coatings shown in Figure 5-41, Figure 5-42 and Figure 5-43 clearly demonstrates that increasing Cr addition progressively decreased the oxide scale thickness of the films, in good agreement with the isothermal oxidation curves in Fig. 5. Cross section EDS profiles of $\text{Ti}_{0.30}\text{Al}_{0.46}\text{Cr}_{0.26}\text{N}$ film (Figure 5-41) show a Ti-O rich layer on the top surface. Below this region, a mixture of Al-Cr-O was formed. These results are in line with the two different regions observed by SEM: a continuous and rough layer on the top, corresponding to TiO_2 , and a porous layer of Al, Cr and O underneath; they also agree with the XRD results. The $\text{Ti}_{0.28}\text{Al}_{0.34}\text{Cr}_{0.42}\text{N}$ film shows a similar oxide scale structure; however, both the thicknesses of the overall oxide scale and the individual oxide layers are smaller. The EDS

chemical profile again shows a Ti-O layer on the top surface and an Al-Cr-O layer underneath. However, the latter is much less porous. Concerning the coating with the highest Cr content, a compact and continuous monolayer about 170 nm thick was formed (see Figure 5-43), which, according to the EDS elemental profiles and XRD results, could be described as $\text{Cr}(\text{Al})_2\text{O}_3$. EDS analysis performed at the oxidized surface detected islands of the Ti-O phase, evenly distributed on the surface (not shown), in good agreement with the TiO_2 detection by XRD diffraction. The presence of this continuous and compact Cr-rich oxide layer, suggests a greater diffusion barrier than Al_2O_3 and $(\text{Cr}, \text{Al})_2\text{O}_3$ phases found in TiAlN and TiAlCrN (low and intermediate Cr content) films, respectively.

The experimental evidence shows that the mechanisms of oxidation are complex and dependent both on temperature and Cr content. It is clear that Cr addition increases the oxidation resistance of the coatings. At 900 °C, the oxide scale of TiAlCrN coatings is different from that of conventional TiAlN, and depends on the Cr content of the film. Chromium was found to promote the formation of a protective amorphous Al-Cr-O layer below a thin Ti-O layer for the $\text{Ti}_{0.30}\text{Al}_{0.46}\text{Cr}_{0.26}\text{N}$ and $\text{Ti}_{0.28}\text{Al}_{0.34}\text{Cr}_{0.42}\text{N}$ coatings, which hindered either the fast Ti ion diffusion to the surface or the inward diffusion of O. For the coating with the highest Cr content, a different oxide scale was grown. A protective $\text{Cr}(\text{Al})_2\text{O}_3$ layer was established on the surface of the film, with TiO_2 islands dispersed on the top. At the initial stage of the oxidation of the $\text{Ti}_{0.30}\text{Al}_{0.46}\text{Cr}_{0.26}\text{N}$ and $\text{Ti}_{0.28}\text{Al}_{0.34}\text{Cr}_{0.42}\text{N}$ films, Al-O forms first, as suggested by the highest affinity to oxygen when compared to Ti and Cr. However, titanium diffuses quickly to the surface to form a Ti-O layer with the oxidation of both Al and Cr underneath. For $\text{Ti}_{0.28}\text{Al}_{0.31}\text{Cr}_{0.51}\text{N}$, due to the high amount of Cr, a $\text{Cr}(\text{Al})_2\text{O}_3$ layer is preferentially formed. After some time, the thickness of the inner Al-Cr-O or $\text{Cr}(\text{Al})_2\text{O}_3$ layer is sufficient to delay further oxidation significantly.

Annealing at 1000 °C results in the growth of similar oxide scales as for 900 °C, but with higher thicknesses. Additionally, oxides which were amorphous at 900 °C became crystalline. Coatings with low and intermediate Cr contents showed a bilayer structure: a TiO_2 layer on the surface and, below, a compact and continuous $(\text{Cr}, \text{Al})_2\text{O}_3$ layer. Similarly to the Cr-rich coatings tested at 900 °C, at the beginning of oxidation, rapid Ti ion diffusion causes the initial formation of a Ti-O layer and, subsequently, the formation of the Cr-Al-O sublayer. However, due to the enhanced diffusion, the thickness of the oxide scales is higher. In the $\text{Ti}_{0.28}\text{Al}_{0.34}\text{Cr}_{0.42}\text{N}$ film, the oxide scale growth progresses more slowly than for the $\text{Ti}_{0.30}\text{Al}_{0.46}\text{Cr}_{0.26}\text{N}$ film, due to the higher amount of Cr. Therefore, an Al-Cr-O sublayer much richer in Cr is formed, which is more resistant to Ti ion diffusion. Oxidation kinetics are reduced and, consequently, the oxidation resistance of the film is improved. Finally, for the $\text{Ti}_{0.28}\text{Al}_{0.31}\text{Cr}_{0.51}\text{N}$ film, due to the very high Cr content, a thin Cr_2O_3 oxide layer, which can contain Al, forms on the surface of the film quickly, with residual TiO_2 islands on the top (almost

not detectable by XRD and SEM cross-section). Such a layer is even more efficient at reducing the inward and outward diffusion of ions and, consequently, improves oxidation performance.

5.2.5.5 Tribological behavior of the films

5.2.5.5.1 Wear rate

The wear rate of coatings tested at different temperatures is shown in Figure 5-44. At room temperature, the wear rate of the films was almost unmeasurable and independent of the chemical composition of the coating (see Figure 5-45 a) and b) for $Ti_{0.47}Al_{0.46}N$ and $Ti_{0.28}Al_{0.31}Cr_{0.51}N$). The only surface change was negligible smoothing of the surface (asperities polishing), which demonstrates the excellent wear resistance of these coatings at room temperature.

At 650 °C, the wear rate of multilayered TiAlCrN was at least five times lower than that of the $Ti_{0.47}Al_{0.46}N$ reference. At this temperature, an abrupt increase in the wear rate of the $Ti_{0.47}Al_{0.46}N$ coating was observed, and a smooth deep wear track was produced (see Figure 5-45 c)). The $Ti_{0.30}Al_{0.46}Cr_{0.26}N$ and $Ti_{0.28}Al_{0.34}Cr_{0.42}N$ films displayed slightly higher specific wear rates when compared to those obtained at room temperature. Wear tracks of these films displayed a rough morphology (see Figure 5-45 d)) which, as discussed later, is correlated to the presence of oxidized material adhered to the wear track, which protects the film from further wear. Interestingly, the wear of the coating with the highest Cr content was very low, even after the test at high temperature.

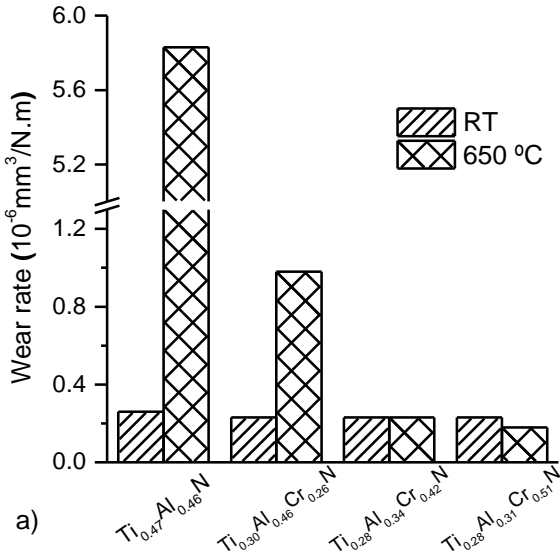


Figure 5-44 Specific wear rate of films

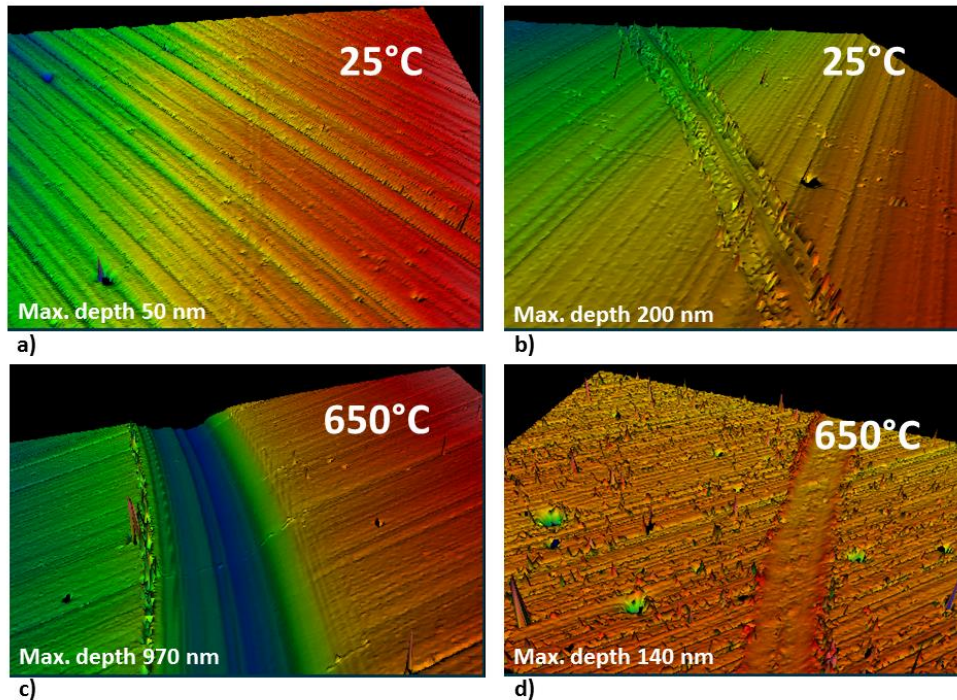


Figure 5-45 3D profiles of the wear tracks of $\text{Ti}_{0.47}\text{Al}_{0.46}\text{N}$ and $\text{Ti}_{0.28}\text{Al}_{0.31}\text{Cr}_{0.51}\text{N}$ films tested at: a) and b) room temperature, c) and d) 650 °C. The 2D XY field has dimensions 1.26 x 0.95 mm.

5.2.5.5.2 Friction coefficient

The coefficient of friction (COF) of the films was quite stable at room temperature. No significant fluctuations were observed during the tribological tests, except for the $\text{Ti}_{0.47}\text{Al}_{0.46}\text{N}$ reference, which displayed a broader COF curve. As expected, two distinct regions - the running-in and steady state zones - could be observed. The running-in period for the $\text{Ti}_{0.47}\text{Al}_{0.46}\text{N}$ film lasted 300 laps, with the COF abruptly increasing from 0.2 to 0.63, the remaining stable. A similar evolution and COF values were reported in reference [65] for $\text{Ti}_{1-x}\text{Al}_x\text{N}$ films tested against Al_2O_3 balls. An increase of the COF from an initial low value of 0.2 to a higher steady-state value 0.5-0.6 was also observed for coatings containing Cr. The running-in the period of these coatings was kept at 1500 cycles. The average COF values of the steady-state stage are plotted in Figure 5-46, where it can be observed that Cr-rich coatings displayed slightly lower COF values than the $\text{Ti}_{0.47}\text{Al}_{0.46}\text{N}$ reference

At a temperature of 650 °C, a slight increase of the COF values was observed for all coatings except for the $\text{Ti}_{0.28}\text{Al}_{0.31}\text{Cr}_{0.51}\text{N}$ film for which the inverse occurred, which is in good

agreement with its lower wear rate. The COF values of Cr-rich coatings were lower than the reference $Ti_{0.47}Al_{0.46}N$ film, and decreased progressively with increasing Cr content. The reference film showed much larger fluctuations of the COF during the tests when compared to the smoother curves of the other coatings.

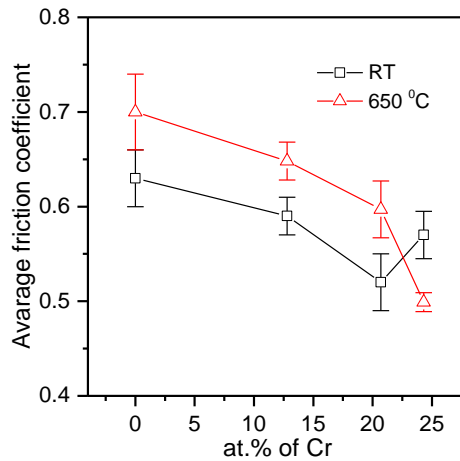


Figure 5-46 Average friction coefficient of films

5.2.5.5.3 Wear mechanisms and surface analysis

The investigation of the interaction between the specimen-counterpart pair, *i.e.*, the dominant wear mechanisms and the wear debris originating from tribological testing, was carried out by SEM-EDS. At room temperature, fine scratches parallel to the relative sliding movement of the ball were observed in the wear track of all coatings, suggesting that polishing wear (abrasion) is the main active wear mechanism. Small adhered wear debris was found evenly distributed over the wear tracks of the films; EDS analysis revealed this to be a mixture of non-oxidized and oxidized particles detached from the coatings, generated by the asperities during the relative movement between the coating and the ball. Similar wear debris was also found adhered to the counter body surface. The formation of oxidized particles occurred due to the continuous movement of the ball and the local increase of temperature on the contact in the top of the asperities.

Consequently, a third body was formed, which prevented the direct contact between parts and protected the film from wear. The well-known lubricious properties of the oxide products, *i.e.*, Ti-Al-O as a reference for $Ti_{0.47}Al_{0.46}N$ film and Ti-Al-Cr-O for Cr containing films, could amplify the protection effect [66]. Moreover, the higher amount of Cr-O in the tribolayer of Cr containing coatings, which have been reported to have a lower coefficient of friction than Ti-O and Al-O oxides, is the origin of the reduction of the COF of Cr-rich films. Therefore, in spite of the lower hardness of Cr multilayered coatings, comparable wear rates were achieved

in relation to the $Ti_{0.47}Al_{0.46}N$ reference. The better performance of Cr-containing films can be interpreted as a combined effect of:

- i) better lubricious properties of the Cr-O phase formed on the wear track, and
- ii) the multilayer structure, which has been reported to be very efficient in obstructing or deflecting notch/crack propagation [67]. This effect was clearly demonstrated by Polcar who studied the tribological performance of multilayer CrAlTiN films with gradient interfaces [47].

For testing at 650 °C, significant differences could be observed between the reference and Cr-containing films. $Ti_{0.47}Al_{0.46}N$ showed a smooth wear track with scratches parallel to the relative sliding movement, suggesting an abrasion wear mechanism (see Figure 5-47 a). EDS analysis performed at the flat worn surface only revealed a low O content, suggesting that the oxides formed were continuously removed during the sliding process. Small oxidized wear debris particles could be sparsely found adhered to the wear track. On the other hand, an irregular surface with a mixture of smooth (polishing wear) and oxidized (signs of adhered material) wear zones was observed in the wear track of multilayered TiAlCrN films, as shown in Figure 6 b), revealing the incomplete formation of an oxide layer. EDS analysis carried out in the wear tracks (grey zones marked in Figure 5-47 b) for $Ti_{0.28}Al_{0.31}Cr_{0.51}N$ film which is representative of all the TiAlCrN films) confirmed that they were mainly composed of O, Ti, Al and Cr, suggesting the presence of Ti-O, Al-O, and Cr-O oxides. Signals from the Cr-O phase increased with increasing Cr concentration in the films, corroborating previous section 5.2.5.4 where the preferential formation of Cr_2O_3 over Al_2O_3 was observed.

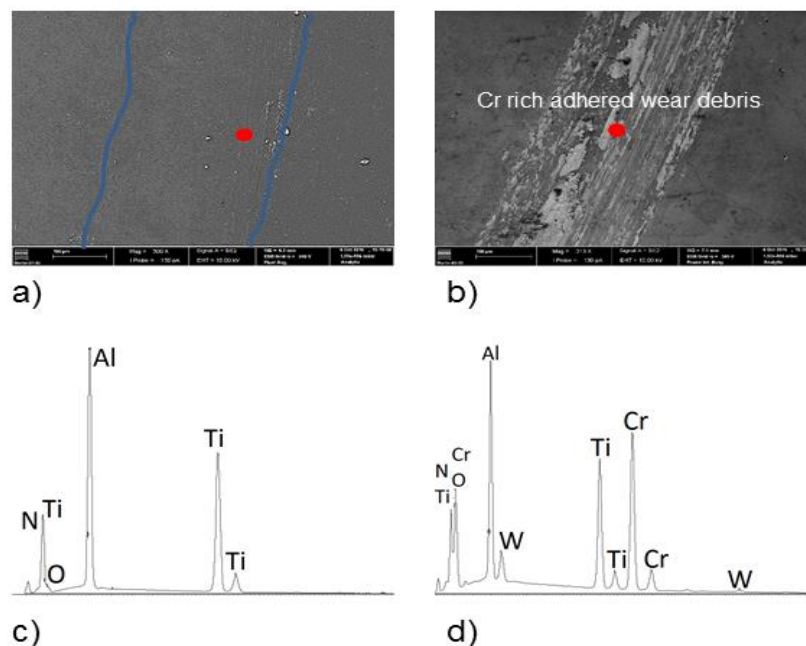


Figure 5-47 SEM pictures of the wear track of films tested at 650 °C. a) $Ti_{0.47}Al_{0.46}N$ reference, b) $Ti_{0.28}Al_{0.31}Cr_{0.51}N$ film

Based on these observations, one can deduce that for the better wear performance of TiAlCrN films over the $Ti_{0.47}Al_{0.46}N$ reference: (i) in case of Cr-containing coatings, Cr-O is preferentially formed over Ti-O and/or Al-O; (ii) oxides richer in Cr are known to have better lubricious properties than Al-O and Ti-O oxides; (iii) lower friction of the Cr-O based layers formed on Cr-containing coatings induces lower shear forces during sliding, which limits the removal of the adhered layer from the wear track; (iv) the oxides adhered to the wear track protect the surface from further wear; (v) the higher the Cr content, the higher the Cr-O formation, and the lower the coefficient of friction and the wear rate.

5.2.5.6 Cutting performance

Cutting tools were coated with the $Ti_{0.47}Al_{0.46}N$ reference, as well as the multilayer TiAlCrN coating with the best tribological performance ($Ti_{0.28}Al_{0.31}Cr_{0.51}N$ film), and their wear resistance was further investigated under high-speed dry drilling conditions. We should mention here that the uncoated WC tool was tested under identical conditions and failed almost immediately with a maximum of 9 holes produced. Table 5-5 plots the number of open holes as a function of the cutting speed.

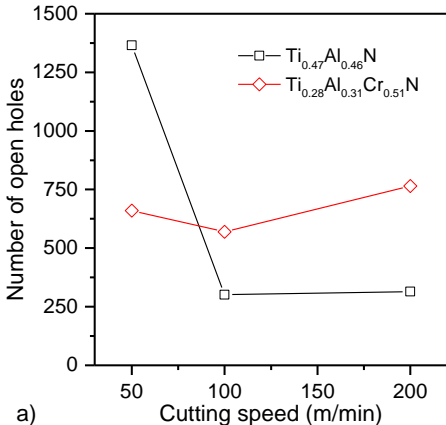


Figure 5-48 Number of holes as a function of cutting speed

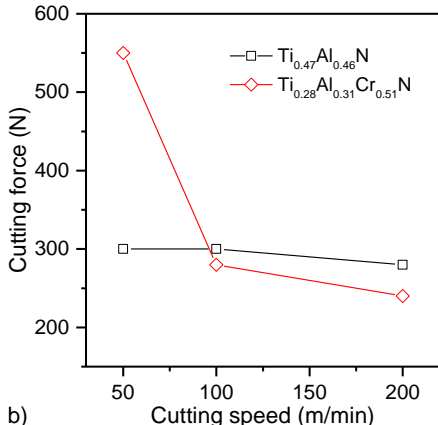


Figure 5-49 Number of holes as a function of average cutting force

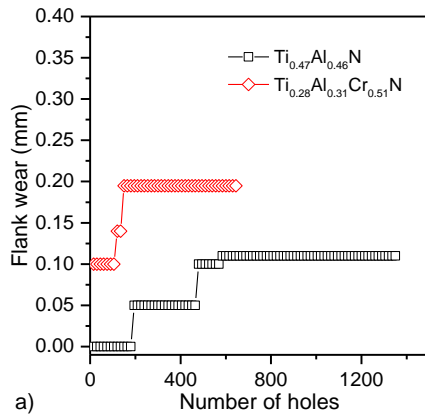


Figure 5-50 Flank wear evolution as a function of the number of drilled holes for a cutting speed of 50 m/min

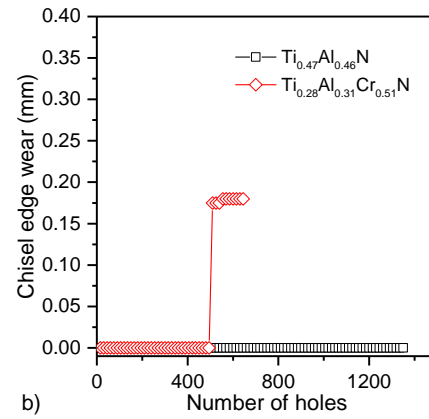


Figure 5-51 Chisel edge wear evolution as a function of the number of drilled holes for a cutting speed of 50 m/min

Sample	50 m/min	100 m/min	200 m/min
Ti _{0.47} Al _{0.46} N	1365	301	315
Ti _{0.30} Al _{0.46} Cr _{0.26} N	780	255	645
Ti _{0.28} Al _{0.34} Cr _{0.42} N	405	285	645
Ti _{0.28} Al _{0.31} Cr _{0.51} N	660	570	765

Table 5-5 Number of holes as a function of cutting speed.

For low cutting speed, the Ti_{0.47}Al_{0.46}N film outperformed the Cr-rich coating by a factor of 2. This agrees well with the lower cutting force measured during the test (see Figure 5-49) as well as with the lower flank and chisel wear, as shown in Figure 5-50 and Figure 5-51. Flank and chisel wear grew faster on the Ti_{0.28}Al_{0.31}Cr_{0.51}N film; consequently, the insert geometry is deteriorated, weakening the cutting edge and, thus, causing the premature failure of the tool. As Ti_{0.47}Al_{0.46}N is the hardest coating (at room temperature), its wear resistance during the drilling test with low cutting speed should be enhanced with respect to the Cr-containing multilayer coating. At such a low cutting speed, a discontinuous chip was always formed and, therefore, very high temperatures are not expected during the cutting process, as the majority of the heat goes into the chips and is dissipated via chip removal [68]. Thermal imaging showed a temperature of ~ 330 °C for Ti_{0.47}Al_{0.46}N and 370 °C for Ti_{0.28}Al_{0.31}Cr_{0.51}N, Figure 5-. Although the contact temperature is undoubtedly higher, these values are very low, and indicate a very low thermal load in the contact.

The higher temperature measured during the machining process arises from friction forces; this was higher for Cr-doped coatings, while the pin-on-disc measured COF was lower for Cr-doped coatings. This inconsistency can be explained by the different siding counterpart. The pin-on-disc was measured with an alumina ball, but the cutting was performed against hard steel.

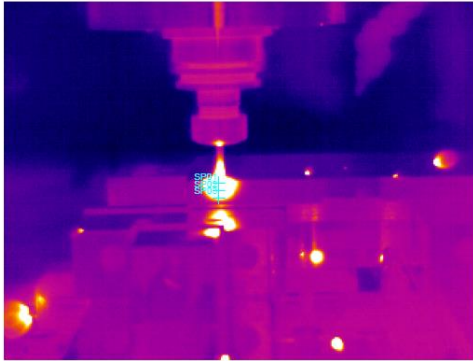


Figure 5-52 Image from thermal imaging camera of cutting at 50 m/min

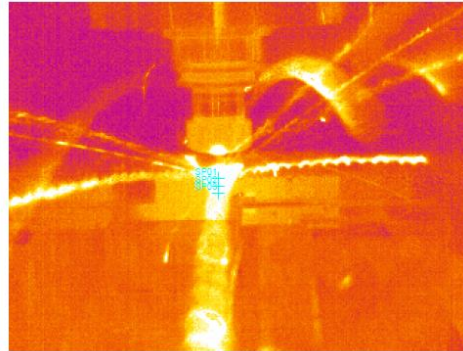


Figure 5-53 Image from thermal imaging camera of cutting at 200 m/min

Consequently, the hardness of the material should be the determining factor controlling the wear resistance at this cutting speed. Similar to what was observed in tribological testing, an abrasive wear mechanism on the cutting surface was observed at low-temperature testing for both films. Also, material from the counter body started to adhere at the cutting edge of the $Ti_{0.47}Al_{0.46}N$ drill after 75 holes.

In fact, this event, which is commonly referred to as 'build up edges' (BUE), has been reported to contribute to the degradation of cutting tool life. It acts as a third body, which promotes the adhesion between the cutting tool and the workpiece, and when the particles detach, the hard abrasive particles wear down the surface. Nevertheless, this should only occur if the detached particles are oxidized; if the adhered material is steel, which is much softer than the coating material, the opposite effect is observed, and the adhered layer protects the coating material. This should be the case in this work, since the O signal acquired at the adhered material by EDS is very low, suggesting that hard oxide particles can only be formed if the release of metal particles can occur, which are then oxidized in the contact.

Upon increasing the cutting speed to 100 m/min, an abrupt decrease of the drilling performance (~ 78% in the number of holes) occurred for the $Ti_{0.47}Al_{0.46}N$ film, whereas only a minor change (14%) was observed for $Ti_{0.28}Al_{0.31}Cr_{0.51}N$ films. Conversely, for the test at 50 m/min, the cutting force showed a slightly lower value for the Cr-rich coating, as for the latter three times as many holes could be drilled. Such behavior corroborates the tribological testing results at high temperature, where much lower wear rates were observed. The degradation of the cutting zone for the $Ti_{0.28}Al_{0.31}Cr_{0.51}N$ film is much slower than for the $Ti_{0.47}Al_{0.46}N$ reference,

as can be concluded from the chisel and flank wear evolution shown in Figure 5-52 and Figure 5-53.

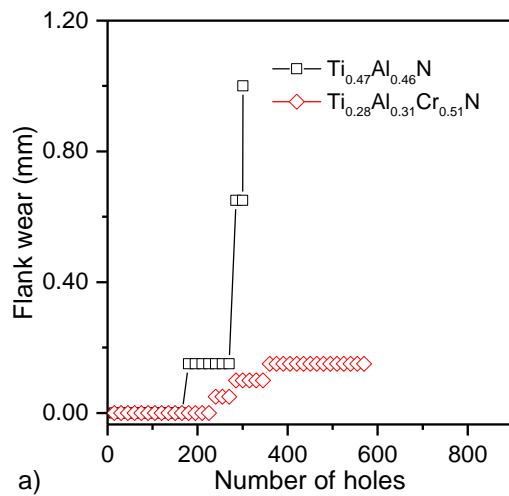


Figure 5-52 Flank wear evolution as a function of the number of drilled holes for a cutting speed of 100 m/min

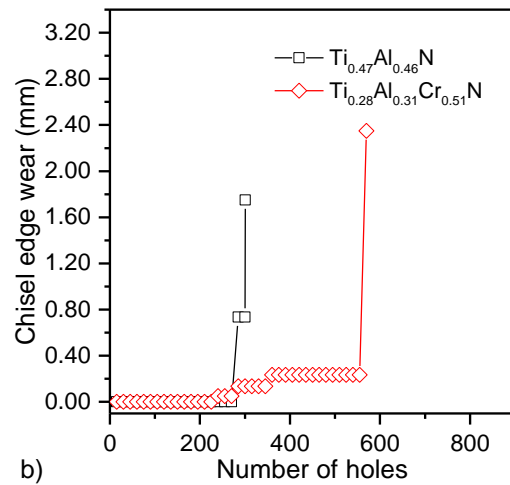


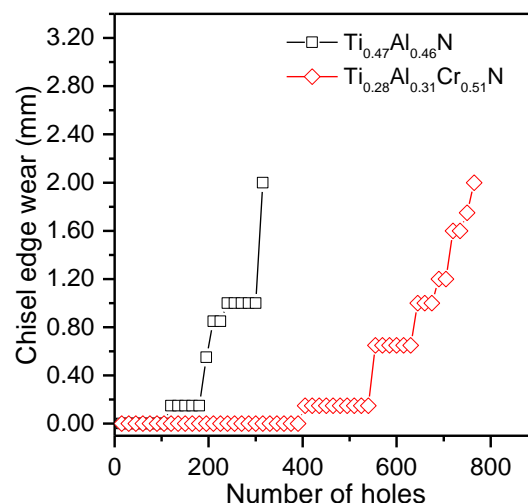
Figure 5-53 Chisel edge wear evolution as a function of the number of drilled holes for a cutting speed of 100 m/min



Figure 5-54 Setup of drilling tests with chip

A different chip type was observed during drilling tests at this cutting speed. After 15 and 240 drilled holes for $Ti_{0.47}Al_{0.46}N$ and $Ti_{0.28}Al_{0.31}Cr_{0.51}N$, respectively, a chip transformation from discontinuous to continuous was observed. The latter chip type will limit the release of the thermal energy, contributing to the heating of the cutting tool surface, and so is more deleterious for the reference coating. Thermal imaging showed a temperature of $\sim 450\text{ }^{\circ}C$ for the $Ti_{0.47}Al_{0.46}N$ film, and a slightly lower value for the coating containing Cr. Again, temperatures in the contact should be much higher, and tribo-oxidation of the coatings is now expected, with the formation of lubricious Cr-O on the cutting zone of the Cr containing coating, which would protect the film efficiently from wearing.

A further increase in the cutting speed to 200 m/min did not influence the drilling performance of the $Ti_{0.47}Al_{0.46}N$ reference; however, a significant improvement in some drilled holes (34%) was observed for $Ti_{0.28}Al_{0.31}Cr_{0.51}N$. It should be pointed out that the final number of holes is even higher than that achieved under much less severe cutting conditions (50 m/min). The trend described above for a cutting speed of 100 m/min, particularly for the cutting force, is further enhanced. The formation of a greater amount of oxide products in the cutting zone, caused by the increase of contact temperature (enhanced by both factors, higher cutting severity and continuous chip formed now from the very first drilled holes), protects the coating more efficiently from wear, which is well evidenced by an absence of the flank wear, and the slower evolution of the chisel edge wear, as shown in Figure 5-55 for both films. The chisel edge wear develops slowly and remains fairly low for a high number of holes, as compared to the tests performed at 100 m/min. Therefore, the cutting zone area remains higher for a longer period, extending the cutting performance of the drill. Harris et al. [69] also reported an increase of the cutting performance of TiCrAlN coatings under more aggressive cutting conditions (cutting speed increased from 38 to 51 m/min). The $Ti_{0.28}Al_{0.31}Cr_{0.51}N$ film showed a slower chisel wear evolution as a function of the number of drilled holes when compared to $Ti_{0.47}Al_{0.46}N$. We can conclude here that the nanolayered TiAlCrN coating outperforms the reference monolithic TiAlN at higher cutting speeds, and is thus more suitable for harsh dry sliding contact conditions. Finally, it should be emphasized, that in any of the tested cutting speeds, the uncoated WC carbide drill could never drill more than nine holes. Thus, any of the coated drill solutions has a much better cutting performance than the uncoated WC tools.



5.2.6 Conclusion – Cutting tools

There are several conclusions to be taken from this section. Concerning the multilayer morphology of the coating, a robust simulation technique was introduced and verified to help to design desired coating morphology. Depending on the sputtering rate, power applied to target, and the speed of the rotation table, it is possible to predict the amount and nature of the single layers in the multilayered coating. To obtain a coating with a regularly distributed multilayered structure, it is necessary to use a three-axis rotation table, otherwise the mutual dependency of the table and tower rotation will cause an elemental imbalance in the coating structure.

In the multilayered coatings, a higher amount of chromium lead to an increased deposition rate and to the increase of hardness of the coating. Also, the increase of Cr lead to higher intensity of the <200> peak, and a decrease in intensity of the <111> peak. The oxidation stability is also increased for a higher chromium content. Doping the TiAlN coating with chromium increased the onset point of oxidation by about 200°C, from 800°C to 1000°C. The reason for this is the formation of a protective Al-Cr-O layer under the Ti-O top layer. The Al-O protective layer formed by the TiAlN coating was not able to hinder Ti atom diffusion to the surface at a temperature of 900°C, whilst Al-Cr-O prevented diffusion much more effectively. The best oxidation resistance was observed for the $Ti_{0.28}Al_{0.31}Cr_{0.51}N$ coating, *i.e.*, that with the highest Cr content. The tribological testing at 650°C showed similar trends. The coatings containing more chromium showed extensive formation of a protective and lubricious Cr-O layer; the Cr-O layer outperformed Al-O and Ti-O, as formed by other compositions.

The cutting performance showed very interesting behavior. At a lower cutting speed (50 m/min) the TiAlN coating outperformed all of the Cr-doped coatings by more than a factor of two. At a high cutting velocity (200 m/min), $Ti_{0.28}Al_{0.31}Cr_{0.51}N$ outperformed the TiAlN coating again by a factor of two. These results correspond very well with the previously mentioned destruction of cutting tools. At lower cutting speeds, the hardness is the most important property to increase the cutting tool lifetime, but at high cutting speeds, especially without cooling, the ability to withstand high temperatures in an oxidizing atmosphere is more important. The main destruction process at high temperatures was driven by chisel edge wear. It was found out that during machining the cutting tools developed a protective layer of Cr-Al-O. In this case, the wear rate derived from pin-on-disc tests showed good correlation with the cutting performance. However, the higher temperature measured during the machining process, which arose from friction forces, was higher for Cr-doped coatings, while the pin-on-disc measured COF was lower for Cr-doped coatings.

5.3 Development of coating for aluminum high pressure die casting

5.3.1 Motivation

As was mentioned in section 4.3.2.3, there are two main failure mechanisms for HPDC, wash-out damage (caused by molten aluminum and alumina crystals, originating from oxidation in the furnace) and thermal fatigue checking (caused by low cycle fatigue in steel samples and an increase of stresses). Despite the high number of works reporting the improvement of the lifetime of HPDC dies, just a few have tested the tribological properties of aluminum and PVD coatings at high temperature, and the influence of the coating on heat checking resistance. Also, the effects of coating properties on the development of internal stresses are not clear. The first motivation for this section is to compare five coatings extracted from the literature as the most promising candidates for shielding steel against aluminum corrosion and other wash-out damage processes, as proposed by Lin [56]. Secondly, we determine the influence of different coating properties and the effect of nitriding the steel, on the development of internal stresses in the coatings caused by thermal cycling.

Also, I consulted with numerous companies concerning the problematics of HPDC and found out that same coating on the same core pins can have very different effects when applied to HPDC and rheolitic die casting, while the difference between these two processes is only the injection speed of the molten aluminum. Moreover, from industrial experience, it can be determined that the coating chemistry is not the only important factor influencing coating productivity, but also the deposition technique [53]. To ensure this, the objective of this section is to deposit all coatings using the same sputtering apparatus to avoid any problems concerning incomparable results from using different techniques (arc evaporation, sputtering), and to test all the coatings the same way with the possibility to compare the influence of basic material properties on the coating performance.

Although the service tests could provide more accurate information about the performance of the HPDC coated dies, it is time-consuming and not feasible for industry due to the very high cost. The tribological performance was investigated in order to check particular properties of the coating, namely: the adhesion of aluminum against coatings, abrasion resistance, and resistance against aluminum corrosion.

The experimental part is divided into two separate sub-experiments to determine the influence of the aforementioned effects on the general behavior of the coating. Part one deals with the design of inner bonding within an elastic layer (base layer), and the second one with the design of the outer contact layer (shield layer) [56].

5.3.2 Base layer development

For testing the thermal cycling stress, four chromium-containing coatings with different morphologies and mechanical properties were chosen. Moreover, most authors stress the need to use nitrided steel instead of un-nitrided [54]. To examine the importance and influence of nitriding on thermal stress behavior, the samples were deposited on plasma nitride samples, as well on the untreated. Figure 5-56 shows the test course of the coated test samples.

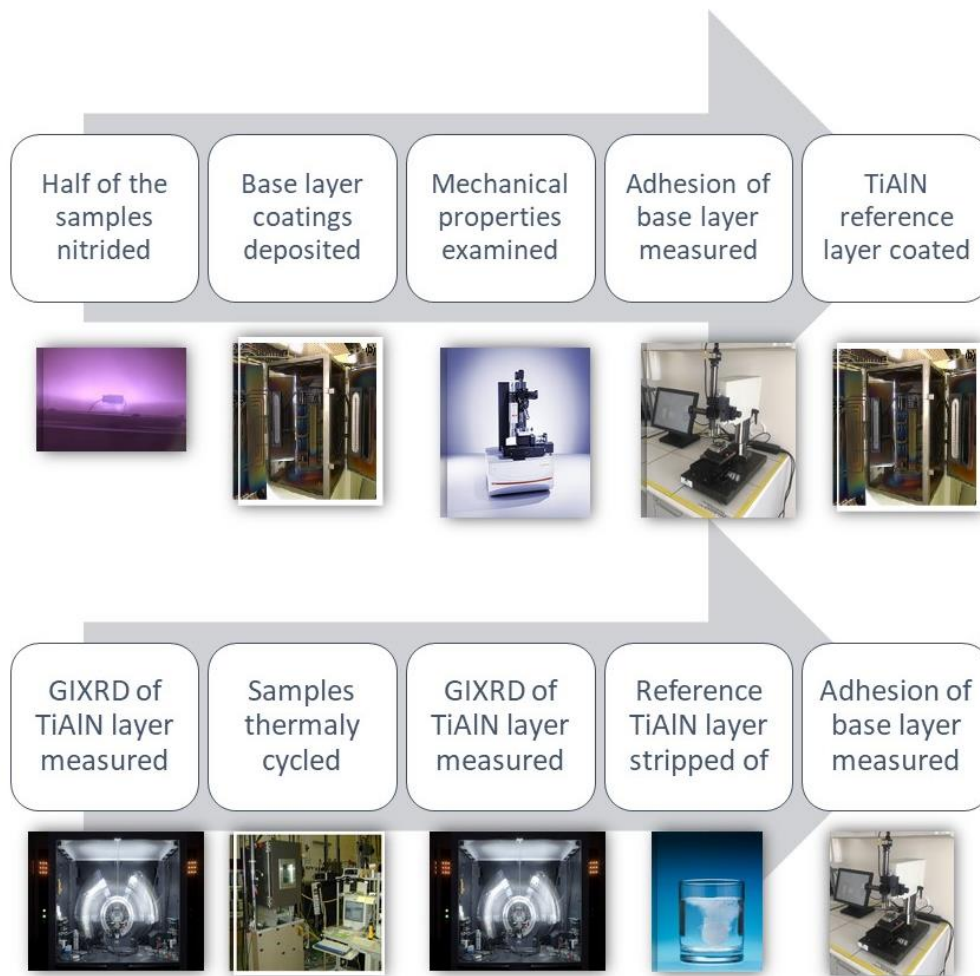


Figure 5-56 Test course of base layer

5.3.2.1 Testing samples

The substrates used were polished tool steel X153CrMoV12 test samples, with diameter 22 mm, and Dievar® (Chromium-molybdenum-vanadium steel; C 0,35%, Si 0,2%, Mn 0,5%, Cr 5%, Mo 2,3%, V 0,6%) steel blocks, which are common for aluminum die casting applications, with dimension 20x7x5,5 mm. Four of the Dievar samples were plasma nitrided for better orientation, and are hereafter labeled with “n-”. All blocks were polished on one side. In each

coating batch there was one nitrided and one unnitrided (labelled as “u-”) block, hung with double-fold rotation to assure an even distribution of the coating.

5.3.2.2 Sputtering process

The coatings were sputtered from Al₇₀Cr₃₀, Al₆₀Cr₃₀Ti₁₀, Cr and TiAl (Ti target with 48 Al plugs along the racetracks) targets. All coatings were sputtered in an Ar:Kr:N₂ atmosphere, with the inlet flow of the gasses set to 220, 50 and 65 sccm respectively. All four coatings had a Cr adhesion layer and a CrN transient layer. The MF substrate bias was kept at -50 V, and the deposition temperature at 300°C. The multilayered CrN/TiAlN coating consists of 40 multilayers, where first 20 are CrN-rich, and the last 20 are TiAlN-rich. Details are shown in Table 5-6 Sputtering conditions for base layer.

Sample designation	AlCrN	AlCrTiN	CrAlTiN	mCrN/TiAlN
Multilayered period thickness (nm)	-	-	-	39
Power applied to target TiAl ₄₈ (W)	-	-	-	7000
Power applied to target Al ₆₀ Cr ₃₀ Ti ₁₀ (W)	-	6000	5000	-
Power applied to target Al ₇₀ Cr ₃₀ N (W)	5000			
Power applied to target Cr (W)	3000	1000	3000	5000
Substrate temperature (°C)	300	300	300	300
RF substrate bias (V)	-50 V (250 kHz)			

Table 5-6 Sputtering conditions for base layer

5.3.2.3 Coating evaluation

After deposition, adhesion was evaluated using a Scratch tester and the Rockwell adhesion test. Mechanical properties were evaluated using a nanoindenter. After these tests, the Dievar blocks were prepared for coating again, and coated with a 2 µm-thick reference TiAlN layer acting as a measuring layer. The architecture of the final coating on the block is shown in Figure 5-57.

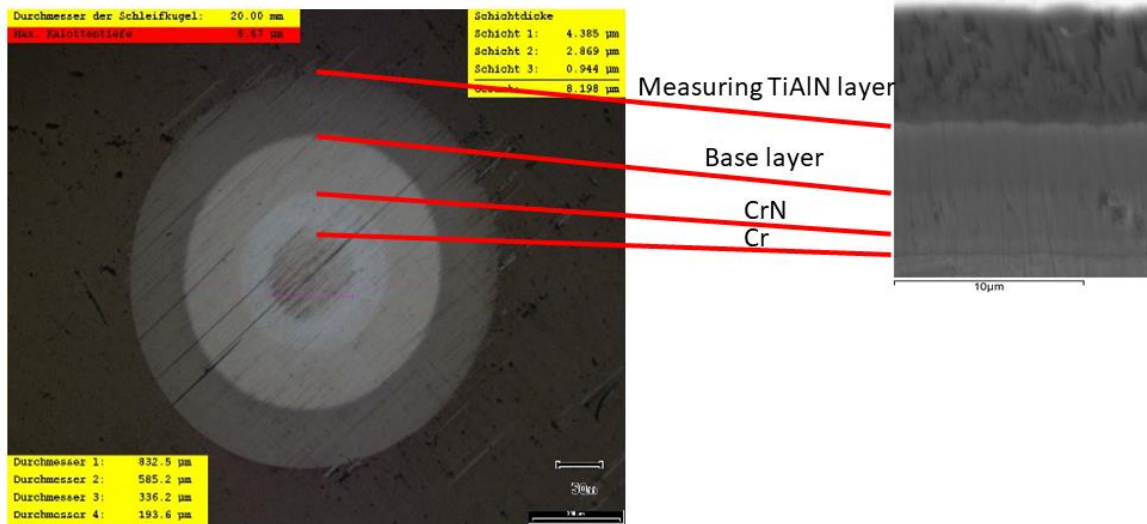


Figure 5-57 Calotest cross section and SEM cross section of base layer architecture

The TiAlN measuring layer was measured by GIXRD, scanning only the TiAlN layer and not the base coating. After the reference measurement, the samples were subjected to the thermal cycling on an MTS 880 servo-hydraulic testing machine for thermo-mechanical fatigue, which should copy the thermal conditions used in the aluminum die casting process. The cycling was performed 100-times as [56] showed is a sufficient amount of cycles to reach the maximum level of stress in the coatings.

After the thermal cycling, the samples were again measured by GIXRD, with the same conditions as for the determination of the level of stress accumulated in the coating. Then the TiAlN measuring coating was stripped down in a solution of hydrogen peroxide, which dissolves the TiAlN coating but not Cr-based coatings. Again, scratch and Rockwell adhesion tests were performed on the Dievar blocks with the same conditions, to see the change in adhesion prior to and after the thermal cycling.

5.3.3 Shield layer development

The tribological performance was compared for these coatings: AlTiN, CrAlTiN, AlTiSiN, AlCrTiSiCN and $(CrAl)_2O_3$). As was summarized in section 4.3.2.3, these coatings have the potential to be used for protecting the surface of HPDC molds. The coatings were tested by pin-on-disc sliding against aluminum at room temperature, and more importantly at high

temperature (650 °C), aiming to reproduce as close as possible the interaction between aluminum and the HPDC die surface, in order to rank their applicability as a coating material. The base layer testing course is shown in Figure 5-58.

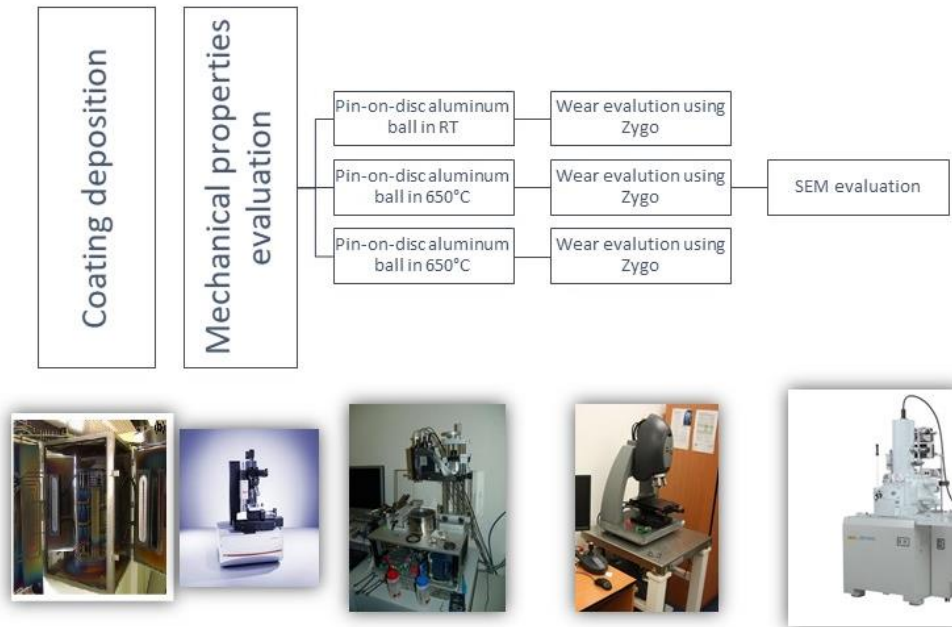


Figure 5-58 Shield layer development course

Aluminum balls could reproduce the interaction occurring in the die surfaces due to its melted state at high temperature. The same is true for tribological tests with a harder and more resistant counterpart (Al_2O_3 balls), which ensure that the wear volume loss of coatings will be overestimated in relation to the expected loss in actual service conditions.

There were three main characteristics inspected: a) adhesion to aluminum – measuring the coefficient of friction against aluminum in room temperature b) resistance against abrasive wear at high temperature – sliding against alumina ball at 650°C c) Resistance against molten aluminum corrosion– sliding with aluminum ball at a temperature of 650°C.

5.3.3.1 Sputtering process

The coatings were deposited on polished, round, 22 mm tool steel samples, which were ultrasonically cleaned prior to deposition. There were five different coatings deposited on the same sputtering machine, using two of the four sputtering sources in total. The deposited coatings were TiAlN, $(\text{AlCr})_2\text{O}_3$, CrAlTiN, TiAlSiN and TiAlCrSiCN. The deposition parameters are reported in Table 5-7.

Power applied to target (kW)											
	Adhesi on layer	Working gas flow (mln)	Reactive gas flow (mln)	Bias (V)	Depositi on time (min)	TiAl4 8	Al60Ti 40	Cr	Al60Cr30Ti10	TiSi 23	Al70Cr30
AlTiN		240	130	40	180	7	7				
CrAlTiN	CrN	240	110	50	60			3	6		
AlTiSiN	AlTiN	240	133	40	150		7			5	
CrAlTiSiCN	CrAlTiN	170	143	60	180				5	6	
(CrAl) ₂ O ₃	CrAlN	245	52	30	180			4.3			5

Table 5-7 Deposition parameters for shield coating

5.3.3.2 Coatings evaluation

After deposition, brief characterization, *i.e.*, adhesion, hardness, and thickness testing, was carried out. The coatings were then tested using a high-temperature pin-on-disc tribometer, which has been used as a standard method to evaluate the interaction between the coating and the counterpart. The tribological tests were performed against an aluminum ball at room temperature and at 650°C. The pin-on-disc test using an alumina ball was performed in 650°C.

The wear tracks of the coatings, caused by aluminum and the alumina ball, were inspected by Zygo 3D profilometer to determine the wear rate, wear profile, and character of the damage. To characterize and determine the cause of tribological behavior, samples tested at 650°C with an aluminum ball were inspected by SEM, and EDS analyses of the wear track was performed.

5.3.4 Results and discussion – High pressure die casting

5.3.4.1 Base layer characterization

5.3.4.1.1 Chemical composition and mechanical properties

The elemental chemical composition measured by EDS is shown in Table 5-8, along with hardness, Young elastic moduli, H/E ratio, and H³/E² ratio. In all coatings, except mTiAlN/CrN, there is a lower amount of nitrogen than the 50% necessary to form a proper solid solution. This was also observed in our previous study (section 5.1.3).

The highest hardness was measured for the mTiAlN/CrN coating with the multilayered nanostructure. This can be explained by the multilayer hardening effect, as discussed in section 3.7.1. The highest H/E and H³/E² ratios were present for the AlCrN coating, followed by the AlCrTiN coating. It is expected that the coatings with a higher H/E and H³/E² ratio, often associated with toughness [37], will have the best resistance against thermal fatigue, as they

should be able to accommodate stresses elastically with the least amount of boundary movement.

	T	H	E	H/E	H³/E²	Al	Cr	Ti	N
AlCrTiN	8.2	19.7	238	0.82	0.135	35.1	19.83	5.46	39.6
CrAlTiN	7	22.6	308	0.73	0.122	36.83	36.42	3.18	36.8
mTiAlN/CrN	5.2	25.2	361	0.7	0.123	6.69	27.64	11.47	53.28
CrAlN	5.6	22.7	275	0.83	0.154	29.64	37.33	x	33.03

Table 5-8 Chemical and mechanical characterisation of base layer coatings

5.3.4.1.2 Adhesion

Results from the Rockwell adhesion test and scratch test before (ad) and after thermal cycling treatment (tt) are shown in Table 5-9. Each value is calculated as the mean of two measurements. Lc2 force was chosen as the main criterion for scratch test failure. Coatings with Lc2 higher than 50 N are highlighted in the table because coatings with adhesion lower than 50 are not usable in industrial applications, and so are not considered hereafter.

	Lc2 ad	Lc2 tt	Loss of adhesion
u- AlCrTiN	67	62	5
n- AlCrTiN	73	39	34
u- CrAlTiN	10	15	-5
n- CrAlTiN	46	59	-13
u- mTiAlN/CrN	100	28	72
n- mTiAlN/CrN	24	2,5	21,5
u-CrAlN	38	31	7
n-CrAlN	51	19	32

Table 5-9 Adhesion testing results of as-deposited samples (AD) and thermally treated samples (TT)

The lowest loss of adhesion (Lc2 ad – Lc2 tt) was measured for u-AlCrTiN, followed by n-CrAlN and n-AlCrTiN, for both nitrided and unnitrided blocks. Interesting behavior is seen for the CrAlTiN coatings, where the adhesion increased for both the nitrided and unnitrided form. This effect can likely be attributed to the nature of scratch testing, where determination of the Lc value is the main subjective criterion. Nevertheless, the u-AlCrTiN coating exhibits the highest adhesion after thermal testing, and multilayered TiAlN/CrN coatings exhibit the worst,

even if the multilayered u-TiAlN/CrN coating had the best adhesion in the as-deposited state. This is same behavior that was seen by the multilayered coatings in section 5.2.5.3.2.

5.3.4.1.3 Stress analysis

Figure 5-59, Figure 5-60, Figure 5-61 and Figure 5-62 present XRD patterns of TiAlN coatings deposited on top of the base layer in the as-deposited state and thermally treated state. For all coatings, there are (111) and (200) peaks visible, and in both states all coatings showed preferential (111) orientations. All thermally treated samples exhibit an XRD shift to higher angles, indicating an increase of tensile stress. These results are in good agreement with [56] and [70].

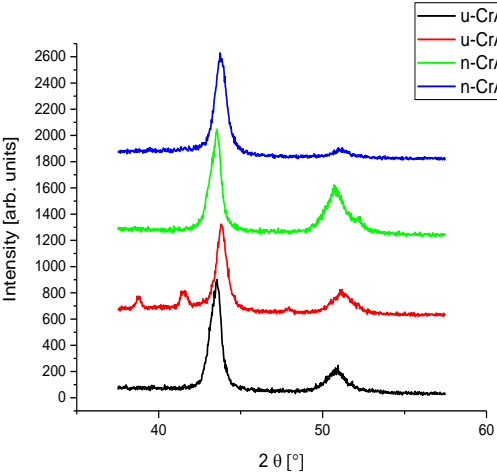


Figure 5-59 XRD spectra of CrAlTiN coating

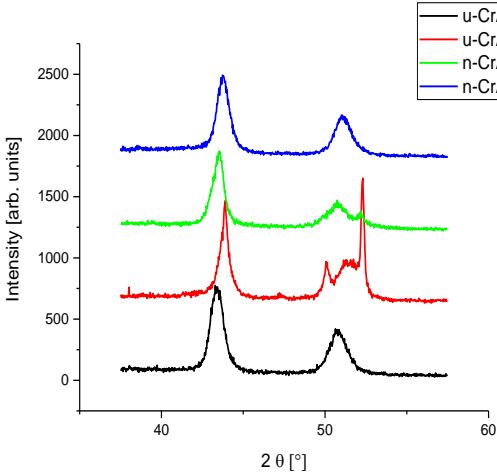


Figure 5-60 XRD spectra of CrAlN coating

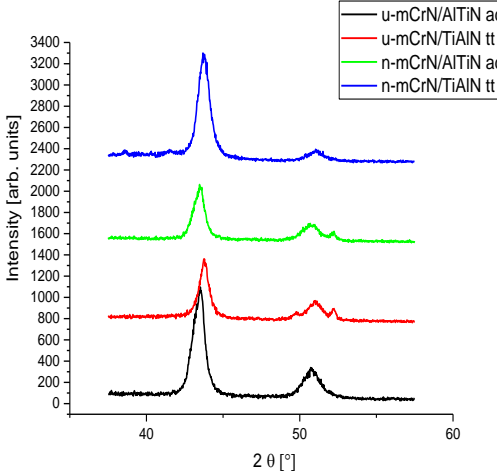


Figure 5-61 XRD spectra of mCrN/TiAlN coating

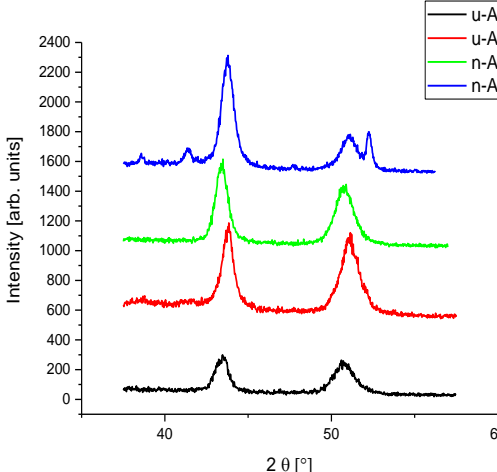


Figure 5-62 XRD spectra of AlCrTiN coating

Table 5-10 Position of (111) of TiAlN coating deposited on different coatings as-deposited and thermally treated with corresponding stress change. Peak positions have been determined by a Gaussian peak search, performed using the Origin analysis software.

The lattice constant a was derived using Bragg's law, and the difference, Δa , was added to Equation 5-4 in order to compute the difference in internal stresses in the as-deposited coating and in the thermally treated coating.

$$\Delta\sigma = \frac{\Delta a}{a_{ad}} * \frac{1 + \nu}{E}$$

Equation 5-4

Where σ is the biaxial stress, a_{ad} is the lattice parameter of as-deposited coating, ν is Poisson ration, and E is the elastic modulus of TiAlN.

	ad	tt	Δ [°]	Δa [nm]	$\Delta \sigma$ [GPa]
	(111) [°]	(111) [°]			
u-AlCrTiN	43.4155	43.7686	0.3531	0.03217	2.07
n-AlCrTiN	43.4095	43.7655	0.356	0.03244	1.78
u-CrAlTiN	43.4771	43.8309	0.3538	0.03214	2.07
n-CrAlTiN	43.4721	43.7763	0.3042	0.02767	2.08
u-mCrN/AlTiN	43.4168	43.759	0.3422	0.3119	2.00
n-mCrN/AlTiN	43.066	43.7427	0.312	0.02843	1.83
u-CrAlN	43.4	43.8531	0.4533	0.04123	2.65
n-CrAlN	43.4686	43.7645	0.2959	0.02693	1.73

Table 5-10 Position of (111) of TiAlN coating deposited on different coatings as-deposited and thermally treated with corresponding stress change

As for the individual coatings, CrAlN exhibits the lowest tensile stress level change after thermal treatment (1,73 GPa) for the nitrated sample, as well as the highest stress increase for the un-nitrated sample (2,65 GPa).

During the hot phase of the thermal cycling test, the coating is under compressive stress. This stress comes from a lower thermal expansion coefficient (7.5×10^{-6}) than the tested steel (13.3×10^{-6}). Mitterer et al. [70] measured the increase of compressive stress during thermal cycling for TiN, and at 650°C it was about 0.1 GPa higher. Due to the compressive stress during the hot period, local plastic deformation can occur. Plastic deformation is driven by lattice defect relaxation and grain boundary sliding, the latter leading to nucleation sites for

microcracks. During the cold period, tensile stresses are applied to the coating, as the surface chills faster than the bulk, and a temperature gradient is formed. After the coating is cooled to the starting temperature, it exhibits more tensile stress than in the as-deposited state, proving that plastic deformation took place, as explained in section 3.6.3.

The stress is increased with every new cycle, up to a point where the accumulated stresses get relaxed with the onset of microcracks. This point usually appears in the first 100 cycles [56] [71]. As the plastic deformation is the primary driving force for the formation of stresses, more ductile coatings are suggested by different authors [70] to have better heat-checking resistance and lower accumulated stresses, leading to cracks.

To prove the effect of the amount of accumulated stress on mechanical properties, different material properties (H, E, H/E, H/E² and H³/E²) were correlated against the measured tensile stress increase in the coatings. The standard MS Excel statistical toolbox was used to perform the correlation. The results are shown in Table 5-11 Material properties correlated with tensile stress change

	<i>H/E</i>	<i>H3/E2</i>	<i>nitrided</i>	<i>H</i>	<i>E</i>	<i>Unnitrided</i>
<i>H/E</i>	1,00					
<i>H3/E2</i>	0,81	1,00				
<i>nitrided</i>	0,93	0,91	1,00			
<i>H</i>	-0,79	-0,28	-0,57	1,00		
<i>E</i>	-0,94	-0,56	-0,77	0,95	1,00	
<i>Unnitrided</i>	0,71	0,92	0,71	-0,22	-0,49	1,00

Table 5-11 Material properties correlated with tensile stress change

Only a strong correlation (>0,9) was found for the H/E ratio in nitrided samples, and the H²/E³ ratio for both nitride and untreated samples; both are plotted on Figure 5-63 and Figure 5-64.

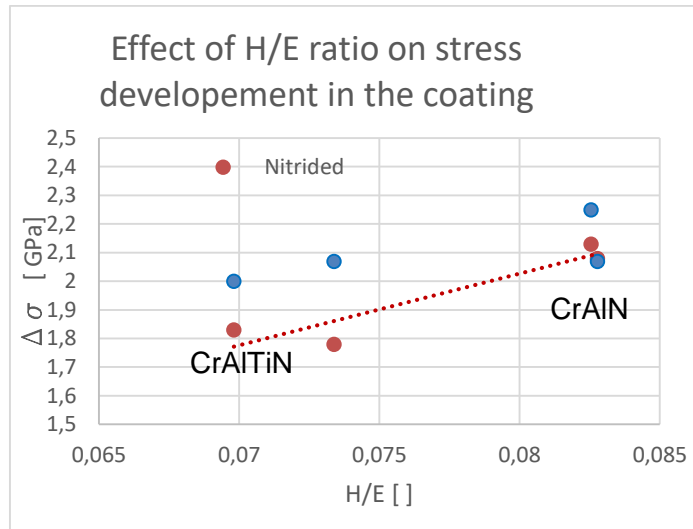


Figure 5-63 Effect of H/E ratio on stress development in the coating

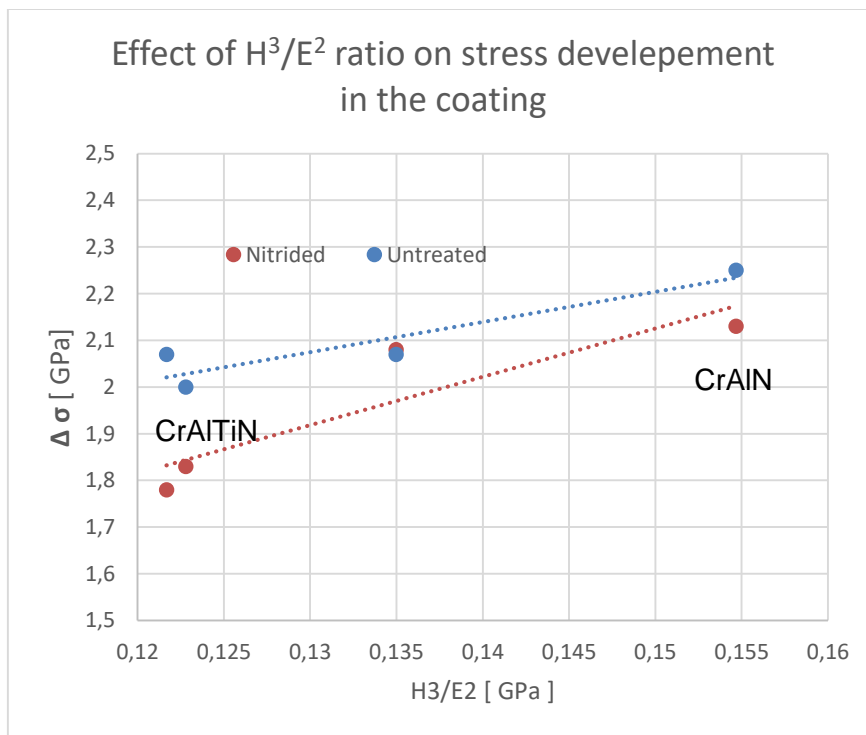


Figure 5-64 Effect of H^3/E^2 ratio on stress development in the coating

As explained in section 3.7.3, the H/E ratio characterizes the resistance of the material to elastic deformation, while the H^3/E^2 ratio represents the ability of a material to dissipate energy at the onset of plastic deformation during loading. According to this, lower stresses will be accumulated in coatings with a lower H^3/E^2 ratio, as the coating has a lower tendency to plastic deformation.

5.3.4.2 Shield layer

5.3.4.2.1 Chemical composition, mechanical properties and morphology of the films

Table 5-12 displays the chemical composition of the coatings measured by EDX, the thickness, hardness, and Young's modulus of the coatings, as well as the adhesion critical loads. All the coatings displayed a stoichiometric composition with N (in the case of nitrides) and O (in the cases of oxides) slightly higher than 50 at.%. The AlCrSiTiCN coating exhibits a large excess of non-metal elements, but its precise characterization is not the goal of this study.

	AlTiN	AlTiSiN	CrAlTiN	AlCrSiTiCN	(CrAl) ₂ O ₃
Chemical composition	Al-26.53 Ti-18.98 N-54.49	Al-11.12 Ti-31.4 Si-3.01 N-54.46	Al-18.16 Ti- 2.51 Cr-26.4 N-53	Al-14 Ti-1.96 Cr-7.68 Si-2.18 C-11.1 N-63	Al-11 Cr-32 O-57
Thickness	1.84	1.6	1.8	1.5	2.8
Hardness [GPa]	30.3 ± 3	25.8 ± 4	29 ± 4	28.9 ± 3	28 ± 7
Young's modulus [GPa]	407 ± 37	297 ± 44	361 ± 47	367 ± 31	354 ± 54
Critical load LC2 [N]	72	90	76	53	77

Table 5-12 Chemical composition in at% measured by EDX and mechanical properties

All coatings displayed very good adhesion in both the Mercedes test and scratch test. The HF value was always HF1 or HF2. All coatings showed very good first coating chipping critical load (Lc2), revealing the strong adhesion of the coatings to the substrate.

All coatings displayed a comparable hardness and Young's modulus (in the range of H: 26- 30 GPa and E: 354-407 GPa), ensuring reasonable mechanical properties for the good wear behavior of the films in service. The highest hardness was measured for the CrAlTiN coating, followed by CrAlTiSiCN and (CrAl)₂O₃.

Figure 5-65 shows a cross section of the (CrAl)₂O₃ coating. The (CrAl)₂O₃ coating shows a columnar morphology, proving that the column shape originated from the adhesive CrAlN layer. Due to the hardness of the coating and the columnar structure, it is non-amorphous. The rest of the coatings exhibited a columnar structure similar to the coatings shown in section 5.2.5.2.

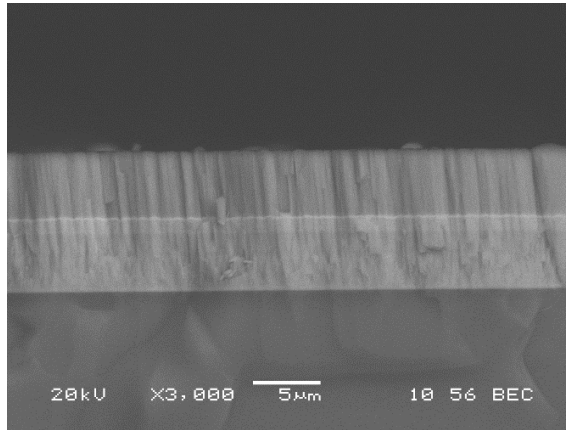


Figure 5-65 SEM cross-section of $(CrAl)_2O_3$ coating with AlCrN adhesion layer

5.3.4.2.2 Tribological properties

Figure 5-66 shows the coefficients of friction for all coatings against different balls and temperatures. In general, the highest coefficient of friction was recorded during sliding against aluminum at 650°C, while the lowest was for sliding against an Al_2O_3 ball.

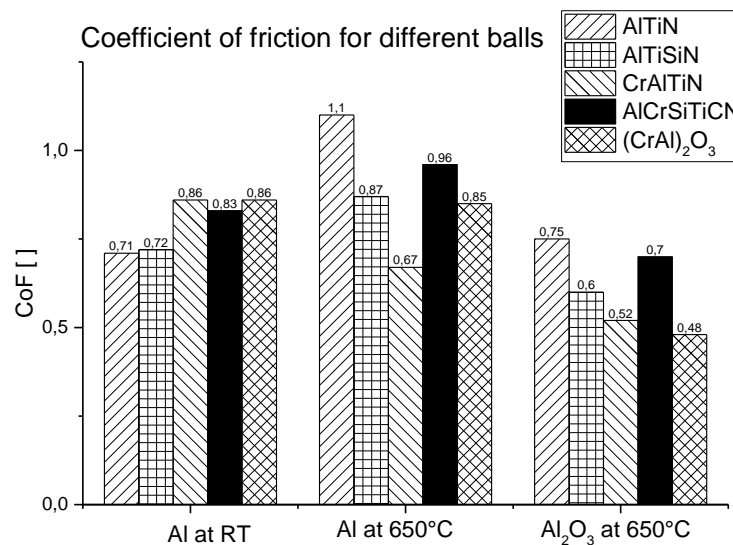


Figure 5-66 Coefficient of friction for aluminum balls at RT and 650°C, and for an alumina ball at 650°C against the coatings

5.3.4.2.2.1 The coefficient of friction against the aluminum ball at room temperature

The evolution of the coefficient of friction during sliding of the aluminum ball at room temperature (RT) is shown in Figure 5-67, along with the steady-state values. The evolution of the coefficient of friction for all coatings followed the same behavior. The running in period

lasted 1000 cycles, where the COF exponentially increased from a value of about 0.3 to its steady-state value. The lowest COF was found for the AlTiN and AlTiSiN coatings at 0.71 and 0.72 respectively, while the other coatings had a near-similar coefficient of friction about 15% higher. CrAlTiN, CrAlTiSiCN and $(\text{CrAl})_2\text{O}_3$ all exhibited higher friction against an aluminum ball, as they all contain Cr.

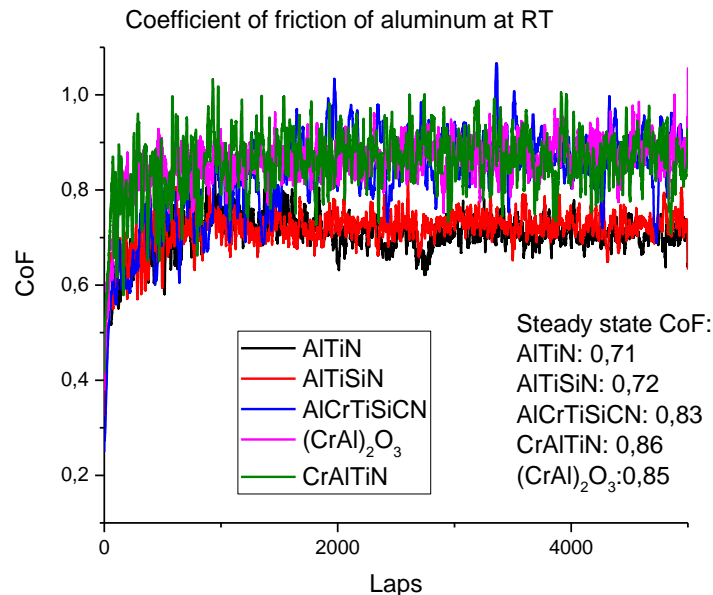


Figure 5-67 Evolution of the coefficient of friction for an aluminum ball at RT

5.3.4.2.2.2 The coefficient of friction against the aluminum ball at 650°C

Figure 5-68 shows the development of the COF during the sliding of the aluminum ball at 650°C. For a better representation, the data was smoothed. The coefficient of friction (COF) of the films was quite stable for all films except $(\text{CrAl})_2\text{O}_3$. The COF of $(\text{CrAl})_2\text{O}_3$ fluctuated from 0.5 to 1.2 during the measurement, and for the last 1000 laps settled at the value 0.75. M. Vilaseca et al. [72] connected this behavior with the high adhesion of aluminum and its compounds to the surface, and the forming and spalling of the transition layer. This adhered layer was found on 3D scans of the wear tracks, as shown in the following section. The $(\text{CrAl})_2\text{O}_3$ coating was the only one with this transition layer, and a fluctuation of the coefficient of friction. Thus these results are in good agreement with one another.

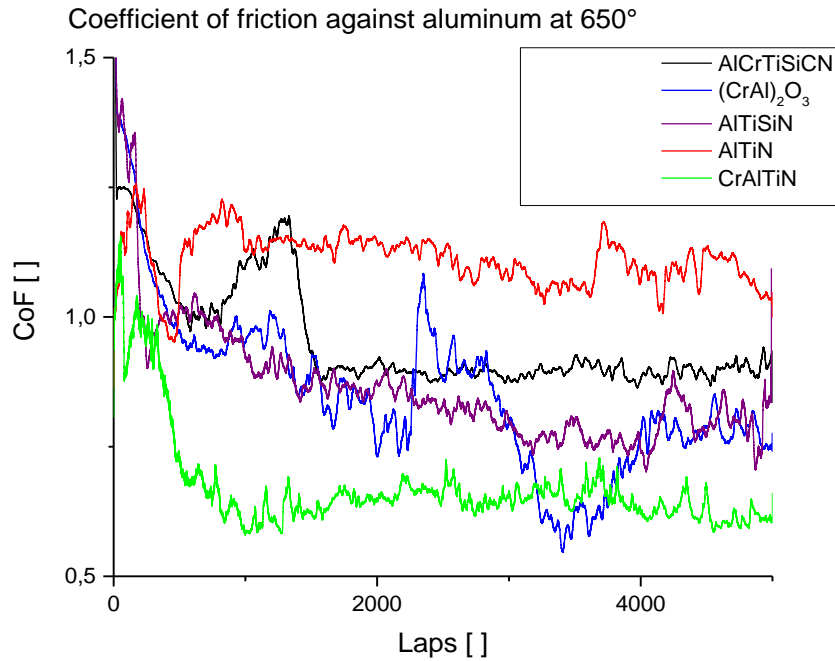


Figure 5-68 Evolution of coefficient of friction for aluminum ball at 650°C

Two regions of the COF evolution can be distinguished: the running in and the steady state. For all coatings except TiAlN, the running in COF was significantly higher than in the steady state. The running in phase lasted around 500 laps, after which the COF for TiAlCrSiCN, TiAlCrN and TiAlSiN was stabilized at the steady-state value. The drop of the COF after the running in period is associated with abrasion and plastic deformation of the aluminum ball at 650°C. This temperature is close to the melting point of aluminum (660,3°C), so the ball was brushed out during this period, as shown in Figure 5-69. After the running in phase, there was an equilibration phase, and the COF was led by adhesion forces of aluminum against the coatings. The lowest COF at high temperature was measured for CrTiAlN, and the highest for the AlTiN coating.



Figure 5-69 Damaged aluminum ball after test

	Point	Al	Cr	Ti	N	O
CrAlTiN wear track	1	26	33,5	3,1	23,8	13,6
	2	50,2	3,1			46,6
	3	55,3	1,3	1	29,5	12,8

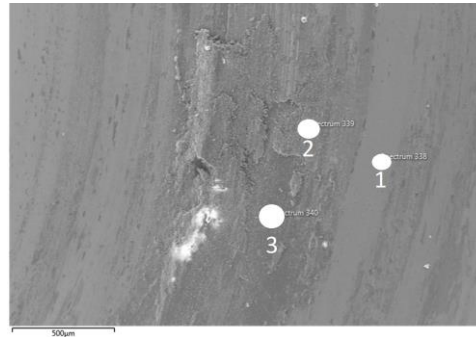


Figure 5-70 Wear track of CrAlTiN coating scanned by SEM

	Point	Al	Cr	Ti	N	O
AlTiN wear track	1	26,2		20,3	41,5	10
	2	39,3		0,6		60,1

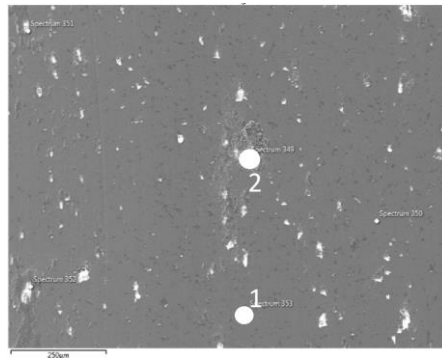


Figure 5-71 Wear track of AlTiN coating scanned by SEM

	Point	Al	Cr	Ti	N	O
CrAlTiN ball	1	68,9	0,3			30,8
	2	86,3				13,7

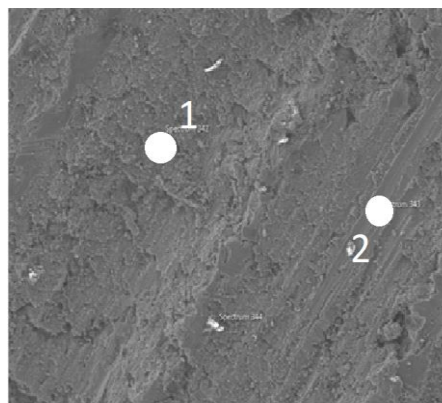


Figure 5-72 Ball surface after sliding on CrAlTiN coating scanned by SEM

	Point	Al	Cr	Ti	N	O
AlTiN ball	1	42,8		1,1		56,1
	2	76,9				23,1

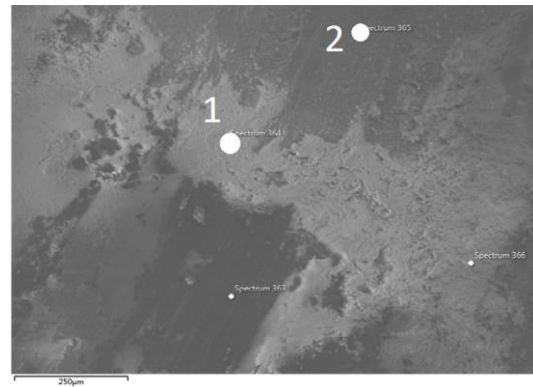


Figure 5-73 Ball surface after sliding on AlTiN coating scanned by SEM

Table 5-13 Chemical compositions of different areas in corresponding wear tracks and ball surfaces

Figure 5-70 and Figure 5-71 show SEM images from the wear track of the coatings, and the worn area of the aluminum ball. Elemental compositions measured by EDX are summarized in Table 5-13 Chemical compositions of different areas in corresponding wear tracks and ball surfaces.

As can be seen, the center of the wear track of the CrAlTiN coating is almost completely a fully-oxidized AlO_x oxide layer, while on the borders of the wear track there is a significant amount of the nitride coating. The formation of the protective layer on TiAlCrN at these temperatures was shown in section 5.2.5.4. The wear track of the AlTiN coating shows only very small islands of AlO_x , displayed as white dots on the SEM image, and most of the wear track is the original nitride coating. The ball scars for both coatings show aluminum oxides across the entire surface. Thus, the surface chemical composition of the tribological coating – ball (pair) changed during sliding to AlO_x vs AlO_x for CrAlTiN coating and AlTiN vs. AlO_x for AlTiN coating. The formation of aluminum oxide on top of CrAlTiN facilitates a lower coefficient of friction. The lower coefficient of friction of the oxide – oxide contact correlates very well with the results discussed below.

5.3.4.2.2.3 The coefficient of friction against alumina ball

Figure 5-74 shows the behavior of the coefficient of friction against the Al_2O_3 ball at 650°C . The variation in the coefficient of friction of the coatings was in general much smoother than for the aluminum ball. This can be associated with a weaker interaction between the hard, stable alumina ball and the coatings. The lowest coefficient of friction was measured for the

(CrAl)₂O₃ coating and the highest for the AlTiN coating. This confirms the reason for the low coefficient of friction of CrAlTiN against the Al ball, as discussed earlier.

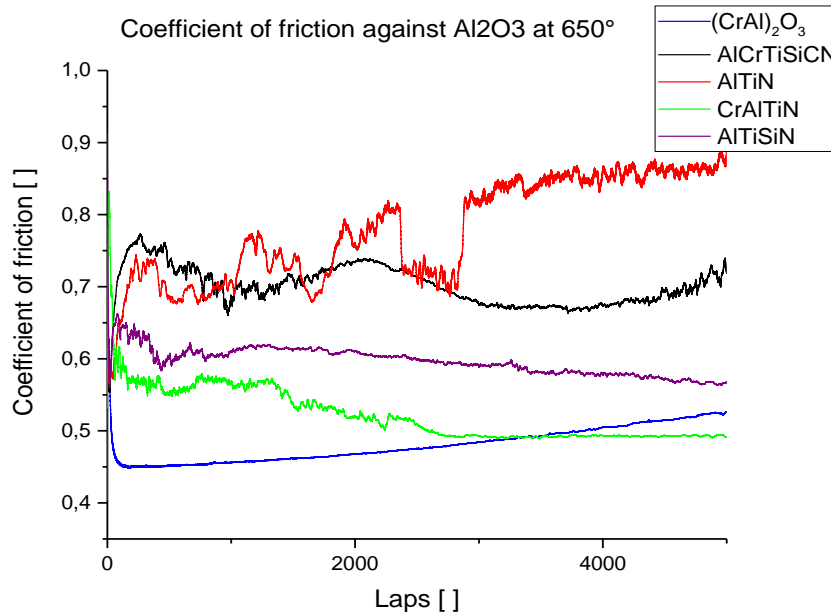


Figure 5-74 Evolution of coefficient of friction for Al₂O₃ ball at 650°C

5.3.4.2.3 Wear rate

The wear rates of the coatings against aluminum and the alumina ball at 650°C are shown in Figure 5-76 and Figure 5-75. In both cases, the wear rate was lowest for the (CrAl)₂O₃ coating and highest for the AlCrSiTiCN coating. The other coatings showed almost similar wear rate. The wear rates of AlTiN, AlTiSiN and CrAlTiN coatings are quite comparable, taking into account the error bars.

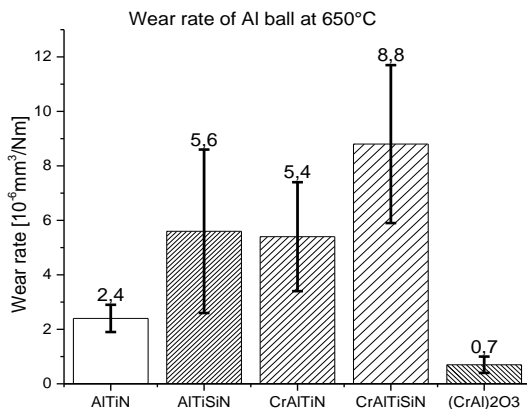


Figure 5-76 Wear rate of coatings tested against aluminum ball at 650°C

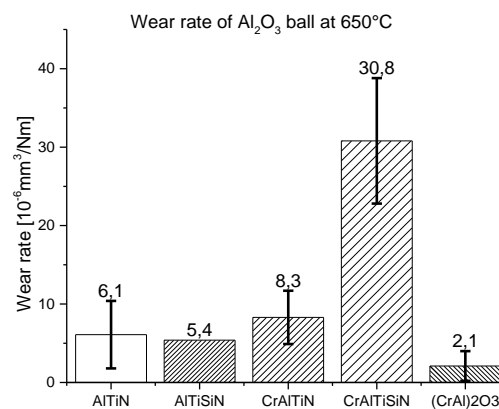


Figure 5-75 Wear rate of coatings tested against Al₂O₃ ball at 650°C

5.3.4.2.3.1 Wear rate and wear mechanism against the aluminum ball

Figure 5-78 – Figure 5-81 display the 3D scan of the wear track of the tested coatings after testing with the aluminum ball. For the TiAlCrN, TiAlN and TiAlSiN coatings, a clear deep groove in the wear track is evident. This defect is also visible, and confirmed, on the 2D wear profiles shown on Figure 5-77.

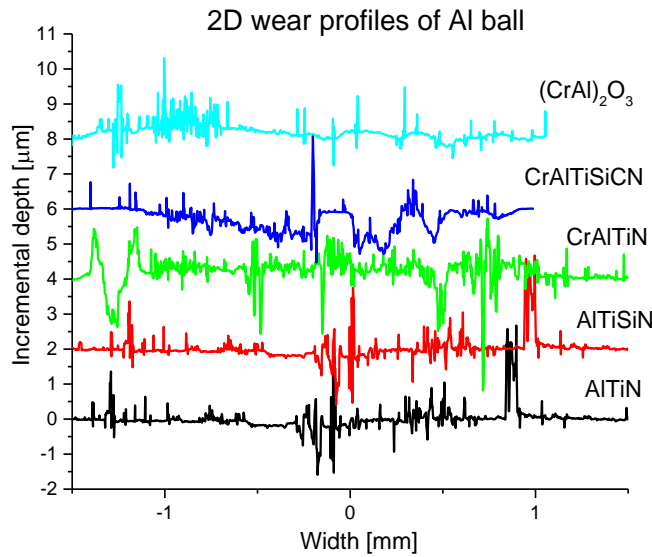


Figure 5-77 2D profiles of coatings tested with Al ball at 650°C

The wear scar is caused by the abrasion effect of hard bodies of Al_2O_3 formed from oxidized aluminum from the ball [73], as reported in the previous section. AlTiN and AlTiSiN are damaged mainly in the center of the wear track, but the CrAlTiN coating is damaged on the borders of the wear track, where the protective AlO_x layer was not formed, as shown in Figure 5-80. The $(\text{CrAl})_2\text{O}_3$ coating does not have this groove and withstands the testing intact, but shows a significant build-up layer associated with the fluctuation of the COF. The CrAlTiSiCN coating shows severe damage, most likely caused by cohesion problems of this coating at high temperature.

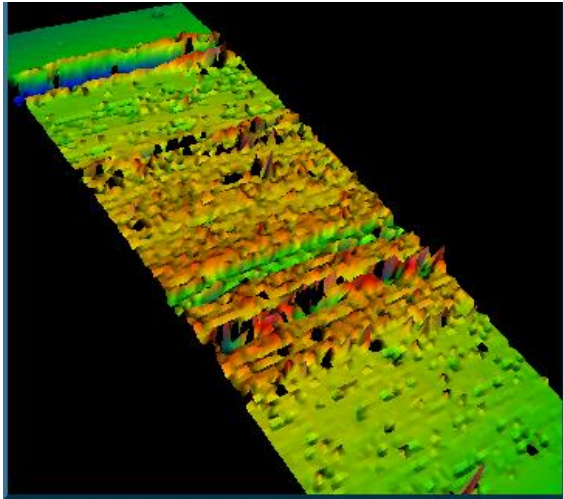


Figure 5-78 3D profile of TiAlN coating tested with Al ball at 650°C. The 2D XY field has dimensions 3.25 x 0.95 mm.

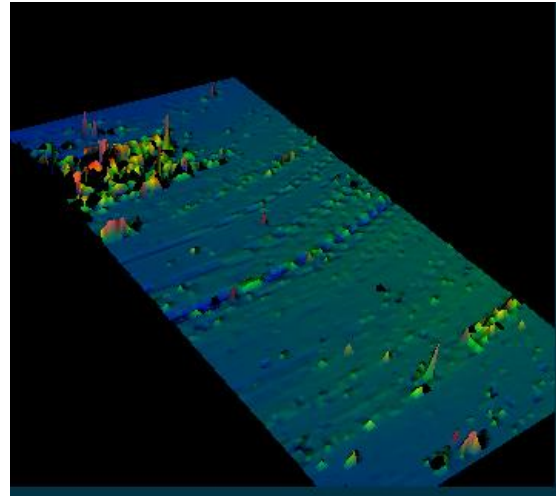


Figure 5-79 3D profile of TiAlSiN coating tested with Al ball at 650°C. The 2D XY field has dimensions 1.45 x 0.95 mm.

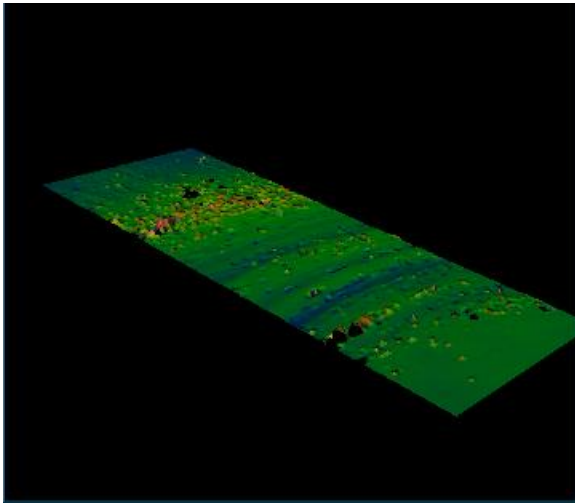


Figure 5-80 3D profile of TiAlCrN coating tested with Al ball at 650°C. The 2D XY field has dimensions 3.25 x 0.95 mm.

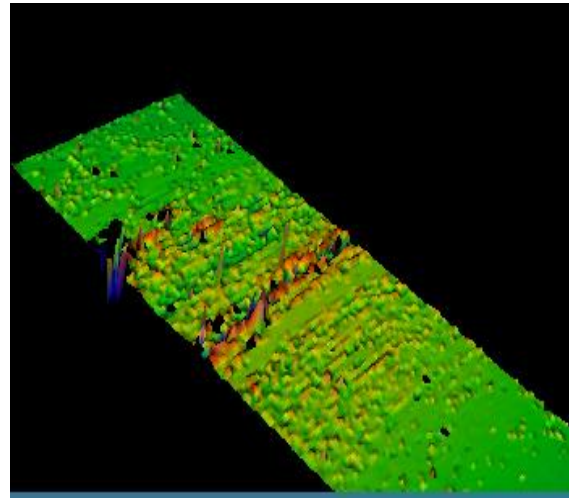


Figure 5-81 3D profile of (AlCr)₂O₃ coating tested with Al ball at 650°C. The 2D XY field has dimensions 3.25 x 0.95 mm.

5.3.4.2.3.2 Wear rate and wear mechanism against Al₂O₃ ball

The 2D wear profiles of all coatings are shown in Figure 5-82, and the 3D scans in Figure 5-83 Figure 5-86. The CrAlTiN, AlTiN and AlTiSiN coatings show similar wear profiles. It is visible that the wear is caused by plowing effects, because the wear profile is relatively smooth. For the TiAlCrSiCN coating, one can see cohesive failure, identifiable by sharp edges of the holes in the coating. The lowest wear rate was discovered for the (CrAl)₂O₃ coating, almost one order of magnitude lower than the other coatings. The was also mild wear to a depth of 200 nm. Also, the build-up (very significant for other coatings) was smaller, signifying less material transport during the sliding process.

To ensure a low wear at high-temperature, oxidation resistance and thermal stability are more important than mechanical properties (e.g. hardness) as detailed in section 5.2.5.5. The working assumption is that the excellent behavior of the $(\text{CrAl})_2\text{O}_3$ coating can be assigned to its superior oxidation resistance and thermal stability, as previously reported [74].

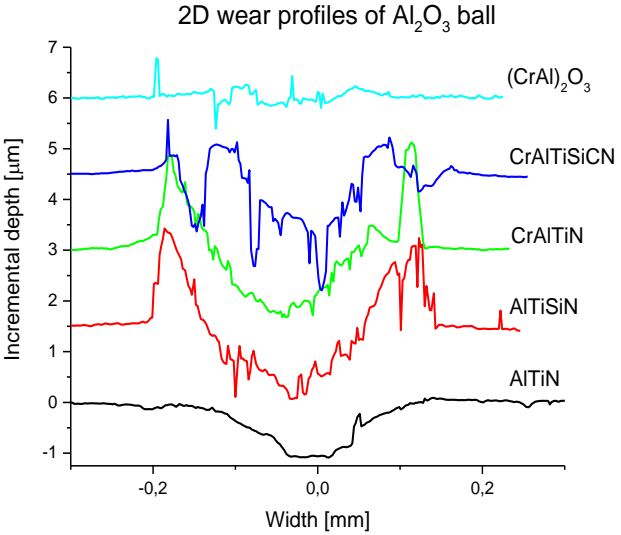


Figure 5-82 2D profiles of coatings tested with Al₂O₃ ball at 650°C

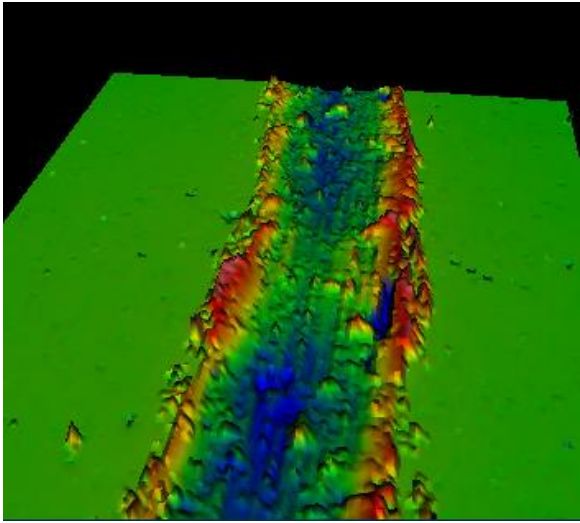


Figure 5-83 3D profile of AlTiN coating tested with alumina ball at 650°C. The 2D XY field has dimensions 1.26 x 0.95 mm.

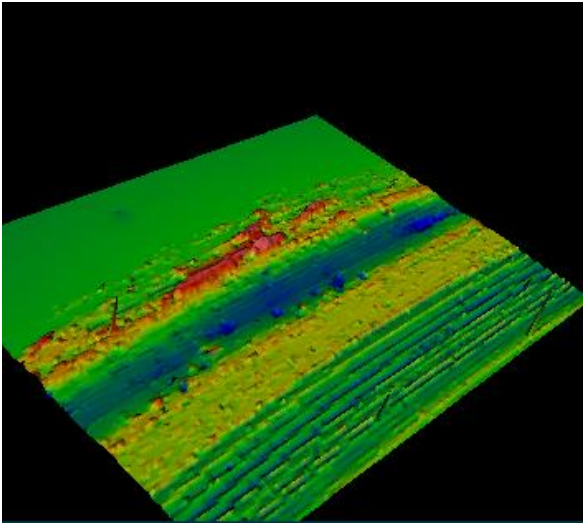


Figure 5-84 3D profile of TiAlSiN coating tested with alumina ball at 650°C. The 2D XY field has dimensions 1.26 x 0.95 mm.

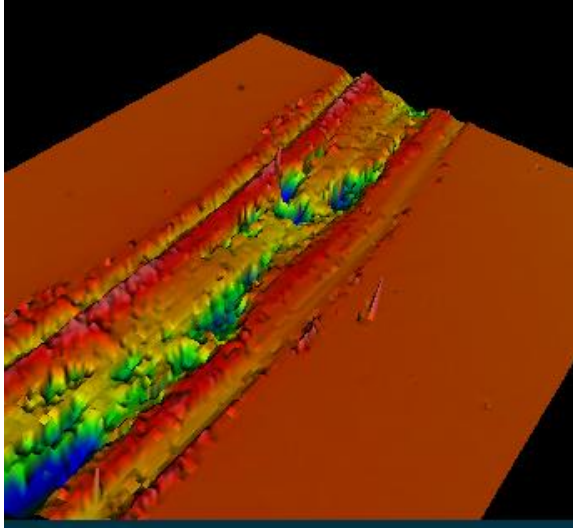


Figure 5-85 3D profile of TiAlCrSiCN coating tested with alumina ball at 650°C. The 2D XY field has dimensions 1.26 x 0.95 mm.

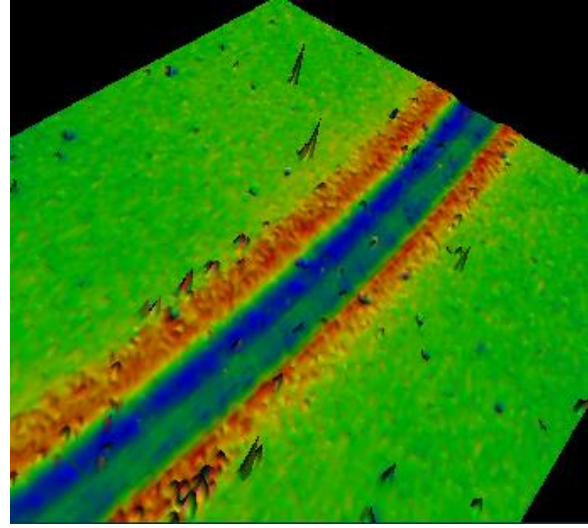


Figure 5-86 3D profile of $(\text{CrAl})_2\text{O}_3$ coating tested with alumina ball at 650°C. The 2D XY field has dimensions 1.26 x 0.95 mm.

5.3.5 Conclusion – Aluminum high pressure die casting

This part of the thesis focused more with the optimization of coatings for specific industrial uses, and with methods of evaluating the evolution in its behavior. The three key properties tested on the adhesive and stress-relaxing base layer were: adhesion after thermal cycling tests, loss of adhesion due to thermal cycling, and stress development during thermal cycling. Second, the influence of nitriding on these properties was investigated. The best adhesion was observed for the CrAlTiN coating on an un-nitrided substrate, and for the AlCrTiN coating on a nitrided substrate. The Lc2 was around 60N, guaranteeing sufficient adhesion for industrial use. The multilayered mCrN/AlTiN coating suffered the greatest loss of adhesion, which anyway was generally poor.

All coatings exhibited an increase of tensile stresses in the range 1,73 – 2,65 GPa. The lowest change in internal stress was observed for the nitrided CrAlN sample, and for the nitrided AlCrTiN sample, at 1,73 and 1,78 GPa respectively. More importantly, a strong correlation between the development of intrinsic tensile stresses and the mechanical ratios H/E and H^3/E^2 was observed. Coatings with lower ratios showed a smaller increase in tensile stress. The improvement of the coating behavior on the nitrided substrate was observed by thermal cycling tests. All coatings with nitride samples showed a smaller increase in tensile stresses.

Figure 5-87 summarizes the ability of all coatings to be used as base layer for best performing coating. In generally, the best combination was the AlCrTiN coating with a nitrided substrate.

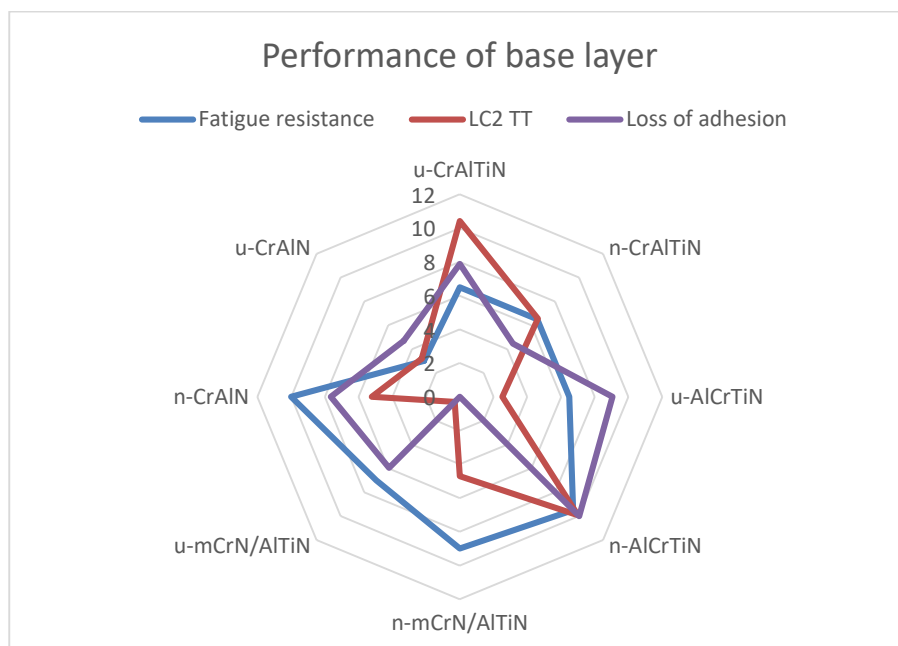


Figure 5-87 Evaluated performance of different candidates for base layer

The $(\text{CrAl})_2\text{O}_3$, AlTiN, AlCrSiTiCN, AlTiSiN, and CrAlTiN coatings were characterized according to their tribological behavior. Three main attributes are expected for the outer coating: resistance against abrasion, low adhesion to molten aluminum, and high resistance to aluminum corrosion. Resistance against abrasion was tested by aluminum ball sliding. Adhesion to aluminum was derived from the coefficient of friction against an aluminum ball at high temperature. The resistance against molten aluminum was determined by wear behavior at high temperature against aluminum.

The highest resistance to aluminum corrosion was observed for the $(\text{CrAl})_2\text{O}_3$ coating, while all other nitride coatings showed poorer performance; the wear rate of these was almost one order of magnitude higher. This is due to the high temperature stability of the $(\text{CrAl})_2\text{O}_3$ coating and its resistance to oxidation. The lowest adhesion to molten aluminum was observed for the CrAlTiN coating. This coating formed effective Cr-Al oxides at its surface, maintaining low adhesion. The $(\text{CrAl})_2\text{O}_3$ coating also showed low mean adhesion, but the COF was not stable, due to the continuous forming and destruction of the adhered Al layer. The resistance to high temperature abrasion, as measured by sliding an Al_2O_3 ball against the coatings, was again best for the $(\text{CrAl})_2\text{O}_3$ coating, showing half the wear rate than other coatings.

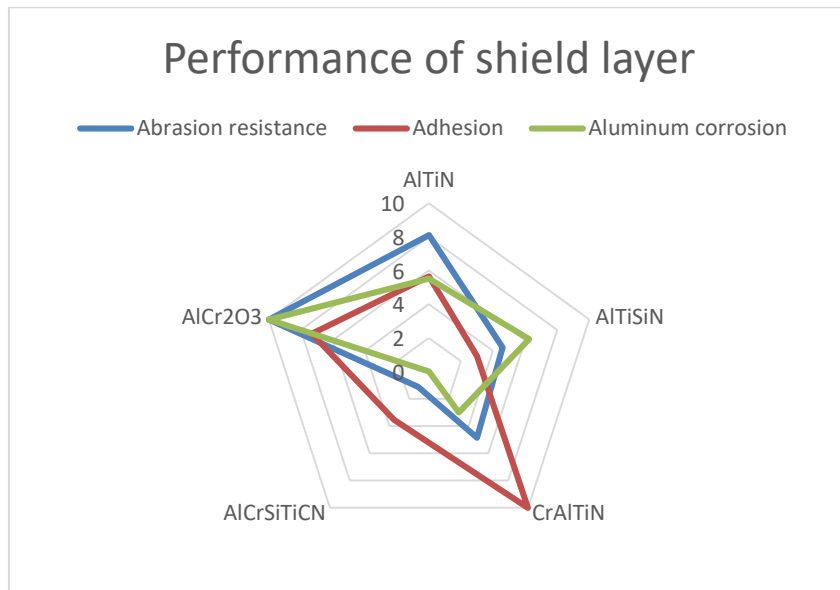


Figure 5-88 Evaluated performance of different candidates for shield layer

Figure 5-88 displays a web diagram of comparative performances of the shield layer coatings. The best performing shield coating was found to be $(CrAl)_2O_3$, mainly due to its resistance against aluminum. If the main problem for the die casting company would be aluminum adhesion, then CrAlTiN is a better candidate.

5.4 Chosen industrial applications solved in AdvaMat s.r.o.

This chapter shows three particular business cases which I solved during the Ph.D. study in the established start-up AdvaMat s.r.o. Although progress was made in all cases, they did not all become realistic business ventures, as explained below.

5.4.1 High pressure aluminum die casting

Customer:

A medium size company (500 employees) producing automotive parts from aluminum. The process in the company starts from aluminum die casting to machining of aluminum, ending with the assembly of more complex parts.



Figure 5-89 Aluminum component used in truck brakes

Task:

To develop a coating that solves durability issues of tools used in the cavities of molds for HPDC. The tools are subjected to mechanical and thermal loads, as explained in section 5.3. The aluminum press has a frequency of about 40 s, with an applied pressure of 70 MPa. The temperature of the aluminum melt is 640°C. After the working cycle, the tools are cooled to 25°C. The task is to develop a coating with which a pin can survive 15,000 injections of aluminum at the most exposed position in the cavity, in front of the hot aluminum inlet.

Coated part:

Core pin with diameter 8 mm and length 150 mm. The material is chromium molybdenum tool steel 50CrMoV13, quenched to a hardness of 48 HRC, with gas-nitrided surface.

Current state:

The lifetime of uncoated pins is 1000 parts. The wear mechanism is partly aluminum erosion and partly micro cracks from heat checking. The solutions from other coating suppliers is an AlTiN and AlCrN coating, which make it possible to increase the lifetime by about 100%. After this period, first micro cracks appear and the molten alumina sticks to the surface.

Developed solution:

After careful consideration of all kinds of factors influencing the wear, I decided to use a dual layer coating consisting of a 2 μm layer of AlTiN and a 1 μm layer of Al_2O_3 . The final number of injections reached 8679. The condition of the pin is seen in Figure 5-90. The lifetime was greatly increased, but still lower than desired. The pins in other positions survived more than 50 000 cycles. As a continuation of this development, the research described in section 5.3 took place.

Result:

The company realized that a more advanced coating than what they are already using can have good results. They also asked all other coating manufacturers and ended up using an AlCrN duplex coating for expensive parts. Smaller pins are not coated, because the price for the pin is so low, that there is no economical reason to coat it.



Figure 5-90 Mold core with four coated pins. There is aluminum sticking visible on the stressed pin marked with red color.

5.4.2 Cutting

Customer:

Medium size company (150 employees) CNC machining, mostly automotive parts from steel and aluminum. The company spends 4 000 € monthly on coating machining tools.



Figure 5-91 Coated double side mills

Task:

To propose a new coating which would lower their expenditure on tools, either by prolonging tool life, or by lowering the price of the coating. Another solution could be to increase the cutting speeds in order to lower machining time.

Coated part:

Double-sided tungsten carbide mills with 4 teeth and a diameter of 12 mm. The mills are used for cutting hardened steel with hardness ca. 54 – 56 HRC. The mill is rotating at 3000 rpm and the feed rate is 500 $\mu\text{m}/\text{tooth}$.

Current solution:

The company is machining most of its cutting tools by itself. The tools are then sent to two different coaters. 80% of the production goes to Germany for arc deposited AlTiN coating, with a very low price; the coating service plus delivery takes 5 days. 20% of the tools are being coated in the Czech Republic, mostly in cases when a very short delivery time is needed (2 days). The tool life of the German AlTiN coating is 45 parts.

Developed solution:

As this testing had a high priority and the tests are quite fast (1 piece takes 15 minutes) more coatings were tested on the tools. The tested coatings were AlTiN, AlTiSiN and the newly developed m-TiAlCrN coating (as discussed in section 5.2). I spent two days with the worker by the cutting machine to ensure all conditions were the same. The tests were performed at the same cutting speed, as well as at 25% and 50% higher speeds. Also, the effect of sandblasting before coating was observed. The results are summarized in Table 5-14.

Mill 12mm			
	Rotation [rpm]	Feed [$\mu\text{m}/\text{tooth}$]	Pieces produced
AlTiN	3000	500	28
AlTiN	4500	750	14
AlTiN blasted	3750	625	18
AlTiN blasted	3000	500	12
AlTiSiN	3000	500	70
AlTiSiN	3750	625	38
AlTiSiN blasted	3000	500	38
AlTiSiN blasted	4500	750	26
TiAlCrN blasted	3750	325	16
TiAlCrN blasted	3000	500	16
TiAlCrN blasted	3000	500	14
TiAlCrN blasted	4500	750	26

Table 5-14 Measured number of pieces produced by particular coating combinations

After testing, a few interesting observations were made. The AlTiN coating failed due to insufficient adhesion. The TiAlCrN coating failed due to insufficient cohesion, but performed better with an increased cutting speed - this is in good agreement with the results presented in 5.2. The wet sandblasting process before coating deposition decreased the life time of the tools. The best coating was AlTiSiN, which increased the life time of the tool by about 50% in comparison to the German made AlTiN coating.

Result:

Our coating provided better tool life, but was also 50% more expensive. As the price of the tool is 10 times more than the price of coating, I thought that our solution is clearly better. Unfortunately, the company stayed with their previous supplier, partly because of the price, but also because the supply chain was already well-established.



Figure 5-92 Calotest of the best performing AlTiSiN coating

5.4.3 Glass molds

Customer:

A large western European corporation dealing with the production of packaging glass, e.g., beer bottles, glass cans, etc.



Figure 5-93 Glass forming process. [AdvaMat s.r.o.]

Task:

To propose an adequate coating for molds made of cast iron, to ensure longer life, but more importantly to remove the need for lubricating the molds during glass forming.

Coated part:

First-stage glass mold made from cast iron with nickel-coated edges.

Current solution:

The one glass forming machine works with up to 20 mold positions at a time. The cycle is very fast: only a few seconds per bottle. To ensure the hot glass (ca. 1000°C) does not stick to the mold surface, the molds need to be lubricated. The lubrication is performed by a manual worker, every 15 minutes. To lubricate the mold, it must be stopped, have the lubricant applied, and then the first four bottles must be scrapped due to the poor quality of the glass surface. Inadequate lubrication leads to poor surface quality, as well as the glass sticking to the mold. When the glass becomes stuck to the mold, it must be replaced by a new one, slowing down the production. All of these processes are time consuming, leading to lower glass quality, whilst also bringing the risk of stopping the whole machine. Different coatings from other coaters were tried (AlCrN, CrAlSiN, etc.), but none of them worked.

Developed solution:

According to previous bad experiences with the coatings, I tried the slightly modified multilayered AlCrN/TiAlN coating, as described in section 5.2. This seemed a good choice because of the high thermal resistance, as shown on Figure 5-35. To ensure good adhesion to the soft cast iron, a few modifications, *i.e.*, a transient adhesion layer, had to be applied.

Result:

The coating exceeded expectations. It was able to maintain its function for a period of more than 168 hours. During that time, there was no need for lubrication and absolutely no scrap. The cost of the coating doubled the price of the glass mold, so right now it is being evaluated to see if it makes economic sense for the company to coat the molds or not.



Figure 5-94 Molds after coating



Figure 5-95 A set of glass molds before coating

6. Summary

6.1 Summary of the research

This work sought to address some of the practical applications of physical vapor deposited thin films. The main aim was to understand the conditions - and all necessary interdisciplinary effects - causing degradation of hard nitride coatings in high temperature environments. The understanding of these effects led, for both cases, to non-cooled metal cutting, and high pressure die casting of aluminum, and to a focused study of the properties of hard coatings.

It was shown, by numerical simulation of the rotation model, that in an industrial setup it is not possible to deposit coatings with evenly distributed atoms when using targets of different composition. The number of rotation axes has a huge effect on the coating. Three-fold rotation leads to a more even distribution, thinner multilayers, and an even distribution of single layers in the coating. Two-fold rotation induces periodical inequality in the coating, leading to areas where the coating is almost single-layered and lacking the desired composition. These areas can be sources of defects of in the coating.

With regards to metal cutting, I clearly showed the greater importance of thermal resistivity of the coatings over its mechanical properties. Even if the hardness of the TiAlN coating was higher than the TiAlCrN coatings studied, the tribological and cutting results showed its greater suitability. The increased Cr content in the Cr-doped coatings led to an increase in hardness due to the more extensive CrN phase in the AlCrN layer. This increase of the CrN phase shifted the preferential growth from (111) to (200), as measured by X-ray diffraction. More importantly, the addition of Cr induced a higher onset temperature of oxidation with respect to the deposited TiAlN coating. The onset temperature was shifted by more than 200°C, showing superior oxidation resistance. The oxidation tests of the TiAlN coating showed the formation of a protective Al₂O₃ layer, accompanied by a porous TiO₂ layer at a temperature of around 800°C. At 900°C, fast Ti ions diffused to the surface and hindered the formation of a protective Al-O layer, leading to fast, full oxidation of the TiAlN coating. Independently of the Cr concentration, the Cr-doped films developed a protective crystalline and compact Al-Cr-O layer under TiO₂ at the temperature of 900°C. This protective layer stopped the oxidation process utterly. At a temperature of 1000°C, the protective Al-Cr-O layer still developed and protected the coating against full oxidation, but the thickness of the oxidized layer was dependent on the amount of Cr in the coating. The best oxidation protection was shown for the coating with the highest Cr concentration. The higher content of Cr in the coating, the more Cr-rich the (Cr,Al)₂O₃ phase.

The pin-on-disc tribological tests showed a superior performance of Cr-doped coatings due to the formation of a protective and lubricious Cr-O tribolayer in the sliding contact. Cr-O

was found to have better tribological properties than either the Ti-O or Al-O tribolayer formed on the TiAlN sample. Moreover, the higher the Cr content, the better the tribological performance, *i.e.*, lower friction and wear. The Cr-doped coatings were outperformed by TiAlN coatings in drilling tests at low cutting speeds. At a cutting speed of 50 m/min, the TiAlN coated drills were able to drill twice as many holes as the Cr-doped ones. This happened because the cutting temperatures were insufficient to induce formation of an oxidation tribolayer, and the wear of the cutting tool was driven mainly by abrasive wear. With increased cutting speeds of 200 m/min, the Cr-doped coating drilled twice as many holes as TiAlN, and drilled twice more than at a cutting speed of 50 m/min. This behavior shows that the $Ti_{0.28}Al_{0.31}Cr_{0.51}N$ is very good candidate for high speed dry cutting, but will perform poorer at lower speeds.

The results from coating development for high pressure die casting is more tricky to interpret because real coated pins with the proposed coatings (nitrided steel -AlCrTiN-(CrAl)₂O₃ coating and nitrided steel-AlCrTiN-CrAlTiN) are still undergoing tests in die casting molds, and the laboratory results are not supported by industrial results.

To reduce heat checking damage of the coating, the nitriding of the steel part prior to coating is advantageous. The lower increase of tensile stresses was observed on the nitrided substrates. It was facilitated by a reduced mismatch of material properties on the coating-substrate boundary for 'nitrided steel + coating', than for 'unnitrided steel + coating'. Another factor influencing the increase of the tensile stresses were the material properties H/E and H^3/E^2 . The coatings exhibiting lower H/E and H^3/E^2 values, that is CrAlTiN, formed lower stress during temperature cycling. The lower stresses will be accumulated in coatings with a lower H^3/E^2 ratio, as the coating has a lower tendency toward plastic deformation. A lower H/E ratio means lower resistance against elastic deformation; thus, the coatings better accommodate dimensional changes during thermal cycling.

For the surface layer in touch with the aluminum melt, other properties are important, primarily low aluminum adhesion to the coating and resistance against aluminum corrosion. Aluminum adhesion was evaluated based on the coefficient of friction against aluminum, and the aluminum corrosion resistance was evaluated based on the wear rate against both aluminum and an alumina ball at 650°C. The lowest coefficient of friction at 650°C was measured for the CrAlTiN and (CrAl)₂O₃ coatings against both an aluminum and alumina ball. The CrAlTiN coating formed a Al-Cr-O tribolayer, thus, the chemistry of the contact surfaces was the same for CrAlTiN and (CrAl)₂O₃. However, the lower coefficient of friction of CrAlTiN against aluminum at 650°C - in comparison to (CrAl)₂O₃ - is attributed to the continuous spallation of the porous Cr-Al-O tribolayer. This behavior explains the one order of magnitude

lower wear rate of the $(\text{CrAl})_2\text{O}_3$ coating against an Al ball, with almost unmeasurable wear compared to the CrAlTiN coating. The third best coating was AlTiN, then the AlTiSiN coating.

6.2 Summary of industrial part

Apart from technical and manufacturing skills, three important aspects of working business needed to be applied: presentation of the company (PR), operation (logistics, *etc.*) and sales. At the beginning of our company we were convinced that our knowledge will persuade any customer to cooperate with us, and that our webpage should serve more like a “business card” than a lurking advertisement. This belief proved wrong during the second year, and we focused more on our presentation, so we acquired some equipment for taking high quality pictures of coated goods, we invested more time in webpage design, and ultimately had to think more like a customer who knows nothing about coating, rather than coating professionals. In 2017 and 2018 we managed to print a good quality article in prestigious Czech journals (Forbes and Hospodářské noviny (Czech equivalent of Financial Times)).

As the number of coating orders increased, the time needed for logistics, accounting, *etc.* also increased significantly. This time effect was underestimated, and as almost everything in our company is run by me, it reduced the time spent on more important tasks. To overcome these issues, a new employee was hired, and logistics and accounting were outsourced to professional companies. Although we knew that sales are the most important aspect of the company and should not be underestimated, I see our biggest space in improvement in this area. My greatest experience was, that even if the customer is convinced during the first or second meeting, they can easily change their mind, because of many other operational problems they may be having, and because of competition from rivals.

Another important discovery has been that a company as small as we are cannot try to fulfill all needs in different areas. This leads to a loss of focus, and the company will not gain the necessary industrial know-how as fast as is required. Although our technical skills in coatings are excellent, the real industrial problems require deeper knowledge, such as the influence of different tool materials, type of cooling, influence of service workers, the will of management to change course, and the relationship of potential customers to our competition. Many times we found a better solution to a particular problem, but the customer placed their order with our competition. The correct way of starting a company of this type could be by choosing just one industry to focus on (metal cutting, plastic cutting), gain some deeper knowledge of the area from minor customers, and then focus on say the 15 biggest potential customers in that area - with the target become the supplier for one of them by any means possible. After some time (a year) of perfect service delivery to that customer, and after training more staff, it may then be time to start acquiring more businesses.

References

- [1] K. Choy, „Chemical vapour deposition of coatings,“ *Progress in Material science*, pp. 57-170, 1 November 2001.
- [2] K. Bobzin, T.Brögelmann, N.C.Kruppe a M.Engels, „Correlation of the Debye sheath thickness and (Cr,Al)N coating properties for HPPMS, dcMS, CAE and PCAE processes,“ *Surface and Coatings Technology*, pp. 233-241, 25 December 2017.
- [3] L. Chen, K. K.Chang, Y. Du, J. R. Li a M. J.Wu, „A comparative research on magnetron sputtering and arc evaporation deposition of Ti-Ak-N coatings,“ *Thin solid films*, 2011.
- [4] J. Vossen, *Thin Film Processes*, Princeton: ACADEMIC PRESS, 1978.
- [5] C. Weissmantel, „Deposition of Metastable Films by Ion Beam and Plasma Techniques,“ *Proc. 9th Int. Vacuum Congress and 5th Int. Conf. on Solid Surfaces*, 1983.
- [6] P. Sigmund, „Theory of sputtering,“ *Physical Review* 184, p. 383, 1978.
- [7] [Online].Available:
<http://labs.physics.berkeley.edu/mediawiki/images/2/24/DischargeStructure.jpg>.
- [8] „Glow discharge,“ [Online]. Available:
http://www.glow-discharge.com/?Physical_background:Glow_Discharges.
- [9] P. Kelly a R. Arnell, „Magnetron sputtering: a review and recent developements and applications,“ *Vacuum* 56, pp. 159-172, 20 September 1999.
- [10] J. Lin, B. Mishra, J. Moore a W. Sproul, „Microstructure, mechanical and tribological properties of Cr_{1-x}Al_xN films deposited bz pulsed-closed field unbalanced magnetron sputtering,“ *Surface & Coatings technology* 201, pp. 4329 - 4334, October 2006.
- [11] P. Moller a L. Nielsen, *Advanced Surface Technology*, Moller & Nielsen, 2013.
- [12] CemeCon, „CemeCon,“ 2019. [Online]. Available: www.cemecon.de.

- [13] M. Gassner, N. Schalk, B. Sartory, M. Pohler, C. Czettel a C. Mitterer, „Influence of Ar ion etching on the surface topography of cemented carbide cutting inserts,“ *International Journal of Refractory Metals and Hard Materials*, pp. 234-239, December 2017.
- [14] P. Panjan, M. Čekada, M. Panjan a D. Kek-Merl, „Growth defects in PVD hard coatings,“ *Vacuum*, 2010.
- [15] J. Vetter a S. Stuber, *Surface coatings technology*, 2003.
- [16] E. Bauer a F. Zeitschr, *Kristallographie 110*, p. 372, 1958.
- [17] K. Oura, *Surface Science: An Introduction*, Springer, 2010.
- [18] A. Nyaiesh, *Thin solid films 86*, pp. 267 - 77, 1981.
- [19] L. Messier, *Vacuum technology*, 1981.
- [20] H. Oettel a R. Wieremann, „Residual stresses in PVD hard coatings,“ *Surface & Coating technology*, pp. 265-273, 1995.
- [21] J. Thornton, J. Tabock a D. Hoffman, „Internal stress in metallic films,“ *Thin solid films 64*, pp. 111-119, 1979.
- [22] H. Windischmann, „Intrinsic stress in Sputter-Deposited Thin Films,“ *Thin Solid Film 45*, pp. 387-396, 1977.
- [23] C. Davis, „A simple model for formation of compressive stress in thin films by ion bombardment,“ *Thin Solid Films 226*, pp. 30-34, 1993.
- [24] W. Hume-Rothery, *Atomic Theory for Students of Metallurgy*, London: The Institute of Metals, 1969.
- [25] P. Sherron, *Diffusion in solids*, McGraw-Hill, 1963.
- [26] P. Mayrhofer, C. Mitterer, L. Hultman a H. Clements, „Microstructural design of hard coatings,“ *Progress in material science*, č. 51, 2006.
- [27] A. David a E. Kenneth, *Phase Transformation in Metal and Alloys*, Boca Raton: Taylor & Francis Group, 2009.

- [28] R. Reed-Hill, *Physical Metallurgy Principles* by, New York: Van Nostrand, 1973.
- [29] Y. Oren, „CahnHilliard Animation.gif,“ 12 June 2007. [Online]. Available: https://commons.wikimedia.org/wiki/File:CahnHilliard_Animation.gif. [Přístup získán 25 April 2019].
- [30] R. Forsen, M. Johansson, M. Odén a N. Ghafoor, „Decomposition and phase transformation in TiAlCrN thin coatings,“ *Vacuum science technology* 30, 2012.
- [31] C. Mitterer, P. Mayrhofer a J. Musil, „Thermal stability of PVD hard coatings,“ *Vacuum*, pp. 279-284, 9 May 2003.
- [32] C. Mitterer, P. Mayrhofer a J. Musil, „Thermal stability of PVD hard coatings,“ *Vacuum* 71, pp. 279-284, 2003.
- [33] T. M. Callisti, „Combined size and structure-dependent deformation and strengthening mechanism in Zr/Nb nano-multilayers,“ *Acta Materialia*, pp. 247-260, 1 February 2017.
- [34] M. Stueber, H. Holleck, H. Leiste, K. Seemann, S. Ulrich a C. Ziebert, „Concepts for the design of advanced nanoscale PVD multilayer protective thin films,“ *J. Alloys Compd*, pp. 321-333, 2009.
- [35] M. B. Hyoungh Seop Kim, „The effect of grain size and porosity on the elastic modulus of nanocrystalline materials,“ *Nanostructured Materials*, pp. 361 - 367, May 1999.
- [36] L. Affonso., *Machinery Failure Analysis Handbook - Sustain Your Operations and Maximize Uptime*, USA: Gulf Publishing Company, 2006.
- [37] J. Musil, J. Sklenka, R. Čerstvý, T. Suzuki, T. Mori a M. Takahashi, „The effect of additon in ZrO₂ thin film on its resistance to cracking,“ *Surface & Coating Technology*, pp. 355-360, 2012.
- [38] T. Tsui, G. Pharr, W. Oliver, C. Bhatia, R. White, S. Anders, A. Anders a I. Brown, „Nanoindentation and nanoscratching of hard carbon coatings for magnetic discs,“ *MRS Proceedings*, pp. 383-447, June 1995.
- [39] R. Franz a C. Mitterer, „Vanadium containing self-adaptive low-friction hard coatings for high-temperature applications: A review,“ *Surface and Coatings Technology*, pp. 1-13, 15 August 2013.

- [40] L. Q, P. Hovsepian, D. Lewis, W. Munz, Y. Kok, J. Cockrem, M. Bolton a A. Farinotti, „Tribological properties of unbalanced magnetron sputtered nano-scale multilayer coating TiAlN/VN and TiAlCrYN deposited plasma nitrided steels,“ *Surface&Coatings Technology*, č. 193, 205.
- [41] K. Bobzin, „High-performance coatings for cutting tools,“ *CIRP Journal of Manufacturing Science and Technology*, 2017.
- [42] G. Fox-Rabinovich, A. Kovalev, M. Aguirre, B. Beake, K. Yamamoto a S. Veldhuis, „Design and performance of AlTiN and TiAlCrN PVD coatings for machining of hard to cut materials,“ *Surface&Coatings technology*, č. 204, 2009.
- [43] J. Lin, X. Zhang, Y. Ou a R. Wei, „The structure, oxidation resistance, mechanical and tribological properties of CrTiAlN coatings,“ *Surface&Coatings Technology*, č. 277, 2015.
- [44] R. Forsén, M. Johansson, M. O. a N. Ghafoor, „Effects of Ti alloying coatings on thermal stability and oxidation resistance,“ *Thin Solid Films*, č. 534, 2013.
- [45] Q. Luo, W. Rainforth a W. Munz, „TEM observation of wear mechanism of TiAlCrN and TiAlN CrN coatings grown by combined steered-arc unbalanced magnetron deposition,“ *Wear*, č. 225, 1999.
- [46] L. Bai, X. Zhu, J. Xiao a J. He, „Study on thermal stability of CrTiAlN coating for dry cutting,“ *Surface&Coatings technology*, č. 201, 2007.
- [47] T. Polcar a A. Cavaleiro, „High temperature behavior of nanolayered CrAlTiN coating: Thermal stability, oxidation, and tribological properties,“ *Surface & Coatings Technology*, č. 257, 2014.
- [48] A. Alberdi, M. Marin, B. Diaz, O. Sanchez a R.E.Galindo, „Wear resistance of titanium-aluminium-chromium-nitride nanocomposite thin film,“ *Vacuum*, č. 81, 2007.
- [49] N.N., „Cutting tools,“ Dedalus Consulting, 2014. [Online]. Available:
www.dedalusconsulting.com.
- [50] A. Schmidt, Titanium aluminium nitride, CemeCon AG, 2005.
- [51] M.Zwierzchowski, „FACTORS AFFECTING THE WEAR RESISTANCE OF FORGING TOOLS,“ *Arch Metall Mater*, p. 1567–1576, January 2017.

- [52] S. C. Cha, *Coatings for vehical applicatios*, Springer, 2015.
- [53] O. Salas, K. Kearns a J. M. K. Carrera, „Tribological behavior of candidate coatings for Al die casting dies,“ *Surface and coatings Technology*, pp. 117-127, 2003.
- [54] K. Cooke, S. Yang, C. Selcuk, A. Kennedy, D. Teer a D. Beale, „Development of duplex nitrided and closed field unbalanced megnetron sputter ion plated CrTiAlN-based coatings for H13 aluminium extrusion dies,“ *Surface&Coatings Technology*, 2004.
- [55] A. Srisvastava a V. Joshi, „A multilayer coating architecture to reduce heat chcecking of die surfaces,“ *Surface&Coatings technology*, 2003.
- [56] J. Lin a S. Carrera, „Design methodology for optimized die coatings: The case for aluminum pressure die casting,“ *Surface & Coatings Technology*, 2006.
- [57] V. Martynenko, A. Yu, A.Rogov a V. Shulga, „Angular distribution of atoms during the magnetron sputtering of polycrystalline targets,“ *Technical Physics*, 04 2012.
- [58] D.R.Lide, *CRC Handbook of Chemistry and Physics*, Boston: CRC Press, 1991.
- [59] L.Chen, J.Paulitsch, Y.Du a P.H.Mayrhofer, „Thermal stability and oxidation resistance of Ti–Al–N coatings,“ *Surf. Coat. Technol.*, pp. 2954-2960, 2012.
- [60] L. Donohue, D. Lewis, W. Münz, M. Stack, S. Lyon, H. Wang a D. Rafaja, „The influence of low concentrations of chromium and yttrium on the oxidation behaviour, residual stress and corrosion performance of TiAlN hard coatings on steel substrates,“ *Vacuum*, pp. 109-114, 1999.
- [61] K. Yamamoto, T. Sato, K. Takahara a K. Hanaguri, „Properties of (Ti,Cr,Al)N coatings with high Al content deposited by new plasma enhanced arc-cathode,“ *Surface & Coatings Technology*, pp. 620 - 626, 2003.
- [62] Y. Xu, L. Chen, B. Yang, Y. Peng, Y. Du, J. Feng a F. Pei, „Effect of CrN addition on the structure, mechanical and thermal properties of Ti-Al-N coating,“ *Surface & Coatings Technology*, pp. 506-512, 2013.
- [63] H. Ellingham, „Transactions and Communications,“ *Journal of Chemistry, Technology and Biotechnology*, p. 125, 1944.

- [64] Y. Xu, L. Chen, F. Pei a Y. Du, „Structure and thermal properties of TiAlN/CrN multilayered coatings with various modulation ratios,“ *Surface & Coatings Technology*, pp. 512-518, 2016.
- [65] Z. Qi, P. Sun, F. Zhu, Z. Wu, B. Liu, Z. Wang, D. Peng a C. Wu, „Relationship between tribological properties and oxidation behavior of Ti_{0.34}Al_{0.66}N coatings at elevated temperature up to 900 °C,“ *Surface & Coatings Technology*, pp. 267-272, 2013.
- [66] G. Fox-Rabinovich, K. Yamamoto, S. Veldhuis, A. Kovalev a G. Dosbaeva, „Tribological adaptability of TiAlCrN PVD coatings under high performance dry machining conditions,“ *Surface & Coatings Technology*, pp. 1804-1813, 2005.
- [67] A. Inspektor a P. A. Salvador, „Architecture of PVD coatings for metalcutting applications: A review,“ *Surface & Coatings Technology*, pp. 138-153, 2014.
- [68] S. Carvalho, E. Ribeiro, L. Rebouta, C. Tavares, J. Mendonça, A. C. Monteiro, N. Carvalho, J. D. Hosson a A. Cavaleiro, „Microstructure, mechanical properties and cutting performance of superhard (Ti,Si,Al)N nanocomposite films grown by d.c. reactive magnetron sputtering,“ *Surface & Coatings Technology*, pp. 459-468, 2004.
- [69] S. Harris, E. Doyle, A. Vlasveld, J. Audy a D. Quick, „A study of the wear mechanisms of Ti_{1-x}Al_xN and Ti_{1-x-y}Al_xCryN coated high-speed steel twist drills under dry machining conditions,“ *Wear*, pp. 723-734, 2003.
- [70] C. Mitterer, F. Holler, F. Ustel a D. Heim, „Application of hard coatings in aluminium die casting - soldering, erosion and thermal fatigue behaviour,“ *Surface & Coatings Technology*, 2000.
- [71] S.Sridharan, L.Xie, E.H.Jordan a M.Gell, „Stress variation with thermal cycling in the thermally grown oxide of an EB-PVD thermal barrier coating,“ *Surface & Coating technology*, pp. 286-296, 2004.
- [72] M. Vilaseca, S. Molas a D. Casellas, „High temperature tribological behaviour of tool steels during sliding against aluminium,“ *Wear*, pp. 105-109, 2011.
- [73] K. Holmberg, H.Ronkainen a A.Matthews, „Tribology of thin coatings,“ *Ceramics international*, pp. 787-795, 2000.

- [74] K. Bobzin, T. Brögelmann, C. Kalscheuer a M. Welters, „Thick HS-PVD (Al,Cr)₂O₃ coatings for challenging cutting and die casting applications,“ *Thin Solid Films*, pp. 131-142, 1 October 2018.
- [75] M. Wendman, „Wendmans view on nanotech,“ [Online]. Available: <http://mark-nano.blogspot.cz/2006/02/another-puzzle-this-time-thin-films.html>.
- [76] „Revise Science,“ [Online]. Available:
<http://www.reviescience.co.uk/2010/images/0911diffusion.jpg>.
- [77] „Wear on cutting edges,“ Sandvik, [Online]. Available:
(http://www.Sandvik.coromant.com/en-us/knowledge/materials/cutting_tool_materials/wear_on_cutting_edges).
- [78] Yamaha Motor Corporation USA, [Online]. Available:
<https://global.yamaha-motor.com/about/technology/spread/007/>.
- [79] CDTooling.com, „Drill Bits,“ [Online]. Available:
<https://www.carbideanddiamondtooling.com/drills.bit.solid.carbide>.
- [80] „Face milling cutters,“ [Online]. Available:
<http://www.osgtool.com/Product-List/Indexable/FaceMillingCutters>.
- [81] K. Bobzin, T. Brogelmann, R. Brugnara a N. Kruppe, „CrN/AlN and CrN/AlN/Al₂O₃ coatings deposited bz pulsed cathodic arc for aluminium die casting applications,“ *Surface & Coatings Technology*, 2015.
- [82] P. Kulhánek, Úvod do teorie plazmatu, AGA, 2011.
- [83] J. Musil a H. Hrubý, „Superhard nanocomposite TiAlN films prepared by magnetron sputtering,“ *Thin Solid Films*, č. 365, 2000.
- [84] W.Z. Li, Q. Chen, T. Polcar, R. Serra a A. Cavaleiro, „Influence of Zr alloing on the mechanical properties, thermal stability and oxidation resistance oc Cr-Al-N coatings,“ *Applied surface science*, č. 317, 2014.

[85] M.Danek, F.Fernandes, A.Cavaleiro a T.Polcar, „Influence of Cr additions on the structure and oxidation resistance of multilayered TiAlCrN films,“ *Surface & Coatings Technology*, pp. 158-167, 2017.

[86] Ceratizit, „Turning,“ [Online]. Available:

<https://commons.wikimedia.org/w/index.php?curid=18494559>.

[87] [Online]. Available: [<https://commons.wikimedia.org/w/index.php?curid=3837309>].

List of publications

Publications related to topic of the thesis:

Publication in international journal:

Daněk, M.; Fernandes, F.; Cavaleiro, A.; Polcar, T. (25%, 25%, 25%, 25%)*

Influence of Cr additions on the structure and oxidation resistance of multilayered TiAlCrN films, Surface & Coatings Technology. 2017, 313 158-167. ISSN 0257-8972.

15 citations; IF 2.906

Publication in international journal:

Fernandes, F.; Daněk, M.; Polcar, T.; Cavaleiro, A. (25%, 25%, 25%, 25%)*

Tribological and cutting performance of TiAlCrN films with different Cr contents deposited with multilayered structure, Tribology International. 2018, 119 345-353. ISSN 0301-679X.

6 citations; IF 2.38

Publications related to other topics:

Publication in international journal:

Bernardo Pimentel, J.; Daněk, M.; Polcar, T.; Cavaleiro, A. (25%, 25%, 25%, 25%)*

Effect of rough surface patterning on the tribology of W-S-C-Cr self-lubricant coatings Tribology International. 2014, 69 77-83. ISSN 0301-679X.

7 citations; IF 2.71

Publication in international journal:

Callisti, M.; Daněk, M.; Yasuda, K.; Evaristo, M.; Tichelaar, F.D.; Cavaleiro, A.; Polcar, T.
(11.2%, 22%, 11.2%, 11.2 %, 11.2%, 11.2%, 22%)*

Ni-Ti(-Cu) shape memory alloy interlayers supporting low friction functional coatings

Tribology International. 2015, 88(1), 135-142. ISSN 0301-679X.

2 citations, IF 2.76

* Percentage is based on V3S database

Annexes:

Matlab code:

```
%Pocitani rezonance v magnetronu
clc;
close all;
clear all;

% % % % Nastaveni% % % %
tm=20*60; %doba depozice
Ts=30; %table speed v procentech
W=[7, 3.7, 4, 7]; %vykon targetu kW

%Intensity vyzarovani
%5000W (Cr= 0.4 nm/s, Ti=0.146 nm/s, Al=0.305 nm/s)
%pomery intenzit (Cr 1, Al/Cr 0.676, TiAl/Cr 0.245)
% pro 3 osy z programu 128: nm/s/kW :0.042, Al 0.028, TiAl 0.01

Al= 0.028; %nm/s/kW
Cr= 0.042; %nm/s/kW
TiAl=0.010; %nm/s/kW

OK=40; %opravna konstanta pro nastaveni tloustky vrstvy
tg1=OK*TiAl*W(1); %nm za vterinu; dle CC tg4
tg2=OK*Cr*W(2); %nm za vterinu; dle CC tg3
tg3=OK*Al*W(3); %nm za vterinu; dle CC tg1
tg4=OK*TiAl*W(4); %nm za vterinu; dle CC tg2

% pak jeste nastavit, ktere targety jsou setejne na radku 225

om1= Ts/30*6; %obvodova rychlost stolu 30==6st za vterinu
om2= 3.0833*om1; %obvodova rychlost veze (1110stupnu na jednu otocku stolu)
% om3= 0.5417*om2; % 195 stupnu otocky na jednu otocku veze - diskretne

t=0:tm; %s

filn=(om1*t); %uhel rotace
fi1=mod(filn,360); %do 360

fi2n=(om2*t);
fi2=mod(fi2n,360); %do 360

fi3n=zeros([1,max(t)]);

l1=135; %polomer stolu
l2=65; %polomer veze

trot=round((Ts/30*3.0833/60)^-1); %Ts/30*3.0833/60; cas kdy se otoci mala
holzna
for j=1:tm
    if mod(j,trot)==0
        fi3n(j:j+trot)=fi3n(j-1)+195; %otocka o 195 stupnu, j+trot je určení
        úhlu do dalšího otočení
    end
end
```

```

end

fi3=mod(fi3n,360); %aby to nebylo nad 360°
% fisr=fi3red*2*pi/360; %prevod na radiany

fi23=mod(fi2+fi3(1:max(size(fi2))),360); % fi2 + fi3 do 360

% fi=sin(om1*t+sin(om2*t+sin(om3*t)));

% plot(t,fi1,t,fi2, t,fi);

p=zeros([4,max(t)]); %matice pro povlak

p1=360-30; %podminka1, uhel -30 deg
p2=0; %podminka1, uhel 0 deg
p3=60; %podminka1, uhel 60 deg
p4=90; %podminka1, uhel 90 deg

p5=180-p4;
p6=180-p3;
p7=180-p2;
p8=180+30;

p9=180-30;
p10=180+p2;
p11=180+p3;
p12=180+p4;

p13=360-p4;
p14=360-p3;
p15=360-p2;
p16=30;

tg=[tg1,tg2,tg3,tg4];

% target 1, condition I, interval 1-3
t111= fi1>=p1 & fi1<360;
t112= fi1>=p2 & fi1<p3;
t113= fi1>=p3 & fi1<p4;

% target 1, condition II, interval 1-3
t121= fi2>=10 & fi2<83;
t122= fi2>=300 | fi2<60;
t123= fi2>=260 & fi2<350;

% target 1, condition III, interval 1-3
t131= fi23>=10 & fi23<83;
t132= fi23>=300 | fi23<60;
t133= fi23>=260 & fi23<350;

% target 2, condition I, interval 1-3
t211= fi1>=p5 & fi1<p6;
t212= fi1>=p6 & fi1<p7;
t213= fi1>=p7 & fi1<p8;

% target 2, condition II, interval 1-3
t221= fi2>=10 & fi2<100;

```

```

t222= fi2>=300 | fi2<60;
t223= fi2>=260 & fi2<333;

% target 2, condition III, interval 1-3
t231= fi23>=10 & fi23<100;
t232= fi23>=300 | fi23<60;
t233= fi23>=260 & fi23<333;

% target 3, condition I, interval 1-3
t311= fi1>=p9 & fi1<p10;
t312= fi1>=p10 & fi1<p11;
t313= fi1>=p11 & fi1<p12;

% target 3, condition II, interval 1-3
t321= fi2>=10 & fi2<83;
t322= fi2>=300 | fi2<60;
t323= fi2>=260 & fi2<350;

% target 3, condition III, interval 1-3
t331= fi23>=10 & fi23<83;
t332= fi23>=300 | fi23<60;
t333= fi23>=260 & fi23<350;

% target 4, condition I, interval 1-3
t411= fi1>=p13 & fi1<p14;
t412= fi1>=p14 & fi1<p15;
t413= fi1>=0 & fi1<p16;

% target 4, condition II, interval 1-3
t421= fi2>=10 & fi2<100;
t422= fi2>=300 | fi2<60;
t423= fi2>=260 & fi2<333;

% target 4, condition III, interval 1-3
t431= fi23>=10 & fi23<100;
t432= fi23>=300 | fi23<60;
t433= fi23>=260 & fi23<333;

for i=1:tm
%   target 1
    if t111(i) & t121(i) & t131(i)
        p(1,i)=tg1;
    end

    if t112(i) & t122(i) & t132(i)
        p(1,i)=tg1;
    end

    if t113(i) & t123(i) & t133(i)
        p(1,i)=tg1;
    end

%   target 2
    if t211(i) & t221(i) & t231(i)
        p(2,i)=tg2;
    end

```

```

end

if t212(i) & t222(i) & t232(i)
    p(2,i)=tg2;

end

if t213(i) & t223(i) & t233(i)
    p(2,i)=tg2;
end

% target 3
if t311(i) & t321(i) & t331(i)
    p(3,i)=tg3;

end

if t312(i) & t322(i) & t332(i)
    p(3,i)=tg3;

end

if t313(i) & t323(i) & t333(i)
    p(3,i)=tg3;
end

% target 4
if t411(i) & t421(i) & t431(i)
    p(4,i)=tg4;

end

if t412(i) & t422(i) & t432(i)
    p(4,i)=tg4;

end

if t413(i) & t423(i) & t433(i)
    p(4,i)=tg4;
end

end

pp=p;
cc=0;
c=0;
for j=1:tm
    if p(1,j-cc)+p(2,j-cc)+p(3,j-cc)+p(4,j-cc)==0

        for k=j-c:tm-1
            p(:,k-cc)=p(:,k+1-cc);

```

```

        end
        cc=cc+1;
    else
        c=0;
    end

end

pp2=p(:,1:tm-cc);

% plot((1:tm-cc),p(1,1:tm-cc),(1:tm-cc),p(2,1:tm-cc),(1:tm-cc),p(3,1:tm-
cc),(1:tm-cc),p(4,1:tm-cc))

% Zobrazení výsledku

tmax=sum(sum(pp2)); %tloušťka cele vrstvy v nm

% převedení osy X z času na tloušťku
x=0:0.1:tmax; %vektor tloušťky vrstvy

%zaokrouhlení příspěvku do vrstvy na 0.1 nm
pp3=round(pp2.*10)/10;

T=zeros(4,floor(tmax*10));
xx=1; %pomocna promenna pocita ve ktere casti T je prave ukayatel

%poměr zastoupení prvku v povlaku
for l=1:max(size(pp3))
    sm=sum((pp3(:,l).*10)); %pomocna promena suma prispevku v case l
    for m=1:sm
        MM(:,m)=pp3(:,l)/sm*10;
    end
    T(:,xx:(xx+sm-1))=MM;
    xx=xx+sm;
    MM=[0;0;0;0];
end

% nastaveni kdyz jsou targety stejne
% matice prispevku z targetu 1 - 4
TT=[T(1,:);T(2,:);T(3,:);T(4,:)];

B=TT.'; %transponovani vysledku do sloupcu pro vykresleni
X=linspace(0,tmax,max(size(B))); %nastaven9 osy X

figure
hold on
h=area(X,B); %vykresleni vysledku funkci area
legend('TiAl','Cr','Al','TiAl')
hold on
% nastavit barvy dle targetu
h(1).FaceColor = [0.9 0.25 0.25];
h(2).FaceColor = [0 0.9 0.5];
h(3).FaceColor = [0 0.75 0.9];
h(4).FaceColor = [0.9 0.25 0.25];

% a=[1,1,1,1,1];

```

```
% konv=conv(povlak,a);  
% k = find(konv==5), %alespon 5 vterin zamirene na jeden target  
% pv=length(k) %pocet vrstev z jednoho targetu  
  
% % % % poznamky% % % %  
% po dosazeni ciste experimentalnich dat je tloustka na cca 1/40 skutecneho  
% povlaku
```